Technische Universität München
TUM School of Natural Sciences

Advancement of PEDOT:PSS as thermoelectric material and the investigation of environmental influences on its performance

Anna Lena Oechsle

Vollständiger Abdruck der von der TUM School of Natural Sciences der Technischen Universität München zur Erlangung einer

Doktorin der Naturwissenschaften (Dr. rer. nat.)

genehmigten Dissertation.

Vorsitz: Prof. Dr. Martin Zacharias
Prüfende der Dissertation: 1. Prof. Dr. Peter Müller-Buschbaum
2. apl. Prof. Dr. Martin Brandt

Die Dissertation wurde am 05.02.2024 bei der Technischen Universität München eingereicht und durch die TUM School of Natural Sciences am 26.02.2024 angenommen.

Abstract

In this thesis, organic semiconducting PEDOT:PSS thin films are investigated in terms of their thermoelectric potential under the influence of different factors. The thermoelectric properties of PEDOT:PSS are strongly dependent and highly tunable due to its particular polymer blend structure of conductive PEDOT-rich domains embedded in a non-conducting PSS matrix. A systematic study is performed, which unravels the thermoelectric property enhancing effects of ionic liquid post-treatment on the structure-electronic-function relation of PEDOT:PSS thin films. Furthermore, the impact of temperature and relative humidity on the thermoelectric parameters, conductivity and Seebeck coefficient, of these post-treated films are determined. For this, the post-treated PEDOT:PSS thin films are examined regarding their morphology, oxidation level, and property relations, mainly using X-ray and neutron scattering studies and ultraviolet-visible spectroscopy, complemented by thermoelectric characterization. Various *in situ* experiments were conducted to investigate the influences of temperature and relative humidity.

Zusammenfassung

In dieser Dissertation wird das thermoelektrische Potenzial von organischen halbleitenden PEDOT:PSS-Dünnschichten in Abhängigkeit verschiedener Einflussfaktoren untersucht. Die Eigenschaften von PEDOT:PSS sind stark abhängig von dessen besonderer Struktur, welche aus leitfähigen PEDOT-Domänen eingebettet in einer nichtleitende PSS-Matrix besteht, und ermöglicht dadurch ein hohes Maß an Variierbarkeit. Anhand einer systematischen Studie werden die Auswirkungen einer Nachbehandlung mit ionischen Flüssigkeiten auf die strukturellen und elektronischen Eigenschaften von PEDOT:PSS-Dünnschichten zur Verbesserung der thermoelektrischen Performance aufgedeckt. Darüber hinaus werden die Auswirkungen von Temperatur und relativer Luftfeuchtigkeit auf die thermoelektrischen Parameter, Leitfähigkeit und Seebeck-Koeffizient, dieser nachbehandelten Filme bestimmt. Hierzu werden die PEDOT:PSS-Dünnschichten hinsichtlich ihrer Morphologie, ihres Oxidationsgrades und ihrer Eigenschaftsbeziehungen untersucht, hauptsächlich mit Hilfe von Röntgen- und Neutronenstreustudien, Ultraviolett-Spektroskopie, sowie thermoelektrischen Charakterisierungsmethoden. Für die Analyse der Temperatur- und relativen Luftfeuchtigkeitseinflüsse werden die Ergebnisse verschiedener *In-situ* Experimente präsentiert.

Contents

Abstract I

Contents III

List of abbreviations VII

1. Introduction 1

2. Theoretical background 7

  2.1 Organic semiconductors 7

    2.1.1 Conductive polymers 8

    2.1.2 PEDOT:PSS 14

    2.1.3 Doping of PEDOT:PSS 16

  2.2 Thermoelectric principles in organic polymers 19

    2.2.1 Basics of thermoelectric effects 19

    2.2.2 Thermoelectric effects 22

    2.2.3 Characterization of thermoelectric materials 25

    2.2.4 PEDOT:PSS as thermoelectric materials 28

  2.3 Scattering methods 30

    2.3.1 Scattering basics 30

    2.3.2 X-ray reflectometry 37

    2.3.3 Grazing-incidence small-angle X-ray scattering 40

    2.3.4 Time-of-flight neutron reflectometry 42

3. Characterization methods 45

  3.1 Spectroscopic characterization 45

    3.1.1 Ultraviolet-visible spectroscopy 45

3.1.2 Fourier-transform infrared spectroscopy 48

3.1.3 Spectral reflectance 51

3.2 Electrical characterization 53

3.2.1 Seebeck coefficient measurement 54

3.2.2 Two-point probe resistance measurements 55

3.2.3 Four-point probe resistance measurements 57

3.2.4 Electrochemical impedance spectroscopy 58

3.3 Structural characterization in real space 63

3.3.1 Surface profilometry 63

3.3.2 Conductive atomic force microscopy 65

3.4 Structure characterization in reciprocal space 66

3.4.1 X-ray reflectometry 67

3.4.2 Grazing-incidence small-angle X-ray scattering 69

3.4.3 Time-of-flight neutron reflectometry 73

3.5 *In situ* characterization environments 75

3.5.1 X-ray analysis voltage-emulation rig 75

3.5.2 Gas flow system 77

3.5.3 Universal chamber for observation of reflectivity with neutrons 79

4. Sample preparation 81

4.1 Materials 81

4.1.1 Substrate materials 81

4.1.2 Poly(3,4-ethylene dioxythiophene):poly(styrene sulfonate) 82

4.1.3 Ionic liquids 83

4.1.4 Additives, solvents, and cleaning agents 84

4.1.5 Additional materials for sample fabrication 86

4.2 Substrate preparation 87

4.2.1 Glass substrates 87

4.2.2 Silicon substrates ... 88

4.2.3 Indium-doped tin oxide glass substrates ... 89

4.3 PEDOT:PSS thin film preparation ... 90

4.3.1 PEDOT:PSS solution preparation ... 90

4.3.2 Spin-coating and annealing ... 91

4.4 Ionic liquid doping ... 92

4.4.1 Doping solution preparation ... 92

4.4.2 Doping and annealing ... 93

4.5 Sample contacting ... 94

4.5.1 Silver paint contacting ... 95

4.5.2 Gold contact evaporation ... 95

5. Ionic liquid post-treatment of thin PEDOT:PSS films ... 97

5.1 ILs as doping agent for PEDOT:PSS ... 98

5.2 Effect of ILs on the PEDOT:PSS oxidation level ... 101

5.3 Effect of ILs on the PEDOT:PSS morphology ... 104

5.4 Model description of IL post-treatment effect ... 113

5.5 Film-aging investigation ... 115

5.6 Summary ... 117

6. Temperature influence on ionic liquid post-treated PEDOT:PSS films ... 119

6.1 In situ temperature investigation of ILs post-treated PEDOT:PSS ... 120

6.2 Evolution of the electrical conductivity ... 122

6.3 Evolution of the morphology ... 126

6.4 Evolution of the oxidation level ... 133

6.5 Model description of the temperature-dependent thermoelectric behavior ... 135

6.6 Summary ... 137

7. Humidity influence on ionic liquid post-treated PEDOT:PSS films ... 139

7.1 Influence factor humidity o IL post-treated PEDOT:PSS ... 140

7.2 Humidity-dependent film resistance 142

7.3 Humidity-dependent morphology changes 144

7.4 Investigation of different conductivity contributions 150

7.5 Model description of the PEDOT:PSS charge transport behavior 153

7.6 Summary 157

8. Humidity influence on electric and ionic charge transport in PEDOT:PSS films 159

8.1 In situ humidity investigation of IL post-treated PEDOT:PSS 160

8.2 Humidity-dependent film swelling and water uptake 162

8.3 Electrochemical investigation of conductivity contributions 172

8.4 Model description of the humidity influence on PEDOT:PSS 175

8.5 Summary 179

9. Conclusion 181

Bibliography 187

List of figures 217

List of publications 221

Acknowledgments 227

List of abbreviations

Ag	silver
AMIM	1-allyl-3-methylimidazolium
ATR	attenuated total reflectance
Au	gold
B^+, B^-	positively and negatively charged bipolaron
C	carbon
c-AFM	conductive atomic force microscopy
CCD	charge carrier density
D	deuterium
D_2O	deuterated water
DCA	dicyanamide
DI-H_2O	de-ionized water
DMF	dimethylformamide
DMSO	dimethyl sulfoxide
DOS	density of states
DWBA	distorted-wave Born approximation
ECM	equivalent circuit model
EIA	effective interface approximation
EIS	electrochemical impedance spectroscopy
EMIM	1-ethyl-3-methylimidazolium

FTIR	Fourier-transform infrared spectroscopy
GISAXS	grazing-incidence small-angle X-ray scattering
GIWAXS	grazing-incidence wide-angle X-ray scattering
H	hydrogen
H_2O_2	hydrogen peroxide
H_2SO_4	sulfuric acid
HCl	hydrochloric acid
holes	polymeric holes
HOMO	highest occupied molecular orbital
IL	ionic liquid
IR	infrared light
ITO	indium-doped tin oxide
Kapton®	Kapton® polyimide
LCAO	linear combination of atomic orbital
LED	light-emitting diode
LMA	local monodisperse approximation
LUMO	lowest unoccupied molecular orbital
MIEC	mixed ionic-electronic conductor
N_2	nitrogen gas
P^+, P^-	positively and negatively charged polaron
PA	polyacetylene
PEDOT	poly(3,4-ethylene dioxythiophene)
PSS	poly(styrene sulfonate)
Pt	platinum

PTFE	poly(tetrafluoroethylene)
PVDF	polyvinylidene fluoride
QP	quasi-particles
RH	relative humidity
RT	room temperature
S^0, S^+, S^-	neutral, positively and negatively charged soliton
SDD	sample-detector distance
SLD	scattering length density
SR	spectral reflectance
SSH	Su-Schrieffer-Heeger
TCB	tetracyanoborate
THF	tetrahydrofuran
TE	thermoelectric
ToF-NR	time-of-flight neutron reflectometry
UNICORN	universal chamber for observation of reflectivity with neutrons
UV-Vis	ultraviolet-visible light
XAVER	X-ray analysis voltage-emulation rig
XRR	X-ray reflectometry
Zn	zinc
Zonyl®	Zonyl® FS-300

1 Introduction

Thermoelectric materials are capable of directly converting thermal energy into electrical power. This feature is based on the Seebeck effect, which describes the emergence of a thermovoltage upon the application of a temperature gradient. Therefore, thermoelectric materials are applicable in thermoelectric generators, which can be used in multiple applications like solar thermal energy harvesting or waste heat recovery. As in several areas of daily life, such as transportation, domestic energy consumption, and in industry, a large fraction of primary energy input is lost as waste heat, thermoelectric materials and their potential to partially recover this waste heat are promising to contribute significantly to global sustainable energy solutions.[1–3]

In general, two classes of thermoelectric materials can be distinguished, namely inorganic and organic. So far, mainly inorganic thermoelectric materials comprising heavy elements like bismuth, tellurium, silver, or lead have been conventionally utilized. However, although this material class provides good thermoelectric properties and temperature stability, it has some disadvantages. For example, these materials often contain toxic and scarce components and are challenging and expensive to process, which limits their field of application.[4, 5] Therefore, the research focus has shifted towards the new and promising class of organic thermoelectric materials, which provide several advantages. They are mainly based on conductive organic polymers, which allow for a cost- and energy-efficient solution-based processability with large-scale deposition techniques like printing, spraying, or dip coating, and they are usually low or non-toxic.[6, 7] Additionally, these organic materials are generally abundant, possess an intrinsically low thermal conductivity, and facilitate the fabrication of thin, lightweight, and mechanically flexible thermoelectric devices. With all their advantageous properties, these organic materials provide the best prerequisites for extensive application in a wide range of thermoelectric devices.[8–10]

For the thermoelectric potential evaluation of a material, three different parameters are crucial. First, the Seebeck coefficient (S), which defines the extent of the thermovoltage in relation to the temperature gradient applied along the material. Second, the electrical conductivity (σ) of the material, and third, its thermal conductivity (κ). All three parameters are combined in the thermoelectric figure of merit ($Z\bar{T}$), which can be used to assess the thermoelectric efficiency of a material. Moreover, the thermoelectric performance of a material can also be evaluated with the thermoelectric power factor ($PF = S^2\sigma$), which will be the assessment parameter utilized for the samples examined in this thesis.[11, 12]

One specific organic material has proven to be especially promising to fit the criteria of an excellent thermoelectric material. It is the polymer blend poly(3,4-ethylene dioxythiophene):poly(styrene sulfonate), PEDOT:PSS, which is the subject of investigations in this thesis. PEDOT:PSS has become a popular and widely investigated material not only for the application as a thermoelectric material, because, in addition to possessing all the aforementioned advantages of organic semiconducting polymers, it also exhibits excellent optical and electronic properties. For example, it can be fabricated into transparent and flexible thin films that achieve hole conductivities of up to 10^3 S cm^{-1}.[13–15]

The exceptional and favorable combination of properties of PEDOT:PSS originates in its particular morphology, namely the composition of two different polymers, which are ionically bound to one another. On the one hand, it consists of the insoluble but excellent semiconductor PEDOT, which facilitates the conductance of positive charge carriers, referred to as holes, and on the other hand, it comprises the non-conductive but highly water-soluble polyanion PSS.[16, 17] As schematically sketched in Figure 1.1, in an aqueous solution, the insoluble PEDOT chains tend to agglomerate and form spherical PEDOT enriched domains, which are surrounded and stabilized by a shell mainly consisting of the water-soluble PSS.[16, 18] If using this aqueous PEDOT:PSS solution to prepare thin films, upon water evaporation, the described core-shell structure leads to the formation of pancake-shaped PEDOT-enriched domains, which are embedded in a matrix of PSS.[19] As PEDOT is accountable for the excellent hole transport within the polymer blend, the intra-domain conductivity is high. For overall film conductivity the holes also need to travel between the PEDOT-enriched domains, however, this inter-domain transport is hindered by the surrounding non-hole conductive PSS matrix.[20, 21] Consequently, the precise arrangement of this particular domain morphology significantly affects the electronic and thermoelectric properties of PEDOT:PSS and, more interestingly, an aimed modification of it allows for their high tunability.

So far, most research has aimed to weaken the electrostatic interactions between PEDOT and PSS chains to favorably customize the domain morphology and to partly remove excessive PSS. Some approaches are based on the treatment of PEDOT:PSS with different solvents[22–26], inorganic salts[27–29], acids or bases[30–33], or surfactants[34–37], which successfully result in an improvement of the electrical conductivity. Others aim to alter the PEDOT oxidation level, for example, with inorganic[27, 28, 38–40] or organic[41–43] reducing agents, resulting in an improvement of the Seebeck coefficient. However, with these methods, usually only one of the thermoelectric parameters σ or S is improved, which can even occur to the detriment of the other. Therefore, approaches especially promising for the thermoelectric application of PEDOT:PSS are methods that simultaneously improve σ and S, such as the post-treatment with ionic liquids (ILs).[44–49]

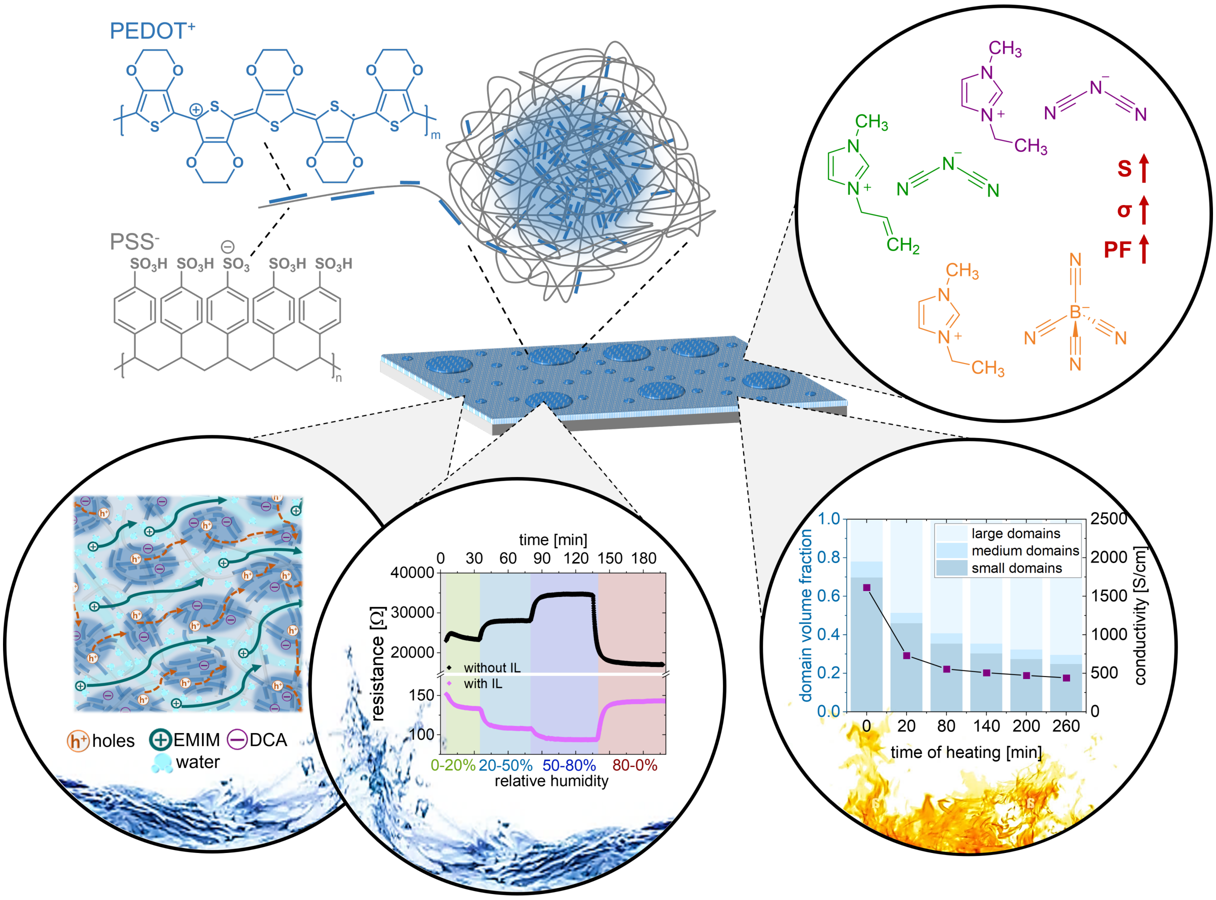

Figure 1.1 Schematic overview of the research topics covered in this thesis. Investigation of the influence of ionic liquid post-treatment on thermoelectric PEDOT:PSS thin films is sketched in the top right. Thermoelectric property changes of EMIM DCA post-treated PEDOT:PSS thin films upon the influence of elevated temperatures are presented in the bottom right image. Adapted with permission from Oechsle et al.[50] Copyright 2022 American Chemical Society. The picture in the bottom center demonstrates the effect of relative humidity on the morphology and electrical resistance of EMIM DCA post-treated PEDOT:PSS thin films. Adapted with permission from Oechsle et al.[51] Copyright 2023 American Chemical Society. A detailed view of the electronic and ionic charge carrier transport in EMIM DCA post-treated PEDOT:PSS thin films upon the influence of the relative humidity is shown in the bottom left sketch. Adapted with permission from Oechsle et al.[52] Copyright 2023 American Chemical Society.

Even though numerous research works present ways to improve PEDOT:PSS for possible future applications, either as a thermoelectric material or in other organic electronics,[53–59] a general and basic understanding of the underlying effects resulting from these improvement methods is often not provided. However, this basic understanding of the effects is essential in terms of the strategic development of these improvement methods and the selection of treatment agents to achieve a purposeful adjustment of the PEDOT:PSS parameters. Furthermore, the effects of environmental influences and the stability of these PEDOT:PSS thin films have not been sufficiently understood and discussed in the literature. However, this is a crucial point that needs to be tackled when considering the suitability of the material for future applications. For example, especially in thermoelectric applications, the PEDOT:PSS-based materials will be exposed to elevated temperatures or various atmospheres over a long time during operation.

Therefore, this thesis addresses the following scientific issues: unraveling the underlying effects on PEDOT:PSS upon IL post-treatment, the investigation of the influence of elevated temperature on the properties and stability of these IL post-treated PEDOT:PSS thin films, and the impact of relative humidity with a focus on the function-morphology correlation and the charge carrier transport specifics of PEDOT:PSS thin films either with or without IL post-treatment.

Fundamental theoretical background is provided in Chapter 2, which is helpful for a better comprehension of the presented work. Furthermore, all in the frame of this thesis utilized characterization methods are explained in Chapter 3, and the materials and procedures used to prepare the examined samples are detailed in Chapter 4.

The first research topic presented in Chapter 5 of this thesis covers the investigation of the different underlying effects of IL post-treatment on PEDOT:PSS thin films that cause the enhancement of the thermoelectric properties. As schematically depicted in Figure 1.1, for this, three different ILs with varying anions and cations are chosen, namely 1-allyl-3-methylimidazolium dicyanamide (AMIM DCA), 1-ethyl-3-methylimidazolium dicyanamide (EMIM DCA), and 1-ethyl-3-methylimidazolium tetracyanoborate (EMIM TCB). The PEDOT:PSS thin films post-treated with different concentrations of these ILs are examined in terms of oxidation level variations using ultraviolet-visible (UV-Vis) spectroscopy, and the results are correlated to the measured Seebeck coefficients. With conductive atomic force microscopy (c-AFM) and grazing-incidence small-angle X-ray scattering (GISAXS), the surface and inner film morphology of these IL post-treated PEDOT:PSS thin films are analyzed, revealing an interrelation with their electrical conductivity behavior. This study successfully investigates the various underlying effects of the IL post-treatment on PEDOT:PSS. A detailed understanding of the relation between the PEDOT:PSS oxidation level, film morphology, and the successfully enhanced thermoelectric performance is presented in dependence of the IL ions characteristics used for post-treatment.

Chapter 6 examines the influence of elevated temperature on EMIM DCA post-treated PEDOT:PSS thin films, as sketched in Figure 1.1. For this, the temperature-dependent conductivity of these thin films is recorded over time, presenting a disparate conductivity degradation behavior for the different EMIM DCA concentrations. With *in situ* UV-Vis spectroscopy studies, the effect of temperature on the polymers' oxidation level is demonstrated, and *in situ* GISAXS measurements evidence the impact of the operation temperature on the inner film domain morphology. The results are correlated to the thermoelectric properties of the IL post-treated PEDOT:PSS thin films and, with this, provide an essential understanding of the degradation processes and the applicability of these thermoelectric materials at different temperature ranges.

In addition, the significant influence of relative humidity in the environment of EMIM DCA post-treated PEDOT:PSS thin films is investigated in this thesis. The work discussed in Chapter 7 first studies the effect of relative humidity on the electrical resistance of PEDOT:PSS thin films post-treated with different concentrations of EMIM DCA. As indicated in Figure 1.1, an interesting humidity-dependent resistance evolution is discovered, which behaves opposite for films that were treated or were not treated with EMIM DCA. The underlying effect of this behavior reversal is examined with *in situ* GISAXS, which allows for the characterization of alterations in the inner films' PEDOT domain morphology upon exposure to elevated relative humidities. Furthermore, electrochemical impedance spectroscopy (EIS) of the PEDOT:PSS thin film samples is performed at different defined relative humidities, which demonstrate an additional ionic contribution to the charge carrier transport in PEDOT:PSS, arising from the within the film incorporated EMIM DCA ions.

Following this finding, the research study presented in Chapter 8 and sketched in Figure 1.1 concentrates on the further investigation of these ionic and electronic charge carrier transport contributions. For this, the humidity-dependent film thickness swelling and water uptake evolution of PEDOT:PSS thin films post-treated with different concentrations of EMIM DCA is measured with *in situ* spectral reflectance (SR) and *in situ* time-of-flight neutron reflectometry (ToF-NR). Additionally, *in situ* EIS investigations are conducted, which enable an insight into the respective humidity-dependent evolution and extent of the ionic and electronic conductivities of differently post-treated PEDOT:PSS thin films. By combining the research results obtained in this study, the effects of relative humidity on the PEDOT:PSS thin film structure and the differently pronounced contributions of electronic and ionic charge carrier transport are better understood. Which also explains the discovered change towards a positive humidity-dependent resistance behavior for EMIM DCA post-treated films, compared to untreated PEDOT:PSS.

In summary, in this thesis the underlying effects of IL post-treatment on PEDOT:PSS are unraveled, and by this, a way to strategically select IL ions for the aimed adjustment of thermoelectric parameters is presented. Furthermore, the temperature-dependent conductivity degradation process and the impact of relative humidity on the charge carrier transport in EMIM DCA post-treated PEDOT:PSS films are demonstrated. Both significantly contribute to a more precise assessment of feasible operation conditions and stability of PEDOT:PSS-based materials, which is crucial for application in thermoelectric devices or organic electronics.

2 Theoretical background

This chapter contains an insight into the theoretical background of chemical and physical concepts, which are relevant for understanding the research scope, the underlying studies, and the results in this present thesis. Section 2.1 introduces the topic of organic semiconductors, more precisely conjugated polymers, and provides details about the structure, properties, and doping specifics of the in this thesis examined polymer PEDOT:PSS. Section 2.2 presents the general aspects of the thermoelectric effect, whereby the focus is put on the Seebeck coefficient and the electronic conductivity in organic polymers like PEDOT:PSS. Section 2.3 covers the basic scattering theories and the fundamentals of the XRR, GISAXS, and ToF-NR characterization techniques.

2.1 Organic semiconductors

Organic semiconductors are usually described as π-conjugated materials mainly consisting of carbon (C) and hydrogen (H) atoms, which can be present in the form of molecules, oligomers, or polymers. As in this thesis, the organic semiconducting polymer PEDOT:PSS is investigated, the following section introduces the fundamentals of this material class and provides a description of PEDOT:PSS itself.

Polymers are macromolecules composed of a sequence of small repeating subunits named monomers, which are covalently bound via a polymerization process. For organic polymers, these monomers are typically based on C-bonds, facilitating up to four covalent bonds and thus enabling the easy formation of long and branching polymer networks. As the formed polymer results in a specific chain constitution, which depends on the used monomers and polymerization reaction, the degree of polymerization, molar mass, and chain length distribution are typical values to describe a polymer.[60] By selecting the monomers and the reaction mechanism, polymer materials can be obtained that achieve desired requirements, like specific solubility, desired optical characteristics, or high electrical conducting properties.

2.1.1 Conductive polymers

Polymers are commonly known and often utilized as electrical insulating materials. However, in 1997, it was discovered that a particular type of polymers can be made electrically conductive via doping.[61] In the following, the simple polymer polyacetylene (PA), which shows an increase of its electrical conductivity by seven orders of magnitude upon chemical doping with iodine vapor,[62] is presented as a model to describe the band structure, charge carrier formation, and charge transport of conductive polymers.

The PA solely consists of carbon and hydrogen atoms connected to build a polymer chain. The C atom has four valence electrons, which allow the formation of up to four covalent bonds. In general, the location probability and behavior of electrons in atoms or molecular bonds can be described by quantum mechanical wave functions called orbitals. When combining atoms to form a molecule, the formation of molecular orbitals can be described with the linear combination of atomic orbital (LCAO) method.[63, 64] If two C atoms bind together to form the small PA monomer unit ethylene (C_2H_4), each C atom's $2s^2$ and $2p^2$ orbitals hybridize to three equal sp^2 orbitals and one p_z orbital. As depicted in Figure 2.1a, the sp^2 orbitals form in total four C-H σ-bonds with the s orbitals of the H atoms and one C-C σ-bond, while the p_z orbitals overlap and form a π-bond, resulting in a double bond between the two C atoms. The π-bonds are crucial for the charge transport in polymers, which will be explained in the following by means of Figure 2.1b. According to the LCAO picture, for ethylene, the two overlapping p_z orbitals of the C atoms, each containing one electron, mathematically combine into two π-orbitals. One low-energy bonding π-orbital and one anti-bonding π^*-orbital, standing for constructive or destructive interference, respectively. If now two more C atoms are added to create butadiene (C_4H_6), the p_z overlapping results in the formation of four π-orbitals, two bonding and two anti-bonding, whereby the electrons are found in the low-energy bonding orbitals according to Pauli exclusion principle and Hund's law. The highest occupied molecular orbital is called HOMO, and the lowest unoccupied molecular orbital is called LUMO, and the difference in the respective energy level of HOMO and LUMO is called the energy gap (E_{gap}). So far, the molecular orbitals have distinct energy levels. However, if more and more C atoms are added to constitute polyacetylene, more and more π- and π^*-orbitals are formed, which continuously narrow the E_{gap} and overlap with each other, consequently leading to the formation of π- and π^*-bands. The creation of this band structure is the origin of the conductivity properties because the electrons are delocalized within the HOMO- and LUMO-bands and can move freely along the polymer backbone. Likewise, as in the valence and conduction bands of inorganic semiconductors.[64]

Due to the orbital overlapping in the PA chain and the thus resulting electron delocalization, one could expect a metallic conductivity behavior along the backbone. However, this would only be true for an ideal, infinite, and linear polymer chain, where all C-C bonds are of similar length with an equidistance a between each C-atom and thus equally distributed electrons.

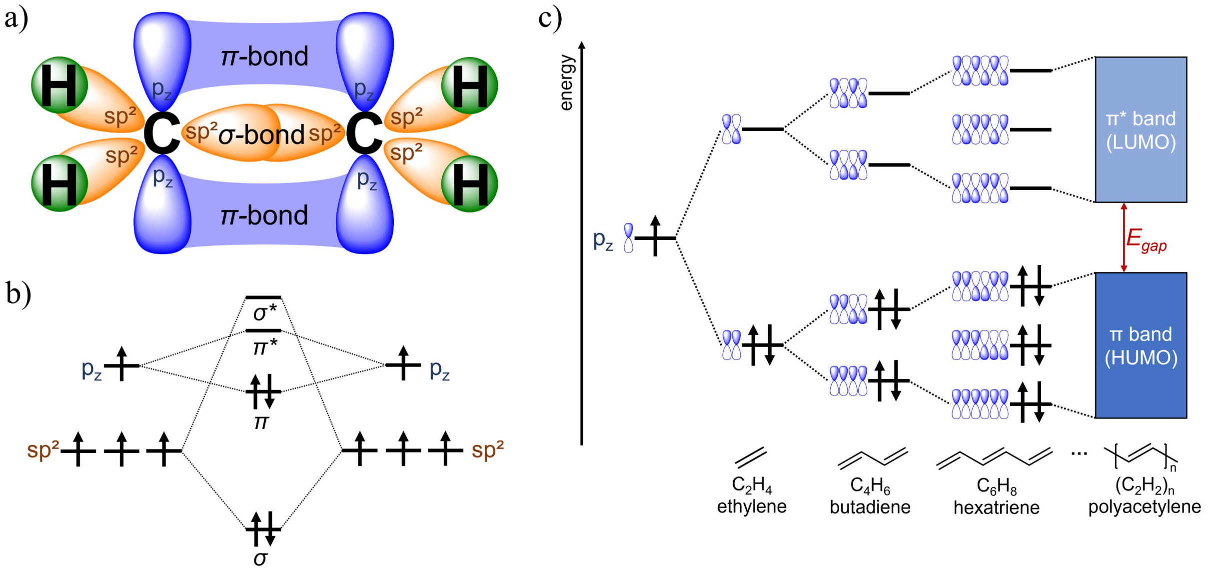

Figure 2.1 Molecular orbital structure in polyacetylene. a) Molecular orbital structure of ethylene, consisting of four C-H and one C-C σ-bonds (orange), and a C-C π-bond (blue). b) Corresponding molecular orbital energy level diagram according to the LCAO, which depicts the energy levels of the bonding and anti-bonding, namely π/π^*- and σ/σ^*-orbitals, respectively. c) Energy diagram schematically describing the continuous p_z-orbital overlap upon increasing polymer chain length. Starting from ethylene and resulting in the formation of polyacetylene with π- (HOMO) and π^*- (LUMO) energy bands, and the energy gap E_{gap} in between. Adapted from Gharahcheshmeh et al.[64]

The band structure of such an ideal 1D-chain is depicted in Figure 2.2a. As each C atom contributes one electron into the p_z-orbital, the band is half-filled up to the Fermi level (E_F), and the chain would show metal-like charge transport. However, according to Peierl's instability theorem[65, 66], this ideal 1D-chain with an equidistant periodic lattice of C atoms that each contribute one electron is unstable and can be easily distorted by the smallest disturbances, e.g. atomic oscillations. As pictured in Figure 2.2b, even the slightest lattice distortion δ results in the formation of alternating bonds with bond lengths of $a \pm \delta$. Thus, this dimerization leads to a new periodicity with $2a$ lattice spacing and results in the opening of a band gap (E_{gap}) inside the band structure. Corresponding to the molecular orbital theory, the formation of a fully occupied binding π-orbital band and an unoccupied anti-binding π*-orbital band is energetically preferred, and the creation of this periodic superlattice reduces the total energy of the system. Overall, this emerging band gap with the E_F located within, explains why PA shows semiconducting properties and a generally insulating behavior.[67]

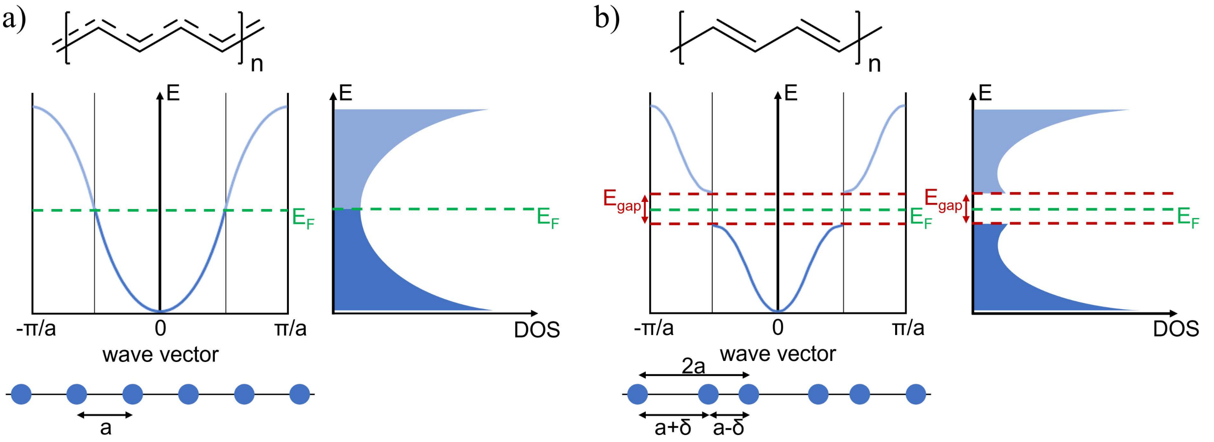

Figure 2.2 Schematic representation of the Peierl's instability theorem. Electronic band structure and density of states in a PA chain according to Peierl's instability theorem. a) For an ideal undisturbed polymer chain with a periodic lattice distance and an energy band, half-filled up to the Fermi Energy E_F. b) Real dimerized polymer chain with a distorted lattice distance, resulting in a superstructure periodicity and an energy band gap E_{gap}. Adapted from the dissertation of Franziska Carina Löhrer.[68]

In polymers like the conjugated polymer PA, chain defects naturally occur, caused, for example, by elimination reactions, impurities, or cross-linking. These defects can lead to the appearance of charge carriers and allow for electrical conductivity in conjugated semiconducting polymers. These charge carriers cannot simply be described by electrons or holes, as in inorganic materials, but by quasi-particles (QPs) that combine lattice distortion and charge.[66] An exemplary depiction of the formation of a soliton QP in the PA chain is shown in Figure 2.3a. Two mesomeric ground states (Phase A and Phase B) of PA are possible; if both exist in one chain, they cause a neutral soliton at their meeting point. This newly created soliton QP state comprises an unpaired electron and is, according to the Su-Schrieffer-Heeger (SSH) theory[69], energetically located within the energy gap. Therefore, this half-unoccupied neutral soliton QP state enables the charge transport along the polymer chain backbone. As a result, the QP, which can be described as a charge density wave, is not localized at one C atom position but can expand over several C atoms; over 14 C atoms in the case of a neutral soliton in PA.[69] There are three types of QPs, each defined by a charge (q) and a spin (s), as depicted in Figure 2.3b. Solitons, which can exist as neutral (S^0), positively (S^+), and negatively (S^-) charged solitons, polarons, and bipolarons, which both can exist either positively (P^+, B^+) or negatively (P^-, B^-)

charged.[60, 66] These different QPs are created, for example, via oxidation or reduction of the polymer chain, or via coupling of QPs, leading either to the formation of new QPs or their annihilation.

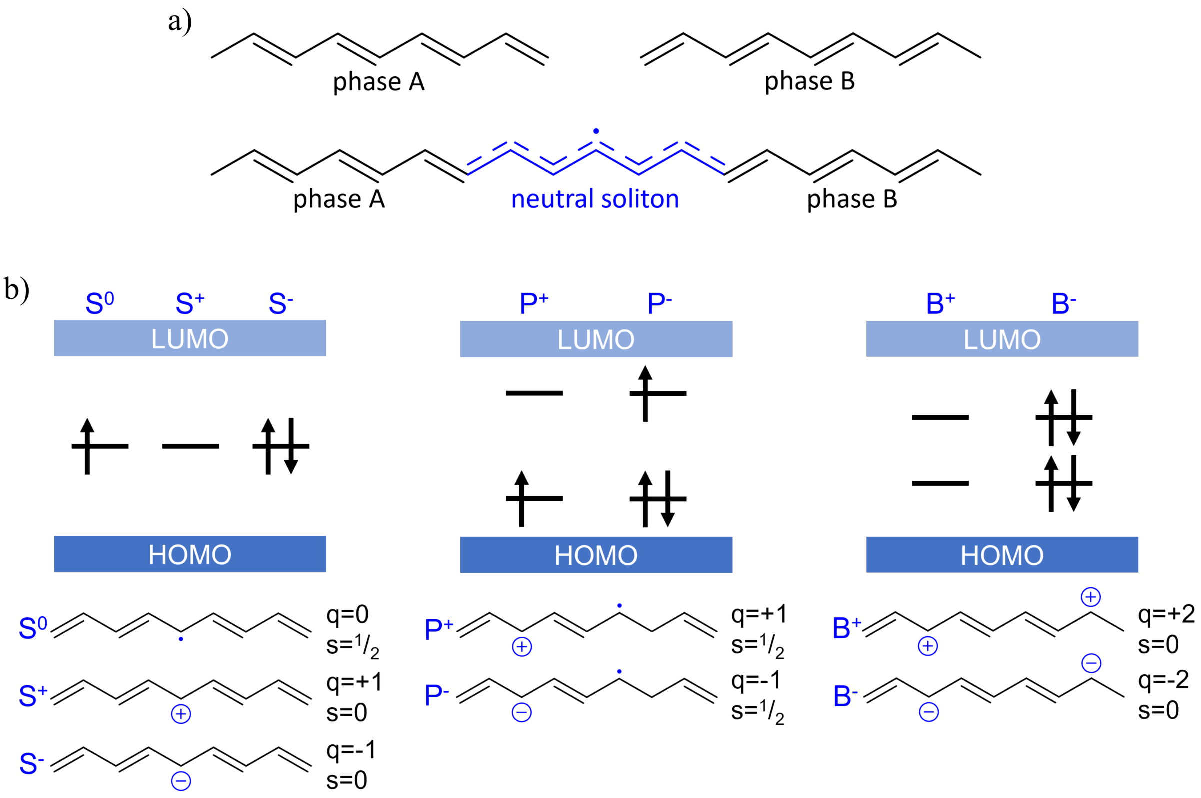

Figure 2.3 Quasi-particles in polyacetylene. a) Exemplary depiction of two mesomeric ground states of PA and the formation of a soliton. b) Different types of QPs with their respective charge (*q*), spin (*s*), and the energy levels formed within the band gap. From left to right, neutral or charged solitons (S^0, S^+, S), charged polarons (P^+, P^-), and charged bipolarons (B^+, B) are shown. Adapted from the dissertation of Franziska Carina Löhrer.[68]

As mentioned before, these QPs are responsible for the charge carrier transport in conductive polymers. In general, two types of transport mechanisms within a polymer can be distinguished: a charge carrier transport along the conjugated polymer backbone and a charge carrier transport from one conjugated polymer backbone to another.[70] The charge carrier transport along the polymer backbone resembles a band-like transport and can be described with the SSH theory[69], mentioned before. The QPs are highly delocalized via the π-conjugated system and thus can move freely along the polymer backbone. However, this band-like transport mechanism is limited by the appearance of chain defects, for example, chain ends or kinks, or by lattice vibrations, which increase with temperature, as they lead to a disruption of the extended π-electron system. Thus, this coherent charge carrier transport is mainly prominent on the microscopic scale within the ordered crystal regions of a polymer. Nevertheless, conjugated polymers are usually not completely crystalline but comprise a high amount of semicrystalline or amorphous polymer regions, as schematically depicted in Figure 2.4a. Thus, for the macroscopic charge carrier movement in these polymer regions, the inter-chain transport between polymer chains comes into play. Hereby, the charges tunnel in a hopping transport between adjacent but overlapping localized energetic states, which can be described with the Bässler's Gaussian disorder model.[71–73] Within this model, the energy landscape of a typical semiconducting polymer, in which band-like transport regimes within crystalline regions are embedded in amorphous polymer regions, is assumed by a disorder-broadened Gaussian density of transport states. These Gaussian distributed energy states are considered independent from each other concerning their site position and energy, pictured in Figure 2.4b. Charge carrier transport can now happen by tunneling between these neighboring energy sites. The probability of these tunneling processes was first theoretically discussed by Marcus[74, 75], however, Miller and Abrahams[76] follow a similar approach. Accordingly, the hopping rate ($\nu_{i,j}$) from one initial localized state (i), with the energy (E_i) to another localized but empty state (j), with the energy (E_j) can be described as follows:

$$\nu_{i,j} = \nu_0 \exp\left(-2\Delta R_{i,j}\gamma\right) \begin{cases} \exp\left(-\frac{E_j - E_i}{k_B T}\right) & ; \ E_j > E_i \\ 1 & ; \ E_j \leq E_i \end{cases} \tag{2.1}$$

In Equation (2.1), ν_0 is the maximum hopping rate, and the first term represents the tunnel factor, with $\Delta R_{i,j}$ being the distance between the two tunnel sites and γ being the inverse localization length. The second term represents the temperature (T) dependent Boltzmann factor, with $E_j - E_i$ being the energy difference between the two states and k_B being the Boltzmann constant. From this model, it becomes clear that a charge transport towards an energetically higher target state ($E_j > E_i$) requires thermal activation, and thus, the conductivity of usual semiconducting polymers increases with temperature. If the target site energy is below the initial site energy ($E_j \leq E_i$) relaxation of the charge occurs, which is independent of the temperature. However, band-like and hopping transport mechanisms need to be considered to describe the charge carrier transport processes in real conducting polymers, as both take place but with different dominance depending on the polymer crystallinity, morphology, and thermal energy.[70] Figure 2.4 pictures a sketch that combines the transport mechanism in the framework of the Gaussian disorder model.[77–80] The possible hopping sites are distributed depending on the disorder of the system, resulting in a Gaussian density of states (DOS, black curve), with the width ϵ being a measure of the energetic disorder. The DOS is partially occupied, which results in a Gaussian distributed charge carrier density (CCD, blue curve), with its center being shifted by $\epsilon^2(k_BT)^{-1}$ to lower energies compared to the DOS, resulting from the thermalization of charge carriers. As sketched in Figure 2.4c, charge carriers which are located in hopping sites that lie energetically between the centers of the DOS and the CCD, and thus near the defined transport energy E_T, can be thermally activated. If $k_BT > 0$, these charge carriers can potentially hop to adjacent higher energy states, while if $k_BT = 0$, these charge carriers relax towards lower energy states.

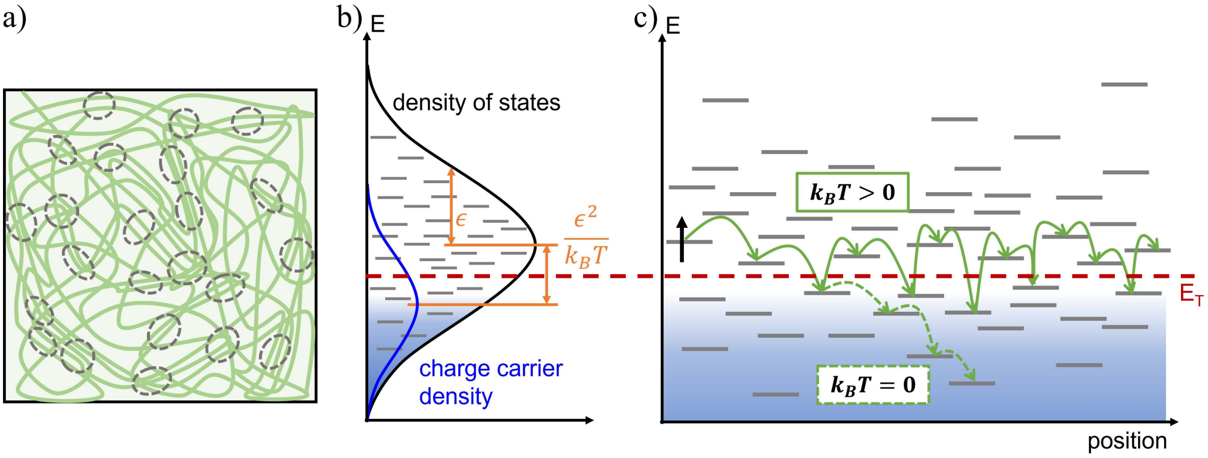

Figure 2.4 Charge transport mechanism in conductive polymers. a) Schematical illustration of the morphology in a semicrystalline polymer, with crystalline and amorphous regions. The grey dashed lines indicate possible charge transport sites. b) Possible energetic states of a conductive polymer, marked as grey lines, within the Gaussian disorder model, including the corresponding DOS (black curve) and CCD (blue curve). c) Possible energetic states as a function of the position. The green arrows present the charge carrier relaxation and the hopping transport possible near the transport energy (E_T). Adapted from the dissertation of Lorenz Bießmann.[81]

The resulting macroscopic charge carrier drift in a conducting polymer comes from the interplay of the inter- and intra-chain transport, and the charge carrier drift velocity $\vec{v}$ is given as:[60]

$$\vec{v} = \mu\vec{E} \tag{2.2}$$

With $\vec{E}$ being the applied electric field and μ the macroscopic charge carrier mobility. Using Equation (2.2) and additionally considering the charge q of the transported QPs and the charge carrier density n_q, the current density $\vec{j}$ can be obtained by:[60]

$$\vec{j} = \sigma\vec{E} = n_q q\mu\vec{E} \tag{2.3}$$

This equation shows that the conductivity σ depends on the charge carrier density, charge carrier mobility, and the charge.

Overall, the conductivity in polymer systems can be improved in two ways, via primary or secondary doping.[82] The primary doping aims to generate more charge carriers within the polymer backbones, which results in an increased amount of available energy states that can overlap and contribute to the charge transport. This charge carrier generation is achieved with either oxidizing or reducing agents by creating positively or negatively charged polaronic and bipolaronic states, respectively. Secondary doping attempts to improve the polymer structure to enhance the inter-chain transport. This improvement can be achieved, for example, by increasing the polymer crystallinity or optimizing the polymer morphology, which consists of highly conductive crystalline regions surrounded by amorphous polymer chains. Secondary doping is usually accomplished via the adjustment of the polymer film preparation procedure or via the addition of additive solvents. In general, both doping mechanisms can be applied to a polymer, whereby primary doping is, in principle, a reversible process, while secondary doping is irreversible. In Section 2.1.3 the primary and secondary doping processes are discussed in more detail for the polymer blend PEDOT:PSS.

2.1.2 PEDOT:PSS

The polymer blend poly(3,4-ethylene dioxythiophene):poly(styrene sulfonate), short PEDOT:PSS, is very popular and widely used as an organic semiconductor due to its water-solubility, mechanical flexibility, optical transparency as a thin film, and potentially high conductivity. It consists of the electrically conductive polymer PEDOT and the electrically insulating but water-soluble polymer PSS. The respective chemical structures are depicted in Figure 2.5a.[62] PEDOT belongs to the class of polythiophene and, is due to its π-conjugated backbone, a positively charged semiconducting polymer that can reach conductivities of up to 10^3 S cm^{-1} in its oxidized state.[21] However, PEDOT is insoluble and infusible, and thus hinders the wide usage in its pure form, which can be overcome when it is, for example, combined with the water-soluble polyanion PSS. The polymer blend synthesis happens via an oxidative polymerization process of PEDOT in the presence of PSS and, in this way, creates a structure of shorter positively charged PEDOT chains electrostatically interacting with the negatively charged PSS chains.[62] In an aqueous solution, PEDOT:PSS forms core-shell particles where the hydrophobic PEDOT is mainly located in the core, surrounded by a hydrophilic PSS shell, as schematically shown in Figure 2.5b. Summarizing, PSS enhances the solubility and stabilizes the positive charges in PEDOT, while PEDOT is the actual conductive polymer. Therefore, a variation of the PEDOT-to-PSS ratio also affects the polymer blend features like electrical, optical, or rheological properties. Stöcker et al. systematically investigated different

PEDOT-to-PSS ratios from 1:1 to 1:30 regarding the influence on thermoelectric properties and found a 1:2 ratio to be the most favorable.[83] Hence, in this thesis, an aqueous PEDOT:PSS solution in a 1:2.5 ratio was used, which is commercially available and whose features are detailed in Section 4.1.2.

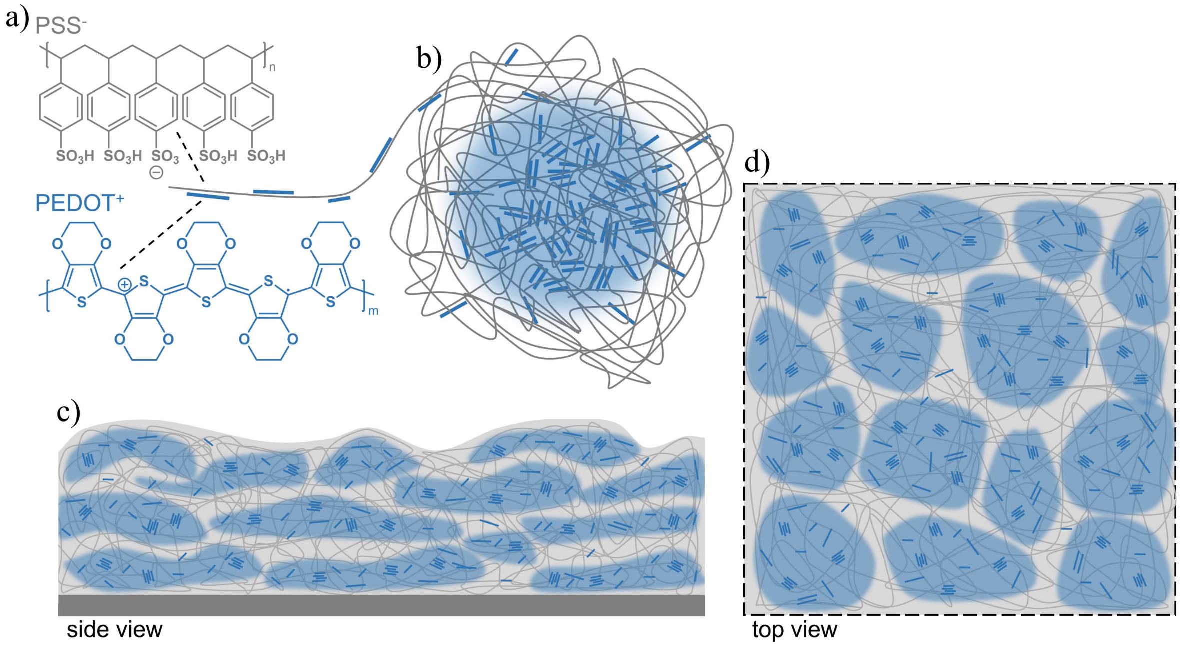

Figure 2.5 Structure of PEDOT:PSS. a) Chemical structures of PEDOT and PSS, which in aqueous solution form the in b) shown PEDOT:PSS polymer blend structure, of a core enriched with the hydrophobic PEDOT surrounded by a shell of water-soluble PSS. The dry PEDOT:PSS thin film morphology with pancake-shaped PEDOT-rich domains within a PSS matrix is depicted from side view c) and top view d). Adapted from Rivnay et al.[84]

When the aqueous PEDOT:PSS dispersion is used to prepare thin films, the spherical core-shell particles form a film structure of pancake-shaped PEDOT-enriched domains embedded in a PSS matrix upon water evaporation.[19] A sketch of the resulting thin film morphology is pictured in Figure 2.5c and d. As mentioned before, PEDOT is the actual conductive polymer responsible for the transport of the positive charge carriers, namely polymeric holes, which will be called holes in the following of this thesis. Thus, the conductivity within the semicrystalline PEDOT-rich domains, referred to as intra-domain, is high, while, in contrast, the hole transport between the domains is hindered by the surrounding matrix of electronically insulating PSS. As the inter-domain hole transport can only happen between adjacent PEDOT chains that reach inside the PSS matrix, the overall conductivity of pure PEDOT:PSS thin films is low, usually around 10 S cm^{-1}.[21] However, this particular polymer blend structure of PEDOT:PSS gives room for a high tunability of the material properties, which will be discussed in more detail in the following section.

2.1.3 Doping of PEDOT:PSS

As introduced in Section 2.1.1, there are, in general, two types of doping methods that can be distinguished. Primary doping aims for the generation of charge carriers, and secondary doping aims for the structural optimization of the semiconductor.

Primary doping in the case of the PEDOT:PSS polymer blend means the increase of positive charge carriers within the PEDOT backbone. This increase can be achieved during the PEDOT synthesis via a chemical or electrochemical polymerization procedure[85–87], or it can be achieved by a treatment with oxidizing agents, for example, oxidizing acids.[30, 33, 54, 88, 89] Figure 2.6a shows the change in the chemical structure of a PEDOT chain upon primary doping, from top to bottom. In the upper row, the undoped neutral PEDOT is depicted, which does not comprise positive charge carriers and represents a semiconductor with a specific band gap (E_{gap}). If the PEDOT backbone is oxidized, meaning an electron is removed, a positive polaron is produced and new energy states are formed within the energy gap. Further oxidation and removal of another electron results in a positive bipolaron with corresponding energy states within the band gap. At very high doping levels and thus a strongly increased concentration of polarons and bipolarons in the PEDOT chains, these energy states can overlap and form broad bands, as sketched in Figure 2.6b, which further minimize the band gap and enable high conductivities.[82] The level of primary doping in the PEDOT:PSS polymer can be observed with UV-Vis spectroscopy, as the energy of the absorption wavelength correlates to the excitation energy of the respective transitions between states.[62] Figure 2.6c shows exemplary UV-Vis absorption curves of rather undoped, medium, and highly doped PEDOT:PSS. Absorption from neutral states appears roughly around a wavelength of 500 nm, marked with red, polaronic states lead to absorption usually around 900 nm and 1900 nm, marked green, and bipolaronic states result in an absorption peak at wavelengths above 1250 nm, marked cyan and purple.[11, 41, 90] As mentioned before, primary doping is, in principle, reversible, meaning that a reduction and thus a decrease in the positive charge carrier concentration, called dedoping, is also possible. For some applications, including thermoelectrics, this dedoping is favorable and can be achieved, for example, with inorganic[27, 28, 38–40] or organic[41–43] reducing agents.

Secondary doping in the case of PEDOT:PSS polymer blend includes a wide variety of different mechanisms aiming for structural optimization.[91, 92] In general secondary doping can be achieved via the addition and treatment with polar solvents like tetrahydrofuran[93], dimethyl sulfoxide[34, 37, 44, 93–96], dimethylformamide[26, 93], sorbitol[97], glycerol[24, 96, 98], ethylene glycol[24, 94, 95], or polyethylene glycol[99].

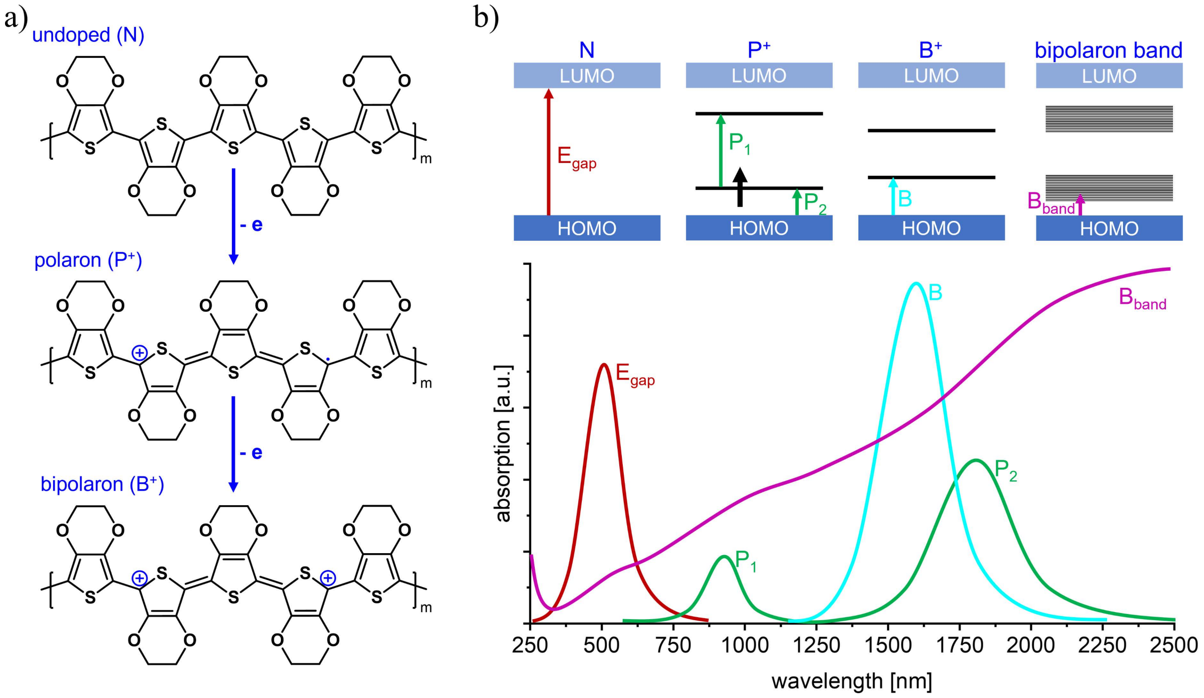

Figure 2.6 Primary doping of PEDOT:PSS. a) Change in the chemical structure of an undoped neutral PEDOT chain upon primary doping, more precisely, the formation of a positive polaron and bipolaron when chemically reducing the oxidation level of PEDOT. b) Schematical view of the band structure and exemplary absorption spectra of PEDOT:PSS in the different oxidation states: undoped (N), slightly doped (P$^+$), medium doped (B$^+$) and highly doped (bipolaron band). Adapted from Bubnova et al.[11]

Furthermore, the presence of surfactants like Zonyl®[34, 36, 37] or the addition of salts[28, 29] and ionic liquids (ILs)[44, 46, 48, 49, 100–103] have proven to be beneficial, and also a treatment with acids[30–32] can strongly increase the conductivity of PEDOT:PSS. These various doping treatments cause different underlying effects, which partially mutually define each other and thus enhance the charge carrier transport. For example, polar molecules can reduce the coulombic attraction between the positively charged PEDOT chains and the negatively charged PSS chains, as sketched in Figure 2.7a.[91, 92] This effect, often referred to as the screening effect, has several beneficial consequences, like a plastification of the polymer chains, which allows an eased rearrangement towards a more rigid orientation of the PEDOT chains. In this way, the positive charge carriers can travel more unhindered along the PEDOT backbone, which is further boosted by the reduced ionic interaction towards the PSS polyanion. Additionally, this more linear chain arrangement allows for a closer packing of the polymer chains, thus increasing the chain order and crystallinity, which contributes to a higher inter-chain transfer probability of the charge carriers. If the screening is strong enough, the separation of the PEDOT and PSS chains can be achieved, resulting in a partial removal of the insulating PSS polymer, which can also lead to a better ordering of the PEDOT chains. Additionally, this diminishment of the PSS matrix enables a morphology rearrangement towards smaller and finer distributed PEDOT-domains with shorter distances between each other, which strongly enhances the inter-domain conductivity. Another effect is the chain confirmation modification, describing the change from a benzenoid towards a quinoid PEDOT chain confirmation, depicted in Figure 2.7b.[91, 92]

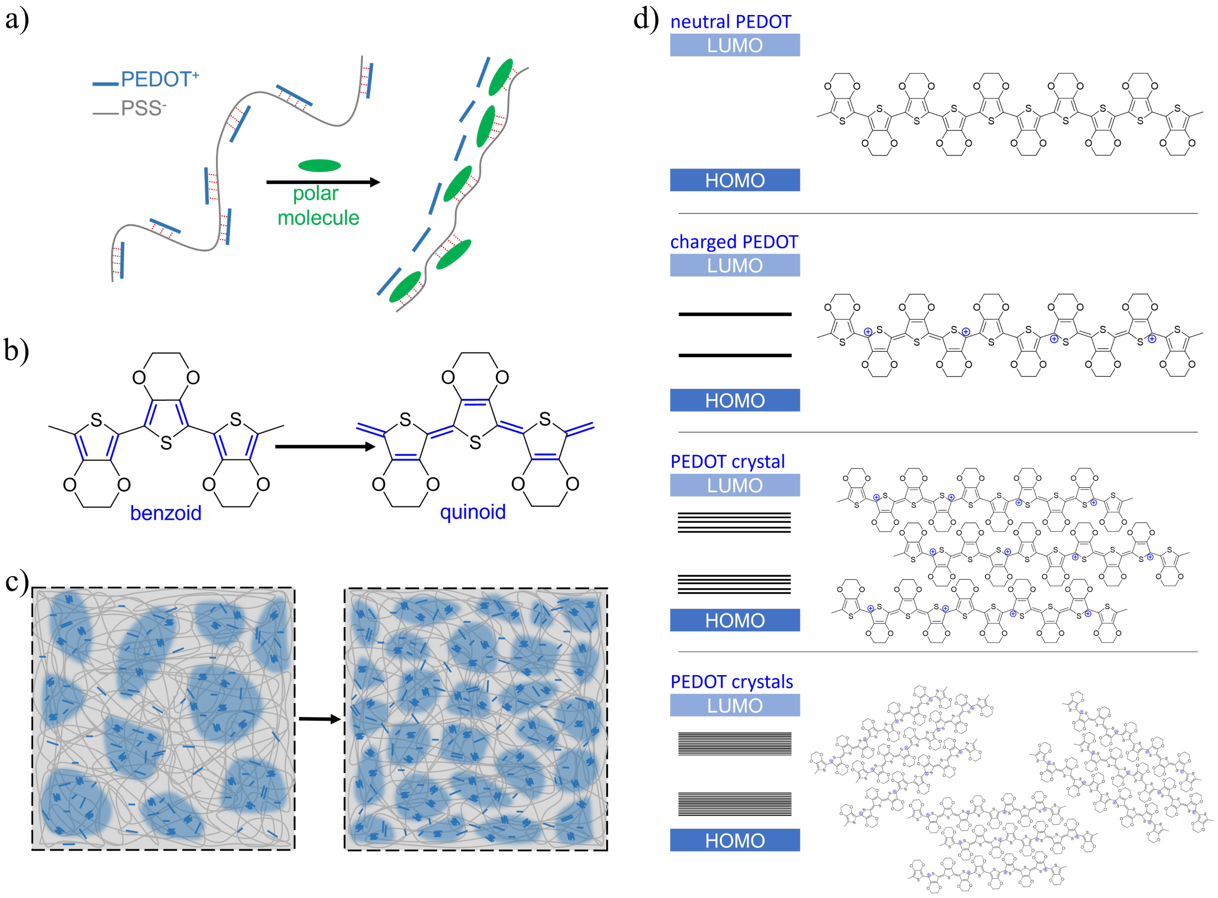

Figure 2.7 Secondary doping of PEDOT:PSS. a) Screening effect, caused by a reduction of the coulombic attraction between the charged PEDOT and PSS chains due to the introduction of polar molecules. Adapted from Mengistie et al.[99] b) Change of the PEDOT chain from the benzoid to the quinoid confirmation. c) Enhancement of the ordering and crystallinity of PEDOT chains, causing an improved intra- and inter-chain conductivity and narrowing of the energy gap. d) Optimization of the PEDOT:PSS morphology towards smaller and more finely distributed PEDOT domains, which increases the inter-domain charge carrier transport. Adapted from Muñoz et al.[104]

In the benzenoid conformation, a distorted PEDOT chain structure with localized charge carriers is favored, while compared to that in the quinoid conformation, the PEDOT molecule owns a more planar structure, allowing for an extended linear PEDOT backbone. Therefore, the from secondary doping resulting preference towards a quinoid structure enables a better intra-chain conductivity, but also a better inter-chain conductivity due to a facilitated PEDOT arrangement. Overall, two achievements in increasing the charge carrier transport can be distinguished, which are schematically depicted in Figure 2.7c and d, respectively. First, the enhancement of ordering and crystallinity of the PEDOT chains leads to a better intra-chain and inter-chain conductivity, as the overlapping of different energy states increases and narrows the energy gap due to the formation of QP bands.[62, 104] Second, the optimization of the PEDOT:PSS morphology towards a PEDOT domain arrangement that improves the inter-domain charge carrier transport, by reducing domain distances and creating PEDOT bridges in between.[24]

2.2 Thermoelectric principles in organic polymers

Thermoelectricity, as the name suggests, describes phenomena resulting from a correlation between the electrical potential gradient ($\nabla\varphi$) and the temperature gradient (∇T). It was discovered in 1822 by Thomas Johann Seebeck,[105] a Baltic German physicist, who detected the first of three separately identified thermoelectric (TE) effects, namely the Seebeck effect. Followed by that, the Peltier effect was described in 1834 by the French physicist Jean Charles Athanase Peltier,[106] and finally, Lord Kelvin (William Thomson) predicted and observed the Thomson effect in 1851.[107] In this section, the basic principles behind thermoelectricity with the encompassed effects are outlined, and the characteristics of PEDOT:PSS as TE material are described more closely.

2.2.1 Basics of thermoelectric effects

For the explanation of processes happening within a TE system, it is essential to mention that they are not in equilibrium and thus are beyond classical thermodynamics. Therefore, the concept of Onsager reciprocal relations in irreversible processes is necessary to describe these non-equilibrium states.[108] This theory establishes linear relations between driving forces and resulting fluxes using proportionality coefficients to present direct- and cross-correlations. Simple examples of these relations are Ohm's law and Fourier's law, which state that the electrical current flow (J) is proportional to the electrical potential gradient ($\nabla\varphi$), and, in the case of the latter, that the heat current flow (Q) is proportional to the temperature gradient (∇T). However, as mentioned before, in a TE system, the correlated driving forces $\nabla\varphi$ and ∇T can both simultaneously influence the electrical and heat current flow, which results in direct- and cross-correlations. Using the Onsager reciprocal relations, the TE system can now be expressed with Equation (2.4) and Equation (2.5):[109, 110]

$$-J_N = L_{11}\frac{1}{T}\nabla\bar{\mu} + L_{12}\nabla\frac{1}{T} \tag{2.4}$$

$$Q = L_{21}\frac{1}{T}\nabla\bar{\mu} + L_{22}\nabla\frac{1}{T} \tag{2.5}$$

Hereby, J_N describes a particle (charge carrier) current flow, which relates to the electrical current flow as $J = e \cdot J_N$ via the elementary charge e. The particle current flow and the heat current flow both depend on the electrochemical potential gradient ($\nabla\bar{\mu}$) and the reciprocal temperature gradient ($\nabla\frac{1}{T}$). The proportionality coefficients L_{ij} of the Onsager theorem represent the direct-correlation (L_{11} and L_{22}) and the cross-correlation ($L_{12} = L_{21}$), and can be determined as follows.

First, the case of no temperature gradient ($\nabla\frac{1}{T} = 0$) is considered. Equation (2.9) becomes:

$$-J_N = L_{11}\frac{1}{T}\nabla\bar{\mu} \tag{2.6}$$

With $\nabla\bar{\mu} = e\nabla\varphi$ and $J = e \cdot J_N$ the electrical current flow results as:

$$J = -L_{11}\frac{e^2}{T}\nabla\varphi = -\sigma\nabla\varphi \tag{2.7}$$

According to Ohm's law, the proportionality factor between the electrical current flow and the electrical potential is the electrical conductivity σ, and thus, the first proportionality coefficient $L_{11}$is given as:

$$L_{11} = \frac{\sigma T}{e^2} \tag{2.8}$$

The second case considers the electrochemical potential gradient to be zero ($\nabla\bar{\mu} = 0$). For Equation (2.5) this leads to:

$$Q = L_{22}\nabla\frac{1}{T} = -L_{22}\frac{1}{T^2}\nabla T = -\kappa_E\nabla T \tag{2.9}$$

$$\text{with } \nabla\frac{1}{T} = -\frac{1}{T^2}\nabla T$$

Thereby, the second proportionality coefficient L_{22} can be determined. With κ_{E}, the thermal conductivity in the case of $\nabla\bar{\mu} = 0$, being the proportionality factor between the heat current flow and the temperature gradient according to Fourier's law.

$$L_{22} = \kappa_E T^2 \tag{2.10}$$

With this, the direct-correlations are explained, and following the cross-correlation will be derived. For this, again assuming the case of $\nabla\frac{1}{T} = 0$, resulting in Equation (2.6), which then can be transformed to:

$$\nabla\bar{\mu} = -\frac{J_N T}{L_{11}} = -\frac{JT}{eL_{11}} \tag{2.11}$$

Inserting this equation and $\nabla\frac{1}{T} = 0$ into Equation (2.5), it results in the relation between the heat current flow and the electrical current flow, with Π being the Peltier coefficient.

$$Q = -\frac{L_{21}}{L_{11}}\frac{1}{e}J = \Pi J \tag{2.12}$$

Using Equation (2.8) this gives us the proportionality coefficients for the cross-correlations:

$$L_{21} = L_{12} = -\frac{\Pi\sigma\mathrm{T}}{e} \tag{2.13}$$

Furthermore, the case of no particle current flow ($J_N = 0$) can be considered to find the relation between the electrochemical potential and the temperature gradient. Therefore, Equation (2.4) is used to get the electrical current flow, which is also zero, see Equation (2.14), and by inserting $\nabla\frac{1}{T} = -\frac{1}{T^2}\nabla T$ and $\nabla\bar{\mu} = e\nabla\varphi$ this leads to Equation (2.15).

$$J = eJ_N = -L_{11}\frac{e^2}{T}\nabla\varphi + L_{12}\frac{e}{T^2}\nabla\mathrm{T} = 0 \tag{2.14}$$

$$\nabla\varphi = \frac{L_{12}}{L_{11}}\frac{1}{eT}\nabla T = S\nabla T \tag{2.15}$$

Hereby, S is defined as the Seebeck coefficient, which can be also written as $S = -\frac{\Pi}{T}$.

By using Equation (2.15) and $\nabla\bar{\mu} = e\nabla\varphi$, and inserting both into Equation (2.5), one can obtain the thermal conductivity κ_J for the case of no electrical current flow:

$$Q = -\frac{L_{22}L_{11} + L_{12}^2}{L_{11}}\frac{1}{T^2}\nabla T = -\kappa_J\nabla T \tag{2.16}$$

With Equation (2.8), (2.10), and (2.13) a correlation between the thermal conductivities κ_J and κ_E can be obtained. These thermal conductivities respectively represent the cases of no electrical current flow and no electrochemical gradient.

$$\kappa_J = \kappa_E - TS^2\sigma \tag{2.17}$$

$$\frac{\kappa_E}{\kappa_J} = \frac{S^2\sigma}{\kappa_J}T + 1 \tag{2.18}$$

In a TE material the thermal conductivity in an open-circuit configuration (κ_J) is expected to be minimal, and maximal in the short-circuit configuration (κ_E). Therefore, the division of κ_E

by κ_J in Equation (2.18) should be maximized whereby the first term on the right side of the equation represents the thermoelectric figure of merit ($Z\bar{T}$), which will be introduced in more detail in Section 2.2.3.

Summarizing, with the Onsager reciprocal relations, the correlations between the driving forces, electrochemical potential $\nabla\varphi$ and temperature gradient ∇T, and the occurring fluxes, electrical current flow J and heat current flow Q can be determined. The resulting relations, which explain the different identified TE effects, can be expressed as follows:[110]

$$J = -\sigma\,\nabla\varphi + S\sigma\,\nabla T \tag{2.19}$$

$$Q = S\sigma T\,\nabla\varphi - (\kappa_J + S^2\sigma\mathrm{T})\,\nabla T \tag{2.20}$$

In the next section the three different thermoelectric effects, namely Seebeck effect, Peltier effect, and Thomson effect, will be described on a macroscopic and more applied level.

2.2.2 Thermoelectric effects

In principle three different TE effects, as sketched in Figure 2.8, can be distinguished; referred to as Seebeck effect, Peltier effect, and Thomson effect.[111–113]

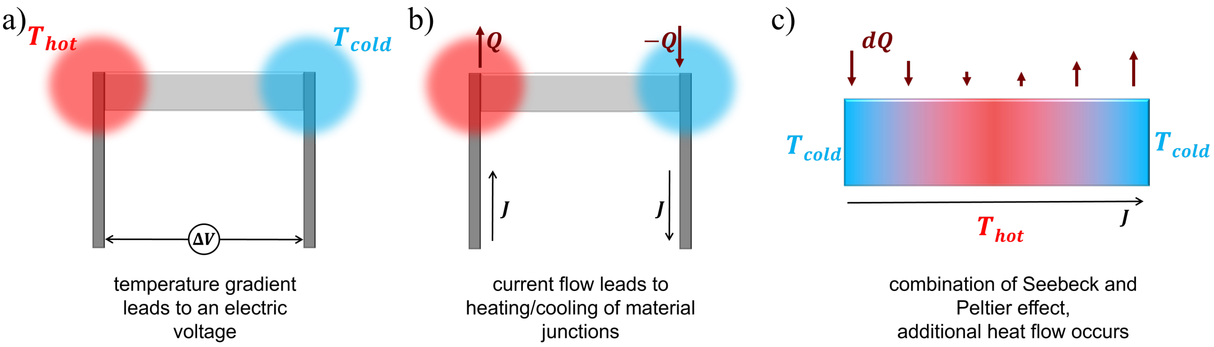

Figure 2.8 Thermoelectric effects. a) Seebeck effect, describing the emergence of an electrical thermovoltage upon the application of a temperature gradient ($\boldsymbol{T_{hot}}$ and $\boldsymbol{T_{cold}}$). b) Peltier effect, describing the formation of a heat current flow ($\boldsymbol{Q}$, dark red arrows) upon the application of an electric current flow ($\boldsymbol{J}$, black arrows) through a material junction. c) Thomson effect, describing the appearance of an additional heat flow along a material ($\boldsymbol{Q}$, dark red arrows), if an electrical current flow ($\boldsymbol{J}$, black arrows) and a temperature gradient ($\boldsymbol{T_{hot}}$ and $\boldsymbol{T_{cold}}$) are applied simultaneously. Adapted from the dissertation of Olga Bubnova.[114]

The Seebeck effect, sketched in Figure 2.8a, describes the emergence of an electrical thermovoltage (ΔV^{therm}) upon the application of a one-dimensional temperature gradient (ΔT = T_{hot} - T_{cold}) on the conjunctions of two dissimilar TE materials (A and B).

The Seebeck coefficient (S) is defined as:[111]

$$S = S_A - S_B = \frac{\Delta V^{therm}}{\Delta T} \tag{2.21}$$

The Seebeck effect, which will be discussed in a bit more detail later, can be potentially used for waste-heat recovery or temperature sensing.

The Peltier effect, sketched in Figure 2.8b, can be observed if an electrical current flow (J) is applied through two different TE materials (A and B), which leads to a heat current flow (Q) and results in a heating or cooling of the respective material conjunctions. The Peltier coefficient (Π) defines as:[111]

$$\Pi = \Pi_A - \Pi_B = \frac{Q}{J} \tag{2.22}$$

The Peltier effect is complementary to the Seebeck effect and can be used for heat pump construction or as refrigerator.

The Thomson effect, sketched in Figure 2.8c, represents a combination of the Seebeck and Peltier effect, namely if an electrical current flow and a temperature gradient are applied on a TE material. This results in an additional heat current flow along the material (dQ). The extend of the Thomson effect is very small and can be described by the Thomson coefficient (Γ):[111]

$$\Gamma = \frac{dQ}{JdT} \tag{2.23}$$

All three effects and their corresponding coefficients are linked with each other as can be described with the Thomson (Kelvin) relations:

$$\Pi = ST \tag{2.24}$$

$$\Gamma = T\frac{dS}{dT} \tag{2.25}$$

It needs to be mentioned that even though these three thermoelectric effects are all reversible, there are additional thermoelectric effects occurring, which are irreversible and prone to reduce the performance of thermoelectric devices.[111–113] First, the Joule heating describes the conversion of useful electric energy, in the form of moving charge carriers, into heat that dissipates and is thus lost. Second, the thermal heat conduction, which leads to an equalization of the different temperatures within a material, and thus a reduction of the temperature gradient.

However, as the focus of this present thesis lies on the application of TE materials in thermoelectric generators to convert a temperature gradient into electric voltage, the Seebeck effect is the most relevant and will be discussed in more detail.[111] Figure 2.9a shows an exemplary thermoelectric material with free positive charge carriers, also called a p-type semiconducting thermoelectric material. Upon application of a temperature gradient ($\Delta T = T_{hot} - T_{cold}$) along the material, as depicted in Figure 2.9b, the free positive charge carriers on the hot side have more thermal energy, gain a higher kinetic energy and are thus more agile in their movement, compared to the ones on the cold side. Eventually this leads to a net diffusion of free charge carriers (diff$_{\mathrm{T}}$, black arrow) towards the cold side, resulting in an accumulation there and depletion on the hot side. As depicted in Figure 2.9c this charge separation along the semiconducting TE material causes the formation of an electrical voltage between the cold and the hot end. However, the increased charge carrier concentration and the arising electrical field due to the charge separation yield to a charge carrier drift (drift$_{\mathrm{E}}$, green arrow) in the opposite direction. Ultimately an equilibrium is reached and the thermovoltage ΔV^{therm} arises.

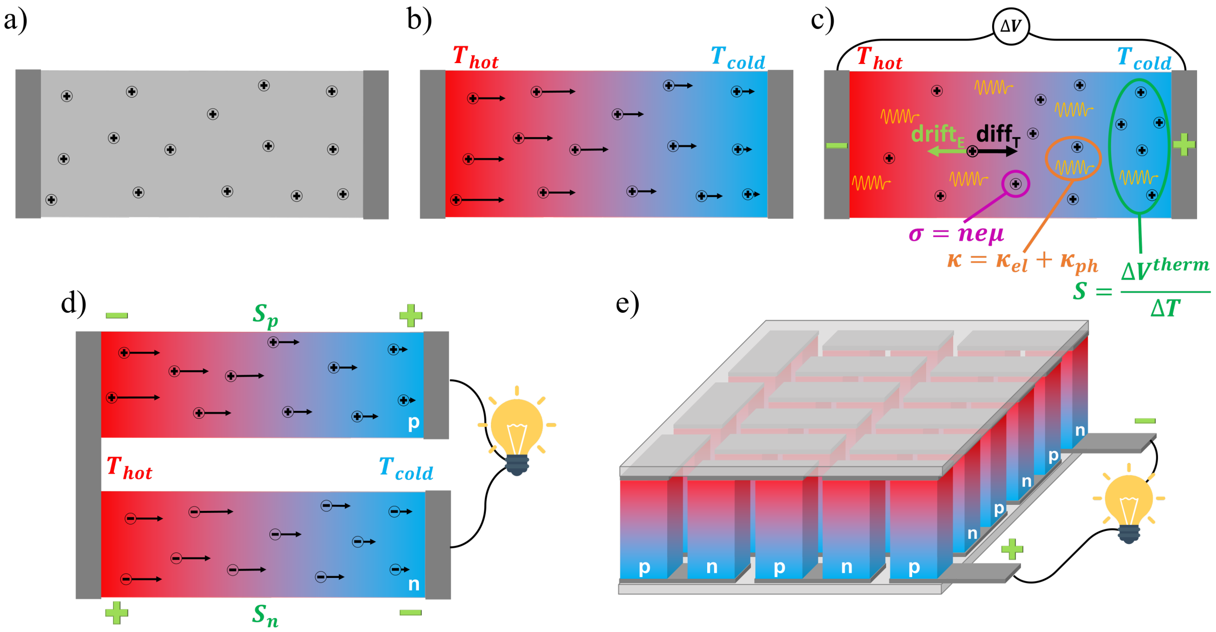

Figure 2.9 Seebeck effect and thermoelectric generators. a) Schematic depiction of a thermoelectric material containing positive charge carriers at thermal equilibrium. b) Arise of a positive charge carrier diffusion towards the cold side upon the application of a temperature gradient. c) The emergence of the resulting thermal voltage along the thermoelectric material and graphical description of the thermoelectric parameters, electrical conductivity $\boldsymbol{\sigma}$ (pink), thermal conductivity $\boldsymbol{\kappa}$ (orange), and Seebeck coefficient $\boldsymbol{S}$ (green). d) Thermoelectric circuit containing a positive (p) and negative (n) semiconducting thermoelectric material. e) Assembly of thermoelectric generator built up by several in series connected thermoelectric elements.

There are three main parameters that can be distinguished to evaluate the goodness of a thermoelectric material. First, the electrical conductivity σ, which should be as high as possible to enable an easy charge carrier transport through the material. Second. the thermal conductivity

κ, which should be ideally low to maintain the applied temperature gradient. Third, the Seebeck coefficient S, which is defined by the amount of resulting thermovoltage upon application of a defined temperature gradient; hence, should be maximal. All three parameters will be discussed more precisely in the following section. The above example considers a p-type material, however, there are also n-type thermoelectric materials. For them, the major charge carriers are negative, which results in the drift and accumulation of negative charge carriers towards the cold side and thus a reversed sign of the resulting thermovoltage as well as the Seebeck coefficient. As pictured in Figure 2.9d, the Seebeck coefficient is defined to be positive for p-semiconducting ($S_p > 0$) and negative for n-type ($S_n < 0$) TE materials. The combination of both creates a thermoelectric element, by connecting them thermally in parallel and electrically in series, linked via a metal conductor. By this the thermovoltages arising in each leg upon the application of a defined temperature gradient add up and thus the overall resulting voltage can be increased. Figure 2.9e shows the typical design of a thermoelectric generator, comprising multiple (N) thermoelectric elements, which are connected in an array to form a thermoelectric module, with a total resulting open circuit thermovoltage of:

$$\Delta V_{total}^{therm} = N(\Delta V_p^{therm} - \Delta V_n^{therm}) = N(S_p - S_n)\Delta T \tag{2.26}$$

2.2.3 Characterization of thermoelectric materials

The performance of a thermoelectric material for thermal to electric energy conversion is influenced by different material properties, the Seebeck coefficient S, the electrical conductivity σ, the thermal conductivity κ, and the temperature of operation $\bar{T}$. All these parameters are comprised in the thermoelectric figure of merit $Z\bar{T}$, mentioned before in Section 2.2.1. This dimensionless TE figure of merit can be determined via Equation (2.27) and directly shows that in general for a good TE material, S and σ should be maximized, while κ should be minimized.[112] Furthermore, $Z\bar{T}$ is correlated to the maximal reachable conversion efficiency η_{max}, as defined in Equation (2.28).[16]

$$Z\bar{T} = \frac{S^2\sigma}{\kappa}\bar{T} \tag{2.27}$$

$$\eta_{max} = \frac{T_{hot} - T_{cold}}{T_{hot}} \frac{\sqrt{1 + Z\bar{T}} - 1}{\sqrt{1 + Z\bar{T}} + \frac{T_{cold}}{T_{hot}}} \tag{2.28}$$

The first term in Equation (2.28) corresponds to the Carnot efficiency, which described the maximum reachable efficiency of a heat engine that operates between a hot and a cold reservoir. The second term incorporates the TE figure of merit and thus the thermoelectric parameters of a certain material at the average temperature $\overline{T}$. Figure 2.10a shows a graphical representation of the relationship between η_{max}, $Z\overline{T}$ and ΔT.

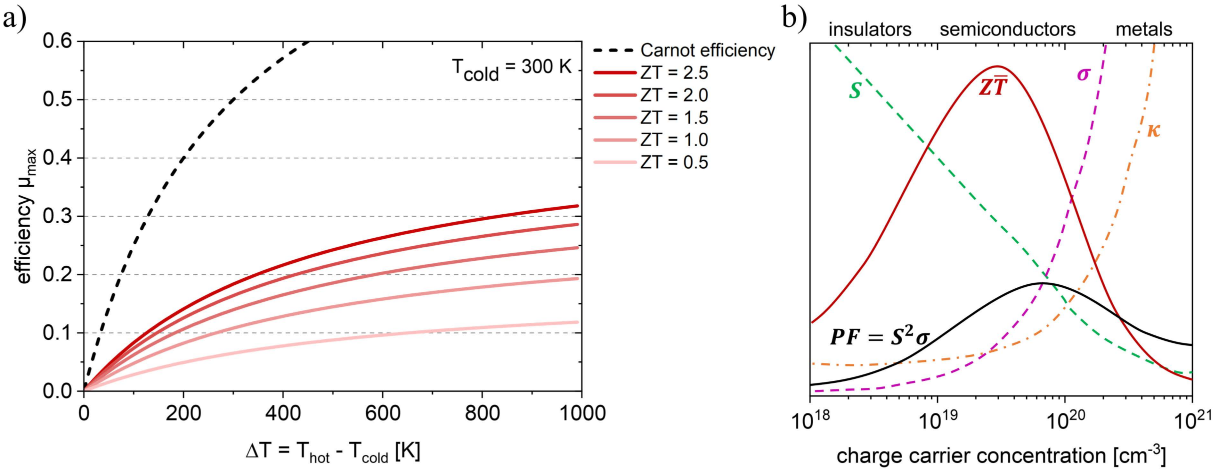

Figure 2.10 Thermoelectric efficiency and parameters. a) Graph showing the maximal achievable efficiency of a thermoelectric material depending on the temperature gradient $\boldsymbol{\Delta T}$ and the thermoelectric figure of merit $\boldsymbol{Z\overline{T}}$, in comparison to the Carnot efficiency (dashed line). b) Schematic plot of the thermoelectric parameters, namely electrical conductivity $\boldsymbol{\sigma}$ (pink), thermal conductivity $\boldsymbol{\kappa}$ (orange), and Seebeck coefficient $\boldsymbol{S}$ (green), thermoelectric figure of merit $\boldsymbol{Z\overline{T}}$ (red) and thermoelectric power factor $\boldsymbol{PF}$ (black), in dependence of the charge carrier concentration. Adapted from Snyder et al.[12]

However, as it is usually very complicated to determine κ of a thin film material, often thermoelectric power factor PF, is utilized to evaluate the goodness of a thermoelectric materials, which is also used in the frame of this thesis:[112]

$$PF = S^2\sigma \tag{2.29}$$

Figure 2.10b graphically shows the correlations of the thermoelectric figure of merit and thermoelectric power factor with the Seebeck coefficient, electrical conductivity, and thermal conductivity.[12] It can also be seen in the graph that nearly all these parameters are dependent on the charge carrier concentration n_q, which results in a dependency of them among each other and thus complicate the selective improvement of a thermoelectric material.[112]

The Seebeck coefficient, which defines the property of a material to convert a temperature gradient into electrical voltage, can be defined with the Boltzmann constant k_B, the elementary charge e, and the Fermi temperature T_F, as follows:[12]

$$|S| = \frac{\pi^2}{3}\frac{k_B}{e}\frac{T}{T_F} \tag{2.30}$$

It shows that the Seebeck coefficient is proportional to the fraction of charge carriers that are free and are effectively contributing to the temperature gradient driven transport of charges, which is expressed by the relation of T and T_F. Hereby underlying is the condition that only charge carriers with energies in proximity of the Fermi level are allowed to participate in the charge transport. The definition of the Fermi temperature is given by Equation (2.31) with the Planck constant h, the effective charge carrier mass m^*, and the charge carrier concentration n_q.

$$T_F = \frac{h^2}{8m^*k_B}\left(\frac{3n_q}{\pi}\right)^{\frac{2}{3}} \tag{2.31}$$

For a good TE material, the Seebeck coefficient should be maximized, and thus, a low charge carrier concentration is favorable according to the resulting proportionality ($S \sim {n_q}^{-2/3}$).

The electrical conductivity of a thermoelectric material can basically be expressed with:[12]

$$\sigma = n_q e \mu \tag{2.32}$$

The direct proportionality with the charge carrier density, $\sigma \sim n_q$, becomes apparent, and μ represents the charge carrier mobility within the thermoelectric material. As the conductivity in a TE material should be as high as possible, a high charge carrier concentration and a high charge carrier mobility is advantageous.

The thermal conductivity κ, is in general composed of two parts, the contribution of phonons κ_{ph}, describing the heat transport via lattice vibrations, and the contribution of charge carriers κ_{ch}, which not only transport charge, but also carry heat through the system.[112]

$$\kappa = \kappa_{ph} + \kappa_{ch} \tag{2.33}$$

$$\frac{\kappa_{ch}}{\sigma} = LT = \frac{\pi^2}{3}\left(\frac{k_B}{e}\right)^2 T \tag{2.34}$$

The phonon thermal conductivity is independent of n, while the contribution of κ_{ch} increases at high charge carrier concentrations, indicated in Figure 2.10b. Hereby, the charge carrier thermal conductivity is related to the electrical conductivity via the Wiedemann-Franz law,[115] defined in Equation (2.34), with the empirical proportionality constant $L = 2.44 \times 10^{-8}$ WΩ K^{-2} being the Lorenz number.[116] Therefore, this leads to the proportionality $\kappa_{ch} \sim n_q$ and the charge carrier concentration should be reduced, to keep the total thermal conductivity low and improve the thermoelectric figure of merit.

It becomes clear from these considerations that the optimization of thermoelectric materials by influencing their individual TE properties is always a juggling act, as they are interconnected with each other. Figure 2.10b shows that in materials with low charge carrier concentration, usually insulators, the Seebeck coefficient is high and κ is low, however, also σ is low, thus resulting in a low $Z\bar{T}$. In the metals region, where n_q is high, the electrical conductivity is strongly increased, however, S is low and κ increases, which also results in a non-optimal $Z\bar{T}$. Therefore, medium charge carrier concentrations like achieved in semiconducting thermoelectric materials are preferable to reach a good thermoelectric performance with a high $Z\bar{T}$, or, as investigated in the context of this thesis, a high PF.

2.2.4 PEDOT:PSS as thermoelectric materials

Thermoelectric semiconductors can either be based on inorganic materials, like bismuth telluride metal alloys, or on organic materials, like conductive polymers. The focus of this present thesis lies on organic TE polymers, more precisely PEDOT:PSS, as they provide certain advantages.[58, 117, 118] For example, in contrast to their inorganic counterpart, thermoelectric polymers are usually low or non-toxic. Furthermore, they are often processable from solution, which allows for an easy and cost-efficient large-scale production with techniques like blade-coating, printing, or spraying. Additionally, most organic TE materials allow for the fabrication of lightweight, flexible, and transparent thin film devices, which facilitates a huge field of possible applications. Another favorable property of TE materials based on semiconducting polymers, is their initially low thermal conductivity and their often-high electrical conductivity. As introduced in Section 2.1.3 for the case of PEDOT:PSS, the TE properties of polymers can be adjusted via doping. With primary and secondary doping, the electrical conductivity can be enhanced by an increase of the charge carrier concentration or the charge carrier mobility, respectively. While, with dedoping the charge carrier concentration can be decreased, which positively influences the Seebeck coefficient. By finding the right balance of doping, the thermoelectric performance of these organic TE materials, evaluated with the TE power factor or the TE figure of merit, can be tuned and optimized.

However, for the case of some polymers, like the here investigated PEDOT:PSS, it is important to note that there is not only an electronic effect to the thermoelectric performance, but ionic contributions are also possible. Ions within the PEDOT:PSS, either anions, but most likely cations that were introduced into the polymer during fabrication or doping procedure can travel through the material and thus contribute with an ionic conductivity and ionic Seebeck effect.[62, 119, 120] The predominant part is the transport of cations through the PSS matrix, which can happen via the various mechanisms schematically depicted in Figure 2.11a, namely intra-chain or inter-chain hopping, directly or via ion clusters. Hereby different influences like the temperature, polymer chain motion mobility or the electrostatic interactions affect the ion transport properties.[21, 121, 122]

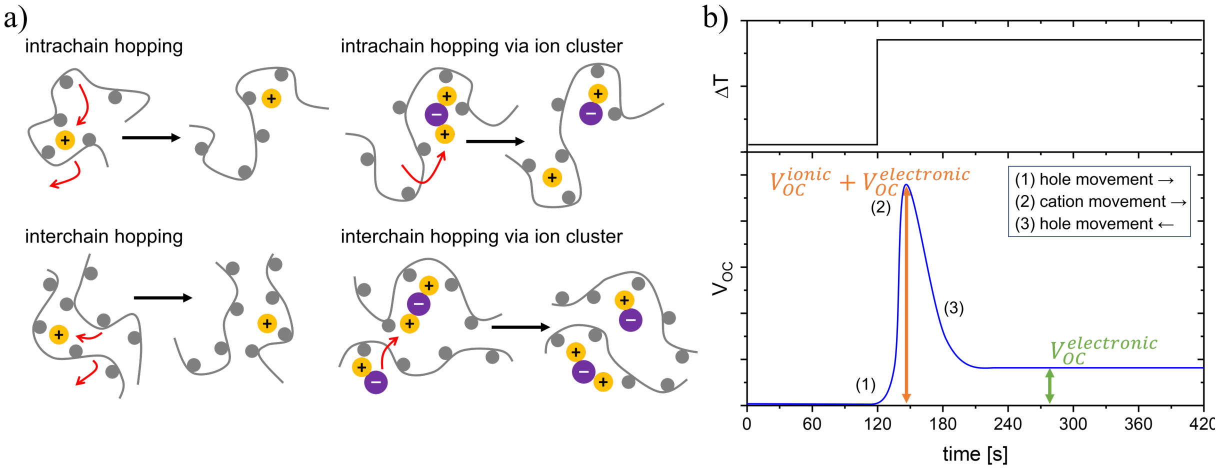

Figure 2.11 Ionic influence on the thermoelectric behavior of PEDOT PSS. a) Possible intra-chain and inter-chain hopping mechanisms, directly or via ion clusters. Shown for the case of cationic species (yellow) transport along the PSS polymer chains, which are depicted as grey lines with the grey dots representing the polar sulfonate group. Adapted from Xue et al.[123] b) Exemplary description of the initial but short-term contribution of ionic species to the arising thermovoltage, called Soret effect, when applying a temperature gradient on a mixed ionic and electronic conducting thermoelectric material. Adapted from Ail et al.[124]

An ordered and directed ion charge transport can be caused either by a prevailing electric potential force, for example during conductivity measurements, or by a temperature gradient, like during the application as thermoelectric material. The latter being described as thermophoresis, or Soret effect, which can contribute to the total thermal voltage of a mixed conducting TE material, as shown in Figure 2.11b.[119, 122, 124] However, as the ions are not able to cross over into the electrodes, like it is possible for electronic charge carriers, this leads to the accumulation of the ions at the cold electrode interface and the formation of an ion concentration gradient. Thus, a driving force in the opposite direction arises, which eventually results in an equilibrium state corresponding to the contribution of only electronic charge carriers.[124] Therefore, even though the effect of ions on the TE properties can be high, it is only lasting for a short-time. Nevertheless, this dynamic influence needs to be considered when investigating thermoelectric materials with ionic and electronic charge carrier contributions, like PEDOT:PSS.

2.3 Scattering methods

In this thesis, scattering techniques are used as main method to investigate the inner structure of PEDOT:PSS thin films to correlate it to their thermoelectric properties and characterize morphological changes upon different treatments and ambient influences. In general, these methods are based on elastic scattering, which means that the energy of the incident X-ray or neutron beam (E_i) hitting the sample, does not change during the scattering event and is the same as for the final detected X-ray or neutron beam ($E_f = E_i$). More importantly, all scattering techniques conducted in this thesis allow the probing of a large thin film area, in the millimeter to centimeter range, and thus provide statistically relevant information about the inner structure of the sample. The basic principles of scattering and the hereby utilized techniques, grazing-incidence small-angle X-ray scattering (GISAXS), X-ray reflectometry (XRR), and time-of-flight neutron reflectometry (ToF-NR), are introduced in the following sections.

2.3.1 Scattering basics

The underlying principle of the scattering investigation concept is that an incident beam, of either X-rays or neutrons, responds to a variation of the refractive index (n) at its surface or interfaces, respectively. The incident beam can be generally described as a wave, with the wave amplitude Ψ_0, position vector $\vec{r}$, and wave vector $\vec{k_i}$.[125]

$$\Psi_i(\vec{r}) = \Psi_0 \exp(i\vec{k_i} \cdot \vec{r}) \tag{2.35}$$
$$\text{with } k = |\vec{k_i}| = \frac{2\pi}{\lambda}$$

In general, the refractive index describes how a wave travels within a specific material, hence it is dependent on the wavelength λ and position $\vec{r}$. It can be defined as:[125, 126]

$$n(\vec{r},\lambda) = 1 - \delta(\vec{r},\lambda) + i\beta(\vec{r},\lambda) \tag{2.36}$$
$$= 1 - \frac{\lambda^2}{2\pi}\Re(SLD) + i\frac{\lambda^2}{2\pi}\Im(SLD) \tag{2.37}$$

Hereby, $\delta(\vec{r},\lambda)$ describes the dispersion and $\beta(\vec{r},\lambda)$ the absorption of the material. Both properties can be also expressed with the real and imaginary part of the scattering length density, $\Re(SLD)$ and $\Im(SLD)$, respectively. The scattering length density (SLD) measures the extent of the scattering effect of a material and is dependent on its physical density and its intrinsic scattering power. X-rays scatter at the atomic shell, thus the scattering scales with the electronic density of a material, while neutrons scatter at the atomic nuclei, hence, it is related to the nuclear scattering length.[127] Both will be detailed later in this section. In general, for hard X-ray ($E \gtrsim 5$ keV) and neutron scattering, the dispersion part is usually very small ($1 \gg \delta^{neutron,\,X-ray} \approx 10^{-5} - 10^{-8}$) and the absorption part is nearly nonexistent ($\delta^{neutron,\,X-ray} > \beta^{X-ray} \approx 10^{-7} - 10^{-8} > \beta^{neutron} \approx 10^{-10} - 10^{-12}$). This results for both, X-ray and neutron beams, in refractive indices slightly below one, according to Equation (2.36).[125, 128]

Furthermore, for the scattering investigation of a sample morphology containing two materials, or a material and its surrounding, the scattering contrast can be defined as:

$$|\Delta n|^2 = \Delta\delta^2 + \Delta\beta^2 \tag{2.38}$$

This scattering contrast relates to the scattering intensity and the signal to noise ratio, and thus is desired to be high, meaning a strong difference between the refractive indices or SLDs of the two materials.[127] In the following, the scattering contrast in the case of X-ray or neutron scattering will be discussed in more detail.

X-ray contrast

For X-ray scattering, the X-ray photons interact with the electron clouds of the atoms present inside the material under investigation. Thus, to approximate the materials scattering length density (SLD^{X-ray}), the atomic scattering factor f_j of an atom j, first introduced by Henke et al.[129], can be used as follows:

$$f_j(\lambda) = f_j^0 + f_j'(\lambda) + i f_j''(\lambda) \tag{2.39}$$

$$SLD^{X-ray} = r_e \rho_e(\vec{r}) \sum_{j=1}^{N} \frac{f_j(\lambda)}{Z_j} \tag{2.40}$$

With Z_j being the total number of electrons in the atom j. Furthermore, r_e and $\rho_e(\vec{r})$ represent the classical Thomson electron radius and the space-dependent electron density, respectively, which can be approximated via:[127]

$$r_e = \frac{e^2}{4\pi\epsilon_0 m_e c^2} = 2.814\ \times 10^{-5}\ \text{Å} \tag{2.41}$$

$$\rho_e(\vec{r}) = \rho(\vec{r}) N_A \sum_{j=1}^{N} \frac{Z_j}{M_j} \tag{2.42}$$

Hereby, e is the elementary charge, ϵ_0 is the permittivity constant, m_e is the electron mass, c is the speed of light, $\rho(\vec{r})$ is the materials mass density, N_A is the Avogadro's constant, and M_j

is the molecular mass of the atom j. Using Equation (2.37) and Equation (2.40), the materials dispersion $\delta(\vec{r},\lambda)$ and absorption $\beta(\vec{r},\lambda)$ during X-ray scattering result as:[125]

$$\delta^{X-ray}(\vec{r},\lambda) = \frac{\lambda^2}{2\pi}\Re(SLD^{X-ray}) = \frac{\lambda^2}{2\pi}r_e\rho_e(\vec{r})\sum_{j=1}^{N}\frac{f_j^0 + f_j'(\lambda)}{Z_j} \tag{2.43}$$

$$\beta^{X-ray}(\vec{r},\lambda) = \frac{\lambda^2}{2\pi}\Im(SLD^{X-ray}) = \frac{\lambda^2}{2\pi}r_e\rho_e(\vec{r})\sum_{j=1}^{N}\frac{f_j''(\lambda)}{Z_j} \tag{2.44}$$

It can be seen that f_j^0+$f_j'(\lambda)$ describes the dispersive component of the atomic scattering factor, leading to refraction, while $f_j''(\lambda)$ is the absorption component, describing the strength of radiation absorption by the material. As mentioned before, elastic scattering is assumed, which means that the change in momentum occurs without energy change of the incident and final beam. Therefore, the momentum transfer defines as the scattering vector $\vec{q} = \overrightarrow{k_f} - \overrightarrow{k_\iota}$. For in the frame of this thesis performed GISAXS, the momentum transfer is small, and thus, for the $\vec{q}$-dependent atomic scattering factor component the approximation $f_j^0 \approx Z_j$ and $f_j' \ll f_j^0$ can be made. Consequently, the refractive index for a homogeneous material, far away from absorption edges, results as:[125, 130]

$$\begin{aligned} n^{X-ray}(\vec{r},\lambda) &= 1 - \delta^{X-ray}(\vec{r},\lambda) + i\beta^{X-ray}(\vec{r},\lambda) \\ &= 1 - \frac{\lambda^2}{2\pi}r_e\rho_e(\vec{r}) + i\frac{\lambda}{4\pi}\mu(\vec{r}) \end{aligned} \tag{2.45}$$

whereby, $\mu(\vec{r})$ represents the linear absorption coefficient of the material.

Summarizing, the contrast for X-ray scattering depends on variations of the electron density between two different materials, or within one material as caused for example from concentration gradients. It is important to mention that the here discussed approximations only hold for hard X-rays ($E \gtrsim 5$ keV), while for soft X-rays ($E \lesssim 5$ keV) a strong wavelength-dependent absorption is observable, because this photon energy is in the right range to excite electrons.

Neutron contrast

Neutrons interact with the nucleus of an atom, which leads to a different scattering length density than for X-ray scattering. Hereby, the scattering length density ($SLD^{neutron}$) is dependent on how a neutron, with a distinct spin state, interacts with the respective nuclei.

This can be described with the coherent scattering length b_j of an atom j,[131] as follows:

$$SLD^{neutron} = \frac{1}{V}\sum_{j=1}^{N} b_j = \rho N_A \sum_{j=1}^{N} \frac{b_j}{M_j} \tag{2.46}$$

with V being the investigated volume unit. As can be seen in Equation (2.46), the $SLD^{neutron}$ can also be expressed using the materials mass density ρ, the molecular mass of the atom j, and the Avogadro's constant N_A.

According to Equation (2.36), the dispersion $\delta(\vec{r},\lambda)$ and absorption $\beta(\vec{r},\lambda)$ part of the refractive index can be also expressed for neutrons:[127, 130]

$$n^{neutron}(\vec{r},\lambda) = 1 - \delta^{neutron}(\vec{r},\lambda) + i\beta^{neutron}(\vec{r},\lambda) \tag{2.47}$$

$$\delta^{neutron}(\vec{r},\lambda) = \frac{\lambda^2}{2\pi} Nb \tag{2.48}$$

$$\beta^{neutron}(\vec{r},\lambda) = \frac{\lambda}{4\pi} N\alpha_a \tag{2.49}$$

Hereby, N is the number density of atoms, b is the bound coherent scattering length, and α_a represents the absorption cross section for neutrons.

Summarizing, the neutron scattering interaction occurs at the nucleus of an atom and is thus strongly dependent on it. Therefore, neutron scattering is very sensitive to isotopes and enables the distinction of chemically similar elements and materials. This is often utilized in the case of hydrogen (H, b_H = -3.74) and deuterium (D, b_D = 6.67) where the difference of the two atoms coherent scattering length b_j is useful to achieve high neutron contrast of certain material components by selective deuteration. Finally, is should be noted that the $SLD^{neutron}$ of a material can be negative, which corresponds to a 180° phase shift of the interacting neutrons during the scattering event.[127]

Scattering geometry

The scattering techniques used in this thesis are based on the two different scattering geometries depicted in Figure 2.12. XRR and ToF-NR are performed using the geometry depicted on the left, often described as specular scattering. GISAXS utilizes diffuse scattering, as depicted in the figure on the right. For both geometries an incident beam with the wave vector $\vec{k_i}$ impinges on the sample under a defined incident angle α_i. This beam then interacts with the sample material and results in a final beam with the wave vector $\vec{k_f}$ exiting the sample under a final angle α_f.

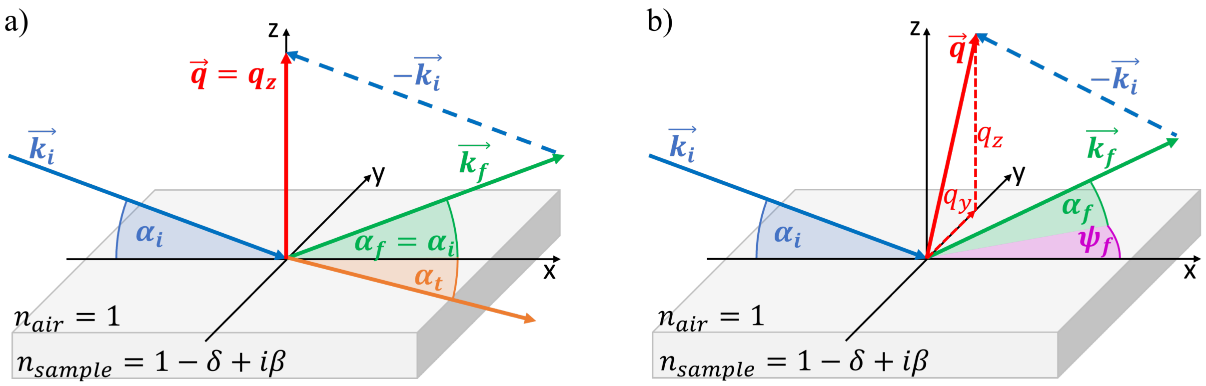

Figure 2.12 Scattering geometry for specular and diffuse scattering. a) Specular reflection geometry where only scattering within the **xz**-plane is taken into account, resulting in $\mathbf{q_y} = 0$, and thus, only a $\mathbf{q_z}$ component and only scattering at the final angle equal to the incident angle $\boldsymbol{\alpha_i} = \boldsymbol{\alpha_f}$ is considered. b) For the diffuse scattering geometry, scattering outside of the **xz**-plane is also recorded, with an additional scattering angle $\boldsymbol{\psi_f}$, thus leading to $\mathbf{q_z}$ and $\mathbf{q_y}$ components. Additionally, also scattering is considered where the final angle can differ from the incident angle ($\boldsymbol{\alpha_i} \neq \boldsymbol{\alpha_f}$). Adapted from the dissertation of Claudia Maria Palumbiny.[132]

As mentioned before, only elastic scattering takes place, which means that during the scattering event no energy transfer occurs and thus the modulus of the incident and final beam is equal.[126, 127]

$$\Delta E = \hbar\omega_f - \hbar\omega_i = \hbar c \left(\left|\overrightarrow{k_f}\right| - \left|\overrightarrow{k_i}\right| \right) = 0 \tag{2.50}$$

$$\left|\overrightarrow{k_f}\right| = \left|\overrightarrow{k_i}\right| = \frac{2\pi}{\lambda} \tag{2.51}$$

However, the wave vector of the incident and final beam changes, which is described via the scattering vector $\vec{q}$, as follows:

$$\vec{q} = \overrightarrow{k_f} - \overrightarrow{k_i} \tag{2.52}$$

As can be seen in Figure 2.12a, for the specular reflection geometry, the scattering only takes place within the xz-plane (q_z, and $q_y = 0$) and the incident and final scattering angles are equal $\alpha_i = \alpha_f$. However, for the diffuse scattering geometry, shown in Figure 2.12b, also scattering outside of the xz-plane is possible, introducing an additional scattering angle ψ_f in the xy-plane (q_z and q_y). Furthermore, in this case of scattering geometry the final exit angle can differ from the incident angle ($\alpha_i \neq \alpha_f$).

If an X-ray or neutron beam hits a sample material, also a transmitted beam with a wave vector $\overrightarrow{k_t}$ and a refracted angle α_t can result, according to the Snell's law:[128]

$$\cos(\alpha_i) = \frac{n_{sample}}{n_{air}} \cos(\alpha_t) = n_{sample} cos(\alpha_t) \tag{2.53}$$

with the refractive index of the surrounding air (n_{air} = 1) and n_{sample}, which represents the respective refractive index of the sample material for X-rays (n^{X-ray}) or neutrons ($n^{neutron}$). As the dispersion part is small but always larger than zero (δ_{sample} > 0), and the absorption part is very small for hard X-rays and neutrons (β_{sample} < δ_{sample}), the refractive index of a sample is usually slightly smaller than one (n_{sample} = 1 - δ_{sample} + $i\beta_{sample}$ < 1). Considering Snell's law, a certain incident angle can be calculated below which no transmission takes place and total reflection occurs. This material specific critical angle α_c can be determined from Equation (2.53), by defining $\alpha_i = \alpha_c$, assuming $\alpha_t = 0$ and using the small angle approximation:[125, 130]

$$\cos(\alpha_c) = n_{sample} \approx 1 - \frac{\alpha_c^2}{2} \tag{2.54}$$

$$\alpha_c = \sqrt{2 - 2n_{sample}} \overset{\beta \ll \delta}{\Longrightarrow} \sqrt{2\delta_{sample}} = \lambda \sqrt{\frac{SLD}{\pi}} \tag{2.55}$$

$$\alpha_c^{X-ray} = \lambda \sqrt{\frac{r_e \rho_e}{\pi}} \quad \text{and} \quad \alpha_c^{neutron} = \lambda \sqrt{\frac{Nb}{\pi}} \tag{2.56}$$

Equation (2.55) is valid for X-ray and neutron beams, however, the right part only holds if the absorption of the material is negligible small ($\beta \ll \delta$). With that resulting in the critical angles for X-ray (α_c^{X-ray}) and neutron scattering ($\alpha_c^{neutron}$), respectively expressed in Equation (2.56).

The critical angle of a material is particularly interesting, for the diffuse scattering geometry, performed in this thesis for the GISAXS experiments. Here, the resulting scattering pattern shows a maximum in the intensity of the diffuse scattered beam under this critical angle, the Yoneda region.[133] This can be explained via the Fresnel reflection (r^F) and transmission (t^F) coefficients, containing the z-components of the modulus of the incident ($k_{i,z}$) and transmitted beam ($k_{t,z}$):[125, 126, 134]

$$r^F = \frac{k_{i,z} - k_{t,z}}{k_{i,z} + k_{t,z}} \tag{2.57}$$

$$t^F = \frac{2k_{i,z}}{k_{i,z} + k_{t,z}} \tag{2.58}$$

$$\text{with } k_{i,z} = k \sin(\alpha_i)$$

$$\text{and } k_{t,z} = n_{sample} k \sin(\alpha_t) = k \sqrt{n_{sample}^2 - cos^2(\alpha_i)}$$

As the reflection and transmission coefficients are both dependent on the materials refractive index, they consequently depend on the materials critical angle.

The intensities of the reflection and transmission can be calculated with $R^F = |r^F|^2$ and $T^F = |t^F|^2$, respectively. The Fresnel reflection and transmission of an exemplary Si sample (δ = 7.56 × 10^{-6}, for λ = 1.54 Å) with varying absorption coefficients (β), are shown in Figure 2.13a and b dependent on the ratio of incident to critical angle.[126]

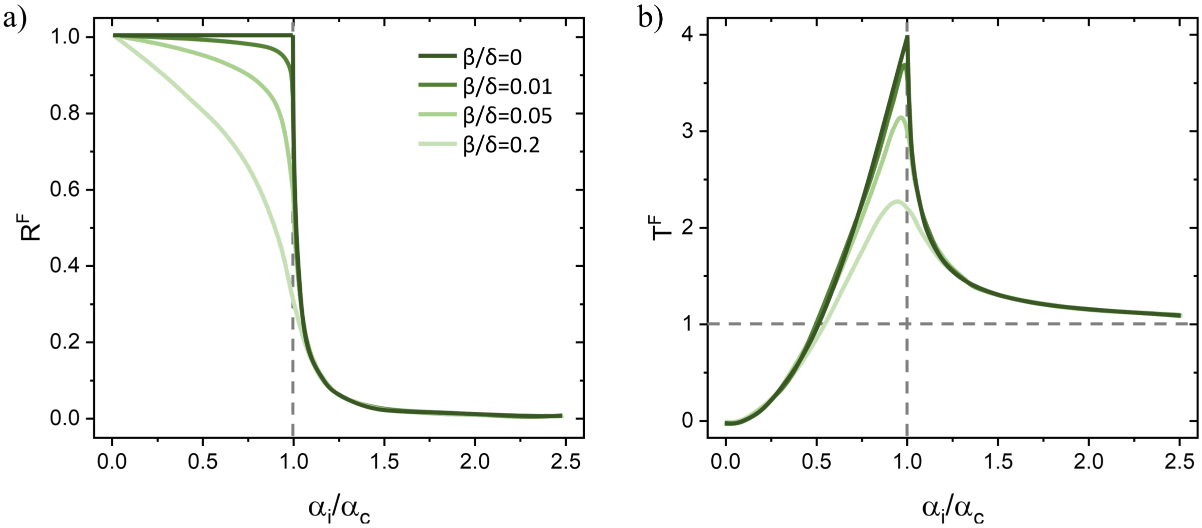

Figure 2.13 Functions of the Fresnel reflection and Fresnel transmission. a) The Fresnel reflection $\boldsymbol{R^F}$ and b) Fresnel transmission $\boldsymbol{T^F}$plotted for an exemplary Si sample ($\boldsymbol{\delta}$ = 7.56 × 10^{-6}, for $\boldsymbol{\lambda}$ = 1.54 Å), as function of $\boldsymbol{\alpha_i/\alpha_c}$.[126] For $\boldsymbol{\alpha_i} < \boldsymbol{\alpha_c}$, total reflection occurs, and a strong reflection decay happens for $\boldsymbol{\alpha_i} \geq \boldsymbol{\alpha_c}$. For the Fresnel transmission a maximum with a four times enhanced intensity is observable at $\boldsymbol{\alpha_i} = \boldsymbol{\alpha_c}$, which is caused by the interference of the reflected and transmitted wave. For both reflection and transmission, the intensity is damped upon increased absorption ($\boldsymbol{\beta} > 0$) of the material. Adapted from the dissertation of Lorenz Bießmann.[81]

If the absorption is negligible and the incident angle is below the critical angle ($\alpha_i < \alpha_c$), the Fresnel reflection intensity shows a constant total reflection. Hereby, an evanescent wave along the interface occurs, which only probes the first few nanometers of the sample and thus only provides lateral structure information. With higher incident angles ($\alpha_i \geq \alpha_c$), the beam penetrates into the material and the reflection intensity strongly decays towards zero. Compared to that, the Fresnel transmission intensity starts at zero for very small incident angles ($\alpha_i \ll \alpha_c$), increases with increasing α_i, and reaches a sharp maximum if the incident angle corresponds to the critical angle of the material ($\alpha_i = \alpha_c$). This maximum arises, as at this exact angle, the reflected and transmitted beams are in phase with each other for a short vicinity along the surface, and thus, constructive interference occurs. This leads to the doubling of the transmitted beam amplitude and consequently the enhancement of the Fresnel transmission intensity by the factor of four, all while conservation of energy applies. At higher incident angles ($\alpha_i > \alpha_c$), the transmission decays towards unity. For both, R^F and T^F, an increased absorption β of the material results in a dampening of the functions.[128]

These trends describe why the transmitted beam intensity is enhanced if the incident beam angle matches the critical angle of the material ($\alpha_i \approx \alpha_c$). However, the reciprocity theorem applies here, which basically states that light transmits in the same way, either from the source to the detector or reversed, from the detector to the source.[128, 135, 136] Thus, it means in this case that if the exit angle of a scattered beam is close to the critical angle of the material ($\alpha_f \approx \alpha_c$) its intensity also gets enhanced, which results in an amplified scattering band, often referred to as Yoneda peak.[133]

In the following chapter the three different scattering techniques applied in the frame of this thesis are introduced in more detail. Hereby, XRR and ToF-NR utilize the specular scattering geometry, while GISAXS uses the diffuse scattering geometry.

2.3.2 X-ray reflectometry

The XRR technique utilizes the specular scattering geometry shown in Figure 2.12a. Hereby, the incident angle (α_i) is varied and the scattering intensity at the exit angle ($\alpha_f = \alpha_i$) is measured with a detector. The scattering is only detected in one plane, meaning that the out-of-plane angle is $\psi_f = 0$ and only the q_z component of the scattering vector $\vec{q}$ is considered. As the modulus remains constant ($k_i = k_f = \frac{2\pi}{\lambda}$) for elastic scattering, q_z results as:

$$q_z = 2k_f \sin(\alpha_i) = 2k_{f,z} \tag{2.59}$$

If and how an incident beam is scattered depends on the materials properties. Because as mentioned before and described with Snell's law (Equation (2.53)), a beam gets partially reflected and refracted, respectively, if it experiences a change of the refractive index at the films surface or interfaces within the film. Furthermore, as introduced in Section 2.3.1 the corresponding reflectivity and transmission intensities are given via the Fresnel reflection and transmission coefficients as $R^F = |r^F|^2$ and $T^F = |t^F|^2$, respectively.

Now, with XRR investigation of a thin film sample, which is usually prepared on a substrate and is surrounded by air, its vertical refractive index variations, film thickness, and film roughness can be determined. For an ideal thin film sample, which is completely homogeneous, reflection only happens at the interfaces between the air and material, and between the material and substrate. However, for a real thin film sample the situation is more complicated, and therefore a model using the Parratt's recursive formulae is needed.[137, 138]

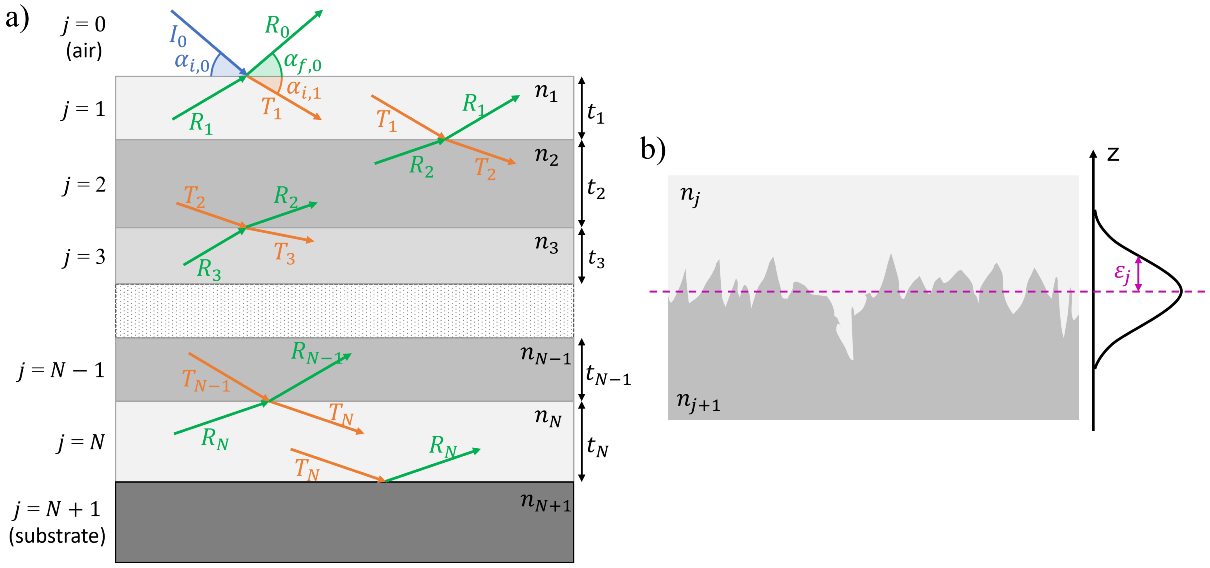

Figure 2.14 X-ray reflectometry investigation method. a) Schematic illustration of the XRR method and basic principle behind the Parratt's recursive formulae to model the reflectometry data of a sample with multiple ($\boldsymbol{N}$) stacked layers, with the thickness $\boldsymbol{t_j}$ and refractive index $\boldsymbol{n_j}$. b) Layer roughness model, which uses a Gaussian distribution of valleys and peaks, respectively to the mean layer height (pink dashed line). Adapted from Filies et al.[138]

Hereby, the thin film is assumed to consist of multiple (N) stacked layers, with the thickness t_j and refractive index $n_j = 1 - \delta_j + i\beta_j$,which are sandwiched between an infinite air ($j = 0$) and an infinite substrate layer ($j = N + 1$), as indicated in Figure 2.14a.[128] At each of the interfaces, a certain ratio of reflection and transmission occurs. According Equation (2.59), hereby, the wave vector transfer into the j layer results as $q_j = 2k_{z,j}$, and with that $k_{z,j}$ can be expressed as:[128, 131]

$$k_{z,j}^2 = \left(n_j k_j\right)^2 - k_{x,j}^2$$
$$k_{z,j} \approx \sqrt{{k_j}^2 - 2\delta_j k_j^2 + 2i\beta_j k_j^2} \tag{2.60}$$

With this, and by neglecting multiple reflections (indicated by the $'$), the Fresnel reflection coefficient (see Equation (2.57)) at the interface between the layer j and $j + 1$, can be written as:

$$r'_{j,j+1} = \frac{n_j \sin\left(\alpha_{i,j}\right) - n_{j+1} \sin\left(\alpha_{i,j+1}\right)}{n_j \sin\left(\alpha_{i,j}\right) + n_{j+1} \sin\left(\alpha_{i,j+1}\right)} = \frac{q_j - q_{j+1}}{q_j + q_{j+1}} \tag{2.61}$$

By calculating the reflectivity starting from the bottom, namely at the interface between the lowest layer ($j = N$) and substrate ($j = N + 1$), it results in Equation (2.62), as here no multiple reflections are present. However, for the next layer on top ($j = N - 1$) the reflectivity now includes multiple reflections and thus results in Equation (2.63).

$$r'_{N,N+1} = \frac{q_N - q_{N+1}}{q_N + q_{N+1}} \tag{2.62}$$

$$r_{N-1,N} = \frac{r'_{N-1,N} - r'_{N,N+1} p_N^2}{1 + r'_{N-1,N} r'_{N,N+1} p_N^2} \quad \text{with } p_j^2 = \exp\left(i q_j t_j\right) \tag{2.63}$$

Hereby, p_j^2 is the phase factor, which considers how the X-ray beam travels through the layer j with a thickness t_j, gets attenuated.[128] This calculation is continued for the $N - 2$ layer, $N - 3$ layer and so on until the top and infinity air layer ($j = 0$) is reached.

However, the computation method only holds for ideal layers with sharp interfaces. Therefore, an additional roughness modeling is complemented to account for the interface roughness.[138, 139] As depicted in Figure 2.14b a Gaussian distribution of the valleys and peaks with respect to the mean height of the layer, with the deviation parameter ε_j, can be used to approximate the respective interface roughness. This results in the roughness coefficient ξ_j, which can be used to correct the before introduced reflectivity as follows:[125, 138]

$$\tilde{r}_{j,j+1} = r_{j,j+1} \xi_j \tag{2.64}$$

$$\xi_j = \exp\left(-2 k_{z,j} k_{z,j+1} \varepsilon_j^2\right) \tag{2.65}$$

Summarizing, during the XRR measurements, the incident angle (α_i) is varied while a detector is mounted respectively to record the scattering intensity resulting at an exit angle of $\alpha_f = \alpha_i$. The hereby measured intensity of the specular reflection in dependence of the incident angle, can then be used to model the vertical structure and composition of the samples, including different stack of multiple layers with thicknesses and interface roughnesses, according to the method introduced in this section. Thus, it can provide information about the inner films refractive index alterations resulting from concentration gradients or enrichment layers. A more precise description of the experimental execution and practical analysis of the XRR measurements preformed in the frame of this thesis are provided in Section 3.4.1.

2.3.3 Grazing-incidence small-angle X-ray scattering

The GISAXS technique utilizes, in contrast to XRR, the diffuse scattering geometry shown in Figure 2.12b. Hereby, the incident angle α_i is fixed to a very shallow angle of $\alpha_i < 1$, so that the X-ray beam hits the sample in the grazing-incidence geometry. This results in a larger footprint of the beam allowing the examination of an increased sample volume, despite the thin film thickness, and thus provides a higher statistical relevance.[140] The diffuse scattering is then recorded on a 2-dimensional detector, which is placed in a certain sample-detector distance (SDD). In the case of GISAXS, the SDD is typically chosen in a range of 1.3 – 5 m to enable the investigation of the diffuse scattering with small exit angles, which provides information about inner film structural features of mesoscale size (≈ nm to µm).[141] In principle, for the grazing-incidence wide angle X-ray scattering (GIWAXS), the SDD can be reduced to a range of 0.1 – 0.5 m, to obtain information about inner film structures in the atomic distance range (≈ Å to nm), often used for crystallographic characterization.[141] However, the GIWAXS method was not used in the frame of this thesis, and thus, only the GISAXS method is discussed in the following. As mentioned before with the GISAXS method diffuse scattering is detected, meaning that also out-of-plane scattering with the angle $\psi_f \neq 0$ is considered. The scattering vector for the GISAXS geometry results as:[130, 142]

$$\vec{q} = \begin{pmatrix} q_x \\ q_y \\ q_z \end{pmatrix} = \frac{2\pi}{\lambda} \begin{pmatrix} \cos(\psi_f)\cos(\alpha_f) - \cos(\alpha_f) \\ \sin(\psi_f)\cos(\alpha_f) \\ \sin(\alpha_i) + \sin(\alpha_f) \end{pmatrix} \tag{2.66}$$

When treating scattering in the grazing-incidence geometry, additional reflection and refraction effects between the sample and substrate occur, which complicate the situation. These perturbation effects can be accounted for with the distorted-wave Born approximation (DWBA)[136, 143], which is a theoretical first-order correction approach to the simpler Born approximation. Hereby, as graphically presented in Figure 2.15, four different scattering scenarios are accounted for in the DWBA: a) the simple scattering of an incoming wave, b) the scattering of an incoming wave with subsequent reflection at the sample-substrate interface, c) a reflection at the sample-substrate interface prior to scattering, and d) reflection prior and subsequent to the scattering.[141, 144] This means that within the DWBA the resulting scattering intensity is considered a superposition of all the above-described scattering events.

The analysis of the resulting scattering pattern recorded on the 2-dimensional detector can be carried out via simulation using different analysis tools.[142, 145–147] However, in this thesis only the lateral structure information are of interest and thus the data can be reduced to line cuts along the q_y direction and obtained at a fixed q_z. These horizontal line cuts are usually extracted at the Yoneda peak position of the material of interest, because here the scattering intensity is enhanced, as explained in Section 2.3.1.[140] Furthermore, the effective interface approximation (EIA) is applied, which only considers lateral correlations by assuming that scattering takes place at only one effective interface.[144, 148–150]

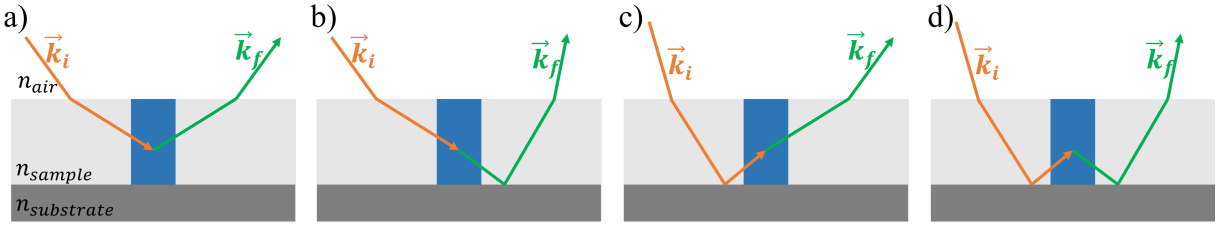

Figure 2.15 Scattering and reflection events in the frame of the DWBA. Graphical depiction of different scattering and reflection combinations, which are considered in the DWBA. a) Directly scattered beam, b) Scattering and subsequent reflection, c) reflection prior to the scattering, and d) reflection prior and subsequent to the scattering event. Adapted from Hexemer et al.[141]

Thereby, usually time-consuming and computationally intensive simulations can be reduced, and the differential scattering cross-section of the incident X-ray beam with the sample results as:[144, 148, 149]

$$\frac{d\sigma}{d\Omega} = \frac{A\pi^2}{\lambda^4}|\Delta n|^2\left|t_i^F\right|^2\left|t_f^F\right|^2 P(\vec{q}) \propto P(\vec{q}) \tag{2.67}$$

$$P(\vec{q}) \propto N|F(\vec{q})|^2 S(\vec{q}) \tag{2.68}$$

The differential scattering cross-section defines the normalized amount of scattered photons $d\sigma$ that exit in the elementary solid angle $d\Omega$ and thus is proportional to the scattering intensity. Hereby, as the incident angle α_i is typically fixed during a measurement, the illuminated sample area A is constant, and the X-ray wavelength λ and the scattering contrast $|\Delta n|^2$ usually do not change during the experiment. Furthermore, when analyzing horizontal line cuts also the exit angle α_f is fixed, and thus, the Fresnel transmission intensities of the incident and exiting X-ray beam, $\left|t_i^F\right|^2$ and $\left|t_f^F\right|^2$, remain invariable. Consequently, the scattering cross-section and the scattering intensity directly scale with the diffuse scattering factor $P(\vec{q})$ as indicated in Equation (2.67).[140, 148] In the case of GISAXS, the diffuse scattering factor incorporates information about mesoscale sized scattering structures within the sample. As expressed in Equation (2.68), $P(\vec{q})$ is proportional to the number of scattering objects N, the form factor $F(\vec{q})$ describing the respective size and shape of a scattering object with approximately homogeneous refractive index, and the structure factor $S(\vec{q})$ describing the spatial distribution of these scattering objects.[136, 144, 151] However, a real sample does not only contain monodisperse scattering objects which are homogeneously distributed, but usually contains a variety of different sized scattering objects with diverse spatial distributions. To account for that, an effective average form factor is introduced according to the local monodisperse approximation (LMA).[141, 142, 152] Based on this, $P(\vec{q})$ can be expressed as an incoherent superposition of j types of scattering objects with different counts, form factors, and structure factors as expressed in Equation (2.69).[153, 154]

$$P(\vec{q}) \propto \sum_j N_j \left\langle \left|F_j(\vec{q})\right|^2 \right\rangle S_j(\vec{q}) \tag{2.69}$$

Hereby, only coherent scattering for objects of the same group is presumed, and the contributions of the different types of scatterers with their respective form and structure factors are independent of each other. Furthermore, correlated to these form and structure factors, the sizes (radius R_j) and distances (center-to-center distance D_j) of the scattering objects are described with a Gaussian distribution.[153, 154] For the modeling of the PEDOT:PSS thin films investigated in this thesis, standing cylindrical form factors were assumed for the PEDOT domains,[144, 148, 152] as this shape approximation works reasonable well, due to the rotational symmetry of the real pancake-shaped PEDOT domains[19] described in Section 2.1.2. The structure factor was defined by assuming a 1-dimensional para-crystal lattice arrangement[144] to introduce a short-range order of the scattering PEDOT domains according to Hosemann et al.[155] A more elaborated description of the model, applied in the frame of this thesis to analyze GISAXS data, can be found in the dissertation of Dr. Christoph Schaffer.[153] The detailed specification of the experimental procedure, selected measurement parameters and preformed analysis of the GISAXS investigation is provided in Section 3.4.2.

2.3.4 Time-of-flight neutron reflectometry

The ToF-NR investigates the specular scattering similar to XRR introduced in Section 2.3.2. However, both techniques differ in obtaining the data. For XRR a monochromatic X-ray beam is used and the incident angle (α_i) is varied, while the scattering intensity at the exit angle ($\alpha_f = \alpha_i$) is measured. However, compared to the brilliance, high flux, and low energy divergence that synchrotron X-ray sources enable, neutron sources usually provide a neutron flow with a broad energy distribution and lower flux.[127] If this polychromatic neutron beam is narrowed down to be nearly monochromatic, the neutron flux would be reduced even further. Therefore, the time-of-flight mode is usually applied to perform neutron reflectometry.[156–158] Hereby, the incident angle is fixed, and the energy or wavelength of the neutrons is varied. This is done by cropping the continuous incident neutron beam with a system of different choppers, into sets of neutrons of defined velocity and travel time. These neutrons are then guided onto and interact with the sample, and are afterwards recorded on a detector along with their respective time of arrival.[134, 159] With this information the velocity of the neutrons ($v^{neutron}$) and consequently their wavelength ($\lambda^{neutron}$) can be obtained according to the de Broglie wavelength equation:[134]

$$\lambda^{neutron} = \frac{h}{m^{neutron} v^{neutron}} \tag{2.70}$$

Hereby, h is the Plack's constant and $m^{neutron}$ is the mass of the neutrons. Another characteristic that must be considered is that due to the mass of neutrons, they are subject to gravity, in contrast to X-rays.[160] This effect of gravity, which is more severe for slower and lower energetic neutrons, influences the incident angle (α_i) as well as the impact position on the detector.

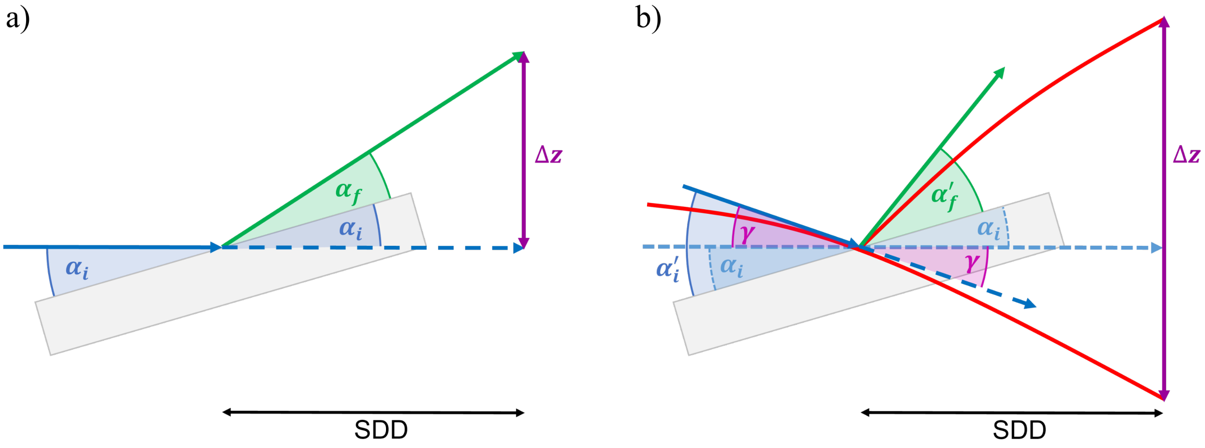

Figure 2.16 Gravitational effect in neutron scattering methods. a) Neutron scattering without the gravitational effect. b) Influence of the neutron mass and effect of gravitation on neutron scattering events, which lead to a divergent neutron trajectory (red line) and altered real angles $\boldsymbol{\alpha_i'}$ and $\boldsymbol{\alpha_f'}$. Adapted from the dissertation of Monika Rawolle.[160]

Compared to Figure 2.16a without gravity influence, Figure 2.16b shows how the actual incident angle (α_i') changes due to the gravitational effect dependent on the energy of the respective neutron, which can be described as $\alpha_i' = \alpha_i + \gamma$. Using the specular scattering geometry and considering that the incident, the directly transmitted and the reflected neutron beams are all subjected to the same gravitational effect, $\alpha_i' = \alpha_f'$ applies and the actual incident angle can be geometrically obtained via:[160]

$$\tan\left(\alpha_i' + \alpha_f'\right) \overset{\alpha_i'=\alpha_f'}{\Longrightarrow} \tan(2\alpha_i') = \frac{\Delta z'}{SDD} \tag{2.71}$$

Eventually, the single neutrons within the different arriving neutron sets are recorded in single-neutron mode and are then binned according to their wavelength. Depending on the chosen binning size, the desired energy resolution can be customized.[159, 161, 162] For ToF-NR experiments, only the specular reflection geometry is of interest, thus the scattering vector results as:[134]

$$\mathrm{q}_z = \frac{4\pi}{\lambda}\sin\left(\alpha_i'\right) \tag{2.72}$$

This equation is the same as Equation (2.59) and the resulting reflectivity curves are similar to the curves obtained from XRR. However, both techniques provide a different sensitivity due to the in Section 2.3.1 introduced scattering contrast of X-rays and neutrons. Nevertheless, the basic theory and data interpretation is equal as described in Section 2.3.2 and further information about the ToF-NR technique and analysis are detailed by Cubitt et al.[159, 162] The measurement procedure, experiment and setup details for the in this thesis conducted ToF-NR investigations are provided in Section 3.4.3.

3 Characterization methods

This chapter contains the description of all characterization methods used throughout this thesis to investigate the properties of PEDOT:PSS thin films post-treated with ionic liquids (ILs). First, in Section 3.1, the spectroscopic characterization techniques are provided, and the electronic characterization techniques are detailed in Section 3.2. The structural characterization was split into two parts depending on if the data were obtained in real space, given in Section 3.3, or in reciprocal space, given in Section 3.4. The last Section 3.5 in this chapter describes the sample environments and experimental setups used for the *in situ* characterizations. Parts of the characterization method specifics provided in this present chapter are based on previous publications.[50–52, 163]

3.1 Spectroscopic characterization

For spectroscopic characterization of the thin PEDOT:PSS films the following three methods, described briefly in this section, were used. Utilizing ultraviolet-visible (UV-Vis) spectroscopy, the optical absorption of the differently treated samples was investigated. Furthermore, Fourier-transform infrared (FTIR) spectroscopy gave insight into the molecular polymer-ionic liquid interaction and spectral reflectance (SR) provided information about the thickness and refractive index of the polymer films.

3.1.1 Ultraviolet-visible spectroscopy

Ultraviolet-visible spectroscopy was performed to determine the oxidation level of the treated PEDOT:PSS thin film samples. More precisely, this method allows for the detection of neutral, polaron and bipolaron states in the PEDOT polymer chain, as described in Section 2.1.3, and provides information on the charge carrier concentration. As mentioned in Section 2.2.3, the electrical conductivity and Seebeck coefficient are dependent on the charge carrier concentration. Therefore, the effect from different sample treatments on the thermoelectric properties can be correlated to changes in the oxidation level using UV-Vis spectroscopy. This is demonstrated in Chapter 5 and Chapter 6.

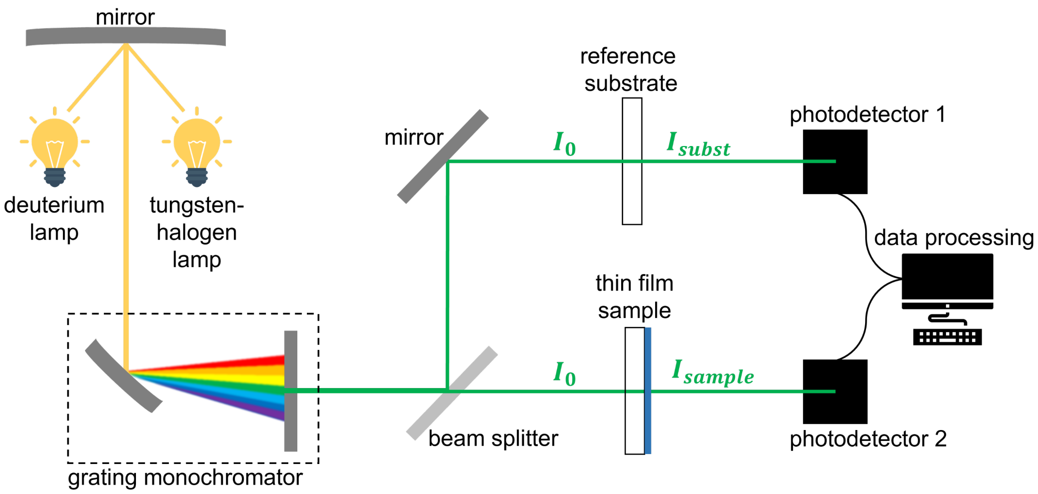

Figure 3.1 Working principle of UV-Vis spectroscopy. Schematic depiction of the UV-Vis spectroscopy setup and the optical path of the light. The light provided by two light sources is transformed into monochromatic light of defined wavelength and then split into two beams, both with the intensity $\boldsymbol{I_0}$. One of the beams is guided through an empty substrate as a reference and one is guided through the thin film sample. Both resulting wavelength-dependent intensities $\boldsymbol{I_{subst}}$ and $\boldsymbol{I_{sample}}$ are then collected on photodetectors and further processed to obtain the UV-Vis absorption spectra. Adapted from Rocha et al.[164]

For the UV-Vis spectroscopy examinations in this thesis, a *Lambda 35* spectrometer by *PerkinElmer* was used. This spectrometer contains a deuterium and a tungsten-halogen light source that enables a maximum wavelength range of 280 – 1100 nm, thus covering the entire visible light spectrum from the ultraviolet range to the infrared range. The measurements were performed in transmission mode, which required the usage of transparent substrates like glass and ITO glass. The slit width was 1 nm, and the scanning speed was set to 480 nm min^{-1}. Before every measurement series, a 100 % transmission baseline, and a 0 % transmission blocked-beam baseline calibration was performed. For the *in situ* UV-Vis measurements a *MBB1D1* broadband (360 – 1020 nm) light-emitting diode (LED) from *Thorlabs Inc.* was placed below a small hole in the sample stage and a *CAS 140 CT Compact Array* spectrometer from the company *Instrument Systems GmbH* was mounted above the hole into the lid of the measurement chamber, as detailed in Section 3.5.1. The *in situ* measurements were also performed in transmission mode and a glass substrate was used as reference sample. The working principle of UV-Vis spectroscopy is sketched in Figure 3.1 and the basics are explained in the following.

First, the wavelength spectrum coming from the installed light sources, is transformed by a grating monochromator into a beam with a specific tunable wavelength. The monochromatic light is then split into two beams, both with the wavelength-dependent initial intensity $I_0(\lambda)$: One beam is guided through a reference substrate and one beam is guided through the sample. The respective resulting intensity spectra of the reference substrate $I_{subst}(\lambda)$, and the sample $I_{sample}(\lambda)$, are recorded on photodetectors. The collected intensity data are then processed and the wavelength-dependent transmission spectra of the PEDOT:PSS thin film is obtained.

The transmittance of a sample $T_{sample}(\lambda)$, which in this case is composed of the transmittance of the substrate $T_{subst}(\lambda)$ and the transmittance of the thin film $T_{film}(\lambda)$, compares the intensity of the light before passing through the sample and after passing through the sample. This results in the following Equation (3.1):

$$T_{sample}(\lambda) = T_{film}(\lambda)\, T_{subst}(\lambda) = \frac{I_{sample}(\lambda)}{I_0(\lambda)} \tag{3.1}$$

Accordingly, the transmittance of the reference substrate is defined as:

$$T_{subst}(\lambda) = \frac{I_{subst}(\lambda)}{I_0(\lambda)} \tag{3.2}$$

Combining Equation (3.1) and Equation (3.2), the transmittance of the investigated polymer thin film is obtained as:

$$T_{film}(\lambda) = \frac{I_{sample}(\lambda)}{I_{subst}(\lambda)} = e^{-\alpha_{film}(\lambda)\, t_{film}} \tag{3.3}$$

Furthermore, as shown in Equation (3.3), the transmittance of the investigated film can be associated with the films absorption coefficient $\alpha_{film}(\lambda)$ and the thickness of the film t_{film}, via the Lambert Beer law, which neglects losses due to reflection and scattering on the sample.

Additionally, the absorbance $A(\lambda)$ of a material, which is often of interest in spectroscopy, is related to the transmittance $T(\lambda)$ with:

$$A(\lambda) = -\log_{10} T(\lambda) \tag{3.4}$$

Combining Equation (3.3) with Equation (3.4) the absorption coefficient $\alpha(\lambda)$ of the investigated thin film can be expressed either as a function of its absorbance $A_{film}(\lambda)$ or its transmittance $T_{film}(\lambda)$:

$$\alpha_{film}(\lambda) = \frac{1}{t} A_{film}(\lambda) \ln 10 = -\frac{1}{t} \ln T_{film}(\lambda) \tag{3.5}$$

In this thesis, the transmittance spectra of the examined thin films were measured and the respective film thicknesses, obtained from surface profilometer characterization described in Section 3.3.1, were used to calculate and plot the respective absorption coefficient spectra with the unit [nm^{-1}].

3.1.2 Fourier-transform infrared spectroscopy

Fourier-transform infrared spectroscopy enables the examination of the molecular structure within the PEDOT:PSS thin film samples, after post-treatment with ILs. More precisely, FTIR spectroscopy was utilized in Chapter 5 to determine the presence and interactions of the respectively applied IL molecules within the PEDOT:PSS film.

For this, an attenuated total reflectance (ATR) FTIR spectrometer *Frontier*™ from the company *PerkinElmer*® with a diamond/zinc selenide crystal was used. The in this thesis presented ATR-FTIR measurements were conducted with the help Shujin Hou. The thin film samples were pressed onto the crystal with an electronic force gauge to ensure reproducible contact, and a wavenumber range of 650 – 4000 cm^{-1} was investigated. The *PerkinElmer*® software *Spectrum*™ was used to perform the baseline correction on the measured FTIR spectra. The basic measurement principle and device structure is depicted in Figure 3.2 and is described in short in the following.

FTIR spectroscopy measures the absorption of IR radiation by the investigated sample material to gain information about the state and local environment of the molecules inside the sample. This is possible as different vibrational modes of molecules can be excited by the absorption of a respective radiation energy. In the case of IR radiation absorption, only vibrational modes which result in a change of the molecules dipole moment can be activated. Hereby, the respective absorbed radiation and the excited molecule vibration match in their frequency. A sketch of the different IR-active vibrational modes is provided in Figure 3.2a. As the molecular vibrational frequency is strongly influenced by the associated atom masses, the potential energy surface, and the vibronic coupling of a molecule, FTIR spectroscopy provides extensive information about the functional group interaction of the molecules inside the sample. The basic outline of the ATR-FTIR measurement setup is given in Figure 3.2b.

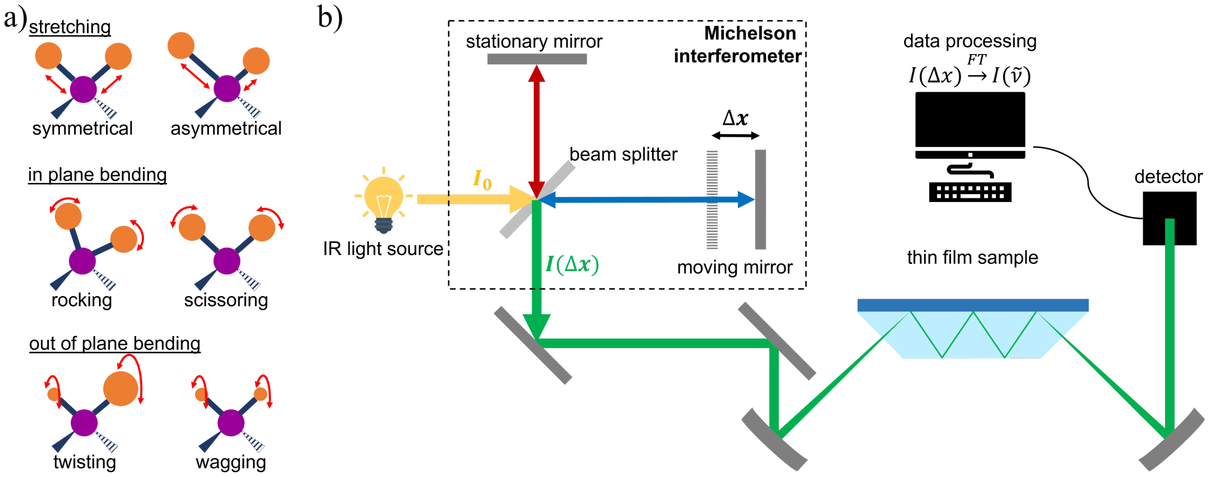

Figure 3.2 Working principle of ATR-FTIR spectroscopy. a) Graphical depiction of the different molecular vibration modes activatable by IR radiation. b) Schematic setup of an ATR-FTIR, where the beam coming from the IR light source is first guided through a Michelson interferometer, to obtain a beam with optical path difference (Δx) dependent intensity. This beam is then guided through a crystal to measure the IR absorption of the sample in ATR mode geometry, before the reflected beam intensity is recorded on a detector. Adapted from the dissertation of Lucas Philipp Kreuzer.[161]

First, a light source produces light in the IR wavelength region, which is guided through a collimator and onto a beam splitter. Here, ideally 50 % of the light is reflected towards a stationary mirror (red arrow) and 50 % of the light is refracted towards a movable mirror (blue arrow). Both light beams are reflected at the respective mirrors and are then recombined at the beam splitter and guided towards the sample. In the ATR geometry, the resulting light beam (green arrow) is not directly guided through the sample but is sent into a crystal in an angle which is below the critical angle, thus resulting in the internal reflection of the beam through the crystal. At the beam reflection points on the sample-crystal interface, an evanescent wave forms, interacts with the sample, and information about the vibrational and chemical information of the material is acquired. Finally, the beam is collected and directed to the detector to record the FTIR absorption data.

The special feature in the entire working principle of the FTIR spectroscopy method is the Michaelson interferometer. Because of its geometry, the two light beams (blue and red) interfere with each other in a destructive or constructive way that is dependent on the optical path difference Δx and the wavelength λ. Equation (3.6) and Equation (3.7) show the respective conditions for destructive or constructive interference, with m being an integer. As a result, Equation (3.8) gives the intensity of the superposition of two light beams with the same wavelength.

$$\Delta x = \left(m - \frac{1}{2}\right)\lambda \tag{3.6}$$

$$\Delta x = m\,\lambda \tag{3.7}$$

$$\mathrm{I}(\Delta\mathrm{x}) = I_0[1 + \cos(2\pi\lambda^{-1}\Delta x)] \tag{3.8}$$

However, both beams consist of light with multiple wavelengths or wavenumbers ($\tilde{\nu} = \lambda^{-1}$). Therefore, following the Euler equation, the intensity of the total resulting beam can be mathematically expressed in dependence of the optical path difference as:

$$\mathrm{I}(\Delta x) = \int_{-\infty}^{+\infty} I(\tilde{\nu})e^{2\pi\tilde{\nu}\Delta x}d\tilde{\nu} \tag{3.9}$$

With Fourier-transformation of Equation (3.9) this corresponds to the wavenumber-dependent beam intensity of:

$$\mathrm{I}(\tilde{\nu}) = \int_{-\infty}^{+\infty} I(\Delta x)e^{-i2\pi\tilde{\nu}\Delta x}d\Delta x \tag{3.10}$$

This means that by varying the moveable mirror position and thus changing the optical path difference, wavenumber-dependent information can be acquired, which is exemplarily depicted in Figure 3.3. Therefore, the intensity spectra of a reference substrate and of the thin film sample are measured in dependence of Δx, named $I_{subst}(\Delta x)$ and $I_{sample}(\Delta x)$, respectively. Using Fourier-transformation the intensity spectra in dependence of the wavenumber, $I_{subst}(\tilde{\nu})$ and $I_{sample}(\tilde{\nu})$ are obtained, with which the absorption spectra $A(\tilde{\nu})$ can be calculated:

$$A(\tilde{\nu}) = -log_{10}\left(\frac{I_{sample}(\tilde{\nu})}{I_{subst}(\tilde{\nu})}\right) \tag{3.11}$$

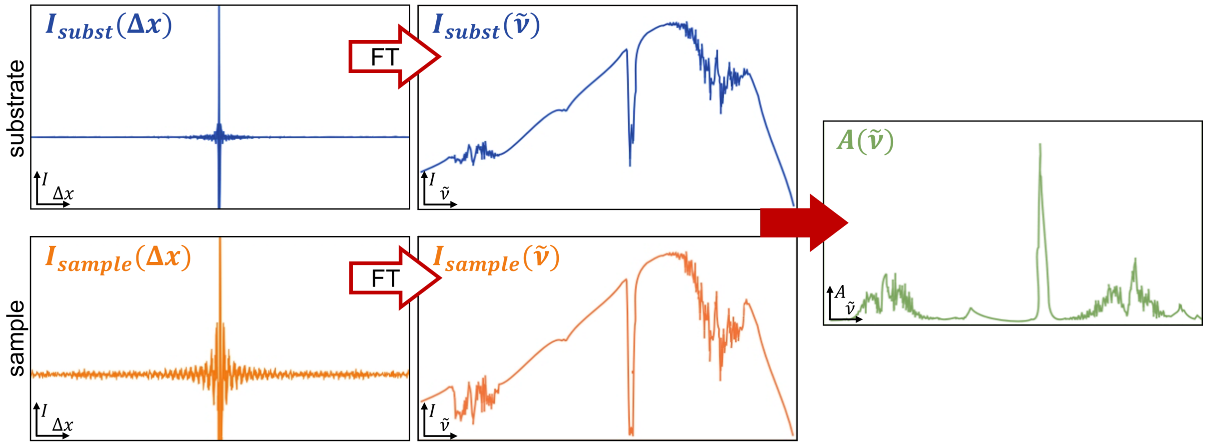

Figure 3.3 Exemplary FTIR spectra and their processing into an absorption spectrum. The graphs on the left shows the optical path length Δx-dependent intensity spectra of an empty substrate (blue) and the thin film sample (orange). With Fourier-transformation the respective wavenumber $\tilde{\nu}$-dependent intensity spectra can be obtained and with these spectra, the wavenumber $\tilde{\nu}$-dependent absorption spectrum (green) can be calculated. Modified from Zwick et al.[165]

3.1.3 Spectral reflectance

Spectral reflectance was conducted to determine the thickness and the effective refractive index evolution of post-treated PEDOT:PSS thin film samples during exposure to various relative humidities. This non-destructive method utilizes interference effects in the with different IL post-treated thin films to follow *in situ* their different water uptake and film swelling behavior, as investigated in Chapter 8.

A *Filmetrics® F20 Film Thickness Measurement Instrument* from the *KLA* company *Filmetrics Inc.* was used for the SR measurements. The instrument was equipped with a *Filmetrics® LS-DT2* light source that contains a deuterium lamp and a halogen lamp, thus providing light in the UV range (180 – 360 nm) or the visible and near-IR range (360 – 1100 nm). For the SR measurements in this thesis only the light of the halogen lamp was used, which was guided with an optical fiber to the thin film sample. The incident light beam was adjusted to have a spot size of around 2 mm by modifying the sample fiber distance (~ 100 mm) and using a lens assembly. Before the start of every measurement, a cleaned silicon reference substrate was placed onto the sample holder. By tuning the incident angle of the beam and the lamp positioning, the intensity of the raw signal was maximized. Then, a reference spectrum of the silicon substrate was recorded and additionally a measurement of the background illumination spectrum, caused by interfering light, was conducted by placing a piece of black cardboard onto the sample holder. Afterwards, the thin film sample prepared on silicon substrate was mounted onto the sample holder and the reflected light spectrum was recorded in 10 s intervals. The obtained data were analyzed using the *FILMeasure* software from *Filmetrics Inc.* to extract the thin film thickness and the effective refractive index via a fitted model. Hereby, best fits were obtained when a two-layer system was assumed, comprised of the SiO_2 substrate and a PEDOT:PSS polymer layer. A sketch of the principle behind the SR measurements is provided in Figure 3.4 and the basic theory is introduced in the following.

The working principle of the SR method, depicted in Figure 3.4a, is based on the reflection and refraction of an incident light when it crosses the interface between materials with different optical constants. These optical constants are, the real refractive index n, which describes the ratio between the velocity of a wave traveling through vacuum and the velocity of a wave traveling through a medium, and the extinction coefficient k, which represents the energy absorption by describing the attenuation of a wave amplitude when it travels through a medium. Both optical constants are combined in the complex refractive index $\hat{n} = n - ik$.

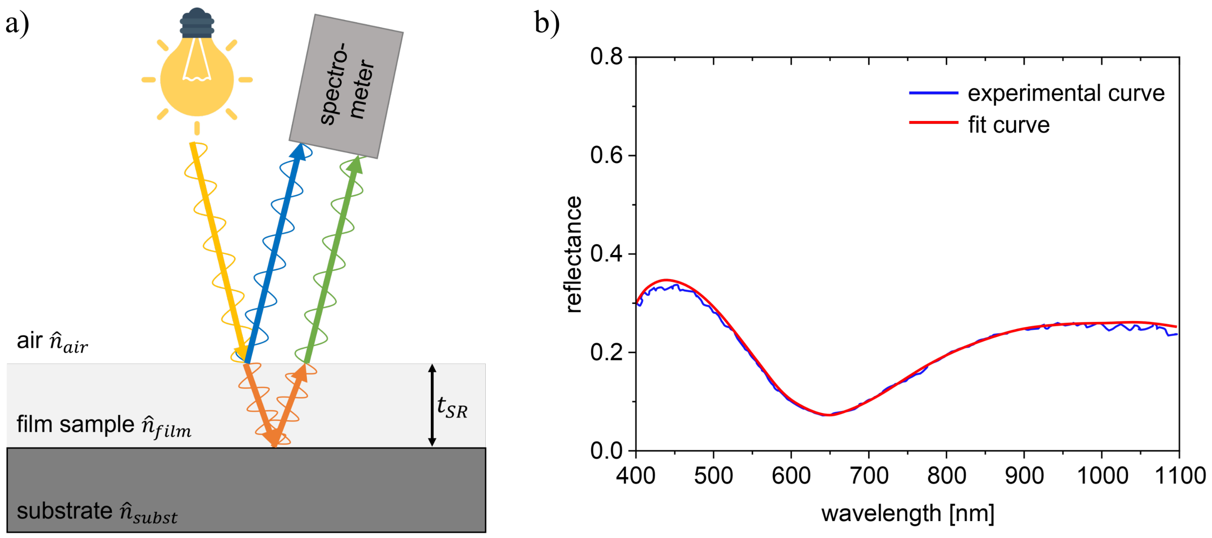

Figure 3.4 Working principle of the SR method. a) Schematic setup of the SR method in which a beam coming from a light source (yellow arrow) is directed perpendicular onto the sample surface. This beam is then partially reflected at the air/film interface (blue arrow) and partially refracted and then reflected at the film/substrate interfaces (orange arrows). Interference between the two reflected beams (blue and green arrows) results in a beam with wavelength-dependent diminished or magnified intensity. In the sketch the incident and exit angles are sketched larger than zero for a better visibility. The resulting beam is then collected with a spectrometer and provides the in b) shown exemplary reflectance curve (blue line), which can then be fitted (red line) to obtain the thickness and refractive index of the sample. Adapted from *Filmetrics Inc.*[166]

For the samples investigated in this thesis, reflection at the interface between air ($\hat{n}_{air}$) and polymer thin film ($\hat{n}_{film} > \hat{n}_{air}$), and reflection at the interface between polymer thin film ($\hat{n}_{film}$) and the silicon substrate ($\hat{n}_{subst} > \hat{n}_{film}$) occur. For the special case of the Fresnel equations at normal incidence, where the incident angle is zero, the reflection coefficients $\hat{r}$ at the two interfaces result in Equation (3.12) and Equation (3.13), respectively:

$$\hat{r}_{air,film} = \frac{\hat{n}_{air} - \hat{n}_{film}}{\hat{n}_{air} + \hat{n}_{film}} \tag{3.12}$$

$$\hat{r}_{film,subst} = \frac{\hat{n}_{film} - \hat{n}_{subst}}{\hat{n}_{film} + \hat{n}_{subst}} \tag{3.13}$$

Due to the SR measurement geometry, both respectively reflected light waves interfere with each other, which results in a wavelength-dependent diminished or magnified intensity of the reflected light recorded with the spectrometer. More precisely, this interference can be constructive or destructive, and is dependent on the refractive index of the film $\hat{n}_{film}$, the film thickness t_{SR}, the wavelength coming from the light source λ, and m being an integer. The respective conditions for the constructive or destructive interference are given in Equation (3.14) and Equation (3.15), respectively:

$$2\, n_{film} t_{SR} = \left(m - \frac{1}{2}\right)\lambda \tag{3.14}$$

$$2\, n_{film} t_{SR} = m\, \lambda \tag{3.15}$$

Overall, in the case of a sample consisting of a single polymer thin film on a silicon substrate, the resulting reflection coefficient as a function of the wavelength is given as:

$$\hat{r}_{sample}(\lambda) = \frac{\hat{r}_{air,film} + \hat{r}_{film,subst}\ e^{-\beta i}}{1 + \hat{r}_{air,film}\hat{r}_{film,subst}\ e^{-\beta i}} \tag{3.16}$$

$$\text{with } \beta = \frac{4\pi\hat{n}_{film} t_{SR}}{\lambda}$$

The wavelength-dependent reflectance of the thin film sample R_{sample}, can be obtained with Equation (3.18) and the resulting graph of an exemplary sample is depicted in Figure 3.4b as the blue line:

$$R_{sample}(\lambda) = \left|\hat{r}_{sample}(\lambda)\right|^2 \tag{3.17}$$

The data were then analyzed by finding a model film, red line in Figure 3.4b, where the following least square expression is minimized:

$$\sum_{\lambda}\left(R^{exp}_{sample}(\lambda) - R^{model}_{sample}(\lambda)\right)^2 \tag{3.18}$$

with $R^{exp}_{sample}(\lambda)$ being the experimentally obtained reflectance at a specific wavelength, and $R^{model}_{sample}(\lambda)$ being the theoretical calculated reflectance of the model film at a specific wavelength. The goodness-of-fit for all the in Chapter 8 presented SR model fits was between 0.8 and 1.0 for all samples at the different humidity stages.

3.2 Electrical characterization

In this thesis, the electrical characteristics of the thin film PEDOT:PSS samples were unraveled by using different methods. With measurements of the Seebeck coefficient (S) changes in the Seebeck effect of the thin films were characterized depending on the ionic liquid post-treatment. With two-point and four-point measurements the respective electrical conductivity of the differently treated thin films was determined. Additional electrochemical impedance spectroscopy (EIS) was preformed to gain a more detailed understanding of the charge carrier transport processes within the PEDOT:PSS films. The basic principles and features of these characterization methods are described in short in this section.

3.2.1 Seebeck coefficient measurement

Seebeck coefficient measurements provide information about the degree of a thermovoltage forming within a material upon the application of a temperature gradient, which is crucial for the implementation as thermoelectric material. In this present thesis, S measurements were performed on differently treated PEDOT:PSS thin film samples, to investigate the influence of the post-treatment with various ILs, as demonstrated in Chapter 5, and to investigate the effect of heat treatment as presented in Chapter 6. The Seebeck coefficients were measured using a custom-designed device, sketched in Figure 3.5, which was developed and build by Xaver Lamprecht.[167]

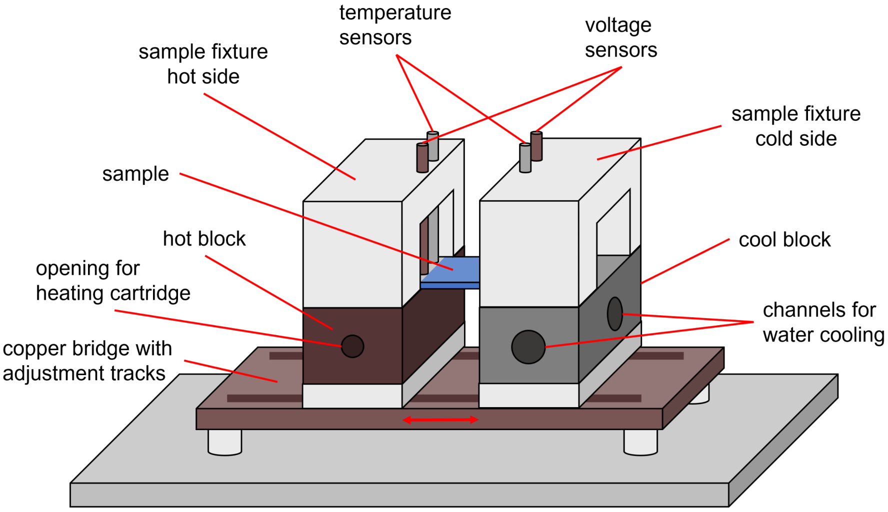

Figure 3.5 Seebeck coefficient measurement setup. Schematic sketch of the setup used to measure the Seebeck coefficient of a thin film sample. Hereby, the sample is placed with one edge on a hot block, which is heated by a heating cartridge, and with the other edge on a cool block, which is cooled via water cooling. The sample is fixed with two sample fixtures and connected with a temperature sensor and voltage sensor on each side. With this the temperature gradient and the arising thermovoltage can be measured, to determine the materials Seebeck coefficient. Adapted from the bachelor thesis of Xaver Lamprecht.[167]

In principle, this device consists of a copper made “cool block”, which is connected to an external water-cooling system, and a copper made “hot block”, which contains a heating cartridge. Both blocks are mounted, with thermal insulating poly(tetrafluoroethylene) (PTFE) spacer in between onto a copper bridge, in a way that allows the flexible adjustment of their distance. On top of each block PTFE made “sample fixtures” are attached, each containing a platinum-100 (Pt-100) resistance temperature sensor and a copper pin as voltage sensor. As sketched in Figure 3.5 the polymer thin film samples are placed with one edge onto the “hot block” and one edge onto the “cold block”. Then all four sensors are lowered on the silver paint covered edges of the sample, described in Section 4.5.1, and are pressed on with a spring, exerting a contact force of ~1 N to ensure a good contacting of the sensors to the thin film sample. The temperature sensors are each connected to a *Model 330 Autotuning Temperature Controller* by the company *LakeShore Cryonics*®. Hereby the temperature controller on the "cold block" measures the temperature T_{cold}, which is controlled by a *JULABO FP50 HL* thermal water bath cycle. While the controller on the "hot block" is connected to a *HQ Power*™ *PS3010 DC Power Supply*, which powers the heating cartridge and thus allows the temperature regulation T_{hot} of the "hot block". With this a defined temperature gradient ΔT can be applied on the sample, which results in the formation of a thermovoltage along the thermoelectric thin film sample. This arising thermovoltage ΔV^{therm} is then measured via the copper pins with a Keithley *SourceMeter*® *2400.*

The Seebeck coefficient S is calculated with the following Equation (3.19):

$$S = \frac{\Delta V^{therm}}{T_{hot} - T_{cold}} = \frac{\Delta V^{therm}}{\Delta T} \tag{3.19}$$

To minimize temperature gradient fluctuations, the "hot block" and "cold block" were pre-tempered to the desired temperatures, usually T_{cold} = 25 °C and T_{hot} = 100 °C yielding a ΔT of 75 K. Only then the sample was placed into the setup and the measurement started using a *MATLAB* script, which continuously recorded ΔV^{therm} and ΔT for 25 min with a speed of 12 measurements per minute. From these obtained 300 measurement points the first 50 were ruled out as the sample temperature was still reaching equilibrium, and only the last 250 were included to calculate the average Seebeck coefficient.

3.2.2 Two-point probe resistance measurements

With two-point probe resistance measurements the conductivity of the in this thesis characterized PEDOT:PSS thin film samples can be determined. Furthermore, the described measurement technique allows the investigation of the film resistance R while they are being subjected to different external influences. In Chapter 6 and Chapter 7 the resistance evolution of PEDOT:PSS thin films post-treated with different EMIM DCA concentrations are examined, while being exposed to elevated temperatures or elevated humidities, respectively. The two-point probe measurements were performed using a converted version of the by Xaver Lamprecht custom-designed Seebeck coefficient measurement setup[167] mentioned before and it is sketched in Figure 3.6.

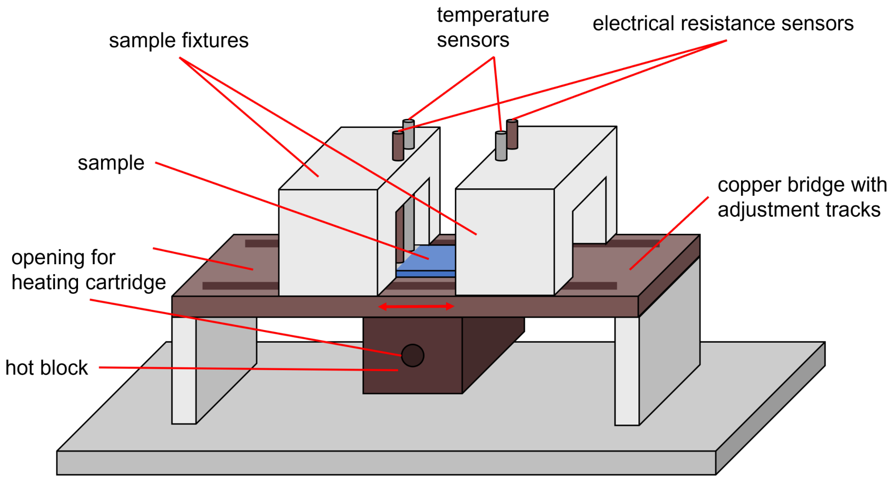

Figure 3.6 2-point probe resistance measurement setup. For measurement of the electrical resistance of a sample in 2-point geometry, the sample is placed on a copper bridge and fixed with two sample fixtures. The sample is connected to two temperature sensors and two voltage sensors, each of which placed on one edge of the sample. A hot block, which can be heated with a heating cartridge, is placed below the copper bridge and with this the electrical resistance of a thin film sample can be measured at different temperatures. Adapted from the bachelor thesis of Xaver Lamprecht.[167]

For the two-point-probe resistance measurements, the copper block containing the heating cartridge, the "hot block", is fixed in direct thermal contact below the copper bridge, which is elevated with PTFE mountings for this purpose. On top of the copper bridge two "sample fixtures" made of PTFE are attached, which contain a Pt-100 resistance temperature sensor and a copper pin as voltage sensor each. The sample is then placed directly onto the heatable copper bridge and connected to the sensors with a spring (contact force of ~1 N) pressing them onto the silver paint covered edges of the sample, described in Section 4.5.1. The temperature sensors are each connected to a *Model 330 Autotuning Temperature Controller* by the company *LakeShore Cryonics*®, with one of them controlling the sample temperature T to the desired set temperature via a *HQ Power*™ *PS3010 DC Power Supply* powering the heating cartridge. The voltage copper pins are connected to a Keithley *SourceMeter*® *2400*, with which a defined voltage V was applied between the pins connected to the thin film sample, and the resulting current J flowing through the sample was measured. With that the resulting film resistance R was calculated using Equation (3.20).

$$R = \frac{V}{J} \tag{3.20}$$

An applied *MATLAB* script facilitates the continuous reading of the resistance R and sample temperature T with a speed of 12 measurements per minute. By now considering the sample geometry with t_{film} being the thickness of the thin film, w being the width of the sample and l

being the length of the sample, therefore, the distance between the silver paint contact areas, the conductivity σ of the thin film can be obtained with Equation (3.21) as follows:

$$\sigma = \frac{1}{R}\frac{l}{t_{film}w} \tag{3.21}$$

For *in situ* investigation of the differently post-treated PEDOT:PSS thin film conductivity while exposing them to either various temperatures or various relative humidities, this two-point resistance measurement setup was mounted into the X-ray analysis voltage-emulation rig, which is described in detail in Section 3.5.1. For the measurements in Chapter 6 the applied constant voltage for the EMIM DCA post-treated samples was 0.01 V and 1 V for the reference sample, while in Chapter 7 a constant voltage of 0.03 V was applied to all samples.

3.2.3 Four-point probe resistance measurements

Four-point probe resistance measurements are commonly applied to acquire the sheet resistance of a thin film sample. In Chapter 5 it was utilized to obtain the conductivity of the PEDOT:PSS thin films in dependency of the for post-treatment used various ILs and their concentrations. Furthermore, the four-point probe resistance measurements were performed as pre-characterization technique to probe and guarantee the successful EMIM DCA doping of the throughout the rest of this present thesis investigated thin film samples. A schematic sketch of the four-point probe resistance measurement technique is presented in Figure 3.7 and the basic concepts are provided in the following.

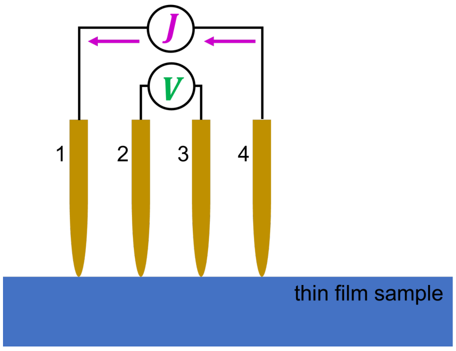

Figure 3.7 4-point probe resistance measurement setup. For the electrical resistance measurement of a thin film sample in 4-point geometry, four pins, with a defined distance to each other, are placed onto the thin film sample. Now an electrical current is applied between pin 1 and 4, while the resulting electrical voltage is measured between pin 2 and 3, and thus, the electrical resistance can be determined. Adapted from the dissertation of Nitin Saxena.[168]

As the name suggests, for the four-point probe resistance measurement four contacting electrodes are placed onto the sample of interest. Hereby the external two electrodes, 1 and 4 in

Figure 3.7, are carrying the current J, while the inner two electrodes, 2 and 3 in Figure 3.7, are sensing the voltage V. Compared to the two-point probe resistance measurement, this measurement geometry is more sensitive and provides more accurate results, as the contact and lead resistances of the measurement setup are eliminated. In this present thesis, a *Cascade Microtech® Inc. C4S 54/5* four-point probe head is used, consisting of four tungsten carbide tips with tip radii of 125 µm that are placed with an equidistant spacing of 1 mm onto the thin film sample and which are slightly and evenly pressed onto the film for good contacting. With a Keithley *SourceMeter® 2400* connected to the four measurement electrodes, the current J is swept from $-1e^{-5}$ A to $+1e^{-5}$ A in 200 steps, while the resulting voltage V is simultaneously recorded. With this measurement geometry the lateral thin film sample dimensions are much larger, and the film thickness is much smaller than the distance between the tungsten carbide tips. Thus, a possible impairment on the current flow, between tip 1 and 4, due to edge effects of the sample can be neglected and the sheet resistance R_{sh} is be given as:

$$R_{sh} = \frac{V}{J}\frac{\pi}{\ln 2} \tag{3.22}$$

$$\sigma = \frac{1}{R_{sh} t_{film}} \tag{3.23}$$

By including the thin film thickness t_{film}, the conductivity σ of the sample can be obtained with Equation (3.23). In this thesis, the 4-point probe measurements were performed on seven different positions on the investigated sample and with corresponding film thicknesses acquired on the same seven positions, the conductivity was calculated and then the results averaged.

3.2.4 Electrochemical impedance spectroscopy

Electrochemical impedance spectroscopy is a useful method to characterize the resistance specifics of a material and thus gives information about its charge carrier transport behavior. EIS is used in Chapter 7 and Chapter 8 to examine differently post-treated PEDOT:PSS thin films in respect to their electronic and ionic charge carrier transport, while the films are being subjected to elevated relative humidities.

In principle EIS can be performed in galvanostatic or potentiostatic mode, meaning either a sinusoidal alternating current is applied, and the potential response is recorded, or a sinusoidal alternating voltage is applied, and the current response is recorded. The latter mode is performed for the EIS measurements presented in this thesis and for this a *VMP-300 Potentiostat* from

BioLogic Science Instruments SAS was used. When conducting this sensitive measurement technique, it is especially important to ensure good contacting of the thin film samples. Therefore, a custom-made probe head was utilized to contact the samples in a four-pin-two-electrode geometry. Additionally, the samples were fabricated to have a special electrode geometry, which has been demonstrated to ensure reliable measurements. As shown in Figure 3.8a several preparations steps were necessary to obtain the special EIS electrode geometry.

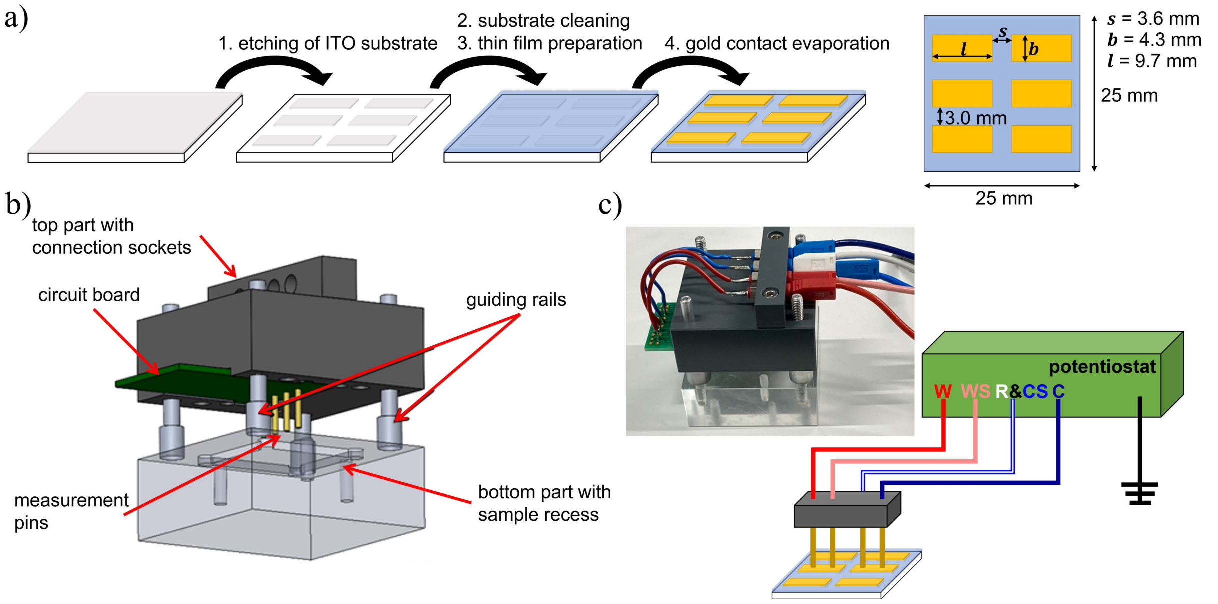

Figure 3.8 EIS sample geometry and measurement setup. a) Schematic depiction of the sample preparation steps to obtain the specific sample geometry for EIS measurements. b) Sketch of the custom-made probe head to conduct in-plane EIS measurements of a thin film sample. It contains a bottom part with a recess for the sample placement, and guiding rails, which allow a precise positioning of the top part. The top part contains four measurement pins that are linked via board to connection sockets, which can be used to connect it to the potentiostat. c) Photograph and outline of the connection geometry of the pins to the potentiostat, with the power cables, working (W, red) and counter (C, dark blue), the sensing cables, working sense (WS, light red) and counter sense (CS, blue), and the reference cable (R, white). Adapted from the master thesis of Tobias Schöner.[169]

In the first step, readily purchasable indium tin oxide (ITO) coated glass was partly etched away leaving six ITO areas with a size of 4.3 mm to 9.7 mm, a lateral and longitudinal distance of 3.0 mm and 3.6 mm, respectively. In the second step this structured ITO substrate is coated with the PEDOT:PSS polymer film and accordingly post-treated. In the third and final step gold electrodes of the same size and at the same position as the ITO areas are evaporated onto the polymer film surface. This special geometry of embedded ITO and top gold electrodes has been shown to enable a more stable film contacting and provides reproducible EIS measurements.[169] The more detailed fabrication procedure for the used EIS samples is provided in Chapter 4.

Figure 3.8b shows the custom-made probe head, which consists of a bottom part, where the sample can be placed in a recess to prevent movement during the measurement. Furthermore, it comprises a top part, which can be, aided by guiding rails, precisely placed in three different positions at a defined height above of one of the three electrode pairs on the sample. The top part contains sockets for the potentiostat cables that are connected via a board to four gold covered pins, *ED90389-ND*, provided by *Digi-Key Corporation*. The pins with respective spacing of 5.08 mm are placed and slightly pressed onto the sample in a way that always two pins are positioned on one electrode. As shown in Figure 3.8c, the outer two pins are connected to the power cables (working W red and counter C blue) while the inner pins are connected to the working sense (WS light red) and the reference plus counter sense lead (R & CS white & light blue). With this four-terminal-two-electrode contacting geometry, where the power and sense cables are separated with one of each on the same electrode, the lead and contact impedances can be eliminated from the measurement. The connected thin films were then measured in potentiostat mode using a single sinusoidal signal with a 20 mV amplitude, while the applied frequency was swept from 7 MHz to 500-5 Hz. The average number of measurements per frequency was between 8 – 12, and while the current measurement sensitivity was set to automatic, the working electrode potential was limited to a maximum measurement range of – 0.07 V to + 0.07 V. The bandwidth factor was set to 8 and the quality indicator tracking was activated. For the measurement and evaluation of the resulting data by equivalent circuit modeling the *BioLogic Science Instruments SAS* software *EC-Lab® Version V11.43* was used. The EIS experiments presented in this thesis were mainly performed in collaboration with the master student Tobias Schöner. The basic principle of the potentiostatic electrochemical impedance spectroscopy is described in the following.

During the measurement, a sinusoidal alternating potential V with the amplitude V_0, the angular frequency $\omega = 2\pi f$, and the phase angle ϕ_V, as described in Equation (3.24), is applied to the sample:

$$V = V_0 \sin(\omega t + \phi_V) \tag{3.24}$$

This applied potential interacts with the investigated electrochemical system, unbalancing it and resulting in a phase-shifted sinusoidal alternating current response J, with the amplitude J_0 and the phase angle ϕ_J, as described in Equation (3.25).

$$J = J_0 \sin(\omega t + \phi_J) \tag{3.25}$$

Inside the sample multiple processes are happening with divergent timescales, which thus respond to different excitation frequencies. Therefore, these processes can be separately investigated by varying the frequency of the applied input potential signal. As shown in Figure 3.9a, during the EIS measurement a frequency sweep of the input potential signal is done, and the respective amplitude and phase angle of the current response provide information about the different processes inside the investigated system.

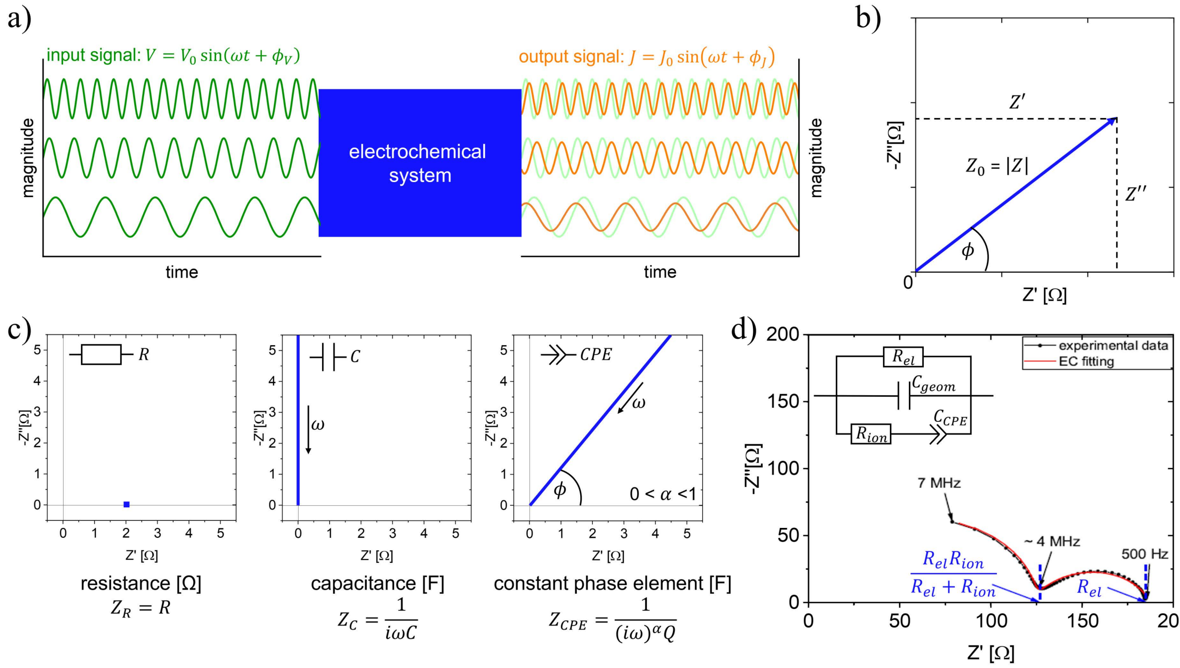

Figure 3.9 Operating principle of EIS. a) A sinusoidal alternating input potential $\boldsymbol{V}$ (green) is applied, which is then influenced by then electrochemical system, resulting in a sinusoidal output current signal $\boldsymbol{J}$ (orange). With these input and output signals, the impedance $\boldsymbol{Z}$ of the electrochemical system is determined, which can be, shown in b), graphically expressed with its real $\boldsymbol{Z}$' and imaginary part $\boldsymbol{Z''}$. c) Nyquist plots of the EC elements used in this thesis, a resistance, a capacitance, and a constant phase element. d) Exemplary Nyquist plot of an IL post-treated PEDOT:PSS thin film sample (black dotted line), together with the ECM fitting curve (red line) and the for this used ECM, in the inset, containing an electronic $\boldsymbol{R_{el}}$ and ionic resistance $\boldsymbol{R_{ion}}$, a geometric capacitance $\boldsymbol{C_{geom}}$ and a constant phase element $\boldsymbol{C_{CPE}}$. Adapted from the master thesis of Tobias Schöner.[169]

Analogous to the Ohm's law, with the input potential signal $\hat{V}$and the output current signal $\hat{J}$ in their complex form, the impedance Z can be obtained as follows, with ϕ being the phase shift:

$$\hat{V} = V_0 e^{i(\omega t + \phi_V)} \tag{3.26}$$

$$\hat{J} = J_0 e^{i(\omega t + \phi_J)} \tag{3.27}$$

$$Z = \frac{\hat{V}}{\hat{J}} = \frac{V_0}{J_0} e^{i(\phi_V - \phi_J)} = Z_0 e^{i\phi} \tag{3.28}$$

Using the Eulers relationship the impedance can be split into its real Z' and imaginary Z'' part, as shown in Equation (3.29) and Figure 3.9b.

$$Z_0 e^{i\phi} = Z_0 \cos(\phi) + i\, Z_0 sin(\phi) = Z' + i\, Z'' \tag{3.29}$$

To visualize and analyze the obtained EIS measurement data they are usually plotted in a Nyquist diagram, with Z' as x-axis and Z'' as y-axis. Now by using circuit elements, some exemplarily shown in Figure 3.9c, the data can be fitted by finding a matching equivalent circuit model (ECM), and thus, information about the electrochemical contributions inside the thin film sample can be obtained.

The EIS data of the IL post-treated PEDOT:PSS thin film samples investigated in this present thesis, could be well described with the ECM depicted in Figure 3.9d. It contains an electronic resistance (R_{el}), a geometric capacitance (C_{geom}) accounting for the connector setup, an ionic resistance (R_{ion}), and a constant phase element (C_{CPE}), corresponding for charge trapping and accumulation in an ionic double layer formed at the electrodes. An exemplary fit of an EMIM DCA post-treated PEDOT:PSS sample is shown as Nyquist plot in Figure 3.9d, respectively. The vertical dashed lines in Figure 3.9d indicate how the R_{el} and R_{ion} of the sample could be obtained also graphically. Using these resistance values, the film thickness t_{film}, and by including the EIS electrode geometry shown in Figure 3.8, the electronic σ_{el} and ionic σ_{ion} conductivities can be calculated as follows:

$$\sigma_{el} = \frac{1}{R_{el}} \frac{s}{b t_{film}} \tag{3.30}$$

$$\sigma_{ion} = \frac{1}{R_{ion}} \frac{s}{bl} \tag{3.31}$$

As a general note, for EIS there are certain factors that need to be considered in respect to the accuracy and validity of the measurements.

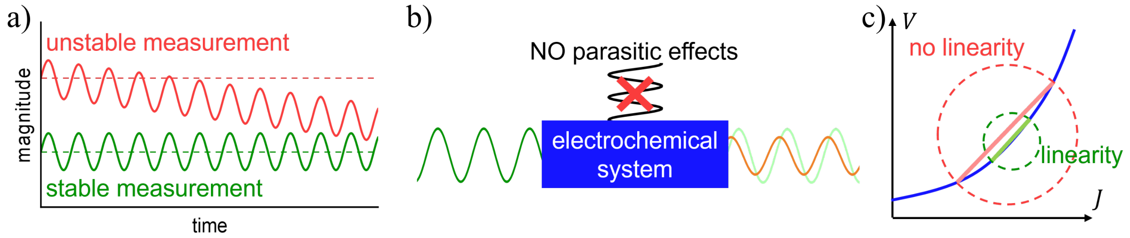

Figure 3.10 Validation factors for EIS. a) Stationarity condition, b) causality condition, and c) linearity condition, which must be met in order to declare the EIS measurements as valid. Adapted from the master thesis of Tobias Schöner.[169]

The first factor, sketched in Figure 3.10a, is the stationarity of the investigated electrochemical system, meaning that during the time of the measurement the system should not undergo any changes, and after the applied signal is stopped, the system should return to its original state. Therefore, for example possible degradation processes happening inside the sample during the measurement should be ruled out. The second factor is the causality, sketched in Figure 3.10b, which means that the response signal should solely be influenced by the electrochemical system investigated and be a result of the applied signal. Therefore, parasitic effects, for example due to long cables and bad contacting, should be reduced as much as possible. The third factor is the linearity of the investigated electrochemical system, meaning that the output signal demonstrates a linear response to the input signal. However, as most electrochemical systems are not naturally linear, this linearity factor can be met by the application of a very small signal amplitude and thus achieving pseudo-linearity, as indicated in Figure 3.10c. One way to verify the fulfillment of these factors is the Kramers-Kronig test. Hereby, a special fitting model circuit is used, which is always in accordance with the Kramers-Kronig relations, that are mathematical equations to connect the real and imaginary parts of a complex function, in this case the electrochemical impedance Z. If the experimental EIS data can be represented with this model circuit, it gives a first indication that the three required factors are met by the electrochemical system.

3.3 Structural characterization in real space

For the structural characterization of the PEDOT:PSS thin film samples in real space, two different methods were applied, which will be briefly introduced in this section. With surface profilometry the thickness of the different post-treated thin film samples was determined. Conductive atomic force microscopy (c-AFM) provides surface information about the topography and the PEDOT:PSS domain structure of the thin film samples.

3.3.1 Surface profilometry

Surface profilometry was applied on the differently post-treated PEDOT:PSS samples to acquire the thickness of the thin films t_{profil}. The method procedure is sketched in Figure 3.11 and described in the following. The film thicknesses of the different PEDOT:PSS samples mentioned in Chapter 5, 6, 7, and 8 were all obtained with surface profilometry, if not otherwise stated.

In this present thesis a *DektakXT®* profilometer from the company *Bruker Nano Surface Division* was utilized, which is equipped with a diamond tip with a stylus radius of 2 µm and a high precision xy-stage. As the film thickness is the intended value, scratches of about 5 mm long and completely down to the substrate were made into the thin polymer films with a needle. Then the sample was placed on the xy-stage and the diamond tip was pressed nearby to the scratch onto the film surface with a small contact pressure, corresponding to 1 mg. By moving the xy-stage, as sketched in Figure 3.11a, the tip is moved perpendicular over the scratch and thereby following its height profile. The scanning speed and scan range were set to 35 µm s^{-1} and 350 µm, respectively.

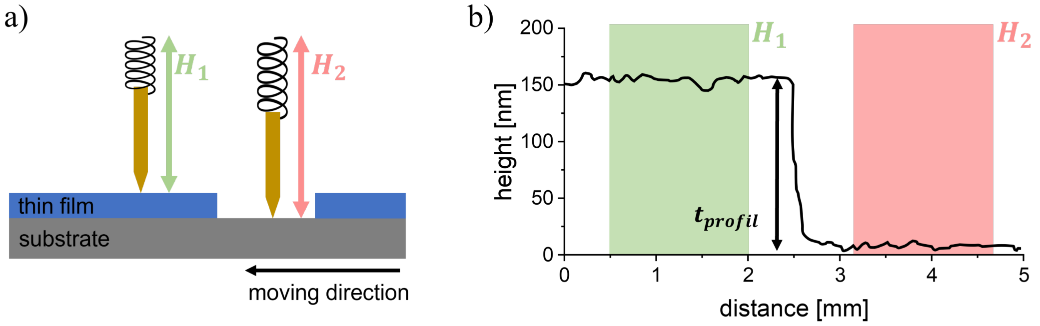

Figure 3.11 Working principle of surface profilometry. a) Depiction of the profilometry measurement setup, with a tip that is slightly pressed with a constant force onto the film surface. By moving the sample in lateral direction, the height profile of the surface is measured. b) Exemplary resulting height profile, from which the height of the film surface $\boldsymbol{H_1}$ (green area) compared to the height of the substrate surface $\boldsymbol{H_2}$ (red area) can be used to calculate the film thickness $\boldsymbol{t_{profil}}$. Adapted from the dissertation of Lucas Philipp Kreuzer.[161]

The height profile, shown in Figure 3.11b, obtained from the vertical deflection of the tip, was analyzed with the *Bruker* software *Vision64®*. The average step height ASH of the scratch and thus the film thickness t_{profil} could be extracted by determining the mean height outside (H_1 green area) and inside (H_2 red area) the scratch and calculating the height difference $t_{profil} = H_1 - H_2$. It is important to mention that this method of thickness measurement can be more or less error-prone, depending on the fragility of the film, because a penetration of the film surface by the moving tip and residual film material within the scratch can affect the result. For the estimation of the medium film thickness of a sample, scratches were made on seven different positions and the determined thicknesses were averaged.

3.3.2 Conductive atomic force microscopy

Conductive atomic force microscopy allows the simultaneous determination of the topography and the electrical current map of a sample surface. This characterization method was used in Chapter 5 to investigate ionic liquid post-treatment induced changes in the PEDOT:PSS thin film surface morphology, which comprises conductive PEDOT domains embedded in a non-conductive PSS matrix. This section explains the basic working principle and specifics of the c-AFM measurements, as depicted in Figure 3.12.

The c-AFM measurements presented in this thesis were conducted by Dr. Hartmut Stadler at the *Bruker Nano Surfaces Division* in Karlsruhe, using a *Dimension Icon® SPM* system that was operated in *PeakForce TUNA™ Mode*. An exemplary square area of 300 nm² was scanned, and the applied bias was set to 200 mV.

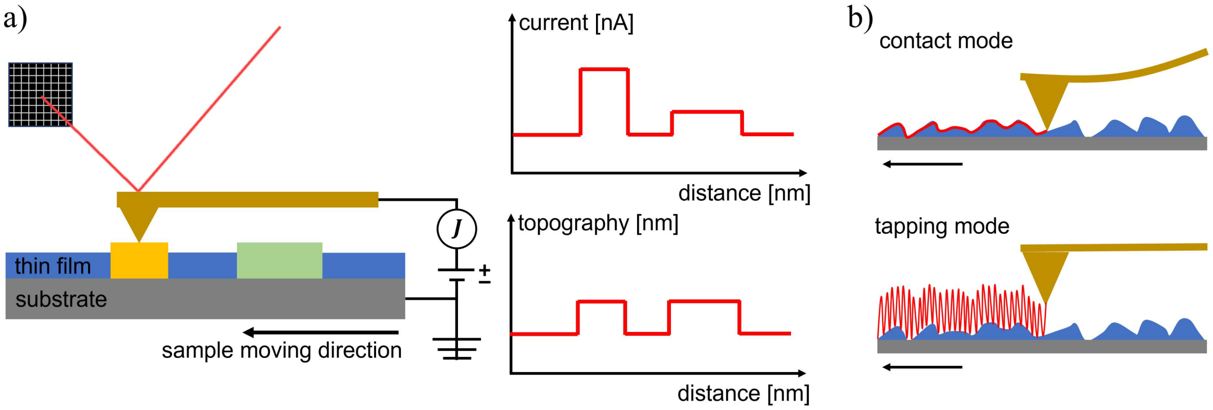

Figure 3.12 Working principle of conductive AFM. a) Schematic depiction of the conductive AFM method, in which a measurement tip on a cantilever scans the sample surface. A laser directed on the cantilever and reflected on a detector determines the height profile as shown in the topography graph on the bottom right. Additionally, a voltage is applied between the measurement tip and the sample substrate, and the resulting current flow is detected while scanning the sample surface. As visible in the current graph on the top right, even if the topography of two sample features is similar, differences in their conductivity properties can be detected. Adapted from Park Systems.[170] b) Different measurement modes that can be applied when investigating a sample with conductive AFM; contact mode and tapping mode. Adapted from Asmatulu et al.[171]

In Figure 3.12a the basic parts of the c-AFM device are sketched. The sample of interest is placed on a xy-stage and an electrically conductive cantilever with a tip is lowered onto the sample. Utilizing a laser that is reflected on the cantilever surface towards a photodetector, the position and movement of the cantilever can be followed when moving the xy-stage and scanning the sample surface. Hereby the forces between the tip and the sample surface follow the Lennard-Jones potential and for c-AFM two different scanning measurement modes can be distinguished, as depicted in Figure 3.12b. The first one is the contact mode, whereby the tip touches the sample surface constantly and due to electronic orbital overlapping repulsive interactions are acting. The second and most frequently used mode is the tapping mode. Hereby the cantilever is stimulated to a vibration below its resonance frequency, in order to achieve only a very short physical contact between the sample surface and the tip, whereby both, attractive and repulsive interaction forces come to play. Compared to the contact mode, the tapping mode prevents mechanical surface damage from the lateral movement of the tip and additionally enables a more reasonable resolution compared to the non-contact mode. The *PeakForce TUNA™* mode performed on the in this thesis investigated IL post-treated PEDOT:PSS thin films, is a special type of tapping mode. It allows the investigation of the fragile polymer films without damaging the surface and additionally allows the simultaneous examination of its electrical properties even at low conductivities. As shown in Figure 3.12a, for this a bias voltage is applied between the tip and the electrically conductive sample substrate, in this case an indium-doped tin oxide (ITO) substrate, as described in Section 4.1.1. Now while scanning the sample surface, a current amplifier is used to measure the current flow between the tip and the sample, whereby conductive sample areas allow the current to pass easily, while non-conductive areas do not. Therefore, with this c-AFM measurements in *PeakForce TUNA™* mode topography maps and electrical current maps of a sample surface can be acquired simultaneously.

3.4 Structure characterization in reciprocal space

In this thesis the structural characterization of the PEDOT:PSS thin film samples was performed, additionally to the real space, also in the reciprocal space. Therefore, three different investigation methods were utilized, namely X-ray reflectometry (XRR), which allows for the investigation of the vertical structure within an investigated thin film. Grazing-incidence small-angle X-ray scattering (GISAXS), which provides information about the inner films lateral and vertical morphology. Additionally, time-of-flight neutron reflectometry (ToF-NR) experiments were performed, which enable the observation of the vertical composition and multiple layer formation within the PEDOT:PSS thin film samples. A basic introduction into the theoretical background behind these characterization techniques is provided in Section 2.3.

3.4.1 X-ray reflectometry

X-ray reflectometry was performed to investigate the vertical morphology of PEDOT:PSS thin films post-treated with ionic liquids. Hereby the X-ray beam interacts with the electrons of the atomic shell of a material, and therefore, this method provides information about the material electron density and thus its X-ray scattering length density (SLD^{X-ray}). Furthermore, this method is performed in the specular scattering geometry introduced in Section 2.3.1, where no scattering outside the xz-plane is considered and the incident angle matches the exit angle ($\alpha_i = \alpha_f$), thus the momentum transfer only happens along the surface normal (q_z). Therefore, the XRR technique provides accurate information about the vertical composition of a thin film sample, including possible enrichment layers or phase segregations, with the related properties, SLD^{X-ray}, layer thickness and roughness. It is utilized in Chapter 8 for the investigation of EMIM DCA post-treated PEDOT:PSS thin films.

The XRR measurements performed in the frame of this thesis, were conducted at ambient room conditions with a *D8 ADVANCE diffractometer* from *Bruker*. The X-ray beam was generated using a copper target ($\lambda_{\mathrm{CuK}\alpha}$ = 1.54 Å), then monochromized and focused by a Goebel mirror, and finally vertically collimated with a 0.2 mm slit onto the sample. To prevent over-illumination at very small incident angles, a tantalum knife-edge collimator was placed closely above the thin film. The at the sample reflected beam was then collimated with 0.1 mm and 0.05 mm slits, and guided through an Cu 0.1 mm absorber, to avoid over-saturation on the detector. Before the measurement, the 2theta-scan, z-scan and rocking-scan were performed for calibration of the direct beam position and the samples height and parallel surface alignment, respectively. Then the absorber material was removed, the knife-edge collimator adjusted and finally the actual sample measurement was started. During this coupled 2theta/theta-scan, the thin film sample is fixed at one position, while the X-ray source and the detector are rotated along the xz-plane, hereby always meeting the condition that incident angle and exit angle are equal. For the in this thesis performed XRR measurement a scan range of 2θ = 0.04 – 2.00° with an increment of Δ2θ = 0.002° was applied. The resulting incident angle dependent reflectivity intensities, recorded at the detector, were then modeled by using Parratt's recursive formulae as introduced in Section 2.3.2. For this, the *IGOR Pro 7.00* software by *WaveMetrics*[172] with the MOTOFIT plugin was utilized, and a three-layer model consisting of the silicon substrate with its oxide layer, a polymer bulk layer and a polymer-air interfacial layer, was applied for all three post-treated PEDOT:PSS films. The schematic sketch of an X-ray reflectometer is presented in Figure 3.13a. The exemplary XRR data shown in Figure 3.13b are used to shortly elaborate the effects of the material properties SLD, thickness and roughness on the reflectivity curves.

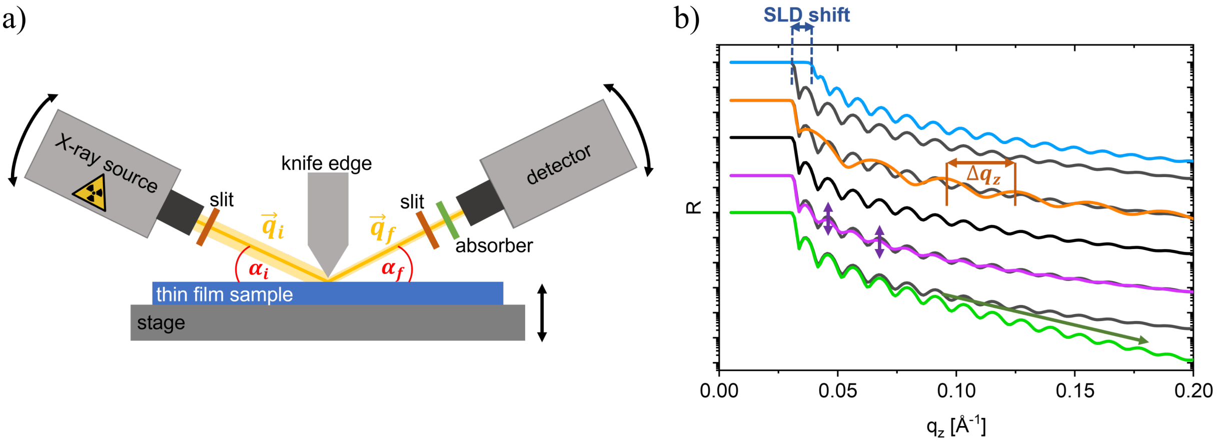

Figure 3.13 XRR setup and working principle. a) Basic sketch of the XRR measurement setup. The X-ray beam coming from the X-ray source, is guided onto the thin film sample with an incident angle of $\boldsymbol{\alpha_i}$, and the reflected beam intensity at an exit angle of $\boldsymbol{\alpha_f} = \boldsymbol{\alpha_i}$ is recorded with an accordingly positioned detector. Different slits, absorbers, and a knife edge, are introduced into the X-ray beam path to shape the beam and prevent over saturation of the detector. b) Exemplary XRR curves to elucidate the influence of the film properties. The black and light gray curves represent the reference curve of a sample consisting of a single thin film layer on a substrate. An increase in the $\boldsymbol{SLD}$ (blue curve) shows in a shift of the critical edge, while a decrease in the film thickness (orange curve) results in a widening of the Kiessig fringes. Furthermore, an increase in the roughness of the substrate (pink curve) leads to a leveling of the Kiessig fringes, while a roughness increase of the film roughness (green curve) causes a steeper drop of the reflectivity curve. Adapted from the dissertation of Lucas Philipp Kreuzer.[161]

From modeling the XRR curves, in principle the following material properties can be determined: SLD^{X-ray}, layer thickness and interface roughness. The SLD^{X-ray} of a material is determinable from the critical edge in the XRR curve, marked with the blue dotted line in Figure 3.13b. This strong drop in intensity marks the angle above which the X-ray beam starts to transmit into the thin film sample. This angle corresponds to the materials critical angle α_c and thus correlates to the materials SLD^{X-ray}, as introduced in Section 2.3.1. The layer thickness of a sample can be obtained from the oscillations in the reflectivity pattern, named Kiessig fringes. As marked here in orange, the distance Δq_z between neighboring Kiessig fringes is related to the layer thickness t_{XRR} by:[173]

$$t_{XRR} \approx \frac{2\pi}{\Delta q_z} \tag{3.32}$$

Finally, the roughness of the interfaces between different layers or between a layer and the substrate or surrounding air, also has an influence on the reflectivity data, as indicated by the green and purple arrows in Figure 3.13b. For once, an increase in roughness strongly decreases the reflected intensity, leading to a steeper slope at higher incident angles and furthermore reduces the amplitude of the Kiessig fringes. Therefore, samples for XRR experiments are prepared on a smooth and highly reflecting silicon wafers substrate.

3.4.2 Grazing-incidence small-angle X-ray scattering

Grazing-incidence small-angle X-ray scattering is a non-destructive technique that was used in the frame of this thesis to examine the inner film morphology of IL post-treated thin PEDOT:PSS films. In this method, the X-ray beam is guided on the sample in a very shallow angle, to enlarge the beam footprint and thus allow the statistical relevant investigation of a greater sample volume. The X-ray beam is then scattered on structures within the film and the diffuse scattering, as introduced in Section 2.3.3, is recorded as 2-dimensional scattering pattern, providing information about the size, shape, and amount of the inner film structures in the mesoscale range. In this thesis, GISAXS was utilized in Chapter 5 to investigate the influence of different IL post-treatments on the PEDOT:PSS morphology. Furthermore, it was used to unravel the effects of elevated temperature and elevated relative humidity on the inner film structure of EMIM DCA post-treated PEDOT:PSS thin films, as described in Chapter 6 and Chapter 7, respectively.

The GISAXS investigations in this thesis were conducted with an X-ray beam energy of 8 keV at the Austrian SAXS beamline at the Elettra-Sincrotrone in Trieste, Italy. For this, the samples were placed and measured in the custom-built measurement chamber described in Section 3.5.1, as it features X-ray transparent Kapton® windows. The incident beam was guided on the sample surface with a shallow incident angle α_i of 0.4 °, for the experiments detailed in Chapter 5 and Chapter 6, and 0.41 ° for the experiments detailed in Chapter 7. The incident angle was selected to be above the materials critical angle ($\alpha_i > \alpha_c$), which was calculated to be 0.169 ° for PEDOT:PSS, to probe the inner film structure and to ensure that the Yoneda region (YR $\alpha_f = \alpha_c$) is distinguishable from the specular reflection (SR $\alpha_f = \alpha_i$). For recording of the resulting 2-dimensional diffuse scattering pattern in the $q_z q_y$-plane, a *PILATUS 1M* detector from *DECTRIS Ltd*, with a pixel size of 172 µm × 172 µm and a total dimension of 981 px × 1043 px, was placed in a sample-detector distance (SDD) of 1949 mm (Chapter 5 and

Chapter 6) and 1800 mm (Chapter 7), respectively. To protect the detector from oversaturation and damage, a beam stop is placed at the position of the specular reflected beam and the transmitted direct beam (DB). Before starting a GISAXS experiment series, a calibration measurement with silver behenate standard is performed to obtain the precise SDD and DB position. Furthermore, after every sample change, an alignment procedure is performed to ensure the precise alignment of the samples angle and height, which is crucial for the correct analysis of the resulting GISAXS data. The schematic experimental setup of the GISAXS experiment and an exemplary 2D detector image is depicted in Figure 3.14a.

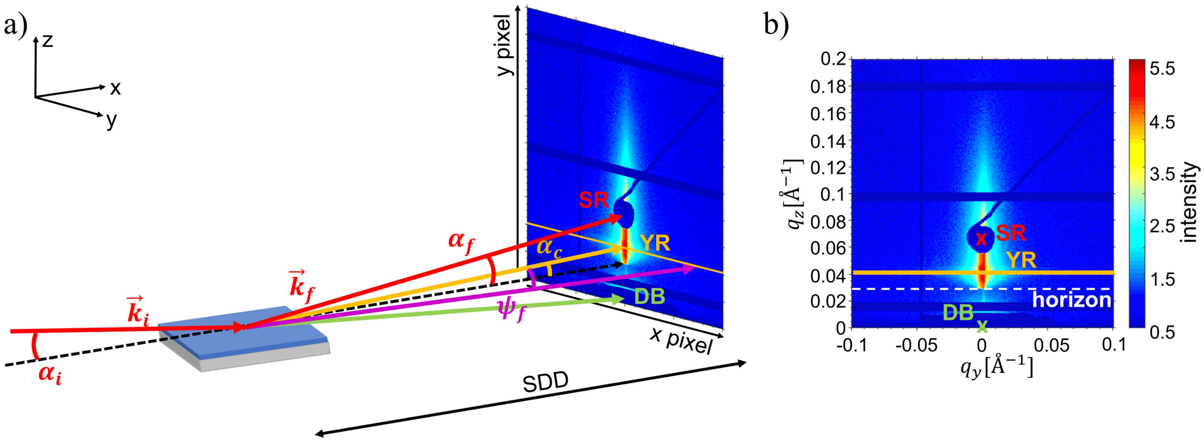

Figure 3.14 GISAXS measurement geometry and evaluation. a) Graphical depiction of the GISAXS measurement geometry, where an incident beam is guided onto the sample in a very shallow incident angle α_i (red). The beam is then scattered within the film and the scattering pattern is recorded on a detector, which is placed at a certain SDD. The recorded 2D detector image collects the vertical α_f and horizontal ψ_f (pink) scattering information, with increased scattering intensity occurring at the specular reflection peak SR (red, $\alpha_f = \alpha_i$, and $\psi_f = 0$) and at the Yoneda region YR (yellow, $\alpha_f = \alpha_c$). The SR and the direct beam DB (green, $\alpha_f = -\alpha_i$) are covered with beam stops to prevent over saturation of the detector. b) The pixel dependent detector image can be converted into a q_yq_z-dependent scattering pattern, which contains all the inner films structural information. Adapted from the dissertation of Lorenz Bießmann.[81]

The resulting 2D detector image contains all the structural information about the inner film morphology. As indicated in Figure 3.14a and b, from this intensity pattern with the real space x and y position of the SR, DB, and the SDD and the pixel size (p), the relevant angles α_i, α_f and ψ_f can be obtain with:

$$\alpha_i = \frac{1}{2} arctan\left(\frac{(y_{SR} - y_{DB})p}{SDD}\right) \tag{3.33}$$

$$\alpha_i + \alpha_f = arctan\left(\frac{(y_f - y_{DB})p}{SDD}\right) \tag{3.34}$$

$$\psi_f = arctan\left(\frac{(x_f - x_{DB})p}{SDD}\right) \tag{3.35}$$

Furthermore, due to the very small angles of the incident (α_i) and exiting (α_f, ψ_f) beam, the small angle approximation can be reasonably applied. With this, the scattering vector $\vec{q}$ can be expressed via Equation (3.36), and the real space xy-detector image can be converted into a reciprocal $q_y q_z$-image.

$$\vec{q} = \begin{pmatrix} q_x \\ q_y \\ q_z \end{pmatrix} = \frac{2\pi}{\lambda} \begin{pmatrix} 0 \\ 2\psi_f \\ \alpha_i + \alpha_f \end{pmatrix} \tag{3.36}$$

This data conversion of the detector image was performed using the open source Python-based software DPDAK v1.4.1.[174] Furthermore, this tool was also utilized to then reduce the 2D GISAXS data by extracting horizontal line cuts at the fixed q_z value of the PEDOT Yoneda peak (calculated critical angle of 0.169 °), as explained in Section 2.3.3. Due to the measurement chamber being designed to cause a very low scattering influence, no background subtraction was performed. The thus obtained horizontal line cuts, which contain the inner films lateral information, were then quantitatively analyzed by modeling them with a Python 2.7 script created by Dr. Christoph J. Schaffer.[153] The here underlying model is described in detail in Section 2.3.3, and is based on the local monodisperse approximation (LMA)[142, 152] in the framework of the distorted-wave Born approximation (DWBA)[142, 143], while additionally possible vertical correlations between interfaces are neglected according to the effective interface approximation (EIA).[148, 150] This results in the diffuse scattering factor defined in Equation (2.69), which is proportional to the recorded scattering intensity distribution. For the in this thesis investigated PEDOT:PSS thin films, a cylindrical form factor[144, 148] was assumed to approximate the rotational symmetry of the real pancake-shaped PEDOT domain structure.[16, 19] Furthermore, the structure factor is approximated by a 1-dimensional paracrystalline lattice[155], accounting for the short-range order of the domain structures within the PEDOT:PSS material. For this horizontal line cut modeling, the respective parameters were adjusted accordingly to obtain an optimized goodness-of-fit parameter χ^2.

For the modeling of the PEDOT domains present within the PSS matrix, exemplarily shown in Figure 3.15, it was found that the best fit results were obtained when assuming three main scattering structures, named large (l), medium (m), and small (s) PEDOT domains. For each of the three domain structures a cylindrical form factor with a Gaussian distribution of the mean associated domain radii (r_l, r_m, r_s) could be distinguished. Additionally, for the large and medium domains, a structure factor with a Gaussian distribution of the mean correlated domain center-to-center distances (D_l, D_m) was identifiable.

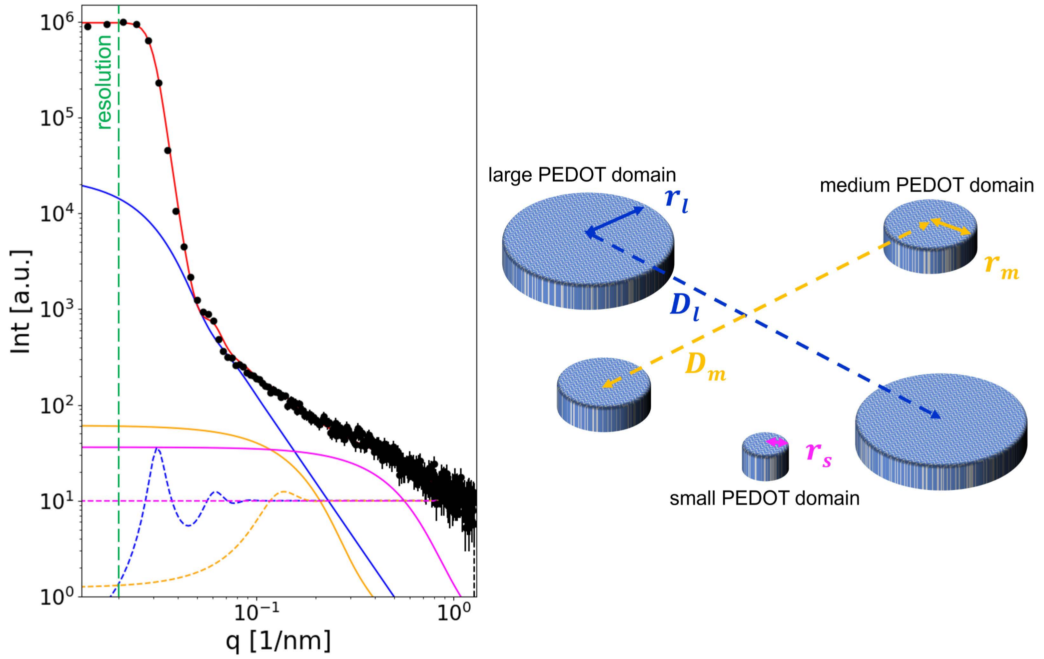

Figure 3.15 GISAXS data modeling. Representative horizontal line cut of an IL post-treated PEDOT:PSS thin film (black dots), shown together with the model fit curve (red). Hereby for the modeling of the GISAXS results, different contributions of large (blue), medium (yellow) and small (pink) PEDOT domains are taken into account, which are schematically depicted on the right with their respectively associated radii (r_l, r_m, r_s) and center-to-center distances (D_l, D_m). Adapted with permission from American Chemical Society, Copyright 2022.[50]

As introduced in Section 2.3.3, the intensity of the respectively obtained form factors scales linearly with the count of the according sized domains.[141] From this approach, the respective quantity distribution of large (N_l), medium (N_m), and small (N_s) PEDOT domains of each investigated sample could be extracted. With this the domain size distribution was computed from the superposition of the Gaussian distributions using the radii ($r_{l,m,s}$) with the respective correlated deviation, and the quantity ($N_{l,m,s}$) of the respective form factors. Additionally, with $r_{l,m,s}$, $N_{l,m,s}$, and the assumption of a cylindrical shape (height h), the relative volume ($V_{l,m,s}$) and with this the respective volume fraction ($NV_{l,m,s}$) of the different presented PEDOT domains was calculated via:

$$V_{l,m,s} = \pi\, r_{l,m,s}^2\, h\, N_{l,m,s} \tag{3.37}$$

$$NV_{l,m,s} = \frac{V_{l,m,s}}{V_l + V_m + V_s} \tag{3.38}$$

3.4.3 Time-of-flight neutron reflectometry

Time-of-flight neutron reflectometry is a useful method to non-destructively examine the vertical layer morphology and material properties of PEDOT:PSS thin films post-treated with ILs. Since neutrons interact with the nucleus of an atom, as introduced in Section 2.3.1, this technique provides information about the vertical composition of the neutron scattering length density ($SLD^{neutron}$). Similar to the XRR technique (Section 2.3.2), only the specular scattering geometry is of interest. However, while during an XRR measurement the wavelength λ is fixed and the incident angle α_i is varied, for ToF-NR measurements it is vice versa. Hereby, the variation of the neutron wavelength is achieved with the time-of-flight method, where choppers crop the neutron beam into bundles of a defined wavelength band. The single neutrons are then detected with their impact position on the detector and their respective time of flight, giving their velocity and thus their corresponding wavelength. In Chapter 8 of this thesis, ToF-NR is utilized to examine different IL post-treated PEDOT:PSS thin films, on their ability to incorporate deuterated water (D_2O) and the influence on their properties, if the ambient relative humidity is increased.

The ToF-NR measurements were performed at the *D17* instrument[159, 175] at the neutron source *Institut Laue-Langevin* (ILL) in Grenoble, France. For these experiments, the custom-built environment chamber introduced in Section 3.5.3 was utilized, as it allows a defined relative humidity control, and contains neutron-permeable aluminium windows. At the *D17* instrument, schematically depicted in Figure 3.16, the chopper system crops the continuous neutron beam into pulses with a wavelength band of 2 to 27 Å, the SDD was set to 3.10 m, and the sample inside the measurement chamber was placed vertically. The operation in ToF-mode was selected to allow the acquisition of data sets across a large q_z range for the thin post-treated PEDOT:PSS films when they are in, or close to equilibrium at the end of each humidity stage; called ‘static data’. Furthermore, the ToF-mode also enabled to obtain data with a high time resolution during the swelling of the thin films, performed at the beginning of every humidity stage; called ‘kinetic data’. For the static ToF-NR measurements two incident angles α_i = 0.5 ° (acquisition time 15 min) and α_i = 2.5 ° (acquisition time 30 min) were used, to comprise a wide q_z-range. The kinetic ToF-NR measurements were performed with a fixed incident angle of α_i = 1.0 °, or α_i = 1.5 °, and with a time resolution of 5.5 s. Additionally, the out-of-reflection-plane divergent incident beam was used to exploit the full available neutron flux. Namely by using a re-binning algorithm for these out-of-reflection-plane divergent beam measurements, the obtained ToF-NR data were reduced and their resolution was improved,[162, 176] reaching a $\frac{\Delta q}{q}$ of 10 %.

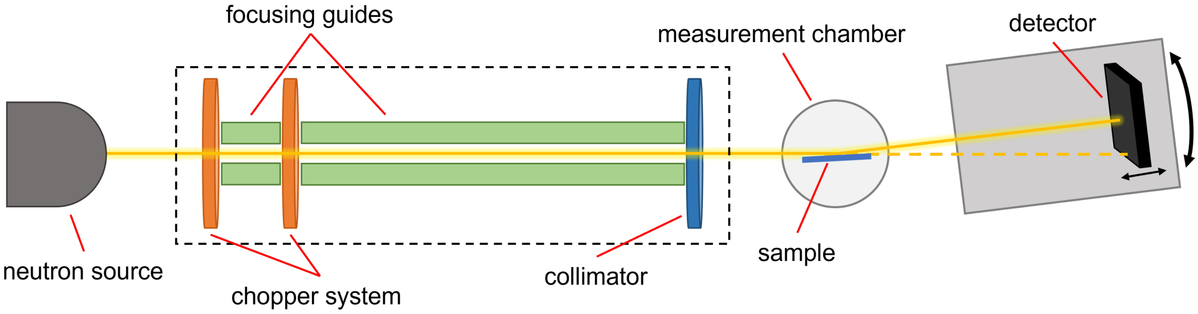

Figure 3.16 ToF-NR setup of the D17 beamline at ILL. Schematic drawing of the ToF-NR measurement setup, where the neutron beam, provided by the neutron source, is copped into neutron pulses with a double disc chopper system and is then guided with a focusing guide. After passing through a collimator, the neutrons impact onto the sample and the reflected neutrons are recorded together with the time of impact on a detector. For the ToF-NR the incident angle is fixed, while the wavelengths of the neutron pulses can be adjusted via the chopper system. Adapted from Saerbeck et al.[175]

The obtained specular reflectivity data were then evaluated similarly as explained in Section 3.4.1 for the XRR method. Using the MOTOFIT plugin for IGOR Pro 7.00 (WaveMetrics)[172], the experimentally obtained ToF-NR reflectivity curves $R(q_z)$ were fitted with a multilayered thin film sample model. Hereby it was found that the thin post-treated PEDOT:PSS films are best described with a three-layered model, consisting of the silicon substrate ($SLD_{Si}^{neutron}$ = 2.07 × 10^{-6} Å^{-2}) with its oxide layer ($SLD_{SiO_2}^{neutron}$ = 3.47 × 10^{-6} Å^{-2}), and a bulk layer of IL containing PEDOT:PSS polymer. The SLD value for D_2O was calculated to be $SLD_{D_2O}^{neutron}$ = 6.36 × 10^{-6} Å^{-2}.[177]

The time-dependent volume fraction $\phi(t)$ of D_2O inside the thin polymer was obtained via Equation (3.39), containing the experimentally measured polymer bulk SLD at the time t ($SLD_{exp}(t)$), the SLD of the dry film in equilibrium at the end of the first drying stage (SLD_{dry}), and the SLD of D_2O (SLD_{D_2O}).

$$\phi(t) = \frac{SLD_{exp}(t) - SLD_{dry}}{SLD_{D_2O} - SLD_{dry}} \tag{3.39}$$

Additionally, to get a more detailed idea about the kinetic ToF-NR data, the time constant for the D_2O uptake (τ) can be obtained. This can be done by first calculating the relative D_2O uptake ($\phi_{rel}^{exp}(t)$) via Equation (3.40), using the maximal amount of absorbed D_2O (ϕ_{final}) of the respective sample. With this, the for every humidity step resulting $\phi_{rel}^{exp}(t)$curves were fitted

($\phi_{rel}^{fit}(t)$) by adapting a humidity sensitive model introduced by Magerl et al.[178, 179], utilizing Equation (3.41).

$$\phi_{rel}^{exp}(t) = \frac{\phi(t)}{\phi_{final}} \tag{3.40}$$

$$\phi_{rel}^{fit}(t) = \frac{\phi(t)}{\phi_{equilibrium}} - \left(\frac{\phi(t)}{\phi_{equilibrium}} - \phi_{rel,0}\right) \exp\left(-\frac{t}{\tau_{humid}}\right) \tag{3.41}$$

Hereby, $\phi(t)$ is the time-dependent volume fraction of D_2O, $\phi_{equilibrium}$ is the maximal absorbed D_2O at the end of the respective humidity step, $\phi_{rel,0}$ is the relative D_2O volume at the beginning of every humidity step and τ_{humid} is the time constant for the D_2O uptake.

3.5 *In situ* characterization environments

Specific requirements on the experiment environment had to be met for the different performed *in situ* characterizations within this present thesis, which was achieved by applying the in this section described *in situ* characterization environments. The X-ray analysis voltage-emulation rig (XAVER) was utilized to perform GISAXS measurements while simultaneously examining the electrical characteristics of an investigated sample under different environmental influences. The gas flow system provides a nitrogen gas flow that can be adjustably enriched with a defined relative humidity and can be flexibly connected to the different experiment chambers. The universal chamber for observation of reflectivity with neutrons (UNICORN) allows the simultaneous examination of the thin film sample with ToF-NR and SR, while applying a defined humidity protocol.

3.5.1 X-ray analysis voltage-emulation rig

The X-ray analysis voltage-emulation rig is a custom-made measurement chamber, designed and built by Xaver Lamprecht[167], which allows the performance of *in situ* GISAXS experiments on thin film samples, while simultaneously exposing them to different ambient influences. In Chapter 5, the chamber was used to create a stable measurement environment of dry nitrogen gas flow at 25 °C, while the morphology of PEDOT:PSS thin film samples post-treated with different ionic liquids and concentrations is investigated. In Chapter 6 the XAVER chamber was combined with the two-point resistance probe setup, described in Section 3.2.2, and was equipped with an LED below the sample stage and a spectrometer in the sample lid, details in Section 3.1.1. Thus, the temperature-dependent conductivity of EMIM DCA post-treated PEDOT:PSS thin films could be recorded while simultaneously collecting GISAXS data and performing UV-Vis measurements, all under a stable dry nitrogen gas flow environment.

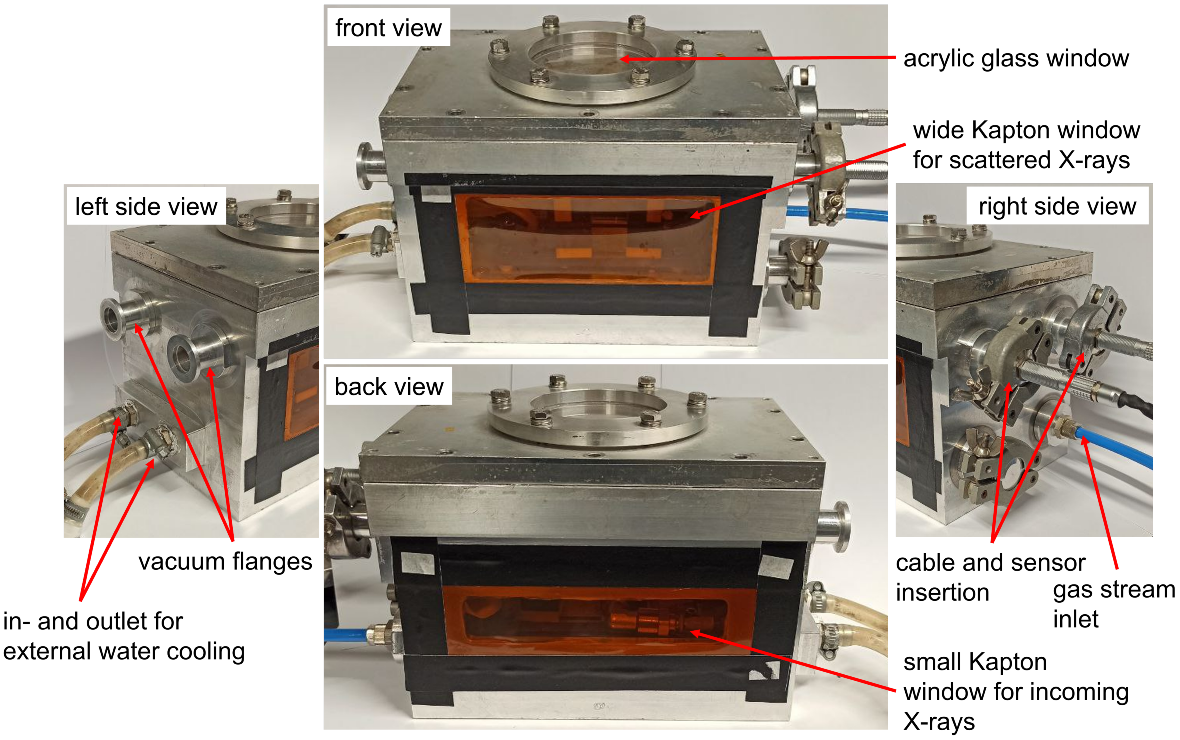

Figure 3.17 XAVER measurement chamber. Photograph of the XAVER measurement chamber, developed by by Xaver Lamprecht[167], showing the lid with the acrylic glass window, the two Kapton® windows for the incoming and scattered X-ray beam, the inlet and outlet for the external water cooling, as well as the inlet for a gas stream. Furthermore, the chamber comprises different vacuum flanges, which can be used for example to airtight insert cables or sensors into the chamber.

In Chapter 7, the XAVER chamber combined with the two-point resistance probe setup was connected to the gas flow system, introduced in Section 3.5.2. This allowed the investigation of the resistance behavior and the morphology alterations of EMIM DCA post-treated PEDOT:PSS thin films, when being exposed to elevated relative humidities. Additionally, by installing the EIS probe head, presented in Section 3.2.4, instead of the two-point resistance probe setup, the charge transport behavior of the thin film samples could be examined as function of the relative humidity of the environment, which is presented in Chapter 7 and Chapter 8. To allow all these various *in situ* measurements, the XAVER environment, sketched in Figure 3.17, was appropriately designed and some of the chamber features are highlighted in the following.

The XAVER chamber, shown in Figure 3.17, is completely made of aluminium and has a external size of 23.5 × 15.5 × 15.0 cm^3 (l × w × h). It contains two windows to allow for the *in situ* GISAXS measurements, one small slit in the front, for the incoming beam and a wider window on the back for the scattered X-ray beam. Both windows are covered with Kapton® polyimide sheets, as this material owns a high X-ray transmittivity and thus the windows can be sealed airtight without causing a strong influence on the scattering experiments. On the top of the chamber the lid can be fixed with O-rings and screws to hermetically seal the chamber. The lid can either contain an acrylic glass window to allow the observation of the experiments, or it can be changed and equipped with a holder for a spectrometer, to allow for *in situ* UV-Vis measurements. On the sides of the chamber an in- and outlet for an external water-cooling circuit is built in, to allow for the Seebeck measurements. Furthermore, six vacuum flanges are recessed into the sides of the chamber, which enable a flexible and airtight insertion of cables and sensors necessary for the various experiments or can be used as in- and outlets for a dry or humidified nitrogen gas stream, to adjust the chambers ambient environment. An additional adapter plate allows the easy mounting of the chamber onto the positioning goniometer setups at the X-ray beamlines, which is important for the position and angle settings for the scattering experiment. Overall, this XAVER chamber can be versatilely adjusted and combined with different measurement setups to enable a wide variety of *in situ* experiments.

3.5.2 Gas flow system

The gas flow system is custom-made to enable the generation of a stable gas flow, which can be adjusted to a defined relative humidity. The gas flow system was developed by Widmann et al.[180] and is used in Chapter 7 in combination with the two-point probe resistance setup and the XAVER chamber, detailed in Section 3.2.2 and Section 3.5.1 respectively. With this, *in situ* investigations of the humidity-dependent electrical resistance and morphology changes of EMIM DCA post-treated PEDOT:PSS thin films were performed. In Chapter 8 the system was combined with the UNICORN chamber equipped with the SR setup, introduced in Section 3.5.3 and Section 3.1.3, or the EIS probe head, described in Section 3.2.4. This allowed for further examination of the humidity-dependent swelling behavior and electrochemical response of the EMIM DCA post-treated PEDOT:PSS thin films with *in situ* ToF-NR, *in situ* SR and *in situ* EIS. Figure 3.18 shows a schematic sketch of the parts and function principle of the gas flow setup.

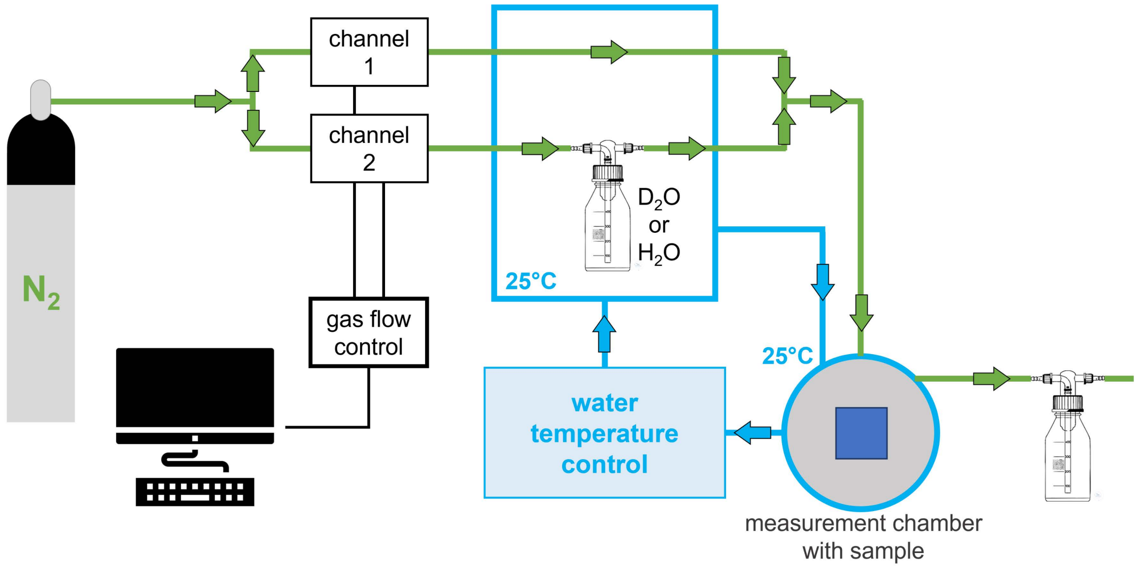

Figure 3.18 Gas flow setup. The gas flow setup, developed by Widmann et al.[180], enables the defined enrichment of a dry nitrogen gas stream (green) with a solvent, in this thesis D_2O or H_2O. For this, a defined volume flow (channel 2) of the dry nitrogen stream is bubbled through a bottle with the respective solvent, and the thus saturated gas stream is then recombined with another defined volume flow (channel 1) of the dry nitrogen gas. The combined gas stream is then guided through the measurement chamber containing the sample. An additional water temperature control system (blue) allows for temperature regulation of the measurement chamber and the gas flow system, enabling the precise adjustment of humidity and preventing condensation effects. Adapted from Widmann et al.[180]

The gas flow setup consists of a dry nitrogen flow (N_2), which is split into two streams. Each leading to gas flow meter valves, whose flow rate can be individually tuned with the gas flow control. Gas stream 2 is then directed through a gas washing bottle filled with de-ionized (DI-H_2O) or D_2O, hereby the N_2 bubbles through the liquid via a filter disc and is thus enriched with D_2O. Now the dry N_2 gas stream 1 and the humidity enriched N_2 stream 2 are recombined and directed into the respective measurement chamber. The relative humidity of the gas stream reaching the experiment chamber can now be adjusted by setting the flow rate of the respective gas flow meter valves accordingly. By using an additional external *JULABO FP50 HL* thermal bath cycle, the temperature of the gas flow system, including the tubing and gas washing bottles, were collectively regulated to a stable temperature of 25 °C. Additionally, the UNICORN chamber, which is introduced in the next Section 3.5.3, can also be connected to this thermal bath cycle for its temperature regulation.

3.5.3 Universal chamber for observation of reflectivity with neutrons

The universal chamber for observation of reflectivity with neutrons is a measurement chamber, which is custom designed and fabricated to enable neutron scattering experiments of a thin film sample while exposing them to a defined relative humidity. The UNICORN chamber developed by Widmann et al.[180] was used to investigate the swelling and water uptake behavior of EMIM DCA post-treated PEDOT:PSS thin films, with humidity-dependent *in situ* ToF-NR and *in situ* SR experiments. The measurement methods are introduced in Section 3.4.3 and Section 3.1.3, respectively, and the results are presented in Chapter 8. The specific chamber design and specifications of the UNICORN chamber are depicted in Figure 3.19 and outlined in the following.

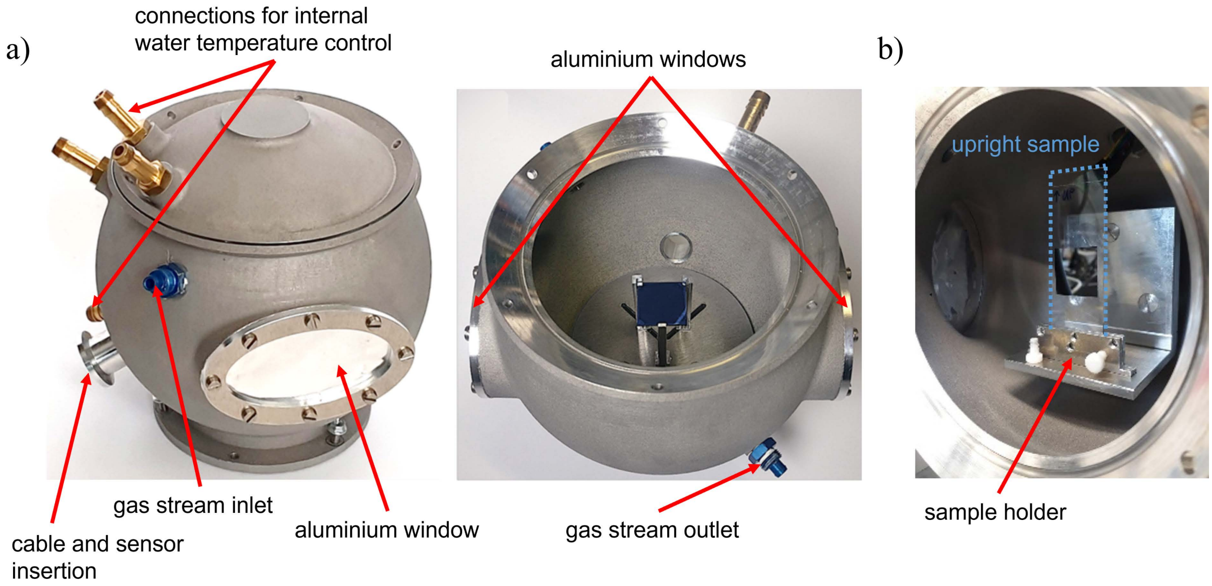

Figure 3.19 UNICORN measurement chamber. a) Photograph of the UNICORN measurement chamber, developed by Widmann et al.[180], showing the aluminium windows for the neutron scattering experiments, and the gas stream in- and outlet, which allow the defined adjustment of the sample environment humidity. An additional vacuum flanch allows the insertion of cables and sensors into the chamber, and with four connectors, the internal liquid channels of the lid and chamber can be connected to a water temperature control. b) Photograph of the L-shaped sample holder inside the chamber, in which the sample is placed vertically and with as little as possible contact to the holder, thus allowing the reduction of measurement disturbances caused by a solid sample holder. Adapted from Widmann et al.[180]

Figure 3.19a shows photographs of the UNICORN chamber. The chamber was designed in a spherical shape and with liquid channels inside the walls and lid, which enables a homogenous temperature control of the chamber and sample, to prevent condensation effects. The chamber was 3D printed from an AlSi10Mg aluminium alloy via selective laser sintering. The internal liquid channels can be connected to a *JULABO FP50 HL* thermal bath cycle to keep the chamber temperature stable at 25 °C. Furthermore, the UNICORN chamber comprises a gas inlet, which can be connected to the gas flow system described in Section 3.5.2 and a gas outlet, enabling the adjustment of the sample environment to a defined relative humidity. With a sensor, inserted airtight via a vacuum flange, the relative humidity and temperature inside the measurement chamber can be monitored. The UNICORN chamber has two elliptical windows on opposite sides, both covered and hermetically sealed with aluminium foil. These aluminium covered windows allow the transmission of incoming neutrons and exiting reflected neutrons during the ToF-NR experiments. In addition, the UNCORN lid can be equipped with a CaF_2 window and a holder for the spectral reflectance measurement setup to perform SR experiments. The sample holder inside the chamber, consists of a L-shaped plate in which the sample can be placed and fixed along its lower end with a screw. By this, the sample is only touching the holder along one side while the rest is free standing. This specific sample mounting, depicted in Figure 3.19b, helps to avoid disturbances on the neutron scattering experiments that would result from a solid sample holder.

4 Sample preparation

This chapter covers the materials, substrates preparation and thin film device fabrication procedures, which were used to manufacture the samples investigated within this thesis. In Section 4.1 all used materials are listed with their characteristics and supplier details. Subsequently, Section 4.2 gives a precise preparation description for the different types of substrates. The exact sequence of the thin polymer film fabrication and the ionic liquid doping procedure is given in Section 4.3 and Section 4.4, respectively. The final sample contacting steps, varying for the corresponding characterization method, can be found in Section 4.5. The sample preparation specifics provided in this present chapter are based on previous publications.[50–52, 163]

4.1 Materials

4.1.1 Substrate materials

In order to meet the respective requirements for the various characterization techniques used in this present thesis, three different substrate materials were utilized as basis for the thin film samples, which will be described in more detail in the following.

Glass substrates

Most of the electronic, structural, and spectroscopic characterizations were conducted on thin film samples prepared on glass substrates; as glass is especially beneficial because of its broad optical transparency and electrically insulating properties. Therefore, standard soda-lime glass microscope slides with a size of 76 × 26 mm² and a thickness of 1 mm, were purchased from *Carl Roth GmbH + Co. KG.* and were cut with a diamond cutter into 30 × 26 mm² sized substrates. These obtained substrates were then subjected to a cleaning procedure, described in Section 4.2.1, before the thin film deposition.

Silicon substrates

For time-of-flight neutron reflectivity (ToF-NR), spectral reflectance (SR), and X-ray reflectometry (XRR) investigations silicon (Si) wafers were used, because they provide excellent substrate conditions for these techniques, namely a very flat surface with a low roughness. The silicon wafers (p/Bor <100>), with a diameter of 100 mm, a thickness of 525 ± 25 µm, a resistivity of 10 – 20 Ω cm, and one side being polished to a roughness < 5 nm, were obtained from *Silicon Materials e. K.*. All silicon wafers were scratched, on their unpolished backside, with a diamond cutter into the desired substrate size of 70 × 70 mm², before subjecting them to the hot acid cleaning, described in Section 4.2.2.

Indium-doped tin oxide substrates

Indium-doped tin oxide (ITO) substrates were used for thin film analysis with electrochemical impedance spectroscopy (EIS) and conductive atomic force microscopy (c-AFM) to meet the respective measurement requirements, namely a patterned or completely conductive substrate surface. Glass slides of 1.1 mm thickness with an ITO layer coating of 100 nm, named ITO SOL 30 substrates, where purchased from *Solems S.A*. The substrates own a sheet resistance of 25-30 Ω sq^{-1} and were precut to a size of 25 × 25 mm² and 17 × 17 mm² for EIS and c-AFM respectively. As described in Section 4.2.3, these substrates were subjected either directly to the appropriate cleaning procedure or in case of the EIS samples, were first patterned by chemical etching.

4.1.2 Poly(3,4-ethylene dioxythiophene):poly(styrene sulfonate)

The main research focus of this thesis lies on the investigation of the polymer blend poly(3,4-ethylene dioxythiophene):poly(styrene sulfonate), short PEDOT:PSS, which consists of the p-semiconducting PEDOT and the electrically insulating PSS polymers. The structure and characteristics of this commonly used conductive polymer blend are described in detail in Section 2.1.2. For all thin film samples characterized in the frame of the present thesis, *Heraeus Clevios™* type PH 1000 PEDOT:PSS was used. The polymer blend was provided by *Ossila Ltd.* with a PEDOT:PSS ratio of 1:2.5, a solid content of 1.0 – 1.3 wt.% in water, a work function of 4.8 – 5.0 eV and a viscosity of < 50 mPa s, according to the supplier. After delivery, the PEDOT:PSS was stored in dark conditions at 4 °C, until it was used without further purification for the thin film preparation, as described in Section 4.3.

4.1.3 Ionic liquids

In the frame of this thesis, ionic liquids (ILs) are used as post-treatment agents, to improve the properties of thin PEDOT:PSS films. In literature ILs are usually defined as liquid electrolytes, which are solely composed of ions, and differ from molten salt by having a melting point below 100 °C.[181] Due to versatile combination possibilities of cations and anions, ILs allow a high tunability of their characteristics eligible for various applications.[182] In this thesis three different ILs were chosen and their different influence on the PEDOT:PSS film properties is investigated in Chapter 5. The chemical structures of these three chosen ILs, namely 1-allyl-3-methylimidazolium dicyanamide (AMIM DCA), 1-ethyl-3-methylimidazolium dicyanamide (EMIM DCA), and 1-ethyl-3-methylimidazolium tetracyanoborate (EMIM TCB) are shown in Figure 4.1a-c, respectively.

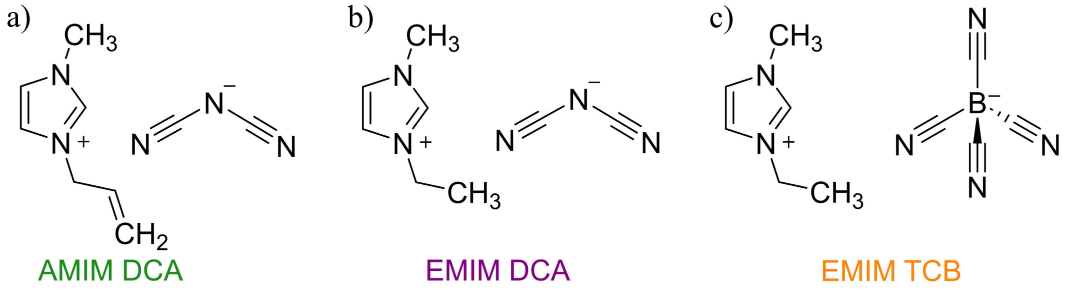

Figure 4.1 Ionic liquids. Chemical structures of the ILs used for post-treatment, a) AMIM DCA, b) EMIM DCA, and c) EMIM TCB.

Hereby it becomes apparent that for the different ILs either the cation or the anion was kept constant compared to EMIM DCA, which allows the exploration of possible effects from the cation or anion features. AMIM DCA (CAS: 917956-73-1) with a given molecular weight of 189.22 g mol^{-1} and density of 1.11 g mL^{-1} at 25 °C, and EMIM DCA (CAS: 370865-89-7) with a molecular weight and density of 177.21 g mol^{-1} and 1.10 g mL^{-1} at 25 °C, respectively, were both purchased from *Sigma-Aldrich* with a purity of $\geq$ 98.5 %. EMIM TCB was supplied by *Merck KGaA* (CAS: 742099-80-5) with a purity of $\geq$ 99.5 % and a given molecular weight of 226.05 g mol^{-1} and a density of 1.04 g mL^{-1} at 25 °C The different ILs were directly used without additional treatment for the IL post-treatment procedure of the PEDOT:PSS films, for which a carrier solvent was facilitated, as described in more detail in Section 4.4.

4.1.4 Additives, solvents, and cleaning agents

In this section all additives, solvents, and cleaning agents utilized in this thesis are listed with their specifics and their chemical structure is shown in Figure 4.2. Sulfuric acid, hydrogen peroxide, hellmanex II, zinc powder, hydrochloric acid, acetone, and isopropanol, are cleaning agents, used during the different substrate preparations described in Section 4.2. The fluorosurfactant Zonyl® FS-300 was used as additive during the PEDOT:PSS film preparation, as detailed in Section 4.3.1. Tetrahydrofuran was facilitated as carrier solvent for the ILs post-treatment, mentioned in Section 4.4.1, and deuterated water was used during *in situ* ToF-NR and *in situ* SR for humidification of the measurement chamber, as described in Section 3.5.2. De-ionized water was applied throughout this thesis for cleaning procedures, as carrier solvent and for humidification in *in situ* investigations. All purchased chemicals in this section were directly used without further purification.

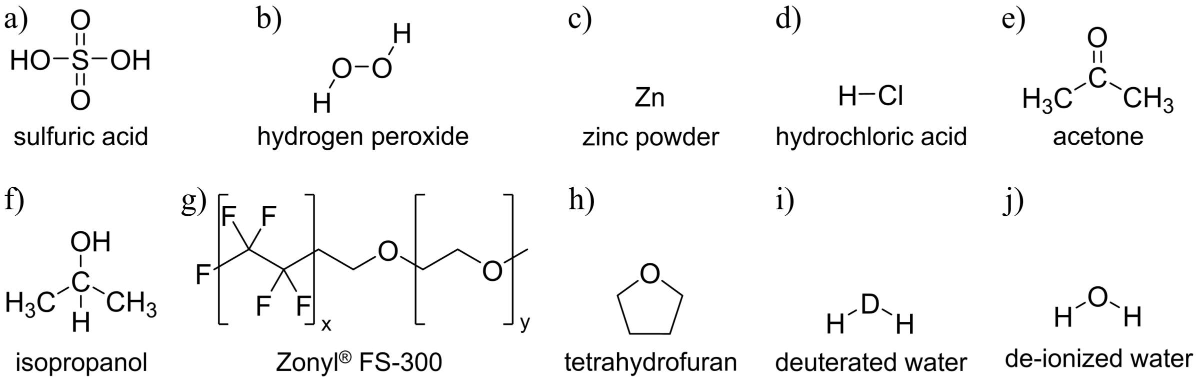

Figure 4.2 Additive, solvents, and cleaning agents. Chemical structures of a) sulfuric acid, b) hydrogen peroxide, c) zinc powder, d) hydrochloric acid, e) acetone, f) isopropanol, g) Zonyl® FS-300, h) tetrahydrofuran, i) deuterated water and j) de-ionized water.

Sulfuric acid

Sulfuric acid (H_2SO_4) with a concentration of 95 % – 98 % was supplied by *Carl Roth GmbH + Co. KG.* (CAS: 7664-93-9). The chemical structure of this high oxidizing inorganic acid is depicted in Figure 4.2a, and its density and molar mass at 25 °C are given as 1.84 g mL^{-1} and 98.08 g mol^{-1}, respectively. The concentrated H_2SO_4 was used for the hot acid bath substrate cleaning, described in Section 4.2.

Hydrogen Peroxide

Hydrogen peroxide (H_2O_2), shown in Figure 4.2b, was also utilized for the hot acid bath cleaning of the glass and silicon substrates, as detailed in Section 4.2. The strong oxidizing agent H_2O_2 was purchased with an assay of 30 – 31 % from *Carl Roth GmbH + Co. KG.* (CAS: 7722-84-1) and owns a declared density of 1.11 g mL^{-1} and a molar mass of 34.02 g mol^{-1} at 25 °C.

Zinc powder

Zinc (Zn) powder, stabilized, with a particle size of < 63 µm, a purity of ≥ 98 %, a density of 7.14 g mL^{-1} and a molar mass of 65.37 g mol^{-1} at 25 °C, was obtained from *Carl Roth GmbH + Co. KG.* (CAS: 7440-66-6). The Zn powder, Figure 4.2c, was used during the etching process to pattern the ITO glass substrates as described in detail in Section 4.2.3.

Hydrochloric acid

The strong inorganic acid, hydrochloric acid (HCl), was supplied with a purity of 37 % by *Carl Roth GmbH + Co. KG.* (CAS: 7647-01-0) and was used for the ITO etching process described in Section 4.2.3. The chemical structure is depicted in Figure 4.2d, and at 25 °C the density and the molar mass are given as 1.19 g mL^{-1} and 36.46 g mol^{-1}, respectively.

Acetone

Acetone, with a noted molar mass of 58.08 g mol^{-1} and a density of 0.79 g mL^{-1} at 25 °C, was purchased from *Carl Roth GmbH + Co. KG.* (CAS: 67-64-1) in a purity of ≥ 99.8 %. Its chemical structure is depicted in Figure 4.2e and the organic solvent was used for the ITO substrate cleaning as described in Section 4.2.3.

Isopropanol

Isopropanol is a commonly used alcohol, shown in Figure 4.2f, with a noted molar mass of 60.10 g mol^{-1} and a density of 0.79 g mL^{-1} at 25 °C. It was obtained in an assay of ≥ 99.8 % from *Carl Roth GmbH + Co. KG.* (CAS: 67-63-0) and was used as cleaning agent for the ITO substrates as detailed in Section 4.2.3.

Hellmanex II

Hellmanex II is a special alkaline cleaning concentrate supplied by *Hellma GmbH + Co. KG.*, with a concentrate density of 1.42 g mL^{-1}. As outlined in Section 4.2.3 hellmanex II was used in diluted form to clean the ITO coated substrates.

Zonyl® FS-300

As described in Section 4.3.1, the fluorosurfactant Zonyl® FS-300 (Zonyl®) was applied in this present thesis as additive to modify the PEDOT:PSS structure.[36] The chemical structure of this non-ionic fluorosurfactant is depicted in Figure 4.2g. It has a given density of 1.10 g mL^{-1} ± 0.05 g mL^{-1} at 20 °C and an concentration of ~ 40 % solids in water. Zonyl® FS-300 is a registered trademark of *E. I. du Pont de Nemours and Company* (CAS: 197664-69-0) and for this thesis Zonyl® was acquired via *Sigma-Aldrich*, as it is been produced by the company's affiliate *Fluka*™.

Tetrahydrofuran

Tetrahydrofuran (THF) is a cyclic ether, depicted in Figure 4.2h, which is commonly used as versatile organic solvent. In this thesis, THF in anhydrous, inhibitor-free from was used as carrier solvent for the ILs post-treatment procedure, described in Section 4.4. It was purchased from *Sigma-Aldrich* (CAS: 109-99-9) and has a declared molecular weight of 72.11 g mol^{-1} and a density of 0.89 g mL^{-1} at 25 °C.

Deuterated water

The chemical structure of deuterated water (D_2O), with a given density of 1.11 g mL^{-1} and a molecular mass of 20.03 g mol^{-1}, is depicted in Figure 4.2i. It was obtained from *Deutero GmbH* (CAS: 7789-20-0) with a purity of 99.95 % and was utilized for the *in situ* ToF-NR investigations in Chapter 8.

De-ionized water

In this present thesis de-ionized water (DI-H_2O), depicted in Figure 4.2j, was used for multiple purposes during the sample preparation procedure and sample characterization. Water was purified and deionized with an *ELGA LabWater System PURELAB® Chorus 1* from *Veolia Water Solutions & Technologies*, achieving a resistivities of 18.2 MΩ cm at 25 °C.

4.1.5 Additional materials for sample fabrication

This section contains a list of additional materials that were utilized during the various thin film sample preparation steps. Polyvinylidene fluoride syringe filter, during PEDOT:PSS solution preparation in Section 4.3.1, Kapton® polyimide tape during the ITO glass patterning outlined in Section 4.2.3, and silver paint and fine gold for sample contacting as detailed in Section 4.5.

Polyvinylidene fluoride syringe filter

Polyvinylidene fluoride (PVDF) syringe filters were used for the PEDOT:PSS solution preparation, detailed in Section 4.3.1. The in this thesis used Whatman® Puradisc 25 syringe filter with PVDF as filter material and a pore size of 0.45 µm were purchased from *Sigma-Aldrich*.

Kapton® polyimide tape

Kapton® polyimide (Kapton®) tape, is a heat resistant sticky tape, which was used during the ITO glass patterning described in Section 4.2.3. It was purchased from *Conrad Electronic SE*.

Silver paint

Conductive silver (Ag) paint was applied for electrical contacting of the thin film samples, as detailed in Section 4.5.1. The in this present thesis used Ag paint was acquired from *Ferro GmbH* through *Conrad Electronic SE*.

Fine gold

Gold (Au) with a fineness of 99.99 % was obtained from *Goldkontor Hamburg GmbH*. As described in detail in Section 4.5.2, it was evaporated on the samples for electrical contacting.

4.2 Substrate preparation

For the fabrication of polymer thin film samples, the substrate properties, as well as a good interaction between the polymer layer and the substrate, are essential to obtain high quality, defect free thin films. Even small impurities or wettability differences on the substrate surface have an impact on the homogeneity and morphology of the prepared polymer films. Therefore, the in this thesis utilized substrates, glass, silicon, and ITO layered glass, were subjected to the various cleaning procedures and treatments, described in this section.

4.2.1 Glass substrates

All glass substrates were cut to a size of 30 × 26 mm² and were then cleaned through a hot acid bath treatment.[183] For this, 45 mL of DI-H_2O was filled into a glass beaker, which is placed in a water bath on a hotplate. Then 70 mL of H_2O_2 was poured into the beaker and after that 165 mL H_2SO_4 was added slowly, to prevent an overreaction. The beaker was then covered with a watch glass to inhibit evaporation, as the water bath was heated to 80 °C. During the heating of the acid bath, the glass substrates were rinsed thoroughly with DI-H_2O, which ensured the removal of dust and glass splinters from the substrate cutting. Afterwards, they were placed into a custom-made acid resistant substrate holder, made of poly(tetrafluoroethylene) (PTFE). As the water bath reached 80 °C, the substrates were immersed into the hot acid bath with the substrate holder. After 15 min the substrates were taken out of the acid bath and subsequently dipped into two 500 mL beakers filled with DI-H_2O to wash off acid residues. An additional thorough rinsing step of every glass substrate with DI-H_2O, before drying them under a nitrogen stream, guaranteed the complete removal of any acidic remnants.

Shortly before the spin-coating procedure the acid bath cleaned, and dried substrates were exposed to an oxygen plasma treatment, using a *Nano Plasma Cleaner* from *Diener Electronics GmbH + Co. KG*. Therefore, these substrates were spread into a glass petri dish, which was put into the plasma oven and exposed to a vacuum of ≤ 0.1 mbar. Then an oxygen atmosphere with 0.4 mbar pressure was applied, by respectively adjusting a simultaneous oxygen flow and vacuum, which allowed the continuous removal of reaction products during the plasma treatment. The plasma was generated by applying a power of 250 W with a frequency of 40 kHz. After 10 min the oxygen flow was turned off while the vacuum was still applied until ≤ 0.1 mbar was reached, to ensure the removal of residual reaction products.

With this two-step cleaning procedure organic compounds on the substrate surface are, on the one hand, removed by the highly reactive and oxidizing hot acids, and on the other hand, are decomposed by oxygen radicals resulting from the oxygen plasma. Furthermore, the hydrophilicity of the substrate surface is increased by activating polar chemical bonds, which enhances the wettability of polar solvents, like the aqueous PEDOT:PSS solutions used in this thesis. However, as this effect only lasts for a couple of minutes, it is necessary to perform the thin film deposition directly after the plasma treatment, to profit from an improved substrate-film interface.

4.2.2 Silicon substrates

The silicon wafers were scratched with a diamond cutter on their unpolished backside, into the desired substrate size of 70×70 mm^2, but not yet broken. The pre-scratched silicon substrates were then subjected to a similar hot acid bath cleaning procedure with subsequent oxygen plasma treatment as described in Section 4.2.1, above. The only difference in the process was an increased volume of the hot acid bath ingredients, namely 54 mL of DI-H_2O, 84 mL of H_2O_2, and 198 mL of H_2SO_4, to ensure a complete immersion of the silicon substrates into the hot acid bath. For this substrate type, the oxygen plasma treatment was also performed directly before the spin-coating procedure, to benefit from the effect of enhanced surface hydrophilicity and thus improved wettability with polar solvents.

4.2.3 Indium-doped tin oxide glass substrates

The ITO substrates for the c-AFM investigation, described in Section 3.3.2, were obtained with a size of 17 × 17 mm² and were directly subjected to a cleaning procedure using isopropanol. For this, the substrates were first rinsed with DI-H_2O to remove any dust, then mechanically cleaned with an isopropanol-soaked cotton wipe, and subsequently placed into a custom-made PTFE substrate holder. The holder with the substrates was immersed into a beaker filled with isopropanol, which was covered with a watch glass and placed into an ultrasonic bath for 10 min at RT. Afterwards, the isopropanol was replaced and the ultrasonic treatment was repeated once more. Then the substrates were thoroughly rinsed with DI-H_2O and dried under a nitrogen stream. Directly before the thin film deposition, these ITO substrates were subjected to an oxygen plasma treatment procedure, as detailed in Section 4.2.1.

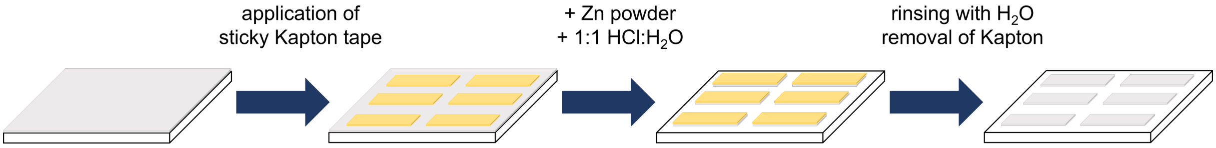

Figure 4.3 Chemical etching of ITO substrates. Chemical etching and cleaning procedure of ITO substrates to create specific patterned ITO electrode geometry.

The ITO substrates for the EIS investigation were acquired in a size of 25 × 25 mm². As described in Section 3.2.4, for this sensitive measurement technique, the ITO layer had to be partly removed to obtain a specific ITO electrode geometry displayed in Figure 3.8. Therefore, the chemical etching process, schematically depicted in Figure 4.3, was performed with the ITO substrates. For this, the areas of the electrodes, meaning the regions where the ITO should not be removed, were first covered with sticky Kapton® tape. Then the uncovered parts were partially sprinkled with a small amount of Zn powder, which serves as catalyst for this chemical etching process. Afterwards, a diluted HCl solution, containing HCl (37 %) and DI-H_2O in a ratio of 1:1, was dropped onto the unmasked regions of the ITO substrate, and was spread and mechanically wiped with a cotton swab. At last, the etched ITO substrates were thoroughly rinsed with DI-H_2O to ensure complete removal of all reagents, before the sticky Kapton® tape was removed. These patterned ITO substrates were then cleaned via an organic cleaning procedure. For this, the DI-H_2O rinsed substrates were placed into a PTFE substrate holder and immersed into a bath of Hellmanex II diluted with DI-H_2O to 2 vol%, which was placed into an ultrasonic bath for 20 min. Then the substrates were removed with the substrate holder, thoroughly rinsed with DI-H_2O and wetted with acetone, before being immersed into an acetone bath and treated for 20 min with ultrasound. Afterwards, the substrates and the holder were removed from the acetone bath and again thoroughly rinsed with DI-H_2O before they were wetted with isopropanol and subjected to ultrasonic treatment for 20 min, while being submerged into an isopropanol bath. After this final cleaning step, all substrates were individually rinsed with DI-H_2O to guarantee no residues of the cleaning agents are left and were then dried under a nitrogen stream. For these patterned ITO substrates also an oxygen plasma treatment, as described in Section 4.2.1, was performed directly before the spin-coating procedure.

4.3 PEDOT:PSS thin film preparation

Even though the usage of different substrates was necessary to meet the respective requirements of the various characterization techniques, the PEDOT:PSS thin film preparation process, described in this section, was kept similar, to ensure the comparability of the different samples. Only the applied solution volume dropped onto the substrates during the spin-coating and doping steps were adjusted to the respective substrate size and material. The different steps of the complete sample preparation procedure are displayed in Figure 4.4.

4.3.1 PEDOT:PSS solution preparation

For the preparation of the spin-casting solution, first the respectively required amount of aqueous PEDOT:PSS solution was treated in an ultrasonic bath for 10 min. This ultrasonic treatment was performed to break down large agglomerates of PEDOT:PSS colloidal particles present in the aqueous solution and thus decrease the risk of film inhomogeneities.

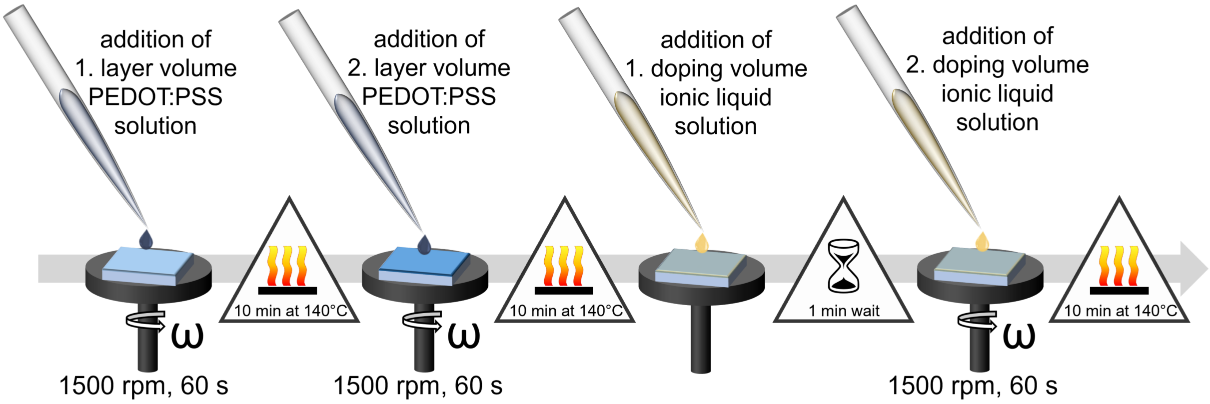

Figure 4.4 Sample preparation procedure. First the first layer of PEDOT:PSS is spin-coated, followed by an annealing step, then the second layer PEDOT:PSS is spin-coated, again followed by an annealing step. IL solution is evenly applied on the cooled down PEDOT:PSS thin film, and after a soaking time of 1 min additional ionic solution is applied, directly followed by a spin-coating step. After a final annealing step, the sample is ready for characterization. Adapted with permission from American Chemical Society, Copyright 2022.[50]

Afterwards, the PEDOT:PSS solution was additionally filtered through a hydrophilic PVDF filter with a pore size of 0.45 µm, to extract remaining large agglomerates and colloidal particles. This filtered PEDOT:PSS solution was then added into a screwcap glass vial, containing the fluorosurfactant Zonyl®. Zonyl® was used as additive because it has been reported to optimize the wettability of the PEDOT:PSS solution with different substrate surfaces, and tune the polymer film morphology towards the achievement of better electrical characteristics.[36] The amount of the surfactant in the screwcap glass vial was chosen to obtain an overall weight content of roughly 1 wt% Zonyl® per aqueous PEDOT:PSS solution. The mixture was then covered with aluminium foil and placed onto a shaker for 2 h to ensure good intermixing, before further usage in the spin-coating process.

4.3.2 Spin-coating and annealing

The respective prepared and cleaned substrates, as detailed in Section 4.2, were used for the thin film coating procedure, immediately after the oxygen plasma treatment. Therefore, they were placed onto a *Delta 6 RT CC* spin-coater from the company *Süss MicroTec SE* and were fixed there via vacuum suction. As depicted in Figure 4.4 a defined amount (1. layer volume) of the prepared PEDOT:PSS solution, described before in Section 4.3.1, was completely spread onto the substrate. Directly afterwards the spin-coating process was started with a total duration of 60 s, a speed of 1500 rpm, and an acceleration level of 9, which results in 4.5 s acceleration and deceleration time, respectively. Subsequently, the PEDOT:PSS coated sample was placed on a 140 °C hot heating plate for a 10 min annealing step and was then cooled down to room temperature (RT). In order to achieve a thicker polymer film, a second PEDOT:PSS layer was applied. Therefore, the already coated samples were placed and fixed onto the spin-coater, and again covered completely with a defined amount (2. layer volume) of the prepared PEDOT:PSS solution. The parameters of the ensuing spin-coating process were kept similar with a speed of 1500 rpm, an acceleration level of 9, and a duration of 60 s. For the second polymer layer, also a 10 min annealing step on a 140 °C hot heating plate was performed before the samples were cooled down to RT and stored dust-free until further usage. Depending on the used substrate material and size, different amounts of the prepared PEDOT:PSS solution, were utilized for the thin film fabrication. A list of the applied solution volumes during the first and second layer deposition step for the various substrate types, is provided in Table 4.1.

Table 4.1 Amount of PEDOT:PSS solution for different substrate types.

characterization methods	substrate material	substrate size [mm²]	1. layer volume [µL]	2. layer volume [µL]
c-AFM	ITO glass	17 × 17	330	435
EIS	ITO glass	25 × 25	440	440
ToF-NR and SR	silicon	70 × 70	5500	5500
others	glass	26 × 30	550	550

4.4 Ionic liquid doping

The doping of the PEDOT:PSS with ionic liquids was performed via a post-treatment procedure, meaning the doping solution was deposited on the already prepared PEDOT:PSS layers. This approach was selected, because the addition of the ILs directly into the aqueous PEDOT:PSS solution led to a gelation of the entire mixture, which made the preparation of thin and homogeneous polymer films unfeasible.

4.4.1 Doping solution preparation

For the application of the ILs onto the PEDOT:PSS layers a carrier solvent was utilized, to be able to adjust different doping concentrations, and to achieve an uniform distribution of the ILs. THF was used as carrier solvent for the samples characterized in Chapter 5, Chapter 6 and Chapter 7, as it showed more significant improvements of the PEDOT:PSS electrical characteristics. However, for the sample investigations in Chapter 8, DI-H_2O was chosen as carrier solvent, because it allowed the fabrication of films with less surface roughness, which was especially important for the ToF-NR and SR measurements.

Table 4.2 Concentrations of ionic liquid doping solutions.

AMIM DCA ρ_N = 5.87 mol × L^{-1}		EMIM DCA ρ_N = 6.21 mol × L^{-1}		EMIM TCB ρ_N = 4.60 mol × L^{-1}	
concentration [M]	[µl] per 1 mL carrier solvent	concentration [M]	[µl] per 1 mL carrier solvent	concentration [M]	[µl] per 1 mL carrier solvent
0.0087	1.48	0.0100	1.61	0.0100	2.17
0.0218	3.71	0.0250	4.03	0.0250	5.43
0.0437	7.44	0.0500	8.05	0.0500	10.87
0.0874	14.89	0.1000	16.10	0.1000	21.74
0.1747	29.76	0.2000	32.21	0.2000	43.48
0.3058	52.10	0.3500	56.36	0.3500	76.09
0.4370	74.45	0.5000	80.52	0.5000	108.70

The three different ILs, AMIM DCA, EMIM DCA and EMIM TCB, introduced in Section 4.1.3, were used for the post-treatment doping procedure. Depending on their number density (ρ_N), calculated from the division of density and molar mass, they were mixed in respective quantities with the according carrier solvent, to obtain the desired concentrations of the IL doping solutions. All the in this thesis investigated concentrations of the different ILs and the applied amounts, are listed in Table 4.2. Additionally, as reference samples PEDOT:PSS films post-treated with the pure carrier solvent, THF or DI-H_2O, were also investigated, in the following denoted with 0 M concentration. The IL doping solutions were subjected to a short ultrasonic treatment, directly before being deposited onto the PEDOT:PSS layer, to ensure a good intermixing.

4.4.2 Doping and annealing

For the doping procedure, the PEDOT:PSS coated substrates fabricated according to Section 4.3, were placed onto the spin-coater and fixed via vacuum suction. As depicted in Figure 4.4, a defined amount of the respective doping solution (1. doping volume) was dropped onto the polymer film, whereby the full coverage of the surface was ensured. The doping solution was allowed to soak in and react with the film for 1 min, before another quantity of the doping solution (2. doping volume) was added. Immediately after, the excess doping solution was spun off, by operating the spin-coater for 60 s with an acceleration level of 9 at a speed of 1500 rpm. Then the post-treated samples were placed for 10 min onto a 140 °C hot heating plate for annealing and complete evaporation of any solvent residues. Afterwards, the prepared doped PEDOT:PSS samples were stored in a container and sealed dust-free until characterization. Similar to the PEDOT:PSS film fabrication, also for the post-treatment procedure, the applied doping solution amounts were adjusted depending on the used substrate base. Table 4.3 lists all utilized doping solution volumes for the different substrate types, during the first and second doping step.

Table 4.3 Amount of doping solution for different substrate types.

characterization methods	substrate material	substrate size [mm²]	1. doping volume [µL]	2. doping volume [µL]
c-AFM	ITO glass	17 × 17	437	437
EIS	ITO glass	25 × 25	400	400
ToF-NR and SR	silicon	70 × 70	5000	5000
others	glass	26 × 30	500	500

4.5 Sample contacting

For some of the characterization techniques the application of electrodes on the post-treated PEDOT:PSS surfaces was necessary, to provide a good contacting with the thin film. Therefore, as described in this section, either conductive silver paint or evaporated gold electrodes were applied.

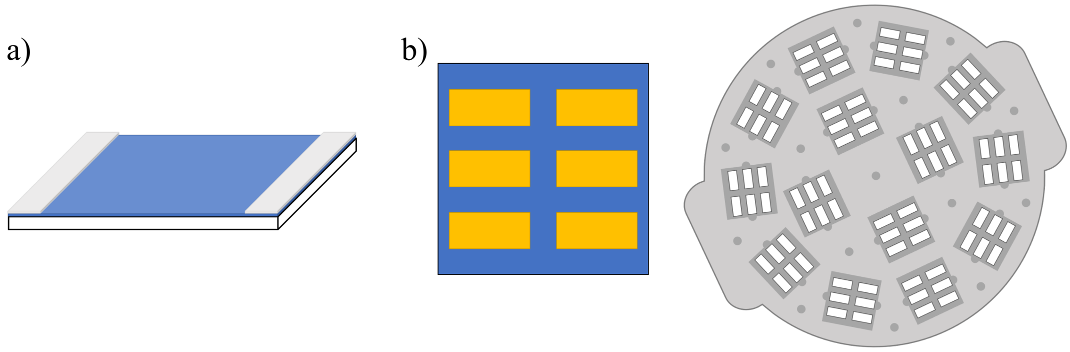

Figure 4.5 Sample contacting. Schematical sketches of a) silver paste contacting geometry, b) gold electrode contacting geometry and mask for gold contact evaporation.

4.5.1 Silver paint contacting

For the Seebeck Coefficient and the two-point probe resistance measurements, described in Section 3.2.1 and Section 3.2.2, respectively, the electrical contacting of the thin polymer film was achieved with conductive silver paint. Therefore, a thin layer of silver paint was applied with a width of roughly 5 mm along the shorter edges of the post-treated PEDOT:PSS samples, as depicted in Figure 4.5a. The silver paint was left to dry for at least 3 min before the samples could be used for investigation.

4.5.2 Gold contact evaporation

As already mentioned in Section 3.2.4, the sample and contacting geometry for the EIS investigations had to be a bit more advanced to ensure a stable measurement. To achieve the desired electrode geometry as shown in Figure 4.5b the gold contacts were deposited via thermal evaporation. For this, the readily prepared post-treated PEDOT:PSS samples were inserted into a glove box under nitrogen atmosphere and placed upside down into a custom-designed shadow mask, which provided space for 14 samples and was designed by Tobias Schöner.[169] Then the evaporation chamber was subject to a vacuum with a pressure in the magnitude of 10^{-5} – 10^{-6} bar. For the first 10 nm gold layer deposition step, the evaporation rate was kept small to 0.2 Å s^{-1}, which minimizes the penetration depth of the gold particles. Afterwards the evaporation rate was increased to 0.6 Å s^{-1} until the entire gold layer reached a thickness of around 80 nm. Overall, around 400 mg fine gold were utilized for each gold electrode evaporation step to prepare 14 samples. At last, the evaporation chamber was returned to normal pressure before the samples could be extracted from the glovebox for further investigation.

5 Ionic liquid post-treatment of thin PEDOT:PSS films

This chapter is based on the publication "*Correlation of Thermoelectric Performance, Domain Morphology and Doping Level in PEDOT:PSS Thin Films Post-Treated with Ionic Liquids*" (A. L. Oechsle, J. E. Heger, N. Li, S. Yin, S. Bernstorff, P. Müller-Buschbaum, Macromolecular Rapid Communications 2021, 42, 20, 2100397; DOI: 10.1002/marc.202100397). Reprinted with permission from Wiley-VCH GmbH, Copyright 2021.

In this chapter the ionic liquid (IL) post-treatment of poly(3,4-ethylene dioxythiophene):poly(styrene sulfonate) (PEDOT:PSS) thin films with 1-ethyl-3-methylimidazolium dicyanamide (EMIM DCA), 1-allyl-3-methylimidazolium dicyanamide (AMIM DCA), and 1-ethyl-3-methylimidazolium tetracyanoborate (EMIM TCB) is compared. Doping level modifications of PEDOT are characterized using UV-Vis spectroscopy and directly correlate with the observed Seebeck coefficient enhancement. With conductive atomic force microscopy (c-AFM) changes in the topographic-current features of the PEDOT:PSS thin film surface due to IL treatment are investigated. Grazing-incidence small-angle X-ray scattering (GISAXS) demonstrates the morphological rearrangement towards an optimized PEDOT domain distribution upon IL post-treatment, directly facilitating the inter-conductivity and causing an increased film conductivity. Based on these improvements in Seebeck coefficient and conductivity, the power factor is increased up to 236 µW $m^{-1}K^{-2}$. Subsequently, a model is developed indicating that ILs, which contain small, sterically unhindered ions with a strong localized charge, appear beneficial to boost the thermoelectric performance of post-treated PEDOT:PSS films.

5.1 ILs as doping agent for PEDOT:PSS

Thermoelectric (TE) materials, introduced in Section 2.2, enable the direct conversion of thermal energy, via temperature gradient, into electrical power, which can be used for example in waste heat recovery or solar thermal energy harvesting.[3, 120] Thus, they provide a promising contribution to global sustainable energy solutions and have gained a lot of attention in recent years.[184–186] So far conventional TEs are mainly based on inorganic compounds of heavy elements like bismuth, tellurium, silver, or lead. These inorganic TE materials achieve auspicious high thermoelectric efficiencies and high-temperature stability, but have many disadvantages, such as being toxic, scarce, expensive, and difficult to process.[5, 187] Thus, current research focuses more and more on the use of organic compounds as TE materials. By using conducting organic polymers, non-toxic, lightweight, flexible, and cost-efficient TE devices could be accessible.[9, 188, 189] Commonly used conductive polymers are usually based on a conjugated backbone structure, like in polyacetylene, polypyrrole, polyaniline or polythiophene.[190] With different techniques of doping[191–193], side chain variations[193] or backbone modifications[194] the thermoelectric performance can be positively influenced.

As one of the most popular and widely investigated TE polymers, PEDOT:PSS, described in Section 2.1.2, combines desirable advantages.[10, 17, 195] First of all, PEDOT:PSS is water-soluble and hence allows for processability from an aqueous solution, which prevents the need for toxic solvents. Moreover, coupled with its easy and cheap commercial availability, this paves the way for an inexpensive industrial upscaling of production with deposition techniques like roll-to-roll printing or spray coating. Besides, this polymer has high mechanical flexibility and high optical transparency when prepared as thin films, opening a wide range of possible TE applications. Most important, however, with PEDOT:PSS high hole conductivities of up to 10^3 S cm^{-1} can be reached.[196] This favorable combination of properties is a result of the special polymer blend structure of PEDOT:PSS. On one part, the poorly soluble π-conjugated polymer PEDOT is the origin of a positive charge carrier conductivity. On the other part, the water-soluble but electrically insulating PSS is ionically bound by arbitrarily directed pendant functionalities on its non-conjugated linear backbones. In aqueous solution and for PEDOT:PSS film fabrication, PSS is required to enable the solubility of PEDOT and to introduce and stabilize the positive charge carriers within the PEDOT backbone.[16, 18] However, when coating the aqueous PEDOT:PSS solution, upon water evaporation a particular film structure of pancake-like shaped PEDOT-rich domains embedded in a PSS-rich matrix is formed, as depictured in Figure 2.5.[19] In these obtained PEDOT:PSS thin films, the insulating PSS matrix acts as a barrier for inter-domain charge carrier transport between the PEDOT-rich domains, diminishing the film conductivity.[16]

Consequently, research to enhance the electrical conductivity (σ) of PEDOT:PSS films, is mostly aiming at the removal of excess PSS.[91] Some successfully exemplified approaches from previous studies, showed that treatments of PEDOT:PSS thin films with acids and bases[30–32, 88, 89] and with solutions of inorganic salts[28, 29] can improve the electrical conductivity. Also, the addition of polar solvents like dimethyl sulfoxide (DMSO)[34, 37, 44, 94, 95], dimethylformamide (DMF)[93], or a surfactant[34, 36, 37] into the aqueous PEDOT:PSS solution leads to a positive effect on σ. Furthermore, Palumbiny et al. showed how the post-treatment with the high-boiling-point solvent ethylene glycol can lead to charge transport preferred edge-on orientation of the PEDOT crystal phase during printing[23], increasing σ up to 1000 S cm^{-1}.[24] In all these studies, the improvement of the film σ is based on changing the PEDOT:PSS thin film morphology, more detailed in Section 2.1.3.

However, to assess the thermoelectric efficiency of one material not only its σ is important, but also its Seebeck coefficient (S). S defines the measure of an arising thermovoltage within a material, upon application of a defined temperature gradient. Therefore, σ and S are usually combined in the power factor (PF, Section 2.2.3) to evaluate the performance of TE materials.[11] Some previous study showed that S increases up to 50 µV K^{-1}, when reducing the positively charged PEDOT backbone by addition of readily available inorganic redox-active or basic salts into the aqueous PEDOT:PSS solution.[27] Though, the hereby induced decrease in the positive charge carrier concentration improved S, on the downside it caused a decrease of σ, as explained in Section 2.1.3. Hence, S and σ show a direct dependency of each other, and therefore a simultaneous improvement of both parameters to obtain a clear rise of the thermoelectric PF is quite challenging. However, this obstacle was overcome when research showed that treatment of PEDOT:PSS with ILs simultaneously increases σ and S.[44–48] ILs are salts that are liquid at room temperature (RT) due to their very low melting points, and enable a flexible combination of ions to easily tune their properties for different applications.[182] It turned out that for PEDOT:PSS the ILs influence the morphology of the polymer blend via interacting with the polymer chains. Besides, the IL anions interact with the PEDOT chain, simultaneously leading to changes in the doping level of the resulting PEDOT:PSS film. So far, a variety of different ILs have been used to improve the PEDOT:PSS properties. Especially, a majority of investigations was focusing on different 1-ethyl-3-methylimidazolium[47, 49, 101, 197]

ILs, such as 1-ethyl-3-methylimidazolium tricyanomethanide (EMIM TCM)[102, 198, 199], 1-ethyl-3-methylimidazolium tetrafluoroborate (EMIM BF_4)[44], or ethyl-3-methylimidazolium bis(trifluoromethylsulfonyl)imid (EMIM TFSI)[103]. For example, Kee et al. achieved σ up to 2000 S cm^{-1} using mixtures of PEDOT:PSS with EMIM TCB.[200] Besides, post-treatment of PEDOT:PSS thin films with the IL EMIM DCA showed a PF enhancement up to 170 µW $m^{-1}K^{-2}$.[100]

In this chapter, the focus lies on the post-treatment approach, using two promising ILs with different anions, EMIM DCA[100, 201] and EMIM TCB.[200, 202] To also allow comparison between different cations, the IL AMIM DCA is probed as well. These different ILs are used in varying concentrations to post-treat the as-prepared PEDOT:PSS thin films and investigate the concentration-dependent effect on the thermoelectric parameters S and σ. It is important to mention that the film preparation procedure, like spin coating settings, ambient conditions, annealing temperatures, and annealing times, etc. could also have an influence on the TE performance of the thin films. Therefore, as the aim is to focus mainly on the effect of the respective ILs, all the film preparation steps are kept as constant as possible to ensure the comparability of the different treated samples. With measurements of UV-Vis spectra, the influence of the ILs on the doping level of the PEDOT:PSS films is revealed. Furthermore, c-AFM measurements performed on selected films, give an insight into the surface-related morphological changes due to IL post-treatment. Existing studies mainly investigate the surface morphology with AFM[44, 46, 95, 199, 202], or investigate the crystalline structure of PEDOT[34, 198, 200]. A detailed investigation of IL treatment effects on the PEDOT:PSS morphology with a focus on the PEDOT domain structure inside the film, so far seems to be missing in the literature. Therefore, the scope of this study is to find a correlation between the thermoelectric performance and the PEDOT:PSS domain morphology upon ILs post-treatment. By using GISAXS a large sample volume is probed to detect structures, of sizes ranging from several to hundreds of nanometers, with high statistical relevance.[148]

For this, PEDOT:PSS thin films are prepared by spin-coating from the aqueous solution and post-treated with three different ILs (EMIM DCA, AMIM DCA, or EMIM TCB) with varying concentrations in THF. The respectively applied IL concentrations are given in Table 4.2. Additionally, PEDOT:PSS films post-treated with pure THF were prepared as a reference sample. A complete description of the used materials, the PEDOT:PSS thin film preparation and IL post-treatment procedures are detailed in Chapter 4, furthermore, the in this chapter utilized investigation methods are described in Chapter 3.

5.2 Effect of ILs on the PEDOT:PSS oxidation level

Figure 5.1a comprises the measured Seebeck coefficients for the respectively IL post-treated PEDOT:PSS thin films. Indicated by the dashed lines, an increase of *S* upon treatment with increasing concentrations of the respective ILs can be seen. The strongest increase of the *S* is obtained for samples treated with EMIM DCA. With this IL, the overall highest *S* of 46 µV K^{-1} at a concentration of 0.35 M was reached. PEDOT:PSS films treated with AMIM DCA show the second strongest increase in *S* up to 40 µV K^{-1}. The weakest increase in the *S* is found for the EMIM TCB post-treated thin films. Nevertheless, the for this IL highest *S* value of 32 µV K^{-1} (at 0.5 M EMIM TCB) still means an improvement compared to the reference sample with *S* = 22 µV K^{-1}. In the literature, the reported *S* increasements for IL treated PEDOT:PSS are usually achieved by directly mixing the ILs into the aqueous PEDOT:PSS solution. By this, values of at most 35 µV K^{-1} were obtained for EMIM DCA[201] or 31 µV K^{-1} for 1-butyl-3-methylimidazolium bromide (BMIM Br).[45] In comparison to this, the here performed EMIM DCA post-treatment approach appears to be more effective.

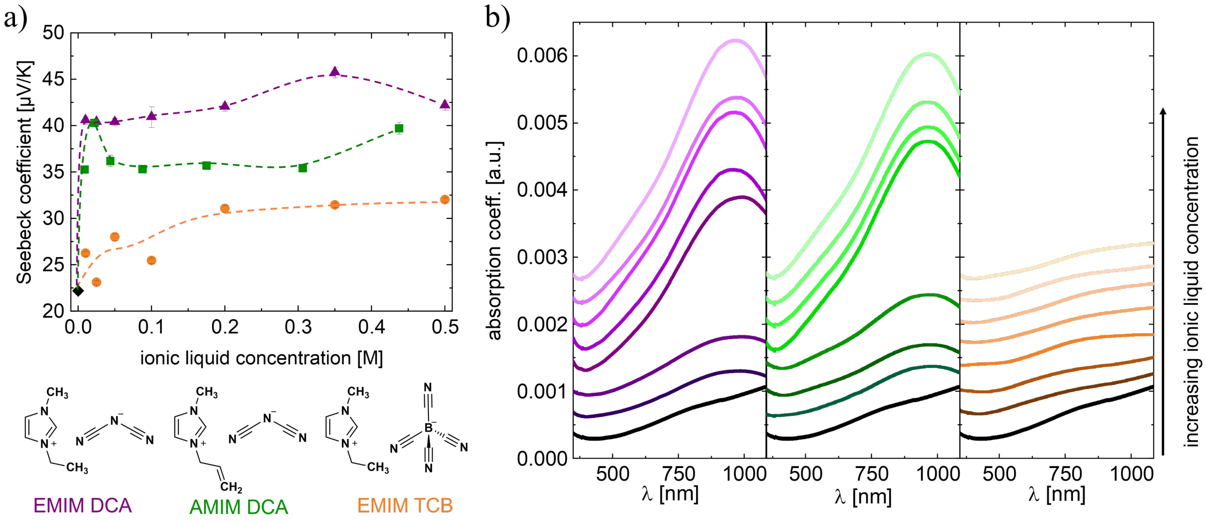

Figure 5.1 ILs post-treatment effect on the oxidation level of PEDOT:PSS. a) Seebeck coefficient and b) UV-Vis spectra of PEDOT:PSS thin films post-treated with solutions of varying IL concentrations in THF. The bottom row in a) shows the chemical structures of the used ILs. EMIM DCA (purple triangles; 0.01, 0.025, 0.05, 0.1, 0.2, 0.35 & 0.5 M), AMIM DCA (green squares; 0.0087, 0.0218, 0.0437, 0.0874, 0.1747, 0.305 & 0.437 M), EMIM TCB (orange circles; 0.01, 0.025, 0.05, 0.1, 0.2, 0.35 & 0.5 M) and the reference sample PEDOT:PSS post-treated with pure THF (black rhombus). In a), the colored dashed lines act as guides to the eye for the Seebeck coefficients. Furthermore, the UV-Vis spectra in b) are presented from bottom to top with respectively increasing IL concentrations, illustrated by gradually lighter colors, and are shifted vertically for sake of clarity. Adapted with permission from Wiley-VCH GmbH, Copyright 2021.[163]

As mentioned in Section 2.2.3, the Seebeck coefficient was reported to have an inverse dependence on the charge carrier concentration of the TE materials.[12, 112, 203, 204] Depending on its oxidation level, the PEDOT polymer backbone can exist as a neutral chain, can contain radical cation charge carriers (i.e. polarons), or can contain dication charge carriers (i.e. bipolarons), more detailed in Section 2.1.3.[16, 41] The presence of these different charge carrier states can be investigated with UV-Vis measurements, as each of them refers to different excitation energy of PEDOT, schematically depicted in Figure 2.6. Therefore, to investigate the effect of the IL post-treatment on the doping level of the PEDOT:PSS films, UV-Vis spectroscopy measurements for all thin films were performed, shown in Figure 5.1b. Based on how PEDOT is synthesized by electrochemical or chemical oxidative polymerization, followed by an electrostatic stabilization of the hereby produced positive charges, due to the addition of the negatively charged counterpart PSS.

The pristine PEDOT:PSS is expected to already possess a high bipolaron concentration. In fact, looking at the absorption curve for the reference sample (bottom black curves in Figure 5.1b), no strong absorption peaks within the measured wavelength range of 280-1100 nm can be observed. However, the absorption seems to grow significantly at wavelengths above 1100 nm, which indicates the beginning of the absorption band attributed to bipolaronic and band states.[27, 41] For the UV-Vis spectra of the EMIM DCA post-treated PEDOT:PSS films (purple; Figure 5.1b), it can be seen that with increasing concentrations of the IL, indicated by gradually lighter colors, the spectra are changing. Already at the lowest EMIM DCA concentration of 0.01 M the emergence of an absorption peak at around 900 nm is observed, which originates from the formation of polaronic states. These polaronic states are formed at the detriment of bipolaronic charge carriers due to a reduction of the PEDOT chain.[41] With increasing EMIM DCA concentrations this peak becomes more pronounced. Moreover, at higher EMIM DCA concentrations (e.g. 0.2 M) a weak absorption band appears at around 600 nm, which arises from the formation of neutral states, i.e. a further reduction of PEDOT. For the PEDOT:PSS thin films post-treated with the IL AMIM DCA (green; Figure 5.1b), similar UV-Vis absorption spectra can be observed. Namely strongly growing absorption bands arising around 900 nm upon the post-treatment with increasing AMIM DCA concentrations, as well as the appearance of weak bands at around 600 nm. It indicates that for this IL the reduction of PEDOT also occurs, which contributes to a transformation of bipolaronic to polaronic and even neutral states. In contrast to EMIM DCA and AMIM DCA, only minor changes are observable in the UV-Vis absorption spectra for PEDOT:PSS thin films post-treated with the

IL EMIM TCB (orange; Figure 5.1b). No noticeable changes are detected for the two lowest EMIM TCB concentrations. With concentrations > 0.025 M the spectra towards the bipolaronic absorption band (at > 1100 nm) seem to flatten and the formation of a slight polaronic absorption peak at around 900 nm is found. This finding indicates that the IL EMIM TCB does cause a not as strong reduction of the PEDOT chain.

For the reduction of the charge carrier concentration and the increase in the Seebeck coefficient, the IL anions are responsible, as during the post-treatment process they react, due to their basicity, with the positively charged PEDOT chains.[100, 201] This also fits well with the observation that the post-treatments with EMIM DCA and AMIM DCA show the most pronounced effects, as both ILs contain the strong basic dicyanamide anion, with a highly localized negative charge. Whereas the tetracyanoborate anion in EMIM TCB has a lower basicity[205], a weaker localized negative charge and is also larger and more sterically hindered than the DCA anion. Therefore, explaining its less pronounced reducing effect on PEDOT and thus the just minor increase of Seebeck coefficients.

As introduced in Section 2.2.4, when measuring the Seebeck coefficient of IL post-treated PEDOT:PSS films the contribution of the so called Soret effect, which describes the thermo-diffusion of particles, must be considered.[120] When the IL ions diffuse into the PEDOT:PSS a mixed ionic-electronic conductor (MIEC) is formed. This means that upon application of a temperature gradient, both holes and IL cations can diffuse and accumulate at the cold side, leading to an electronic and ionic Seebeck coefficient.[124, 206] Though, as reported by Wang et al., this ionic contribution to S for MIECs is only short-term in the very beginning and decreases after a few 100 s due to the incapacity of the ions to pass through the external circuit.[119] Therefore, the Seebeck coefficient measurements in this thesis were designed to contain an initial heating up phase and an additional waiting time. With that the short-term ionic influence on S has already leveled out before starting the data collection and only the stable electronic Seebeck coefficient is measured, as exemplarily shown in Figure 5.2.

However, an additional possible enhancement of the Seebeck coefficient can arise from an energy filtering caused by a layer of ionic conductor, here ILs, on top of the PEDOT:PSS film.[207] Like Guan et al.[208] and Fan et al.[209] explained, a S enhancement could be caused by the generation of potential barriers for the hole transport, filtering the charge carriers with low energy and therefore increasing the electronic Seebeck coefficient. In contrast to the samples from Fan et al.[209], however, for the ILs post-treated PEDOT:PSS films in this thesis, the possible ionic conductor layer on the surface is expected to be very thin in relation to the

PEDOT:PSS layer, as the excess IL solution is spun off. Furthermore, as obvious from the UV-Vis data, the occurring dedoping of the PEDOT:PSS alone leads to a considerable enhancement of the Seebeck coefficient. Moreover, as this ionic contribution is known to be most effective at high humidities and the *S* measurements in this investigation were performed at a low relative humidity (RH), not higher than 40 % RH. It is assumed that the contribution of the energy filtering caused by the Soret effect of the ions has a negligible effect on the Seebeck coefficients values measured of these samples.

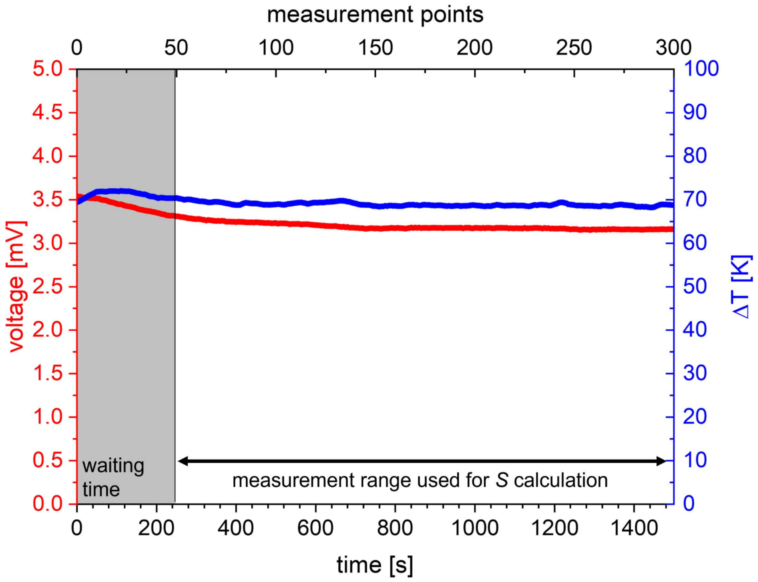

Figure 5.2 Exemplary Seebeck coefficient measurement procedure. Thermovoltage and temperature difference values over the time of Seebeck coefficient measurement of a PEDOT:PSS thin film post-treated with a solution of 0.35 M EMIM DCA in THF. The first 50 measurement points (indicated by grey area) were ruled out in the calculation of the average ***S*** of this sample, to ensure the measurement is performed at equilibrium. Adapted with permission from Wiley-VCH GmbH, Copyright 2021.[163]

5.3 Effect of ILs on the PEDOT:PSS morphology

The influence of IL post-treatment on the conductivity of PEDOT:PSS thin films is shown in Figure 5.3. Indicated by the dashed lines, a strong increase of the conductivities for all three ILs is observed in comparison to the reference sample ($\sigma = 1$ S cm^{-1}). The most pronounced improvement occurs in the EMIM DCA post-treated PEDOT:PSS, where a maximum σ of 1126 S cm^{-1} is achieved at a concentration of 0.35 M. The AMIM DCA post-treated samples reach up to 881 S cm^{-1} at 0.437 M. Although PEDOT:PSS thin films post-treated with EMIM TCB show the lowest σ increase, still a conductivity of 440 S cm^{-1} at the highest IL concentration can be measured. Interestingly, demonstrated for example by Badre et al.[202] and

Kee et al.[200] with a different treatment approach such as directly mixing EMIM TCB into the aqueous PEDOT:PSS solution, film conductivities of above 2000 S cm^{-1} are possible. Nonetheless, compared to literature also investigating the in this study conducted ILs post-treatment approach of PEDOT:PSS, the achieved conductivities are within the norm or even higher. For example, Lou et al. reported σ of around 110 S cm^{-1} for EMIM BF$_4$ post-treatment[44], Yun et al. reached 1038 S cm^{-1} with TFSI post-treatment[210], while post-treatment with EMIM DCA so far lead to σ of up to 900 S cm^{-1}.[100]

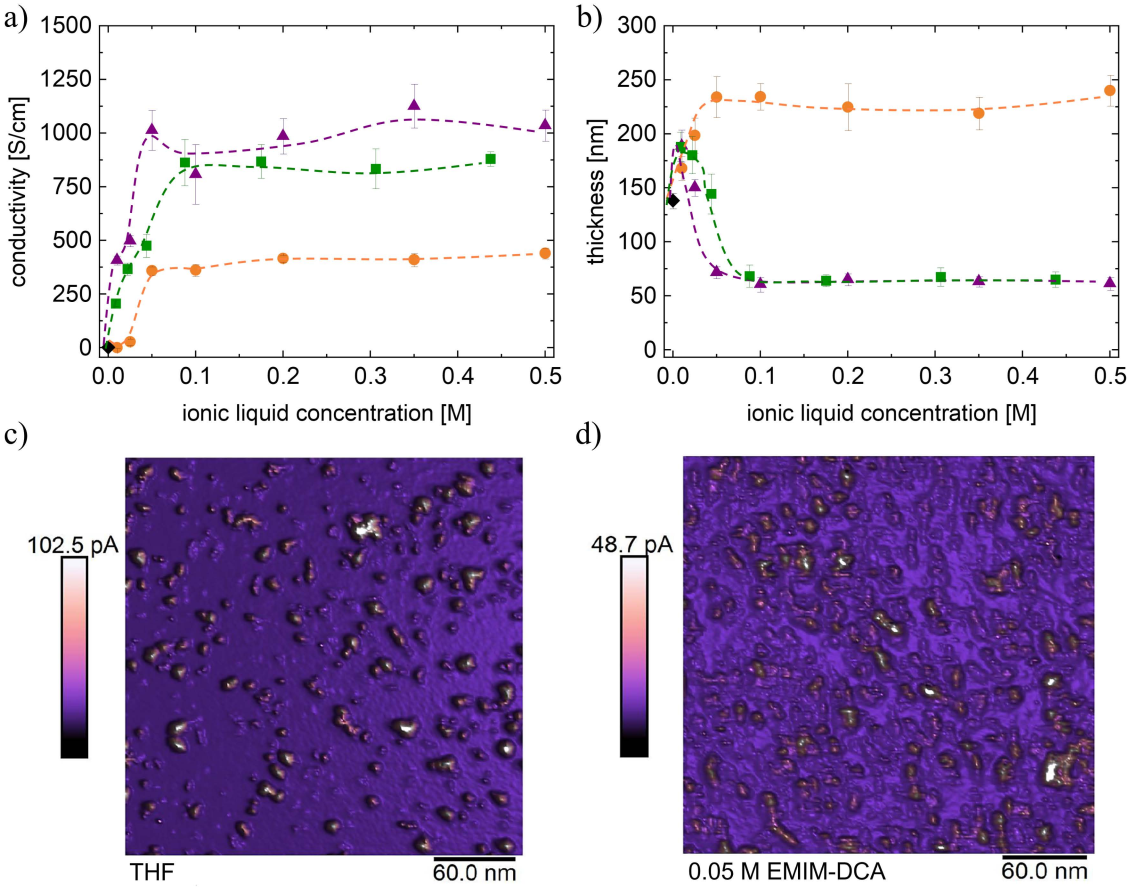

Figure 5.3 ILs post-treatment effect on PEDOT:PSS thin film properties. a) Conductivity and b) film thickness of PEDOT:PSS thin films post-treated with solutions of EMIM DCA (purple triangles), AMIM DCA (green squares), EMIM TCB (orange circles) in THF and pure THF (black rhombus). Colored dashed lines act as guides to the eye. C-AFM images of a PEDOT:PSS thin film post-treated with c) pure THF and with d) a solution of 0.05 M EMIM DCA in THF measured with 300 nm scan range and an applied bias of 200 mV. Adapted with permission from Wiley-VCH GmbH, Copyright 2021.[163]

Known from literature and described in Section 2.1.3, the increase in σ was demonstrated to usually originate from the removal of the non-conductive PSS polymer and conductivity-benefiting morphology changes in the PEDOT:PSS thin films.[24, 44, 91, 95] The film thicknesses of the post-treated PEDOT:PSS films are shown in Figure 5.3b. For EMIM DCA and AMIM

DCA treated films, at small IL concentrations (< 0.05 M) the film thickness increases. However, at higher IL concentrations, a strong decrease in the film thickness results in a value of 60-65 nm, which is about half of the thickness of the reference sample (138 nm). This decrease shows the successful removal of some nonconductive PSS and can be explained as follows: The positively charged IL cations are expected to connect to the partly negatively charged PSS during the post-treatment process. Now by spinning off the excess IL/THF solution, some of the PSS is detached as well. With the reduced amount of insulating PSS matrix around the PEDOT-rich domains, a better inter-domain conductivity can be explained, matching the observed σ trend shown in Figure 5.3a.

Surprisingly, for the post-treatment with the IL EMIM TCB an increase in the film thicknesses up to 240 nm is observed at the highest IL concentration. This permanent increase in the film thickness for EMIM TCB and probably also the initial increase for EMIM DCA and AMIM DCA can probably be explained by the intake of the different IL ions. During the post-treatment step of the PEDOT:PSS thin film, the ILs are expected to diffuse into the polymer film and arrange within the polymer chains. As mentioned before, the cations start interfering with the PSS chains, while the anions interfere with the PEDOT chains, thus accumulating within the PEDOT-rich domains. This additional intake of ions and a probable disruption of the polymer chain ordering could explain the increase in film thickness. Despite spinning off the excess ILs solution and removing a part of the PSS together with the cations, the anions stay inside the film as counterparts for the positively charged PEDOT.

To proof this conjecture and ascertain the presence of the IL ions within the films, FTIR spectra are measured as detailed in Section 3.1.2. The FTIR spectra are presented in Figure 5.4 and overall support the assumption by showing typical FTIR bands for the respective IL anions and IL cations. The black dashed lines in Figure 5.4a indicate the FTIR bands assigned to PEDOT:PSS, namely the C=C aromatic skeletal vibrations at 1570 cm^{-1}, the C=C vibration in the thiophene rings at 1514/1455 cm^{-1}, and at 1170/1114/1060/1035 cm^{-1} showing the sulfonate group of PSS.[211–213] The blue dashed lines in Figure 5.4b indicate the FTIR bands for the C-H vibration in imidazole at 3450/3140/3090 cm^{-1}, showing the existence of the IL cations.[214] The DCA anion is detectable in Figure 5.4c, by the FTIR bands dedicated to the C≡N stretching in the DCA anion (for AMIM DCA and EMIM DCA treated samples) at 2245/2195/2130 cm^{-1}, highlighted with red dashed lines.[214] Furthermore, the shift of the symmetric stretching vibration of $–SO_3^-$, observable in Figure 5.4c, from 1060 cm^{-1} for the reference sample (black dashed line), to 1067 cm^{-1} (EMIM TCB, orange dashed line), 1068 cm^{-1} (EMIM DCA, purple dashed line) and 1070 cm^{-1} (AMIM DCA, green dashed line), respectively, shows the electrostatic interaction of PSS with the IL cations.[215]

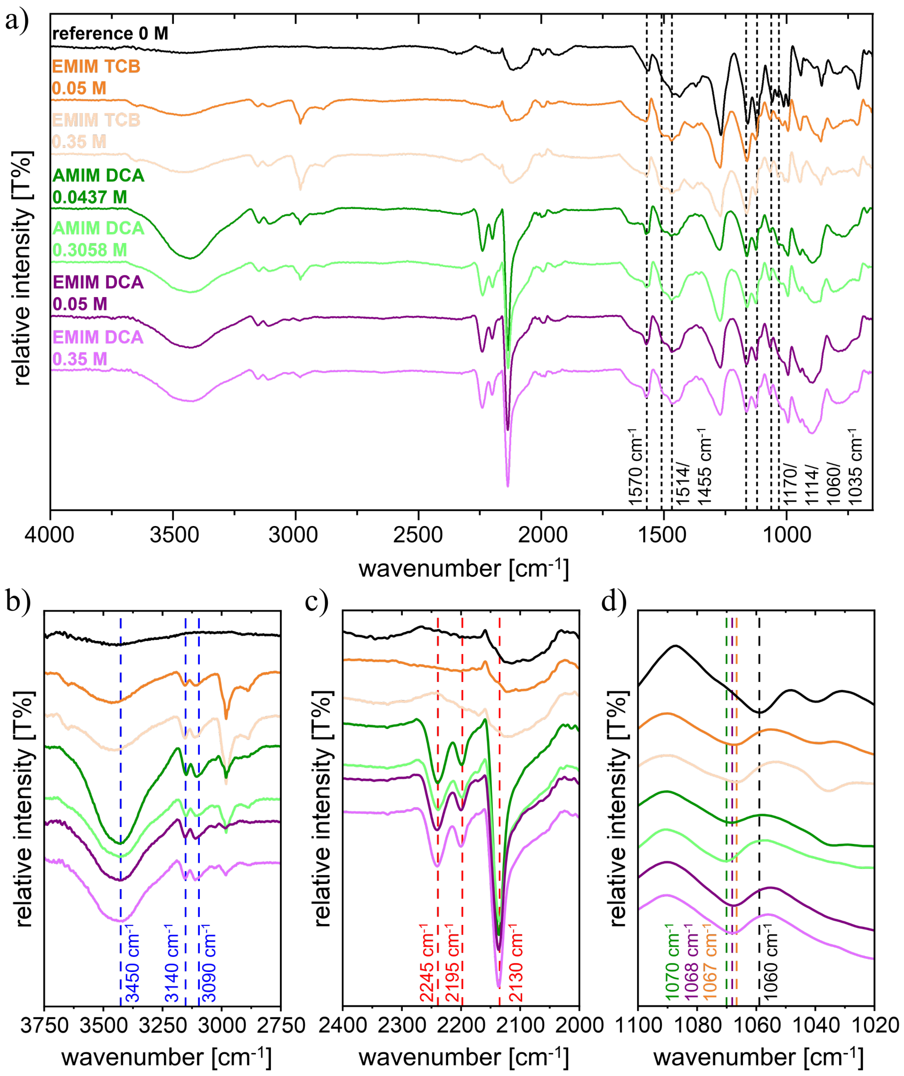

Figure 5.4 ATR-FTIR spectra of IL post-treated PEDOT:PSS films. ATR-FTIR spectra of PEDOT:PSS thin films post-treated with solutions of different concentrated ILs in THF; 0 M reference sample (black), 0.05 M EMIM TCB (orange), 0.35 M EMIM TCB (light orange), 0.0437 M AMIM DCA (green), 0.3058 M AMIM DCA (light green), 0.05 M EMIM DCA (purple) and 0.35 M EMIM DCA (light purple). a) Spectra of the entire measurement range 4000-650 cm^{-1}. Close-up spectra of the wave number range b) of 3750-2750 cm^{-1}, c) of 2400-2000 cm^{-1}, and d) of 1100-1020 cm^{-1}. Adapted with permission from Wiley-VCH GmbH, Copyright 2021.[163]

Interestingly, for EMIM DCA and AMIM DCA the overall film thickness decreases again at increasing ILs concentrations, as apparent in Figure 5.3b, which is explainable by the surpassing of the PSS removal over the thickness gain from ion intake. In contrast to that, for the IL EMIM TCB, the thickness growth effect from the ion intake is expected to be larger, as the ions themselves are bigger than compared to other ILs. Besides, the higher steric hindrance of these ions is also stronger, leading to a weaker diffusion into the polymer film, which could cause a reduced removal of PSS and thus explains the observed lack of thickness decrease upon treatment with EMIM TCB.

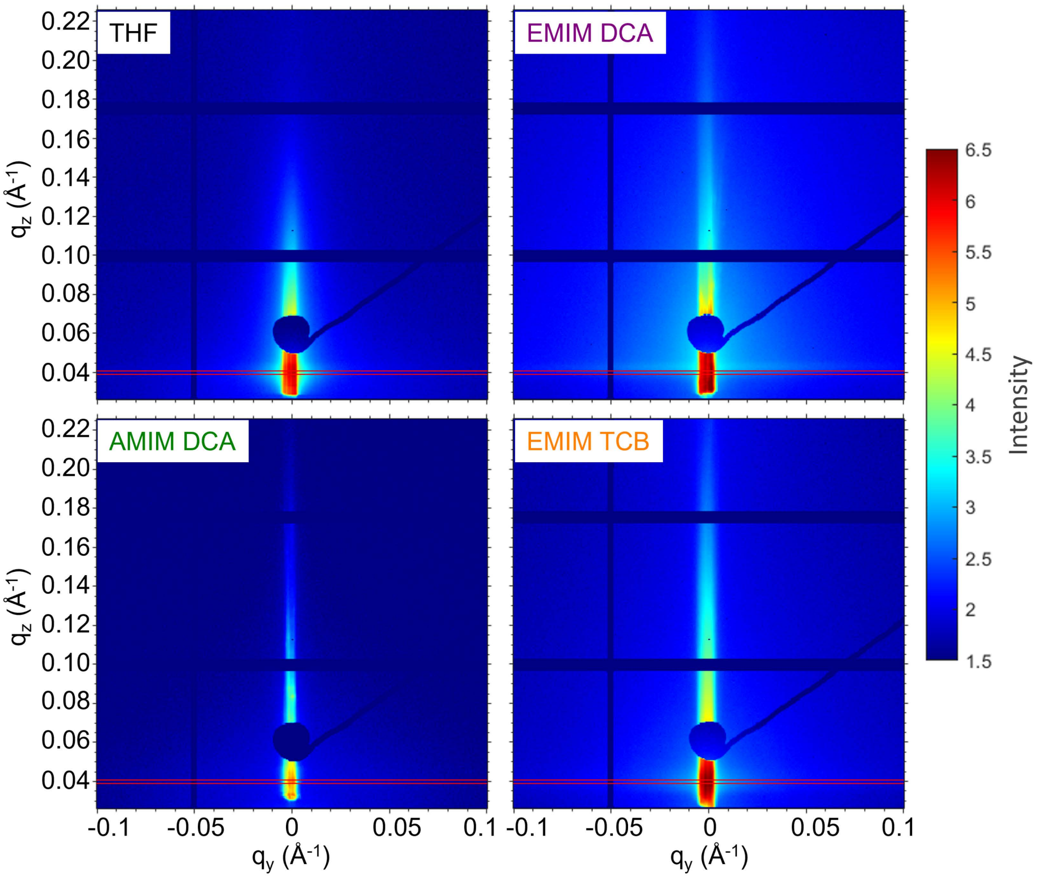

Figure 5.5 Exemplary 2D GISAXS data of IL post-treated PEDOT:PSS films. Exemplary 2D GISAXS data of PEDOT:PSS thin films post-treated with pure THF, 0.35 M EMIM DCA in THF, 0.3058 M AMIM DCA in THF, and 0.35 M EMIM TCB in THF. The red lines mark the position where the horizontal line cuts were taken, corresponding to the Yoneda region of PEDOT. Adapted with permission from Wiley-VCH GmbH, Copyright 2021.[163]

To get a more detailed understanding of the morphological changes induced by the IL post-treatment and to visualize the PSS removal, additional conductive AFM (c-AFM) measurements are performed, as detailed in Section 3.3.2. For the reference sample, PEDOT:PSS treated with pure THF, shown in Figure 5.3c, and for the PEDOT:PSS thin film treated with 0.05 M EMIM DCA, shown in Figure 5.3d. Comparing both c-AFM images, the removal of non-conductive PSS can be directly recognized, as for the EMIM DCA treated film more conductive domains on the film surface are observable, whereas for the reference sample larger low conductive areas are visible. Interestingly, the conductive domains themselves appear less conductive for the IL post-treated film compared to the reference sample. This decrease in conductivity is attributed to the in Section 5.2 discussed reduction of the charge carrier concentration of the PEDOT chains, caused by the IL post-treatment. Moreover, a change from a face-on to a more edge-on PEDOT stacking direction was reported upon EMIM DCA post-treatment by Saxena et al.[100] Such change in the orientation of the crystalline PEDOT domains can give rise to a lower conductivity in the c-AFM measurements since c-AFM measures the conductivity in the out-of-plane direction.

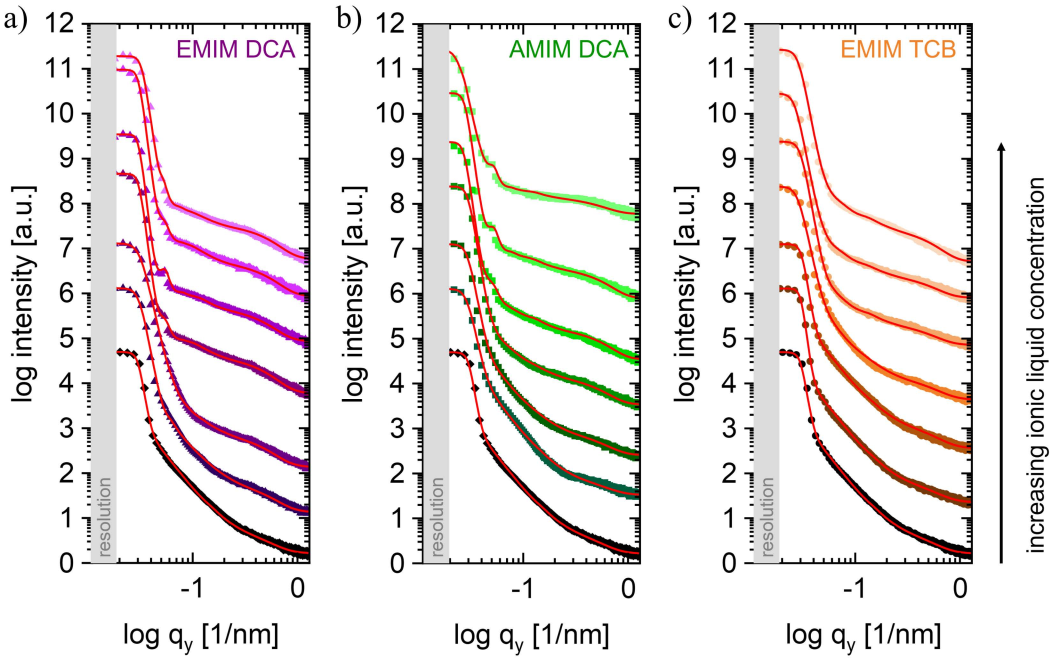

Figure 5.6 Horizontal line cuts of IL post-treated PEDOT:PSS films. Horizontal line cuts together with their fits (red lines) from 2D GISAXS data of PEDOT:PSS thin films post-treated with solutions of EMIM DCA (purple triangles, left), AMIM DCA (green squares, middle), and EMIM TCB (orange circles, right) in THF. The cuts from bottom to top are with increasing IL concentrations, shown by gradually lighter colors, and are shifted along the y-axis for the sake of clarity. The respective lowest line cuts (rhombus black) are the data of the reference sample PEDOT:PSS treated with pure THF. Adapted with permission from Wiley-VCH GmbH, Copyright 2021.[163]

However, as c-AFM measurements are limited to a small local sampling area and provide only the surface information, the inner PEDOT:PSS thin film morphology is probed with GISAXS. This method is introduced in Section 2.3, explaining that due to the grazing-incidence geometry, statistically significant morphology information is accessible with GISAXS.[144] A detailed description of the GISAXS measurement parameters and the data modeling procedure is provided in Section 3.4.2. Exemplary 2D GISAXS images of selected samples are provided in Figure 5.5, with the red lines indicating the position where the horizontal line cuts are performed at the Yoneda region of PEDOT. The resulting horizontal line cuts of all the ILs post-treated PEDOT:PSS thin films are shown in Figure 5.6, with their model fits for further analysis.

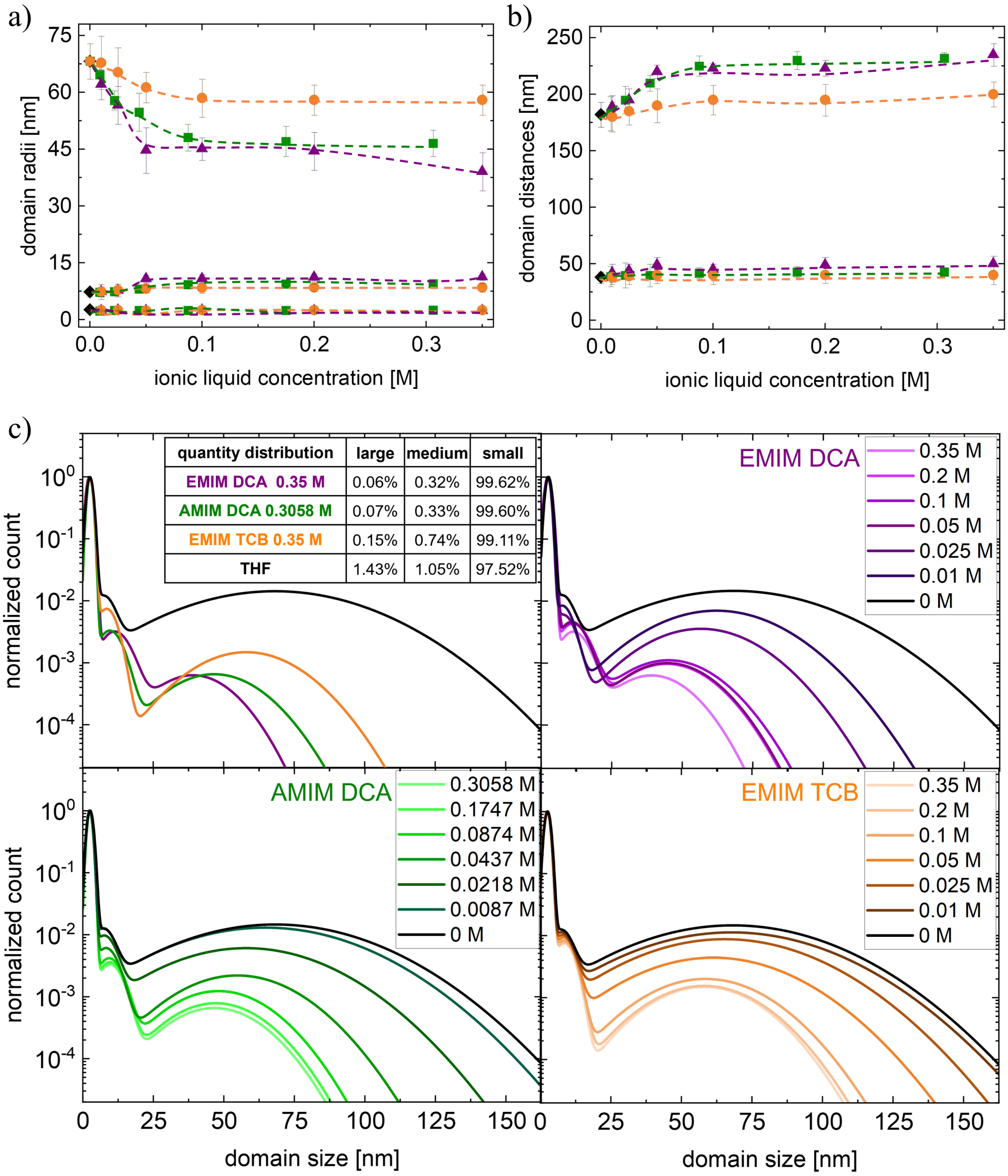

quantity distribution	large	medium	small
EMIM DCA 0.35 M	0.06%	0.32%	99.62%
AMIM DCA 0.3058 M	0.07%	0.33%	99.60%
EMIM TCB 0.35 M	0.15%	0.74%	99.11%
THF	1.43%	1.05%	97.52%

Figure 5.7 ILs post-treatment effect on the inner morphology of PEDOT:PSS films. Film morphology in terms of a) structure domain radii, b) domain distances and c) domain size distribution of PEDOT domains in PEDOT:PSS thin films post-treated with different concentrations of EMIM DCA (purple triangles), AMIM DCA (green squares), EMIM TCB (orange circles) dispersed in THF. As a reference, the data of a PEDOT:PSS thin film post-treated with pure THF (black rhombus) are shown. In a) and b) the colored dashed lines serve as guides to the eye. Adapted with permission from Wiley-VCH GmbH, Copyright 2021.[163]

For modeling of the horizontal line cuts, detailed in Section 3.4.2, three different form factors can be distinguished with the associated domain radii plotted in Figure 5.7a: Large PEDOT domains with radii r_l > 30 nm, medium PEDOT domains with radii r_m = 7-10 nm, and small PEDOT domains with radii r_s = 2-3 nm. The used model also reveals structure factors related to the large and medium-sized PEDOT domains with respective domain center-to-center distances (D_l and D_m) shown in Figure 5.7b. For the small-sized domains, no reliable structure factors could be obtained. Looking at the PEDOT domain radii, upon IL post-treatment a strong shrinkage of the large domains and a small increase of medium-sized domains is observable, while the small domains remain constant in size. Again, EMIM DCA shows the most pronounced effect with a decrease of the large PEDOT domain radius from 68 nm to 39 nm and an increase of the medium PEDOT domain radius up to 11 nm, as compared to the reference sample with 7 nm. AMIM DCA shows a shrinkage of 22 nm of the large, and a growth of 2 nm of the medium domain radii. The weakest effects are observable for EMIM TCB post-treatment and can again be dedicated to the more sterically hindered ions mentioned before. Indicated by dashed lines in Figure 5.7b, additionally a significant increase of the center-to-center distances between the large PEDOT domains is recognizable upon IL post-treatment, which is most considerable again for EMIM DCA and AMIM DCA. This observation means that these large PEDOT-rich domains not only shrink in size, but are on average also further apart from each other, which thus suggests their disintegration. For the medium-sized domains, an increase in the domain distances is also recognized, indicating a decrease in their number, though with a small growth in size.

However, implied by the increase in conductivity and the presumption of PSS removal, at first glance a heightened amount of PEDOT domains would be expected rather than a diminishment. Unfortunately, it was not possible to reliably model the structure factor for the small-sized PEDOT domains from GISAXS data, which would provide the distances for small-sized domains. Nevertheless, as these small domain structures are expected to matter and explain the promotion in the film conductivity, a calculation of the domain size distribution for the IL post-treated PEDOT:PSS thin films was conducted and is presented in Figure 5.7c. This domain size distribution allows for a closer investigation of these small domain structures, and a verification of the disintegration of the large and medium PEDOT domains. The details of this calculations are provided in Section 3.4.2, and the resulting respective quantity distributions ($N_{l,m,s}$), meaning the share of the large, medium, and small domains, are listed in Table 5.1.

Table 5.1 Quantity distribution of PEDOT domains upon IL treatment. Quantity distribution of large, medium, and small PEDOT domains $N_{l,m,s}$ within PEDOT:PSS thin films, dependent on the concentration of the respective ionic liquids, EMIM DCA (purple), AMIM DCA (green), and EMIM TCB (orange), compared to the reference THF sample.

	concentration	quantity distribution [%] N_l	N_m	N_s
EMIM DCA	0.35 M	0.06	0.32	99.62
	0.2 M	0.10	0.42	99.48
	0.1 M	0.11	0.43	99.46
	0.05 M	0.10	0.46	99.45
	0.025 M	0.35	0.59	99.06
	0.01 M	0.69	0.81	98.50
AMIM DCA	0.3058 M	0.07	0.33	99.60
	0.1747 M	0.08	0.36	99.57
	0.0874 M	0.12	0.41	99.47
	0.0437 M	0.22	0.60	99.19
	0.0218 M	0.60	0.88	98.52
	0.0087 M	1.27	1.07	97.66
EMIM TCB	0.35 M	0.15	0.74	99.11
	0.2 M	0.15	0.76	99.09
	0.1 M	0.20	0.83	98.98
	0.05 M	0.43	0.89	98.68
	0.025 M	0.86	0.92	98.22
	0.01 M	1.10	0.98	97.92
THF	0 M	1.43	1.05	97.52

From Figure 5.7c (top right, bottom right and bottom left) and Table 5.1, the following general trend upon IL post-treatment is clearly visible: The large PEDOT domains decrease in size and number; the medium-sized PEDOT domains grow a little in size but decrease in number; whereas the small domains stay constant in size but increase strongly in number. To sum this up, the IL post-treatment leads to a morphological rearrangement towards finer distributed PEDOT domains, with overall reduced domain-domain distances. Since in such films less insulating PSS matrix is separating the conductive PEDOT domains, the charge transport between these conductive PEDOT grains is facilitated. From literature it is known for other PEDOT:PSS morphology changing methods, for example with acid[15, 30] or polar solvents[23, 24, 53, 216–219], that this kind of morphological restructuring and enhancement in the "inter-grain" or "inter-domain" charge transport, leads to an increase in the charge carrier mobility (μ). As introduced in Section 2.2.3, the charge carrier mobility is directly related to the electrical conductivity by $\sigma = n_q e \mu$, as introduced in Section 2.2.3, with e being the elementary charge and n_q being the carrier density.[34] Therefore, the selective removal of PSS with ILs post-treatment and the thus improved inter-domain charge transport due to denser packed conductive PEDOT domains, explains the observed increase in film conductivity.

This general morphological change can be recognized for all three tested ILs. However, as the direct comparison of the respective domain size distributions in Figure 5.7c (top left graph) shows, again the strongest effect can be observed for EMIM DCA, second strongest for AMIM DCA, and third strongest for EMIM TCB.

5.4 Model description of IL post-treatment effect

The with S and σ calculated thermoelectric power factor $PF = S^2\sigma$ for all investigated samples is plotted in Figure 5.8. Elucidated by the dashed lines, for all tested ILs an increase in the PF is observed with increasing IL concentration. The strongest increase is clearly visible for EMIM DCA post-treatment, where a PF of 236 µW $m^{-1}K^{-2}$ is achieved for the 0.35 M concentration. For 0.437 M AMIM DCA, a power factor of 139 µW $m^{-1}K^{-2}$ is reached, and the EMIM TCB treatment with a concentration of 0.5 M gives rise to a maximum PF of 45 µW $m^{-1}K^{-2}$; which is still an immense improvement compared to the not IL treated reference sample (PF = 0.07 µW $m^{-1}K^{-2}$). These findings that the treatment of PEDOT:PSS with EMIM DCA shows stronger PF improvements compared to other ILs, are in good accordance with previous reports. For example, Saxena et al. investigated the post-treatment of PEDOT:PSS with EMIM DCA, EMIM TCB and EMIM BF_4 and obtained a maximum PF of 167 µW $m^{-1}K^{-2}$ for the IL EMIM DCA.[100] Nevertheless, the here reached power factor of 236 µW $m^{-1}K^{-2}$ (0.35 M EMIM DCA) is among the highest reported PF obtained for the IL post-treatment approach on PEDOT:PSS. Higher PFs like shown by Fan et al. reaching 754 µW $m^{-1}K^{-2}$, so far seem only possible via a combination of IL treatment with other preceding methods such as acid and base treatments.[209]

The in this thesis observed huge positive effect of IL post-treatment on the thermoelectric properties of PEDOT:PSS thin films, results from the combined doping level and morphological changes enabled by the special ionic composition of the ILs. For a better understanding of the results, Figure 5.8b illustrates the molecular structures of the PEDOT and PSS polymer chains. It also schematically pictures how these chains arrange within the aqueous PEDOT:PSS solution, forming the typical PEDOT-rich-core PSS-shell like structure, as introduced in Section 2.1.2. By spin-coating this aqueous PEDOT:PSS solution and allowing the water solvent to evaporate, a related pattern remains in the dry film's inner morphology with PEDOT-rich domains (blue spots) embedded in a PSS matrix (grey area) as visualized in the sketch of Figure 5.8c.

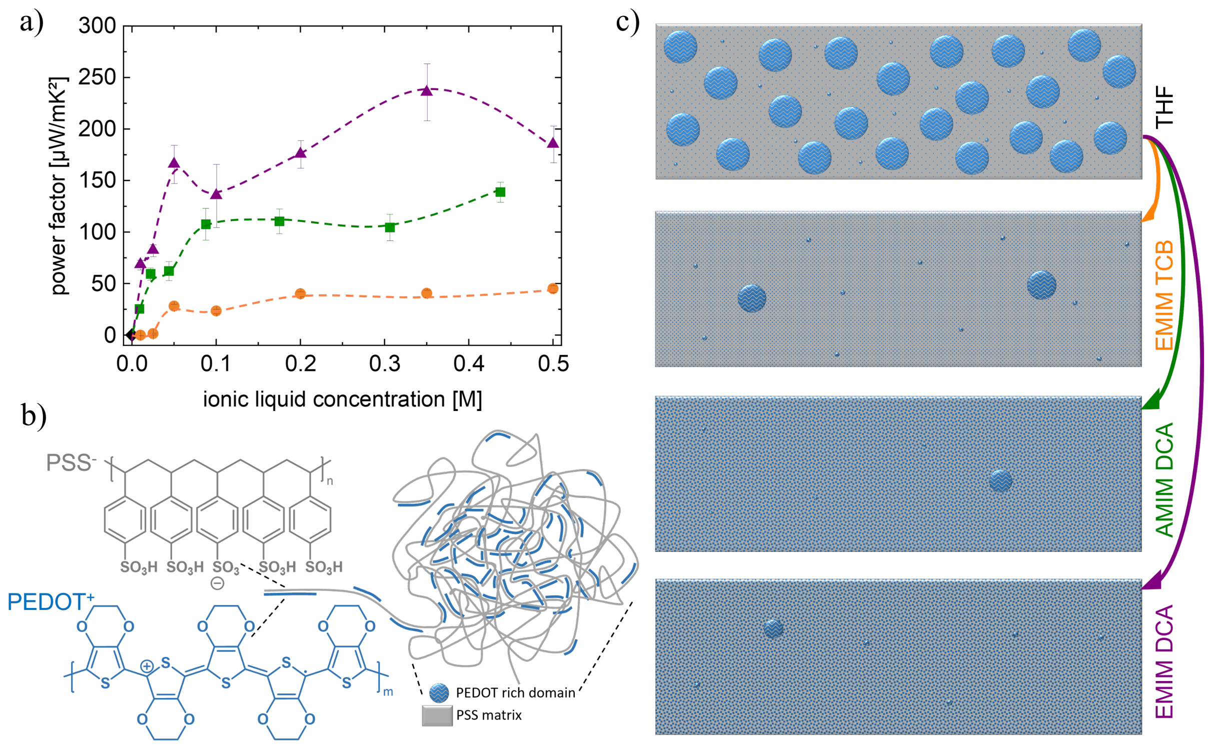

Figure 5.8 Model description of the IL doping effect on PEDOT:PSS films. a) Concentration-dependent power factor of PEDOT:PSS thin films post-treated with the ILs EMIM DCA (purple triangles), AMIM DCA (green squares), EMIM TCB (orange circles) dispersed in THF and treated with pure THF as reference (black rhombus). Colored dashed lines serve as guides to the eye. b) Schematic illustration of the molecular structure of PEDOT and PSS shown together with the sketch of the polymer blend structure inside the PEDOT:PSS thin film, with PEDOT-rich domains embedded in a PSS matrix. c) Schematic illustration of the morphological and doping level changes of the PEDOT:PSS domain structure, induced by the IL post-treatment with EMIM TCB (second from top), AMIM DCA (third from top) and EMIM DCA (fourth from top), shown in comparison to the reference sample (top). All domain size parameter and quantity ratios are in accordance with the results from the GISAXS investigation. The bluish shifted color of the PEDOT-rich domains from light to dark blue indicates the with UV-Vis observed reduction of the PEDOT chains and with this the decrease of charge carrier concentration. Adapted with permission from Wiley-VCH GmbH, Copyright 2021.[163]

In the case of the reference sample, a high number of large PEDOT-rich domains exist together with a few medium-sized domains, and some small-sized domains. The light blue color of these domains indicates the initial high charge carrier concentration within the PEDOT chain. Upon post-treatment with the ILs EMIM TCB, AMIM DCA, or EMIM DCA, depicted from top to bottom in Figure 5.8c, a respectively pronounced diminishing of the large PEDOT domains and a strong increase in the number of smaller domains is observed. In addition to these results, a previous GIWAXS study by Saxena et al.[100] demonstrated that a post-treatment of

PEDOT:PSS with the ILs, EMIM DCA and EMIM TCB, resulted in a decrease of the π-π-stacking distances and a preferred edge-on orientation. Therefore, it is presumed that due to the IL cations caused PSS removal an overall finer and denser packed PEDOT domain morphology appears, yielding an improved conductivity of the PEDOT:PSS film. Furthermore, indicated by the darker blue color of the PEDOT-rich domains, the charge carrier concentration simultaneously decreases, induced by the IL anion interaction with the PEDOT chain, which leads to an increase of the Seebeck coefficients. Like this, the special composition of concurrent reacting IL cation and IL anion allows for the improvement of both TE parameters σ and S. In this thesis, it was found that the most pronounced effects can be achieved for post-treatment with ILs that contain small, sterically unhindered ions with a strong localized charge. However, even though the increase in conductivity is mainly dedicated to the morphological change and the increase in the Seebeck coefficient is mainly dedicated to the doping level change; it is important to mention that a completely clear separation between both observed effects cannot be made. As σ and S are physically connected, they always indirectly affect each other, as described in Section 2.2.3.

5.5 Film-aging investigation

Additionally, for possible future applications of PEDOT:PSS thin films as TE materials, it is important to get an understanding of the long-term air stability of these samples. Therefore, the reference sample and PEDOT:PSS samples post-treated with two different concentrations of the respective ILs, were measured again after a storage time of 22 months at ambient room conditions. The results of the aged samples are compared with the values of the freshly prepared samples in Figure 5.9.

Summarizing the results, for all samples a decrease in electrical conductivity, Seebeck coefficient and power factor, is detected, while for most samples (except the ones post-treated with EMIM TCB) an increase in film thickness is observable. From literature it is known that this observed loss in the TE performance of treated PEDOT:PSS samples can have different reasons. For example, while being stored at ambient room conditions, aging of the samples can be induced by potentially detrimental influences of e.g. oxygen, moisture, light or impurities, while being stored at ambient room conditions.[179, 201, 220–222] However, a detailed study of the aging mechanisms and influences of ambient conditions in IL post-treated PEDOT:PSS thin films is beyond the scope of the work in this chapter, however, it will be focus of the investigations presented in the following Chapter 6, 7, and 8. Nevertheless, even after almost two years of storage time, the IL post-treated PEDOT:PSS thin films examined in this thesis, still show > 62 % of the initial electrical conductivity and between 56-76 % of the initial Seebeck coefficient. Therefore, presenting quite reasonable long-term stabilities under ambient room conditions.

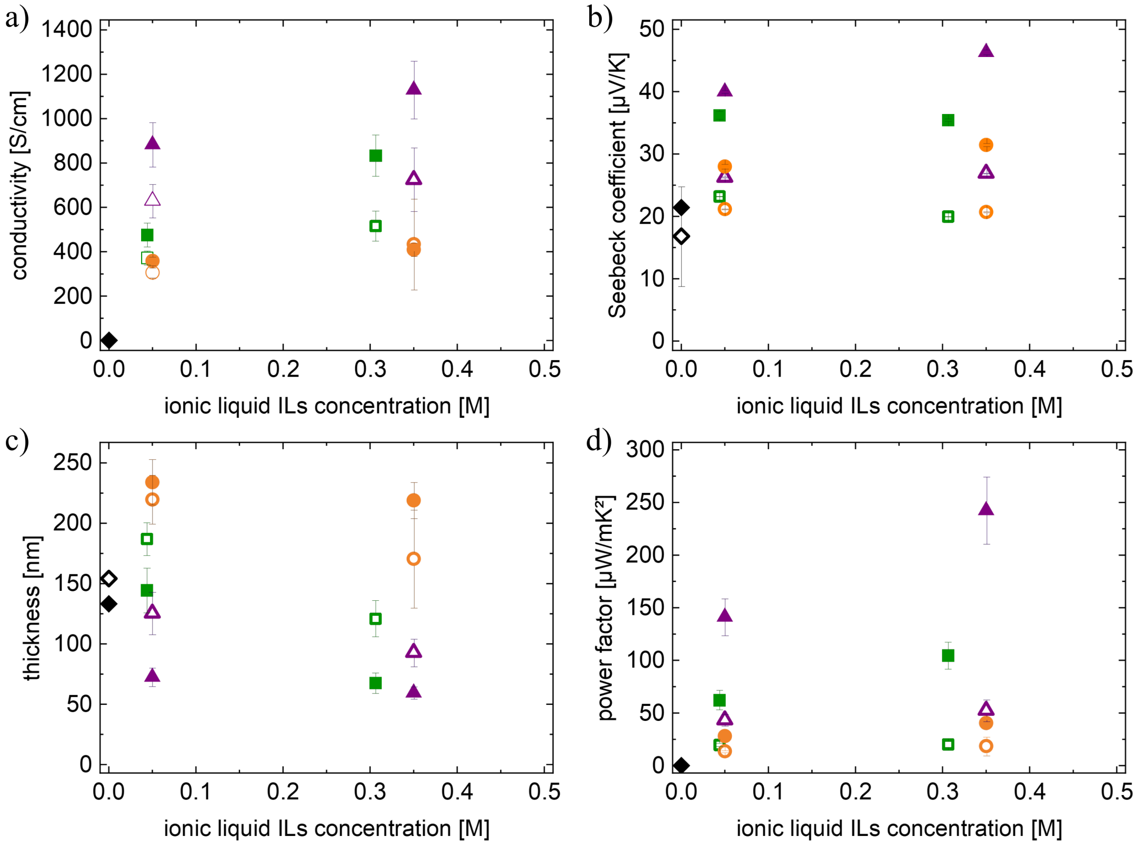

Figure 5.9 Aging investigation of IL post-treated PEDOT:PSS films. a) Conductivity, b) Seebeck coefficient, c) power factor and d) film thickness of PEDOT:PSS thin films post-treated with solutions of EMIM DCA (purple triangles), AMIM DCA (green squares), EMIM TCB (orange circles) in THF and pure THF (black rhombus). Full symbols present the values measured for the freshly prepared samples; hollow symbols show the values of the samples measured after being stored for 22 months at ambient room conditions (20-23 °C and 40-60 % RH). Adapted with permission from Wiley-VCH GmbH, Copyright 2021.[163]

5.6 Summary

It can be concluded that post-treatment of PEDOT:PSS thin films with ILs simultaneously affects the doping level and morphological features, and strongly enhances the thermoelectric properties. On the one hand, the work presented in this chapter has shown that the interaction of the IL anions leads to a decrease in the charge carrier concentration of the conductive polymer PEDOT, and thus result in a strong increase of the Seebeck coefficients. On the other hand, the investigation has proven that an IL post-treatment causes a rearrangement of the PEDOT:PSS film morphology towards smaller and more densely packed PEDOT-rich domains. Hereby, the formation of this fine domain distribution is assigned to the removal of non-conductive excess PSS, by the interaction with IL cations, which leads to an improved inter-domain conductivity and thus an overall increased film conductivity. Furthermore, evidenced by studies of the doping level and by inner film morphological investigations, a model sketch of the synergetic effects of IL anion and cation on the PEDOT:PSS thin films is presented. This model also reveals the influence of the IL ions characteristics, like basicity, charge localization, and steric hindrance, on the optimization potential of thermoelectric properties. This presented study on the IL post-treatment approach, not only demonstrates an approach to reach power factors of up to 236 μW $m^{-1}K^{-2}$, but also it provides a substantial contribution for future research on boosting the thermoelectric performance of PEDOT:PSS films, by suggesting criteria for the ILs selection: Beneficial are ILs that contain small, sterically unhindered ions with a strong localized charge.

6 Temperature influence on ionic liquid post-treated PEDOT:PSS films

> This chapter is based on the publication "*In Situ Observation of Morphological and Oxidation Level Degradation Processes within Ionic Liquid Post-treated PEDOT:PSS Thin Films upon Operation at High Temperatures*" (A. L. Oechsle, J. E. Heger, N. Li, S. Yin, S. Bernstorff, P. Müller-Buschbaum, ACS Applied Materials & Interfaces 2022, 14, 27, 30802-30811; DOI: 10.1021/acsami.2c05745). Reprinted with permission from Oechsle et al.[50] Copyright 2022 American Chemical Society. Experiments were performed in collaboration with the bachelor student Andreas Steinhart.

In this chapter, organic thermoelectric thin films are investigated in terms of their stability at elevated operation temperatures. For this, the electrical conductivity of PEDOT:PSS thin films post-treated with different EMIM DCA concentrations is measured for 4.5 h while heating the films at 50 °C or 100 °C. The changes in the electrical performance are correlated with changes in the film morphology, evidenced by *in situ* GISAXS. It is shown that due to overall increased PEDOT domain distances, the resulting impairment of the inter-domain charge carrier transport can be directly correlated with the observed electrical conductivity decay. With *in situ* UV-Vis measurements, a simultaneously occurring reduction of the PEDOT oxidation level is found to have an additional electrical conductivity lowering contribution due to the decrease of the charge carrier density. Finally, the observed morphology and oxidation level degradation is associated with the deterioration of the thermoelectric properties and hence a favorable operation temperature range is suggested for EMIM DCA post-treated PEDOT:PSS based thermoelectrics.

6.1 In situ temperature investigation of ILs post-treated PEDOT:PSS

Whether in lightweight organic photovoltaics[223–225], flexible organic light-emitting diodes[226–228], organic sensors[229–231], organic field-effect transistors[198, 232–234], transparent organic electrodes[30, 235, 236], or organic thin-film thermoelectrics[8, 10, 11, 118], nowadays organic semiconductors play a fundamental part in the development of new trendsetting devices and applications. The reason for this lies in the advantageous properties of organic semiconductors, like their easy and low-temperature processability from solution, which facilitates a low-cost and energy-efficient film fabrication with large-scale deposition techniques like printing, spray or dip coating.[6, 7] Furthermore, the raw materials are usually abundantly available and enable low or non-toxic, lightweight, and mechanical flexible devices. Besides organic small molecules, like oligothiophenes, fullerene, perylene, or anthracene derivatives, an intense research interest lies in polymer-based organic semiconductors, usually based on polyacetylene, polypyrrole, polyphenylene vinylene, or polythiophene backbones.[237–239] In particular, great attention is paid to the blend PEDOT:PSS, introduced in Section 2.1.2, which comprises the insoluble, however, excellent p-type semiconductor PEDOT, and PSS, a water-soluble partly negative charged polyanion.[16, 17] Besides the before mentioned advantages of organic semiconductors, PEDOT:PSS also exhibits a tunable and potentially high hole conductivity of up to 10^3 S cm^{-1}, which even competes with commonly used transparent electrode materials like indium tin oxide (ITO).[13–15] The key to the easy tunability of its optoelectronic properties lies in the particular polymer blend morphology of PEDOT:PSS.[16, 18, 19] As detailed in Section 2.1.2, in an aqueous solution, the insoluble π-conjugated PEDOT chains agglomerate, forming a PEDOT enriched core, which is surrounded and stabilized by a shell of water-soluble PSS. Upon deposition, the dried PEDOT:PSS thin film forms a morphology of pancake-shaped conductive PEDOT domains embedded in a non-conductive PSS matrix. As a consequence, this insulating PSS matrix forms a barrier for the hole transport between adjacent PEDOT domains, inhibiting the overall electrical conductivity (σ) of the PEDOT:PSS thin film.[20, 21, 34] To overcome this issue, most research concepts focus on the weakening of the electrostatic interaction between the PEDOT and the PSS chains, using various approaches, which consequently allows the removal of excessive PSS, which is described in Section 2.1.3 as secondary doping. For instance, treatments of PEDOT:PSS thin films with acids or bases[30–32], high boiling solvents like ethylene glycol[23–25], or solutions of inorganic salts[27, 28, 31], successfully result in removal of PSS and an increased inter-domain charge carrier transport. An additional way to improve the electrical conductivity of the PEDOT:PSS film is the optimization of its domain morphology via a post-treatment using various solvents, or via the addition of surfactants or polar solvents into the aqueous solution before film deposition.[26, 36, 91, 93] For instance, Gasiorowski et al. achieved conductivities of 966 S cm^{-1} by adding 10% v/v dimethylsulfoxide (DMSO).[240] Further approaches try to combine different treatment methods to increase not only the electrical conductivity but, for example, also the films stretchability with a combined addition of FS-300 Zonyl® and DMSO shown by Dauzon et al.[34]

Since PEDOT:PSS is very promising for the application as an organic thermoelectric material, some research also aims to improve its Seebeck coefficient (S).[8, 10, 199] Successful at simultaneously increasing σ and S is the combination of DMSO and salt treatment[38], or the post-treatment of PEDOT:PSS thin films with ionic liquids (ILs)[46, 48, 49, 100, 210]. Hereby, the IL post-treatment is especially beneficial as with only one treatment step the thermoelectric properties of PEDOT:PSS thin films can be strongly improved. In the study presented in the previous Chapter 5, PEDOT:PSS thin films were post-treated with different ILs in varying concentrations and the resulting effects examined.[100, 163] On the one hand, with investigations of the inner film morphology, it was possible to show the before-mentioned removal of excess PSS and a thereby induced formation of an σ-conducive fine arrangement of small but densely packed PEDOT domains. On the other hand, a doping level change of the PEDOT chains was observed with spectroscopic studies, resulting in a decrease of the charge carrier concentration, which is favorable to the Seebeck coefficient. With this approach, the electrical conductivity could be increased from 1 S cm^{-1} to 1126 S cm^{-1} and the Seebeck coefficient from 22 μV K^{-1} to 46 μV K^{-1} compared to the untreated film.[163]

However, besides the studies concerning the improvement of the optoelectronic properties of PEDOT:PSS thin films, a topic that is rarely investigated and not so well understood to date is the possible degradation of these films under respective operation conditions. When in use as thermoelectric materials, PEDOT:PSS thin films will face high temperatures since a temperature gradient is needed to establish a current flow. Therefore, it is essential to explore their thermal stability and possible temperature-induced degradation processes to verify the applicability and determine usage parameters for a future commercial deployment. To address this issue, in this present study, the thermal stability EMIM DCA post-treated PEDOT:PSS thin films is investigated. This IL was chosen, because EMIM DCA contains small and sterically rather weakly impaired ions, with strongly localized charges, which was found in the previous studies to be beneficial for the optimization of thermoelectric properties.[163] With measurements of the electrical conductivity of the films over the time of heating at elevated temperatures, the extent of thermal degradation dependent on the applied temperature and the EMIM DCA post-treatment concentration is studied. To reveal a possible morphological rearrangement of the PEDOT:PSS domains upon heating, *in situ* GISAXS is performed. Moreover, with *in situ* ultraviolet-visible (UV-Vis) spectroscopy measurements possible simultaneous occurring changes in the oxidation level are examined. Additional measurements of the Seebeck coefficient before and after the heat treatment complement the results. The scope of the work presented in this chapter, is to find a linkage of the thermoelectric properties degradation upon heating, with the changes in the morphological and oxidation level features of EMIM DCA post-treated PEDOT:PSS thin films. With these *in situ* studies, a detailed systematical investigation of the thermal degradation mechanism that is substantial for the applicability of organic thermoelectric devices is provided.

For this study, PEDOT:PSS thin films are prepared and post-treated with varying concentrations of EMIM DCA (0 M as a reference sample, 0.01 M, 0.05 M, and 0.35 M). An extensive description of the PEDOT:PSS film preparation and post-treatment steps, including the used material details, can be found in the Chapter 4. In addition, specifications for the used investigation methods are provided in Chapter 3.

6.2 Evolution of the electrical conductivity

First, the electrical conductivity of the prepared EMIM DCA post-treated PEDOT:PSS thin films is measured over 4.5 h of heating at 100 °C or 50 °C. The respective results are shown in Figure 6.1a, with the greyed-out area marking the heating up process over the first 20 min. For these *in situ* conductivity measurement, the two-point resistance geometry, introduced in Section 3.2.2, was utilized, and the electrical conductivity was determined using the average thicknesses calculated from thicknesses of the respective post-treated thin films before and after heat treatment, as listed in Table 6.1.

In Figure 6.1a, it can be observed that during the heating-up phase, the electrical conductivity of all the EMIM DCA post-treated films first rises a little and then decreases to a different extent. In contrast, the electrical conductivity of the pure THF post-treated reference film steadily rises. This increase might indicate that upon EMIM DCA post-treatment, the type of

Table 6.1 Thin film thicknesses before and after heat treatment. Film thicknesses t_{profil} of EMIM DCA post-treated PEDOT:PSS thin films before and after heating for 4.5 h at 100 °C or 50 °C.

	thickness t_{profil} [nm]	thickness deviation [nm]
0 M	185	± 15
0 M - 100°C	190	± 21
0.01 M	172	± 21
0.01 M - 100°C	166	± 26
0.05 M	66	± 11
0.05 M - 100°C	74	± 18
0.35 M	71	± 10
0.35 M - 100°C	73	± 19
0.05 M	70	± 4
0.05 M - 50°C	87	± 28

primary charge carrier transport is changing from a hopping-like semiconductor behavior to a more band-like metallic charge transport, as introduced in Section 2.1.1.[21] In literature this kind of temperature-dependent charge transport observed for EMIM DCA treated samples, is referred to as fluctuation induced tunneling charge transport.[21]. It could be the result from the rearrangement of the PEDOT:PSS morphology towards smaller and more densely packed PEDOT domains upon IL post-treatments, as shown in the study presented in Chapter 5.[163] Hereby, the formation of closer conductive domains strongly facilitates the inter-domain charge carrier transport and improves the overall electrical conductivity.[21, 93] While, for the untreated PEDOT:PSS thin films, the distances between conductive PEDOT domains are more significant, and the heating enhanced hopping to adjacent energy states for the charge carrier transport is the confining factor here.

However, in this present study, the focus lies on degradation processes happening within post-treated PEDOT:PSS thin films upon the application of a constant, elevated temperature observable in Figure 6.1a between 20 and 270 min of the recorded electrical conductivity evolution. For the 0 M reference sample the electrical conductivity stays nearly constant during the heat treatment at 100 °C. At the same time, the conductivities of 0.01 M, 0.05 M, and 0.35 M EMIM DCA treated samples gradually decrease, more prominent for higher EMIM DCA concentrations. Compared to that, heating a PEDOT:PSS thin film post-treated with 0.05 M EMIM DCA at a constant temperature of 50 °C does not noticeably change the electrical conductivity. Additionally, to ascertain that the electrical conductivity decrease is irreversible, a 0.05 M post-treated PEDOT:PSS thin film is first heated up to 100 °C, kept stable at 100 °C for around 4 h and then cooled down to 30 °C, with the results of the relative electrical conductivity evolution shown in Figure 6.2.

Concluding the observations of Figure 6.1a and Figure 6.2, an irreversible thermal degradation processes is happening within the post-treated PEDOT:PSS thin films, which seems to be less severe for the untreated films.

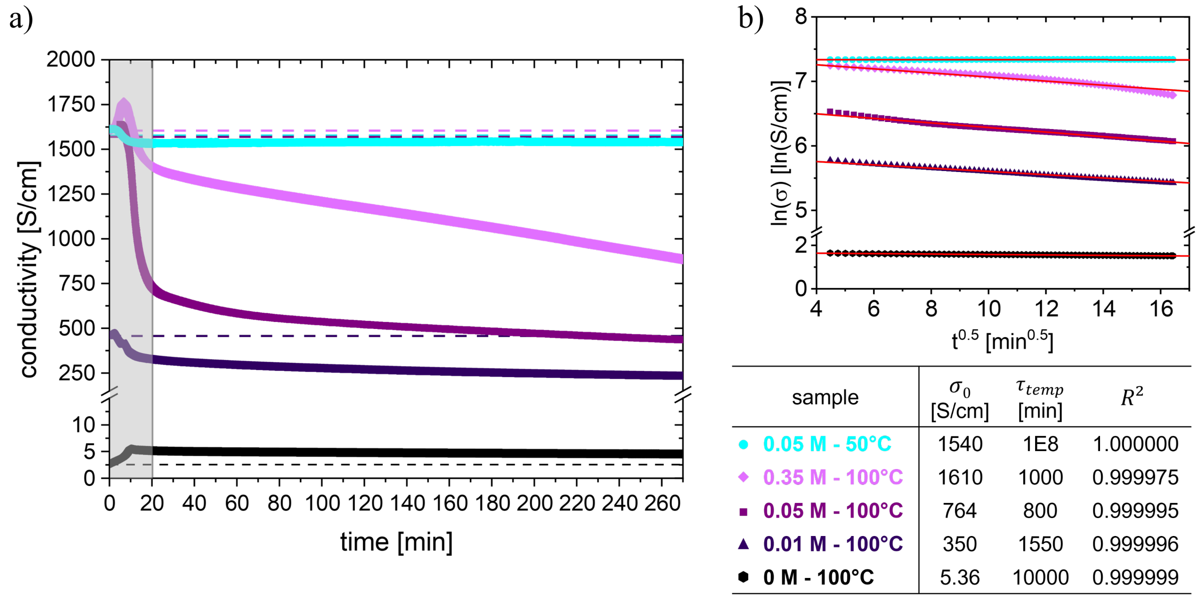

sample	σ_0 [S/cm]	τ_{temp} [min]	R^2
● **0.05 M - 50°C**	1540	1E8	1.000000
◆ **0.35 M - 100°C**	1610	1000	0.999975
■ **0.05 M - 100°C**	764	800	0.999995
▲ **0.01 M - 100°C**	350	1550	0.999996
⬢ **0 M - 100°C**	5.36	10000	0.999999

Figure 6.1 Heat treatment dependent electrical conductivity of EMIM DCA treated PEDOT:PSS films. a) Electrical conductivity evolution over 4.5 h heating of post-treated PEDOT:PSS thin films. Pure THF treated reference sample (black hexagons), 0.01 M (dark purple triangles), 0.05 M (purple squares), 0.35 M (light purple diamonds) EMIM DCA post-treated films heated at 100 °C, and a 0.05 M EMIM DCA post-treated film heated at 50 °C (cyan circles). Greyed-out area marks the heating up process. After 20 min, the respective temperatures were reached and kept constant. Dashed lines indicate the initial conductivities of the samples before the heating experiment. b) Natural logarithm of this electrical conductivity evolution (symbols) plotted together with fits (lines) versus time of stable heating temperature between 20-270 min. With the respective fit parameters listed in the table below. Adapted with permission from Oechsle et al.[50] Copyright 2022 American Chemical Society.

In literature, it is supposed that the increase of potential barriers between the conductive domains, by thermally caused morphological changes, introduces the decrease of the overall film electrical conductivity in pure PEDOT:PSS thin films.[241, 242] For this kind of degradation process upon heat treatment with a stable temperature, the electrical conductivity evolution over the treatment time (t) corresponds to the following Equation (6.1):

$$\sigma = \sigma_0 exp\left[-\left(\frac{t}{\tau_{temp}}\right)^{\alpha}\right] \tag{6.1}$$

With $\alpha = 0.5$ for the PEDOT:PSS typical charge transport, representing holes tunneling between PEDOT conductive domains separated by an insulating PSS matrix.[241] Here, σ_0 is the initial electrical conductivity, and τ_{temp} is the parameter characteristic for the electrical conductivity decay.

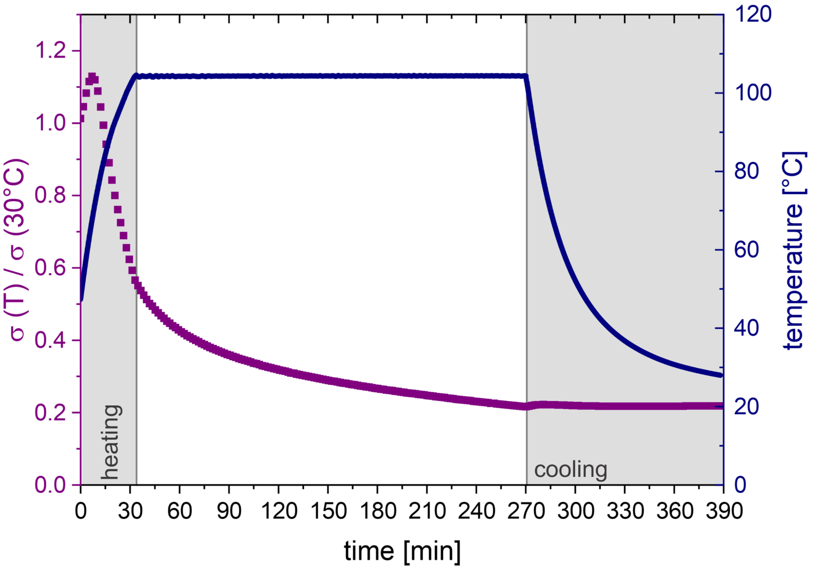

Figure 6.2 Reversibility test of the heat treatment dependent conductivity. Relative conductivity evolution (purple squares, left y-axis) of a 0.05 M EMIM DCA post-treated PEDOT:PSS thin film during a heating and cooling procedure (blue, right y-axis). First the film is heated up to 100 °C (left grey marked area), kept at 100 °C for 4 h and then again cooled down to 30 °C. The conductivity, which drops during heating at 100 °C, is not rising again during cooling of the film; therefore, the film degradation appears to be irreversible. Adapted with permission from Oechsle et al.[50] Copyright 2022 American Chemical Society.

Figure 6.1b shows the experimental and fitted electrical conductivity evolution, during the time of stable temperature between 20 and 270 min, plotted in a logarithmic scale versus $t^{0.5}$ according to Equation (6.1). The respective fit parameters are listed in the table below. First of all, it can be seen that σ_0 of the post-treated PEDOT:PSS thin films increases with increasing EMIM DCA concentrations, being highest for the 0.35 M sample with 1610 S cm^{-1}. This trend is in excellent agreement with the results presented in Chapter 5, showing the positive effect of IL treatments on the electrical conductivity.[163] The 0.05 M EMIM DCA post-treated film heated at 100 °C shows with τ_{temp} = 800 min the most rapid decay in electrical conductivity. The second fastest thermal degradation is observed for the 0.35 M treated film, with τ_{temp} = 1000 min. For samples with even lower EMIM DCA concentration, the τ parameter further increases, meaning a slower thermal degradation process. Interestingly, for the 0.05 M post-treated PEDOT:PSS thin film heated at a temperature of 50 °C an extremely high τ_{temp} value is obtained, which indicates that nearly no thermal degradation happens, and therefore the film seems stable at this operation temperature.

In general, the fits for the electrical conductivity evolution according to Equation (6.1) match very well with the experimental data and encourage the presumption that the electrical conductivity decrease results from structural changes within the PEDOT:PSS films, which will be examined in the following with GISAXS. However, the higher the EMIM DCA post-treatment concentration is, the poorer the fits seem to match the experimental data, as evident from the root mean square error (R^2). This suggests additional σ decreasing processes such as changes in the oxidation level, which will be also discussed following.

6.3 Evolution of the morphology

For the direct investigation and evidence of possible morphology alterations inside the PEDOT:PSS thin films, *in situ* GISAXS measurements are performed during the heat treatment. GISAXS gives access to statistically significant morphology information of thin films by making use of the grazing-incidence geometry.[141, 144, 148] The over the time of heating obtained 2D GISAXS data of the different post-treated samples are shown in Figure 6.3. A complete description of the *in situ* GISAXS measurement specifics and the used procedure to model the obtained data is provided in Section 3.4.2.

The corresponding horizontal line cuts, obtained from the 2D GISAXS data at the critical angle of PEDOT, are shown in Figure 6.4 for all the post-treated PEDOT:PSS thin films from bottom to top over the time of heat treatment. As these horizontal line cuts are performed at the Yoneda region of PEDOT, the model fits, shown as red lines, provide information about the PEDOT structure, namely the PEDOT domain radii, domain distances, and domain size distributions, which are presented in Figure 6.5.

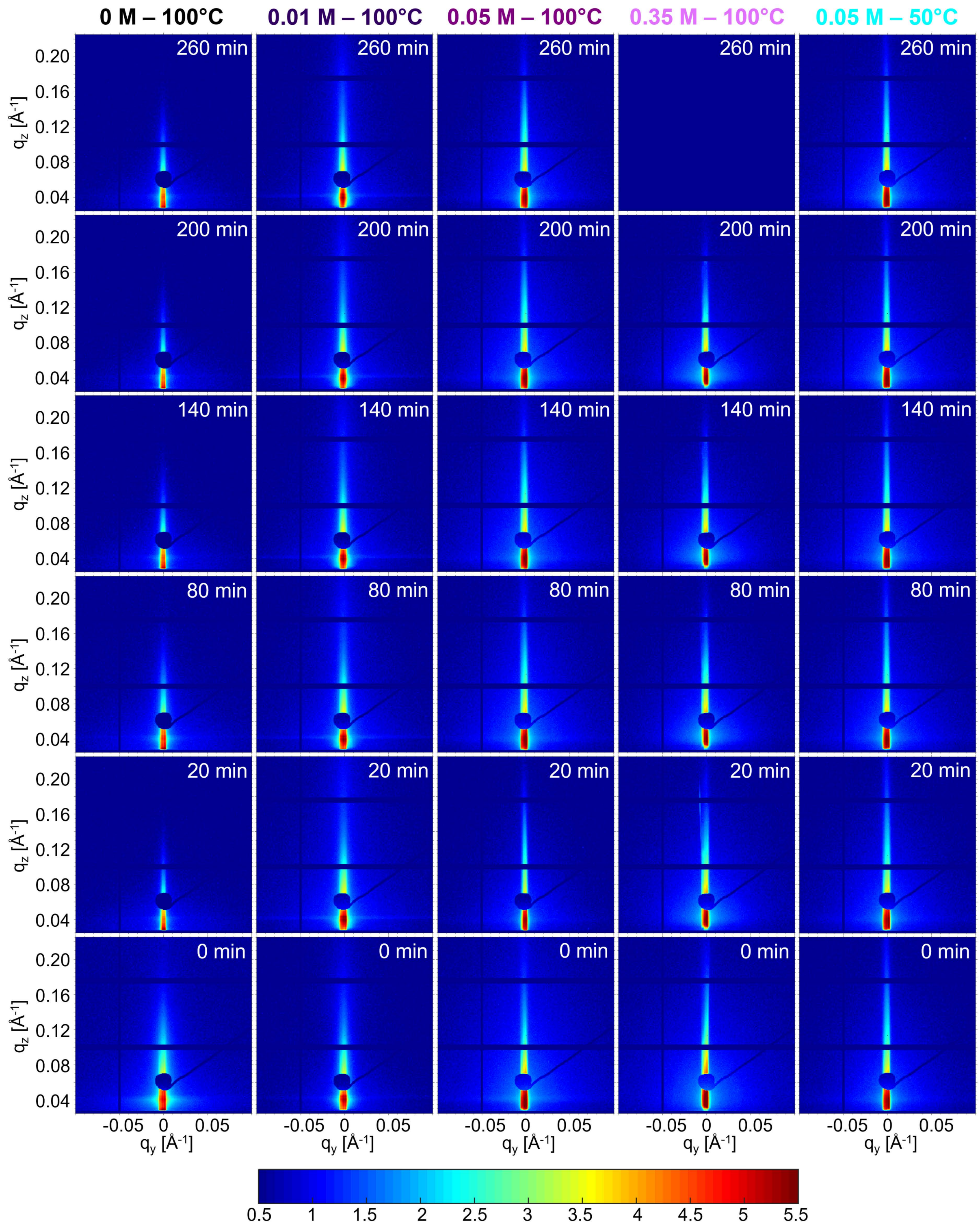

Figure 6.3 2D GISAXS data of EMIM DCA post-treated PEDOT:PSS films upon heating. 2D GISAXS data of the different EMIM DCA post-treated PEDOT:PSS thin films presented from bottom to top over the time of the heat treatment. No GISAXS image could be obtained for the 0.35 M EMIM DCA sample heated at 100 °C for 260 min, due to an interruption of the X-ray beam at the synchrotron facility. Adapted with permission from Oechsle et al.[50] Copyright 2022 American Chemical Society.

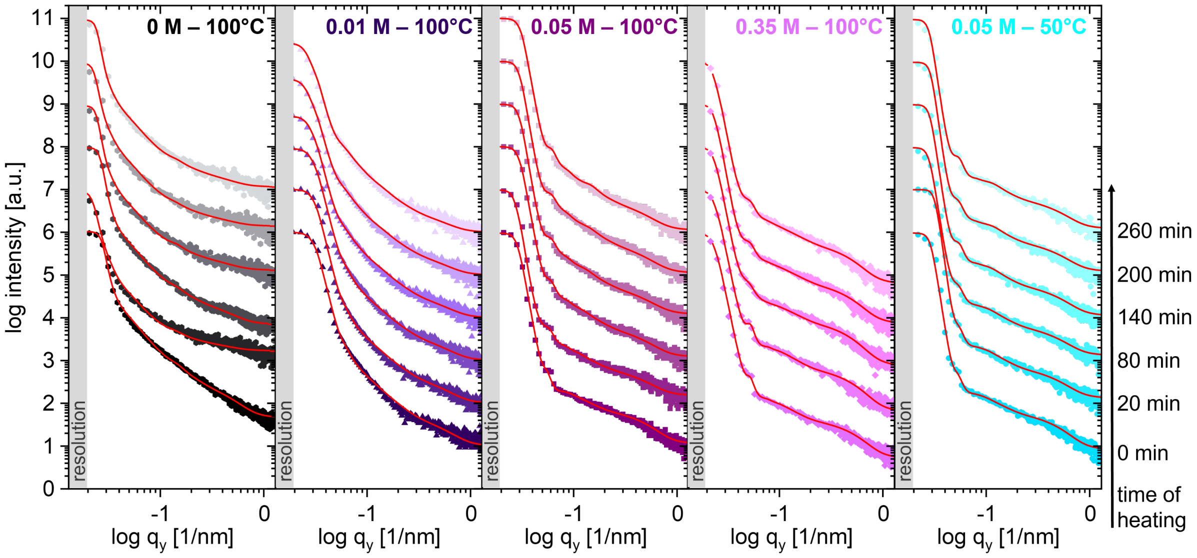

Figure 6.4 Horizontal line cuts of EMIM DCA post-treated PEDOT:PSS films upon heating. From 2D GISAXS data acquired horizontal line cuts of EMIM DCA post-treated PEDOT:PSS thin films, from left to right, 0 M reference sample (black), 0.01 M (dark purple), 0.05 M (purple), 0.35 M (light purple) heated at 100 °C, and 0.05 M (cyan) heated at 50 °C. Indicated by gradually lighter colors and shifted along the y-axis for the sake of clarity, the horizontal line cuts are presented from bottom to top over progressive time of heating. The red lines show the resulting fits of GISAXS data modeling. Adapted with permission from Oechsle et al.[50] Copyright 2022 American Chemical Society.

The best horizontal line cut modeling results are obtained with three cylindrical form factors of different radii. The domain radii of PEDOT domains associated with these form factors are r_l = 39-68 nm for large-, r_m = 7-11 nm for medium-, and r_s = 2-3 nm for small-sized domains, plotted in Figure 6.5a and respectively marked with light blue, blue, and dark blue areas. The model also reveals structure factors with corresponding domain center-to-center distances of D_l = 180-235 nm for the large domains (light blue area) and D_m = 38-50 nm for the medium-sized domains (blue area), shown in Figure 6.5b. No reliable structure factors and therefore no center-to-center distance could be extracted for the small-sized domains.

Apparent from Figure 6.5a and b, for the 0 M reference sample heated at 100 °C and the 0.05 M EMIM DCA post-treated PEDOT:PSS thin film heated at 50 °C, the domain radii and domain distances barely change over time of heat treatment. In contrast, for the 0.01 M, 0.05 M, and 0.35 M EMIM DCA post-treated films a radius increase of the large PEDOT domains, a small decrease of the medium domain radii, and unchanged small domain radii are observed over the 4.5 h of heating at 100 °C. Furthermore, these samples show a decrease in distances between the large-sized domains, and between the medium-sized PEDOT domains, respectively, which means an increase in their corresponding number.

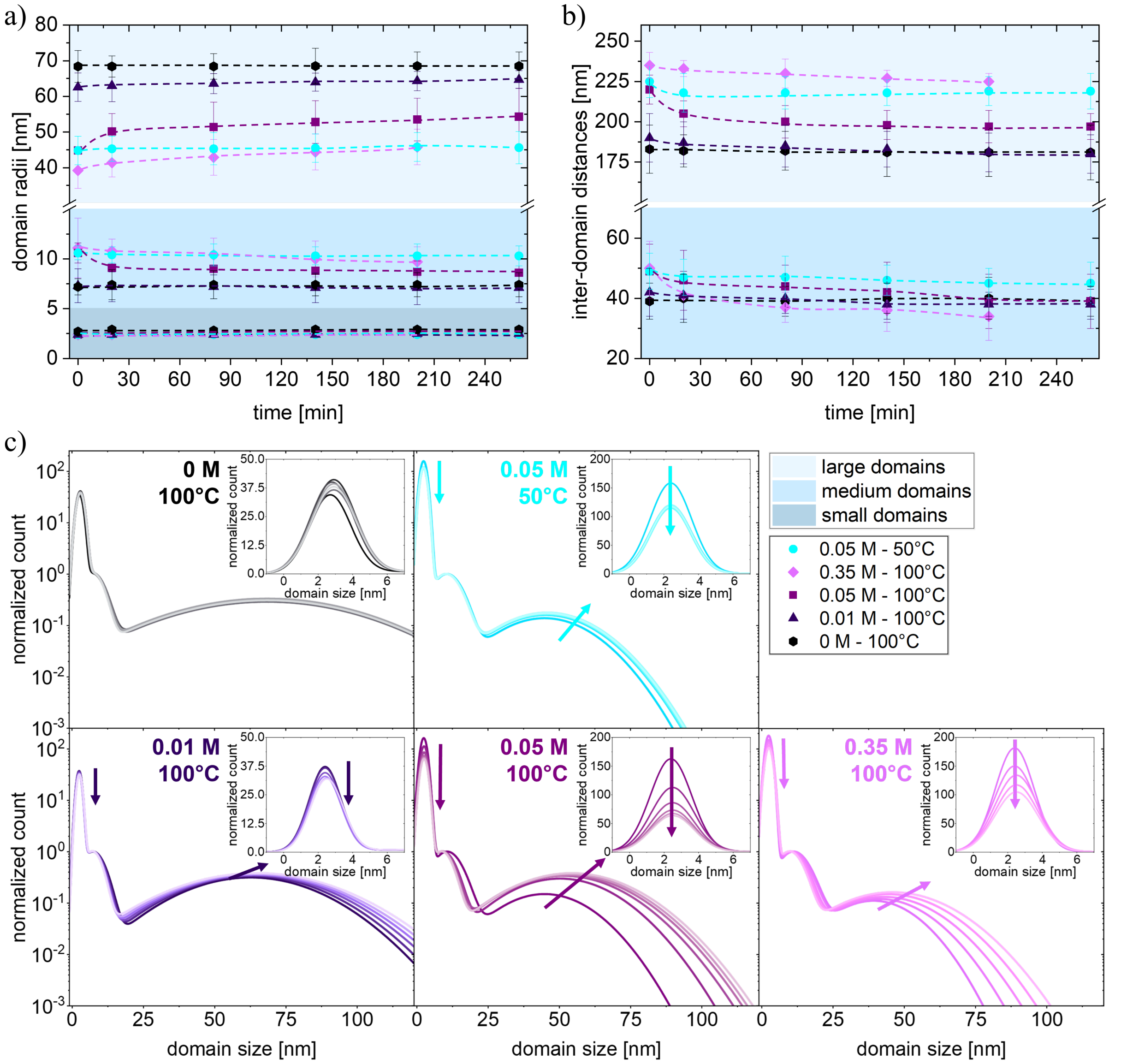

Figure 6.5 Morphological evolution of EMIM DCA post-treated PEDOT:PSS films upon heating. a) Radii of PEDOT domains, b) center-to-center distances between these PEDOT domains, and c) domain size distributions over the time of heat treatment (denoted by lightening up of colors). For the samples 0 M (black), 0.01 M (dark purple), 0.05 M (purple), 0.35 M (light purple) EMIM DCA post-treated PEDOT:PSS thin films heated at 100 °C for 4.5 h and for a 0.05 M EMIM DCA post-treated PEDOT:PSS thin film heated at 50 °C for 4.5 h (cyan). Colored dashed lines and arrows serve as guides to the eye. Adapted with permission from Oechsle et al.[50] Copyright 2022 American Chemical Society.

Overall, these domain radii and distances changes indicate that the large PEDOT domains become bigger and more during heating, while the medium-sized domains become smaller but also increase in amount. At first, one would expect that this number increase of large- and medium-sized conductive domains reduces the inter-domain distances and therefore should be favorable for the overall film electrical conductivity. However, as discussed and presented in the previous Chapter 5 and some literature, the amount of the small PEDOT domains turned out to be crucial when considering the overall inter-domain electrical conductivity within PEDOT:PSS thin films.[22, 24, 46, 163] Therefore, a calculation of the domain size distributions for all the post-treated films during heat treatment was done as described in Section 3.4.2, which gives information about the heat-caused change in the quantity ratio of large, medium, and more important also of the small PEDOT domains. The received quantity fraction values are listed in Table 6.2, and the associated plots are shown in Figure 6.5. These data indicate, elucidated by arrows, a PEDOT:PSS structure rearrangement due to heating the samples at 100 °C. Overall, the large PEDOT domains become larger in size and number, the medium PEDOT domains decrease in size and grow in number. While in contrast, the small-sized PEDOT domains remain constant in their radii, however, strongly decrease in their amount. This alteration can be understood as kind of a merging of the small PEDOT domains towards the formation of larger domains. Interestingly, these observed changes are most prominent for the high EMIM DCA post-treatment concentrations of 0.05 M and 0.35 M when heated at 100 °C and fit well with the measured electrical conductivity degradation trends.

The correlation between the domain morphology and the heat treatment becomes particularly clear when calculating the volume fraction according to Equation (3.38) in Section 3.4.2. Also listed in Table 6.2, the volume fraction of large (light blue), medium (blue), and small (dark blue) PEDOT domains and the electrical conductivity of the respective post-treated films are both plotted in Figure 6.6 versus the time of the heat treatment. First, for the 0 M reference sample, the main volume contribution results from large PEDOT domains. With increasing EMIM DCA post-treatment concentration, the volume fraction shifts towards a more significant contribution of the small domains, clearly showing the formation of an electrical conductivity enhancing finer and denser packed domain morphology. During the 4.5 h heating of the 0 M reference sample at 100 °C, the volume fraction and the electrical conductivity barely change. Also, for the 0.05 M EMIM DCA post-treated sample heated at 50 °C, the electrical conductivity and volume fraction stay nearly constant, except for a slight drop during the 20 min heating-up phase.

In contrast, during the heat treatment of the EMIM DCA post-treated PEDOT:PSS thin films at 100 °C, a continuous shift of the volume fraction towards a more significant contribution of the large domains is observed, strongest for 0.05 M from 20 % to 70 %, and for 0.35 M from 10 % to 30 %. These data also demonstrate and support the hypothesis of the coarsening of the domain morphology for the EMIM DCA post-treated PEDOT:PSS thin film by coalescence of the small domains. Although thereby the volume fraction of large- and medium-sized domains increases, the number of small-sized PEDOT domains surrounding them decreases significantly.

Table 6.2 Quantity and volume distribution of EMIM DCA post-treated PEDOT:PSS films upon heating. Quantity and volume fraction changes of the large, medium, and small PEDOT domains within the post-treated PEDOT:PSS thin films, respectively listed from bottom to top over the time of heating.

	heating time [min]	quantity fraction [%]			volume fraction [%]		
		N_l	N_m	N_s	NV_l	NV_m	NV_s
THF 100°C	260	0.80	2.57	96.64	79.74	2.99	17.27
	200	0.83	2.49	96.69	80.40	2.81	16.79
	140	0.78	2.67	96.56	79.25	3.17	17.58
	80	0.79	2.45	96.76	80.54	2.92	16.53
	20	0.75	2.39	96.87	78.77	2.94	18.29
	0	0.88	2.83	96.28	82.91	2.95	14.13
0.01 M 100°C	260	1.16	3.03	95.81	87.33	2.75	9.92
	200	1.11	2.99	95.90	86.71	2.85	10.44
	140	1.05	2.94	96.01	85.98	2.96	11.06
	80	0.98	2.81	96.22	84.99	3.12	11.88
	20	0.89	2.66	96.45	82.67	3.23	14.11
	0	0.83	2.62	96.56	81.40	3.49	15.10
0.05 M 100°C	260	0.59	1.54	97.88	70.57	4.62	24.81
	200	0.53	1.46	98.01	67.72	4.93	27.35
	140	0.47	1.34	98.19	64.62	5.12	30.26
	80	0.39	1.15	98.47	59.25	5.36	35.39
	20	0.26	0.88	98.86	48.68	5.41	45.91
	0	0.09	0.61	99.30	22.00	8.35	69.66
0.35 M 100°C	260	-	-	-	-	-	-
	200	0.15	0.95	98.90	30.78	8.74	60.47
	140	0.13	0.85	99.03	26.69	8.85	64.46
	80	0.10	0.74	99.16	20.82	9.06	70.12
	20	0.08	0.66	99.26	17.45	9.80	72.76
	0	0.06	0.55	99.39	12.59	9.25	78.16
0.05 M 50°C	260	0.15	0.84	99.01	32.11	9.17	58.71
	200	0.15	0.83	99.03	32.33	9.05	58.62
	140	0.14	0.86	98.99	30.47	9.59	59.94
	80	0.14	0.83	99.03	30.32	9.47	60.20
	20	0.13	0.83	99.04	28.78	9.68	61.54
	0	0.09	0.63	99.29	21.94	8.60	69.46

Consequently, the overall distances between the conductive domains increase, for example between large- and small-sized domains, medium-, and small-sized domains, or small- and small-sized domains, impeding the inter-domain charge carrier transport. Eventually, this behavior reduces the charge carrier mobility (μ) and as $\sigma = n_q e\mu$, with n_q charge carrier density and e elementary charge, as introduced before, and therefore this directly leads to a reduction of the film electrical conductivity.[34] In perfect agreement with that, it can be seen in Figure 6.6 that the electrical conductivity during heat treatment directly follows the volume fraction trend and decreases with declining volume fraction of small domain.

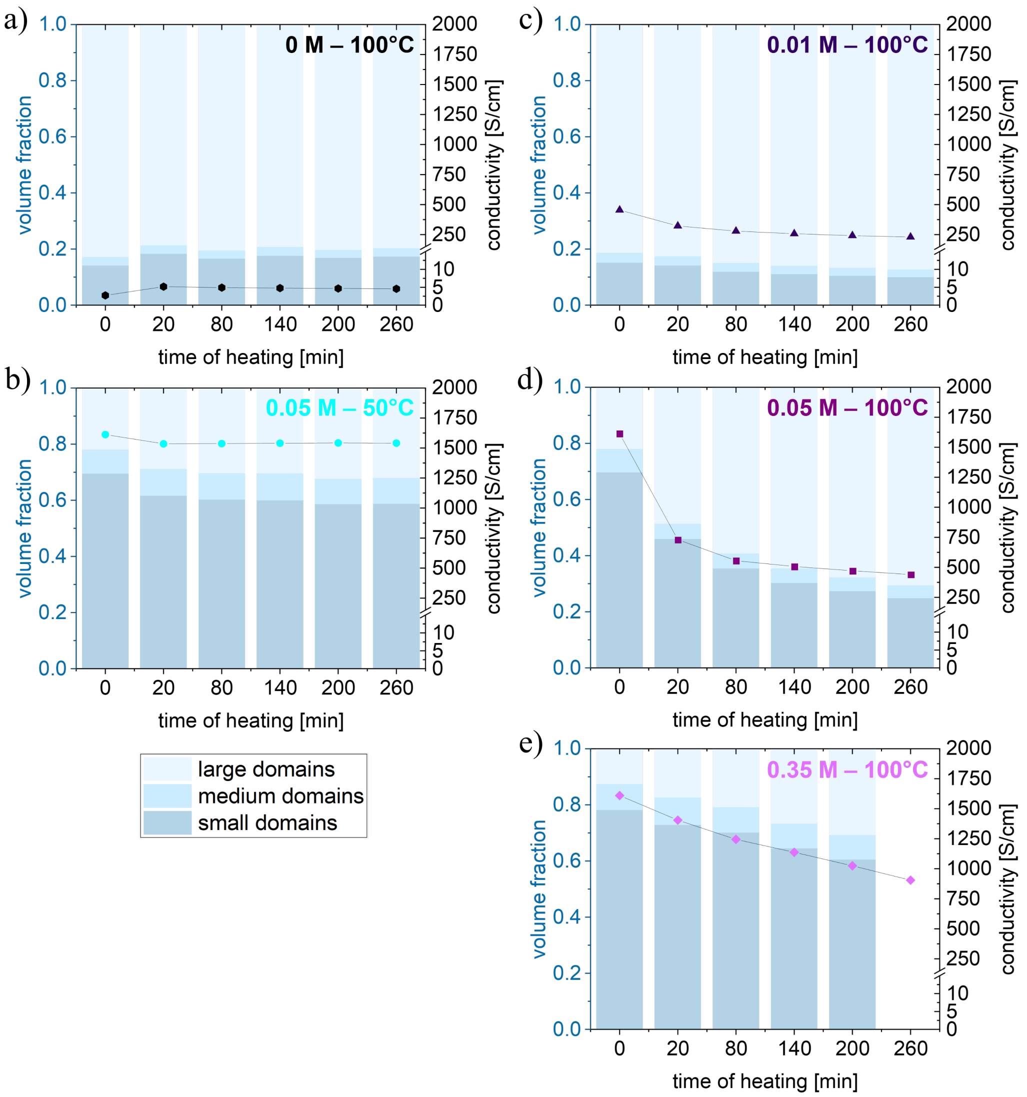

Figure 6.6 Domain volume fraction evolution in EMIM DCA post-treated PEDOT:PSS films upon heating. The blue bars, left y-axis, indicate the distribution evolution of the volume fraction of large (light blue), medium (blue), and small (darker blue) PEDOT domains over the time of heating. For a) 0 M (black), c) 0.01 M (dark purple), d) 0.05 M (purple), e) 0.35 M (light purple) EMIM DCA post-treated PEDOT:PSS thin films heated at 100 °C, and b) a 0.05 M (cyan) EMIM DCA post-treated PEDOT:PSS thin films heated at 50 °C. The symbols connected with lines, right y-axis, present the *in situ* electrical conductivity of these films at the respective time of the heat treatment. Adapted with permission from Oechsle et al.[50] Copyright 2022 American Chemical Society.

The reason for observing the strongest effects for higher EMIM DCA concentrations is likely explained by the plasticizing effect of ILs reported in literature.[47, 102, 199, 201, 243] During the post-treatment step, the ILs ions migrate, intercalate, and interact between the polymer chains, which weakens the electrostatic interaction between PEDOT and PSS chains, and can even cause a break of the ionic crosslinks. Thereby the segmental motion of the polymer chains is enhanced, enabling an easier reorientation, and therefore explaining the more pronounced coarsening of the PEDOT:PSS morphology for high EMIM DCA post-treatment concentrations.

6.4 Evolution of the oxidation level

Known from literature, as introduced in Section 2.1.3 and demonstrated in the previous Chapter 5, the IL post-treatment can also influence the oxidation state of PEDOT.[48, 100, 163, 201] Consequently, it is very likely that the heating at high temperatures of the EMIM DCA post-treated PEDOT:PSS thin films also affects the oxidation level. Therefore, possible changes in the oxidation level of the samples are investigated during the heat treatment with *in situ* UV-Vis measurements, which are detailed in Section 3.1.1. Figure 6.7a shows the *in situ* changes of the characteristic spectra between 400 and 1000 nm of the used broadband LED, shining through the respective samples, upon heat treatment at 100 °C or 50 °C. For the 0.01 M, 0.05 M, and 0.35 M EMIM DCA post-treated thin films, the spectra are changing over the 4.5 h of heating at 100 °C, which indicates a change in the oxidation level. While on the contrary, the 0 M reference sample heated at 100 °C and the 0.05 M EMIM DCA post-treated sample heated at 50 °C only show minor changes in the spectra, suggesting only minor changes in the oxidation level. For a more detailed analysis of possible oxidation level changes, the absorption coefficient in dependence of the wavelength is determined for the all the different post-treated samples, before and after heating. The obtained data presented in Figure 6.7b, show no noticeable changes for the 0 M reference sample between the spectra before and after heat treatment.

However, as indicated by colored arrows, for the EMIM DCA post-treated thin films, a decrease of absorption coefficient is visible around 900 nm and the formation of a new absorption peak around 600 nm. As introduced in Section 2.1.3, it is known from the literature that the polaronic states of PEDOT show up at around 900 nm and neutral states appear at 600 nm.[16, 27, 41]

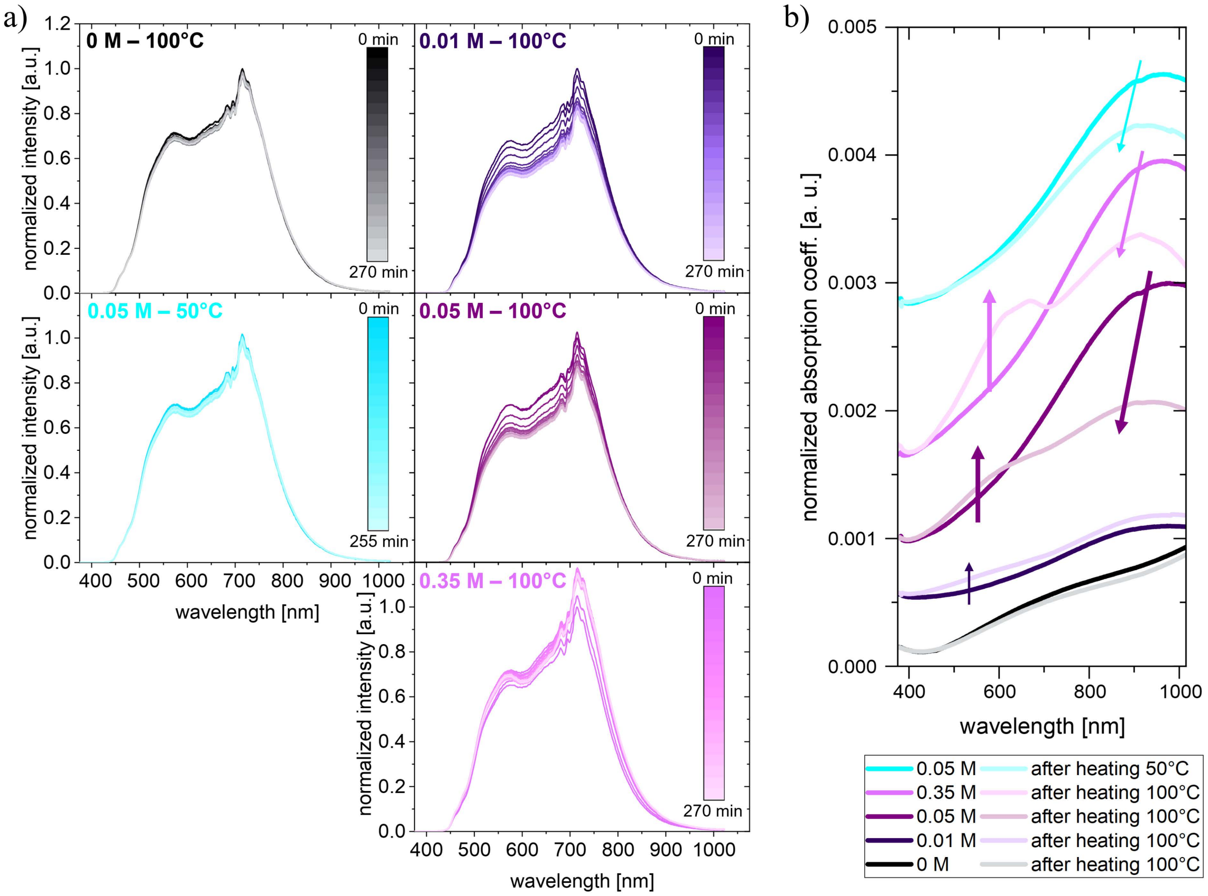

Figure 6.7 Oxidation level evolution of EMIM DCA post-treated PEDOT:PSS films upon heating. a) *In situ* changes in the characteristic spectra of the used broadband LED, shining through the respective EMIM DCA post-treated PEDOT PSS thin films, during 4.5 h heating at 100 °C or 50 °C and b) before and after heat treatment comparison of absorption coefficient versus wavelength for EMIM DCA post-treated PEDOT:PSS thin films. Reference sample 0 M post-treated with pure THF (black), 0.01 M EMIM DCA (dark purple), 0.05 M EMIM DCA (purple), 0.35 M EMIM DCA (light purple) heated at 100 °C respectively, and 0.05 M EMIM DCA heated at 50 °C (cyan). Spectra measured at proceeded heating times are displayed with incrementally lighter colors. Adapted with permission from Oechsle et al.[50] Copyright 2022 American Chemical Society.

Therefore, it can be deduced that upon 4.5 h heating of EMIM DCA post-treated PEDOT:PSS thin films, the oxidation level of PEDOT is reduced. The strongest heat caused formation of neutral states, and therefore the strongest reduction of PEDOT is observed for the EMIM DCA concentration of 0.35 M. As a reduction of the PEDOT oxidation level means a decrease in the number of free positive charge carriers, and therefore a decrease in the charge carrier density n_q. With $\sigma = n_q e \mu$, this confirms the before suspected additional contribution to the electrical conductivity drop, caused by thermal treatment.[34] For this, a possible explanation is the heating-enhanced IL ion migration between the polymer chains. Furthermore, as the IL anions are responsible for the PEDOT reduction, higher EMIM DCA post-treatment concentrations result in a more pronounced oxidation level change at elevated temperatures.

6.5 Model description of the temperature-dependent thermoelectric behavior

As PEDOT:PSS thin films are highly interesting for thermoelectric application, it is necessary to understand how the heat treatment influences their thermoelectric properties. Therefore, in this study also the effects on S and consequently on the power factor ($PF = \sigma S^2$) of these films before and after heating is determined, and the results are listed in Table 6.3. In general, as discussed in previous sections, the heating of EMIM DCA post-treated PEDOT:PSS thin films at elevated temperatures induces a coarsening of the morphology of the PEDOT domains and an additional reduction of the PEDOT oxidation level. Consequently, both lead to a gradual decrease in the film electrical conductivity.

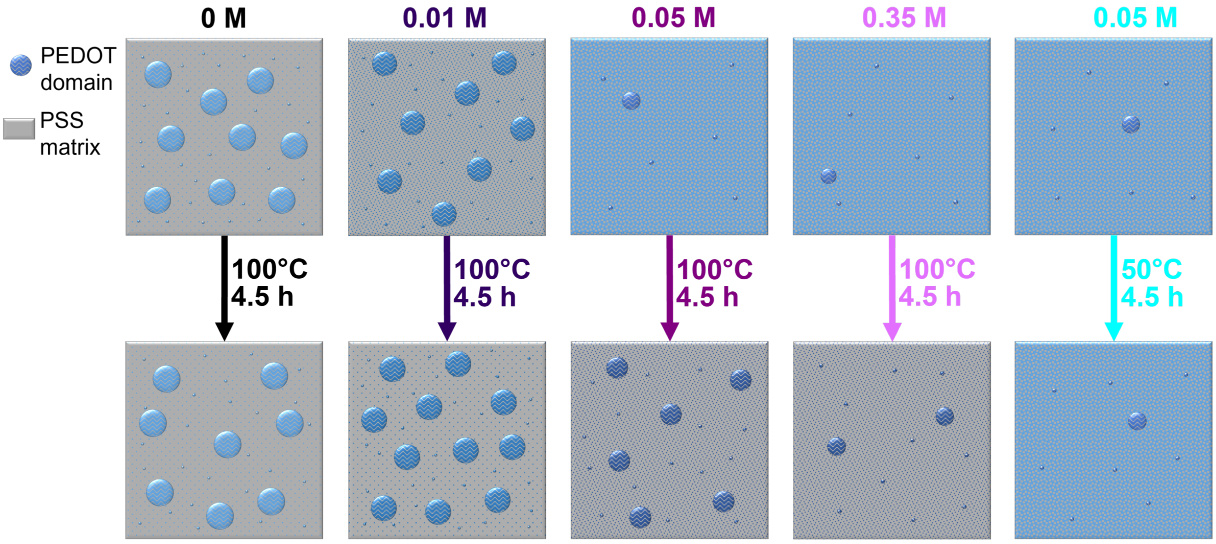

Figure 6.8 Model description of EMIM DCA post-treated PEDOT:PSS films upon heat treatment. Simplistic depiction of the morphology and oxidation level evolution for post-treated PEDOT:PSS thin films upon heating, showing PEDOT domains (blue) in a PSS matrix (grey) with the oxidation level coded in the brightness of the blue color (bright = high). From left to right a) to e), films post-treated with EMIM DCA concentrations of 0 M, 0.01 M, 0.05 M, 0.35 M EMIM DCA heated at 100 °C, and 0.05 M heated at 50 °C. The top row illustrates the initial state of the respective films, and the bottom row shows the state after heating for 4.5 h. Adapted with permission from Oechsle et al.[50] Copyright 2022 American Chemical Society.

For a better understanding of the thermoelectric property evolution, Figure 6.8 schematically illustrates the changes within the morphology and oxidation level occurring upon heat treatment. The different-sized blue spots visualize the large, medium, and small PEDOT domains embedded within a non-conductive PSS matrix (grey). Looking at Figure 6.8a top illustration, which represents the 0 M reference sample, a lot of large and medium-sized PEDOT domains, but only some small-sized domains can be seen. The overall domain-domain distance in this film is quite large, hampering the inter-domain hole transport and explaining the relatively low electrical conductivity of 2.72 S cm^{-1}.

Table 6.3 Thermoelectric properties of EMIM DCA post-treated PEDOT:PSS films upon heat treatment. Electrical conductivity $\boldsymbol{\sigma}$, Seebeck coefficient $\boldsymbol{S}$ and thermoelectric power factor $\boldsymbol{PF}$ for 0 M, 0.01 M, 0.05 M and 0.35 M EMIM DCA post-treated PEDOT:PSS thin films before and after heating at 100 °C or 50 °C for 4.5 h.

	σ [S cm^{-1}]	S [µV K^{-1}]	PF [µW m^{-1}K^{-2}]
0 M EMIM DCA	2.72	19.53	0.10
after heating at 100 °C	4.55	21.93	0.22
0.01 M EMIM DCA	454.15	33.27	50.27
after heating at 100 °C	227.45	34.36	26.85
0.05 M EMIM DCA	1612.28	46.17	343.68
after heating at 50 °C	1540.40	43.57	292.42
after heating at 100 °C	433.02	44.39	85.33
0.35 M EMIM DCA	1609.94	41.12	272.22
after heating at 100 °C	885.65	39.70	139.59

Furthermore, it is visible for this sample that the oxidation level of PEDOT is higher than for the EMIM DCA post-treated samples, depicted by the bright blue color of the spots. Therefore, the charge carrier concentration is higher, which leads to a low Seebeck coefficient of 19.53 µV K^{-1} and a thermoelectric power factor of only 0.10 µW m^{-1}K^{-2}. As the PEDOT:PSS thin films are post-treated with increasing EMIM DCA concentration, top row Figure 6.8b to e, the also in Chapter 5 observed rearrangement in the domain morphology is noticeable. Leading towards a charge carrier transport enhancing finer and more densely packed PEDOT domains, which rises σ up to 1612.28 S cm^{-1}. Because simultaneously the PEDOT chains and therefore the charge carrier concentration is reduced, indicated by the darker blue color of the spots, an S of 46.17 µV K^{-1} can be reached, which results in high PF = 343.68 µW m^{-1}K^{-2}.

However, upon heating the EMIM DCA post-treated samples at 100 °C, a coarsening and further oxidation level reduction of the PEDOT domain structure is visible, depicted in the bottom row of Figure 6.8. As a consequence, the inter-domain charge carrier transport is increasingly hindered and causes a decrease of the electrical conductivity, for example, for the 0.05 M EMIM DCA post-treated film from 1612.28 to 433.02 S cm^{-1}. In principle one would expect that the onward reduction in the charge carrier concentration, which can be observed for the 0.05 M and 0.35 M EMIM DCA post-treated samples upon heating at 100°C, would influence S positively.[12, 203] Though, the morphology caused strong impediment of the charge carrier transport seems to be more influencing and thus explains the observed small S, from 46.17 to 44.39 μV K^{-1} for the 0.05 M-100°C sample and from 41.12 to 39.70 μV K^{-1} for the 0.35 M-100°C sample. Overall, the PF decreases strongest for the 0.05 M treated sample by around 75% to 85.32 μW $m^{-1}K^{-2}$. Compared to that, the heat treatment of this sample at 50 °C, depicted in Figure 6.8e, affects the sample only slightly in its morphology and oxidation level, and the PF drops less pronounced to 292.42 μW $m^{-1}K^{-2}$. As presented in Table 6.3 and Figure 6.8, the changes for the 0 M reference sample and thus the decrease of the thermoelectric properties are just minor.

6.6 Summary

In this chapter, the morphology and oxidation level changes happening within EMIM DCA post-treated PEDOT:PSS thin films are investigated under the impact of elevated temperatures for 4.5 h. With *in situ* GISAXS, it is proven that the domain morphology of PEDOT domains embedded in a PSS matrix undergo a coarsening process during heat treatment, namely, the formation and growth of large domains by coalescence of the small surrounding domains. This diminishing of small PEDOT domains leads to an increase of the overall domain-domain distances and causes higher energy barriers for inter-domain charge carrier transport. With the *in situ* GISAXS results matching very well the observed gradual decrease of the electrical conductivity, the electrical conductivity decrease can be explained with these morphology changes. Simultaneously, a reduction of the PEDOT oxidation level occurs, proven by the formation of neutral states to the detriment of polaronic states in UV-Vis absorption spectra. This decrease in charge carrier density also contributes to the observed electrical conductivity degradation. To summarize, the 100 °C heat treatment-initiated changes and downward electrical conductivity evolution is strongest for the best thermoelectric performing PEDOT:PSS thin films, in fact, the ones post-treated with high concentrations of EMIM DCA. However, a 0.05 M EMIM DCA post-treated film is stable when heated at 50 °C. Therefore, it is crucial to consider and more closely examine the temperature ranges in which respectively treated PEDOT:PSS thin films can be stably operated in future thermoelectric applications. In general, to avoid severe degradation, it is suggested to limit the long-term exposure of the in this thesis investigated EMIM DCA post-treated PEDOT:PSS thin films to moderate temperatures.

7 Humidity influence on ionic liquid post-treated PEDOT:PSS films

This chapter is based on the publication "*Ionic Liquid-Induced Inversion of the Humidity-Dependent Conductivity of Thin PEDOT:PSS Films*" (A. L. Oechsle, T. Schöner, L. Deville, T. Xiao, T. Tian, A. Vagias, S. Bernstorff, P. Müller-Buschbaum, ACS Applied Materials & Interfaces 2023, 15, 40, 47682-47691; DOI: 10.1021/acsami.3c08208). Reprinted with permission from Oechsle et al.[51] Copyright 2023 American Chemical Society. Experiments were performed in collaboration with the master student Tobias Schöner and the bachelor student Lewin Deville.

In this Chapter, the humidity influence on the electronic and ionic resistance properties of thin post-treated PEDOT:PSS films is investigated. In particular, the resistance of these PEDOT:PSS films post-treated with three different concentrations (0 M, 0.05 M, and 0.35 M) of EMIM DCA is measured while being exposed to a defined humidity protocol. A resistance increase upon elevated humidity is observed for the 0 M reference sample, while the EMIM DCA post-treated samples demonstrate a reverse behavior. Simultaneously performed *in situ* GISAXS measurements evidence changes in the film morphology upon the varying humidity, namely an increase in the PEDOT domain distances. This leads to a detriment in the inter-domain hole transport, which causes a rise in the resistance as observed for the 0 M reference sample. Finally, electrochemical impedance spectroscopy (EIS) measurements at different humidities reveal additional contributions of ionic charge carriers in the EMIM DCA post-treated PEDOT:PSS films. Therefrom a model is proposed, which describes the hole and cation transport in different post-treated PEDOT:PSS films dependent on the ambient humidity.

7.1 Influence factor humidity o IL post-treated PEDOT:PSS

PEDOT:PSS, introduced in Section 2.1.2, is one of the most important and well-known hole conducting polymers for organic electronics, as it brings a lot of positive features, such as its excellent hole conductivity, its low toxicity, its good optical and mechanical properties.[17, 196, 244] All these advantages come along with being processable from aqueous solution, which enables an easy and cheap large-scale device fabrication by printing, spraying, or dip coating.[6, 7, 245] Therefore, nowadays the semiconductor PEDOT:PSS can be found in a wide variety of applications, like photovoltaics[54, 246], transistors[55, 247], thermoelectrics[10, 56], light-emitting diodes[57, 248, 249], sensors[58, 250], displays[251, 252], bioelectronics[59, 253], and many more. A lot of these advantages of PEDOT:PSS compared to other polymer-based organic semiconductors result from its unique polymer blend structure, consisting of the excellent p-type semiconductor PEDOT and the water-soluble polyanion PSS. In aqueous solutions, this polymer composition leads to the formation of a stable core-shell arrangement of hydrophobic PEDOT-rich cores enclosed by a hydrophilic PSS shell.[18] When using this aqueous solution to prepare thin PEDOT:PSS films, for example by spin-coating, this core-shell structure continues to exist in the form of pancake-shaped PEDOT enriched domains, which are surrounded by a PSS matrix.[16, 19] However, with PEDOT being the hole conducting polymer, while PSS is blocking the hole transport, this PSS matrix around the PEDOT enriched domains represents a barrier for the charge carriers that needs to be overcome to facilitate the electrical conductivity of PEDOT:PSS films.[20, 21] Literature suggests multiple approaches to improve the overall electrical conductivity and lower this hindrance of the inter-domain hole transport. Mainly achieved through the removal of excessive PSS, for example by treatment with high boiling solvents[22–24], inorganic salts[27, 28, 38], acids or bases[30–32, 54], surfactants[34–36], or polar solvents[26, 34]. One of these approaches to improve the properties of PEDOT:PSS is the post-treatment of thin PEDOT:PSS films with ionic liquids (ILs).[46, 49, 100] In the study presented in Chapter 5, which was performed to investigate different ILs for the PEDOT:PSS post-treatment, it has been found that especially the IL EMIM DCA can strongly improve the PEDOT:PSS domain morphology towards smaller and finer distributed PEDOT domains.[50, 163] Thus, a better network of more closely located conductive domains with less insulating PSS in between is created, resulting in an increase of the electrical conductivity higher than 1600 S cm^{-1}.[50, 163] A positive side effect of this IL treatment is the simultaneous improvement of the Seebeck coefficient of the thin PEDOT:PSS films, especially interesting for the use as organic thermoelectric material.[100, 163] However, the initial motivation to perform the in this chapter presented humidity study was given by the observation that the resistance of the PEDOT:PSS films is not just influences by temperature, as presented in Chapter 6, but also change with the ambient room humidity. More interestingly, this change seems to be different dependent on their post-treatment. In general, the influence of the humidity on PEDOT:PSS has been addressed in literature before, mainly describing an increase of the film's resistance, and thus suggesting a deterioration of the conductivity upon increasing humidity.[254–257] For example, Zhou et al. presented a PEDOT:PSS nanowire-based respiration sensor, which can measure the humidity of the breath by recording the changes in the nanowire resistance.[258] Furthermore, Kuş et al. studied the effect on the electrical properties of pure PEDOT:PSS up to a relative humidity (RH) of 90 %, whereby they discovered that below 80 % RH the film resistance increases with the humidity. However, above this humidity, the film reaches a water uptake saturation leading to the formation of a water film on top of the PEDOT:PSS film, resulting in a decline of its resistance behavior.[259]

In the research work presented in this chapter, it is shown that the conductivity deteriorating effect of elevated humidity on thin PEDOT:PSS films is completely reversed when these films are post-treated with EMIM DCA. This change of the negative humidity dependency towards a positive one, meaning achieving an increase in the conductivity of PEDOT:PSS films with the humidity, could be of crucial importance for applications. Especially considering the wide range of PEDOT:PSS applications in which exposure of the polymer to the ambient humidity cannot always be ruled out, or is even desired as for example in sensor devices.[58]

Therefore, the causes for this reversed film behavior are explored by first performing *in situ* resistance measurements of differently post-treated thin PEDOT:PSS films, while exposing them to a defined humidity protocol. Furthermore, to reveal changes happening in the special PEDOT:PSS domain morphology upon humidity variation, *in situ* GISAXS measurements are performed simultaneously. With additional *in situ* EIS measurements possible electronic and ionic contributions to the charge carrier transport are investigated, occurring differently at distinct RH steps. With this systematic examination, including *in situ* studies and a therefrom developed hole and cation transport model, it is contributed to a better understanding of the humidity dependency of post-treated PEDOT:PSS thin film properties, which is likely to be essential for a variety of applications.

For this investigation of the influence of humidity on EMIM DCA post-treated PEDOT:PSS films, the samples are prepared via a spin-coating procedure as described in Chapter 4.[50] As in this study the aim is to only examine the effect of the IL, three different EMIM DCA concentrations are chosen for the post-treatment, 0 M (reference sample), 0.05 M, and 0.35 M while keeping all the other sample preparations steps, i.a. the Zonyl® addition, constant. These concentrations are chosen based on the previous investigations presented in Chapter 5,[163] where we found that a EMIM DCA post-treatment with 0.35 M lead to outstanding thermoelectric properties, and the 0.05 M concentration provided the best compromise between improved thermoelectric properties and film fragility. A detailed description of all the used materials and film preparation steps is provided in Chapter 4, and the investigation methods details, including respective sample geometries can be found in the Chapter 3.

7.2 Humidity-dependent film resistance

First, the resistance of the respective prepared EMIM DCA post-treated PEDOT:PSS films is measured while they are placed inside a measurement chamber in which the air humidity is controlled. This approach allows to expose the samples to defined relative humidities, while simultaneously recording their resistance. Figure 7.1a shows the resistance evolution over time of the stepwise increase and decrease of the humidity, for each of the thin PEDOT:PSS films post-treated with different EMIM DCA concentrations. While Figure 7.1b shows the applied humidity protocol and Figure 7.1c the actual measured relative humidity within the chamber during the respective measurements.

In Figure 7.1a the resistance of the 0 M reference PEDOT:PSS film is observed to be overall markedly higher than that of the 0.05 M and 0.35 M EMIM DCA post-treated films. At the starting point of 0 % RH the 0 M reference sample has a resistance of $R = 23030\ \Omega$, the 0.05 M a $R = 135.3\ \Omega$, and the 0.35 M sample a $R = 151.5\ \Omega$. Considering the sample geometry and using the different film thicknesses listed in Table 7.1, which are obtained with surface profilometry described in Section 3.3.1, a rough estimation of the corresponding initial conductivity of the thin films can be made according Section 3.2.2. For the 0 M reference sample, the conductivity is 3 S cm^{-1}, which is significantly lower than the once of 0.05 M and 0.35 M post-treated samples, with 1556 S cm^{-1} and 1242 S cm^{-1}, respectively.

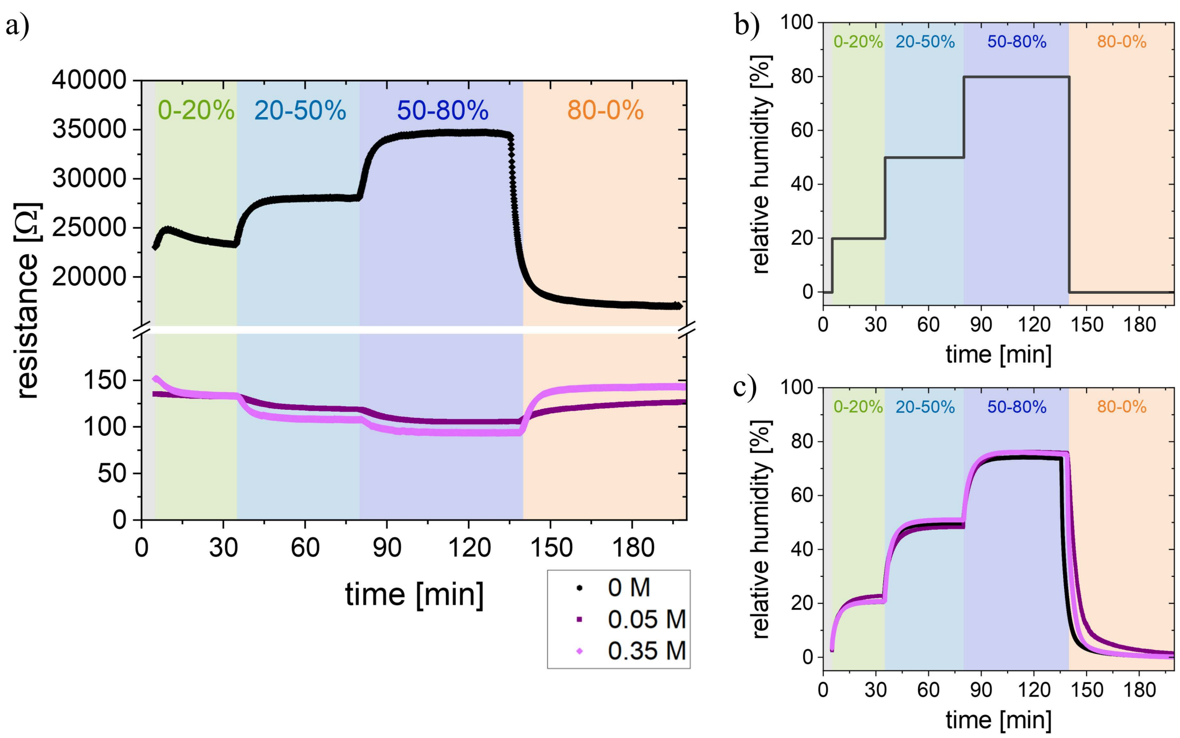

Figure 7.1 Humidity-dependent electrical resistance of EMIM DCA treated PEDOT:PSS films. a) Measured film resistance of differently post-treated PEDOT:PSS films while undergoing a stepwise increase in the ambient relative humidity over a total time period of 200 min. b) Applied humidity protocol and c) relative humidity recorded simultaneously within the measurement chamber. The different PEDOT:PSS films examined are post-treated with pure THF 0 M (black hexagons), with 0.05 M EMIM DCA (purple squares) or with 0.35 M EMIM DCA (light purple diamonds), respectively. Adapted with permission from Oechsle et al.[51] Copyright 2023 American Chemical Society.

Table 7.1 Thin film thicknesses of IL post-treated PEDOT:PSS. Film thicknesses t_{profil} of the prepared PEDOT:PSS thin films post-treated with different concentrations of EMIM DCA.

	thickness t_{profil} [nm]	thickness deviation [nm]
0 M	144.3	± 11.5
0.05 M	54.8	± 10.7
0.35 M	61.3	± 2.4

These findings match very well with the in Chapter 5 discussed context that the increase of the EMIM DCA post-treatment concentration leads to an improvement of the PEDOT:PSS film conductivity.[50, 163] Nevertheless, it is important to mention that the measurements of the film thicknesses, used to estimate the respective start conductivities, were only possible at lab room humidity of 30 % RH. However, in literature it has been reported that thin PEDOT:PSS films experience swelling when exposed to high humidity conditions,[179] and hence the real start conductivity values might deviate slightly. Furthermore, the film swelling during the humidity alteration adds another change that would be necessary to be considered when discussing the film conductivities. As with the setup utilized for this study, it is not possible to measure the *in situ* thickness changes. This study only focuses on the film resistance and its respective evolution caused by the humidity variations.

In Figure 7.1b it can be seen that the actual chamber humidity during the experiment behaves, except for minor setup-related differences, the same for all three samples, while the resistance profiles, shown in Figure 7.1a, differ from each other. For the 0 M reference sample, the resistance increases with increasing relative humidity from 23030 Ω at 0 % RH, over 23690 Ω at 20 % RH and 28180 Ω at 50 % RH, to 34460 Ω at 80 % RH, and decreases again back to 17010 Ω when the humidity is decreased. On the contrary, the resistance of the 0.05 M and 0.35 M EMIM DCA post-treated PEDOT:PSS films decrease with increasing relative humidity, from 135.3 Ω and 151.5 Ω at 0 % RH to their minimum of 105.7 Ω and 93.7 Ω at 80 % RH, respectively. A reduction of the RH at the end of the humidity cycle increases their resistance back to 126.8 Ω and 142.9 Ω. For all three samples measured, the slight reduction of the resistance compared to the starting value is probably explainable by the varying drying time (0 % RH) before and at the end of the humidity experiment. It might result in a different humidity level inside the thin film samples and thus can explain the irreversible seeming resistance.

In previous research studies, the trend observed for the 0 M reference sample has already been mentioned, often in respect to a possible use in humidity sensor applications.[58, 257, 258] However, the here observed complete reversal of this humidity-dependent resistance behavior upon IL post-treatment of the PEDOT:PSS films is very contraintuitive and has so far not been reported. Thus, the subject of this study is its further investigation.

7.3 Humidity-dependent morphology changes

Multiple preceding research works and the studies presented in the previous chapters have shown that the specific domain structure of PEDOT:PSS plays a crucial role when considering its resistance. Therefore, *in situ* GISAXS measurements are also performed in this study, to investigate the inner film morphology of the different post-treated PEDOT:PSS films,[148] while simultaneously exposing them to varying relative humidities. A detailed description of the *in* *situ* GISAXS experiment, containing all beamline specifics and analysis procedures can be found in Section 3.4.2.

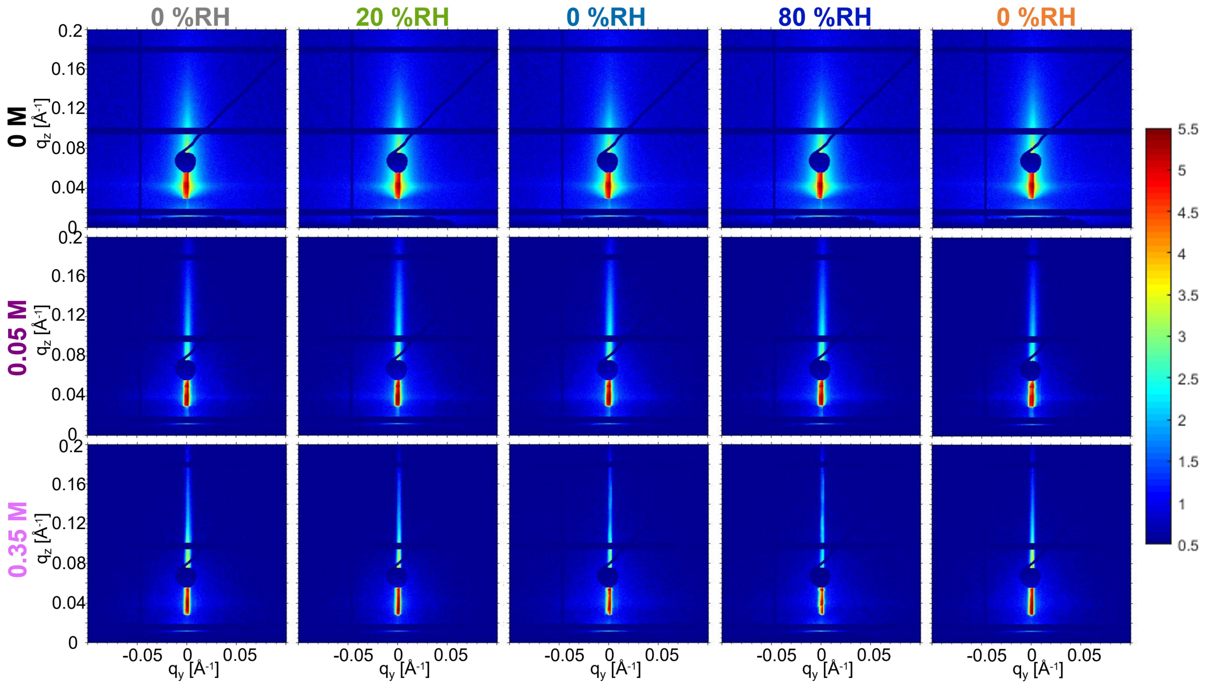

Figure 7.2 2D GISAXS data of EMIM DCA post-treated PEDOT:PSS films at different humidities. Exemplary 2D GISAXS data for 0 M (black, top), 0.05 M (purple, middle), and 0.35 M (light purple, bottom) EMIM DCA post-treated PEDOT:PSS thin films, from left to right shown respectively at different humidity steps. Adapted with permission from Oechsle et al.[51] Copyright 2023 American Chemical Society.

Exemplary 2D GISAXS data of the three differently treated PEDOT:PSS films, are shown in Figure 7.2 for each exemplary at the different humidity steps, 0 % RH, 20 % RH , 50 % RH, 80 % RH, and again 0 % RH. Horizontal line cuts were obtained from all the measured 2D GISAXS data at the Yoneda region of PEDOT. These contain information about the PEDOT domain structure, which is extracted by using the model described in Section 3.4.2. All horizontal line cuts are shown in Figure 7.3 together with their respective model fits as red lines. The structural information and values obtained from the model fits can be found in Figure 7.4a-f and Table 7.2 for the 0 M, 0.05 M, and 0.35 M EMIM DCA post-treated PEDOT:PSS films, while undergoing the procedure of varying relative humidity.

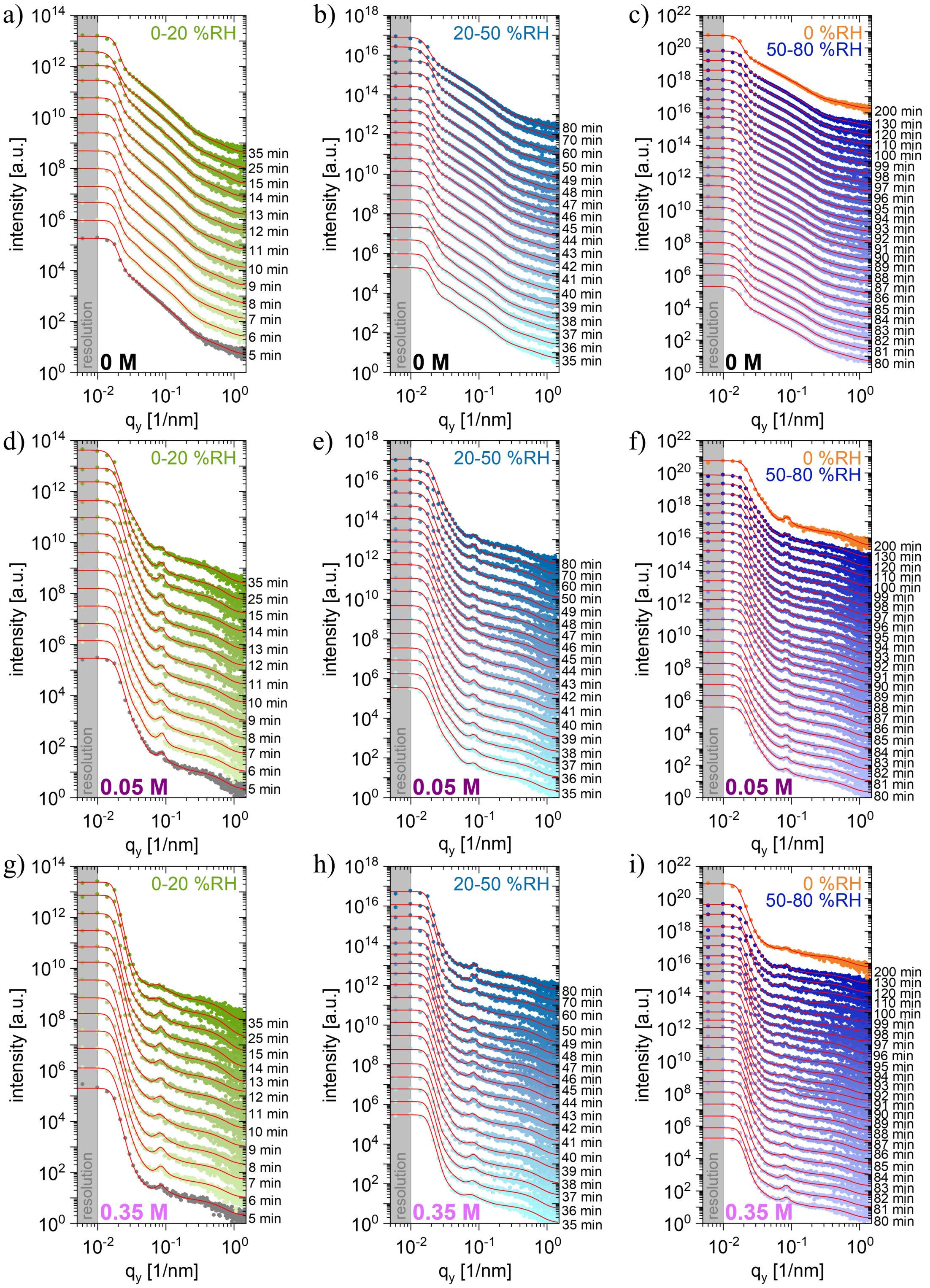

Figure 7.3 Horizontal line cuts of EMIM DCA post-treated PEDOT:PSS films at different humidities. Horizontal line cuts of a)-c) 0 M (black, top), d)-f) 0.05 M (purple, middle), and g)-i) 0.35 M (light purple, bottom) EMIM DCA post-treated PEDOT:PSS thin films. From left to right upon facing different humidity steps (0-20 % RH, 20-50 % RH and 50-80-0 % RH). The data are displayed from bottom to top, indicated by gradually darker colors, over the processing time of the humidity step. The red lines show the GISAXS data modeling results. For sake of clarity, the horizontal line cuts and corresponding fits are shifted along the y-axis. Adapted with permission from Oechsle et al.[51] Copyright 2023 American Chemical Society.

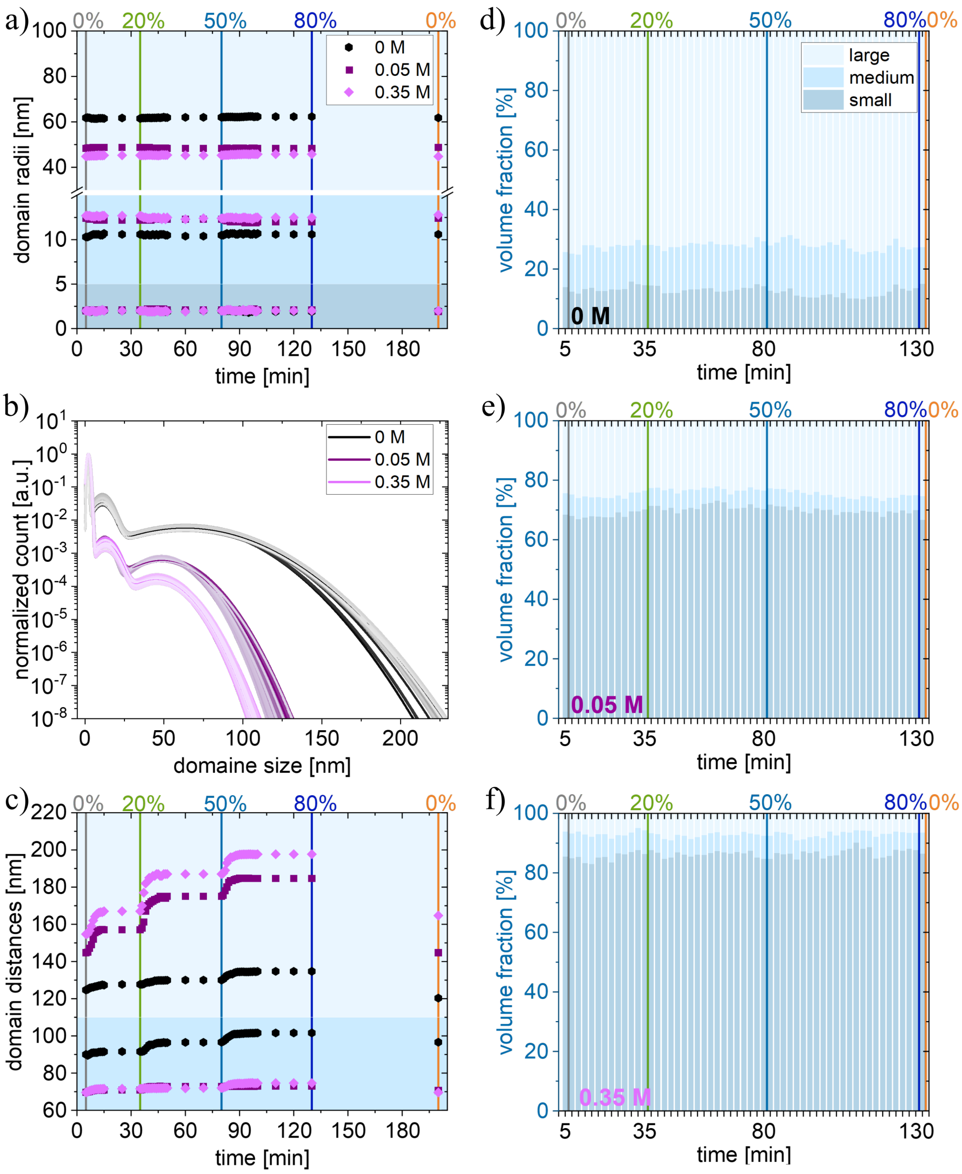

Figure 7.4 Morphological features of EMIM DCA post-treated PEDOT:PSS films at different humidities. From horizontal line cut modeling acquired information about the morphology of the thin PEDOT:PSS films while facing different relative humidities; post-treated with 0 M (black), 0.05 M (purple), or 0.35 M (light purple) EMIM DCA, respectively. a) PEDOT domain radii, b) evolution of the PEDOT domains size distribution, normalized to the "small" domains and with gradually lighter colors depicting the progressing time, c) PEDOT domain distances, and d)-f) volume fractions of large (light blue), medium (blue), and small (dark blue) PEDOT domains. Adapted with permission from Oechsle et al.[51] Copyright 2023 American Chemical Society.

Figure 7.4a shows the PEDOT domain radii (r_l, r_m, r_s), whereby for each of the three different samples three different domain sizes, here named as large (light blue area), medium (blue area), and small domains (dark blue area) can be distinguished. In good agreement with the work shown in the previous chapters,[50, 163] it is found that the domain radii for the small domains have a size around 2 nm for all three samples, while the medium domain radii are a bit larger for the 0.05 M and 0.35 M samples with ~ 12.5 nm, compared to the 0 M reference sample with ~ 10 nm. Also matching the preceding results, the radii for the large PEDOT domains seem to become smaller with increasing EMIM DCA concentration, starting from around 62 nm, over 48.5 nm to 45 nm. When looking at the evolution over time of the stepwise humidity variations, no obvious changes can be observed for any of the samples; suggesting that the size of the PEDOT domains is unaffected by the RH.

Furthermore, the respective domain size distributions, shown in Figure 7.4b, match quite well with results reported in the previous chapters, evidencing a lower amount ratio of large N_l and medium domains N_m, and a significantly higher amount of small domains N_s for the EMIM DCA post-treated PEDOT:PSS compared to the 0 M reference sample.[50, 163] As overall the number of the small and medium domains exceeds by far the number of large domains, these small and medium domains can be seen as the primary promoter of hole transport, and thereby explain the initial lower film resistance of the IL treated samples.[24, 163] This change of the PEDOT:PSS domain morphology upon IL post-treatment, which is dedicated to the removal of excessive PSS,[100, 200] can be outlined more noticeably when comparing the volume fraction distributions $VN_{l,m,s}$ of the different samples, shown in Figure 7.4d-f.

Table 7.2 Quantity and volume fraction of EMIM DCA post-treated PEDOT:PSS films at different humidities. Exemplary quantity and volume fraction evolution of the large, medium, and small PEDOT-rich domains within the 0 M (top), 0.05 M (middle), and 0.35 M (bottom) EMIM DCA post-treated PEDOT:PSS thin films. The values are listed from bottom to top for the respective ambient relative humidity.

	relative humidity	quantity fraction [%]			volume fraction [%]		
		N_l	N_m	N_s	NV_l	NV_m	NV_s
0 M	0	0.49	2.83	96.68	72.65	12.34	15.01
	80	0.48	3.12	96.40	72.81	13.64	13.55
	50	0.49	3.65	95.86	70.76	14.97	14.27
	20	0.51	3.19	96.30	72.00	13.50	14.50
	0	0.54	3.08	96.38	74.31	11.79	14.00
0.05 M	0	0.06	0.28	99.66	25.42	7.89	66.69
	80	0.07	0.22	99.71	25.05	5.07	69.88
	50	0.06	0.25	99.69	23.55	6.16	70.29
	20	0.06	0.27	99.67	23.56	6.31	70.13
	0	0.06	0.28	99.66	24.36	7.30	68.34
0.35 M	0	0.01	0.20	99.79	6.50	7.08	86.42
	80	0.01	0.17	99.82	6.58	5.79	87.63
	50	0.02	0.24	99.74	7.60	7.73	84.67
	20	0.01	0.23	99.76	5.70	7.96	86.34
	0	0.01	0.24	99.75	6.13	8.37	85.50

Over the time of the experiment, indicated by progressively lighter colors in Figure 7.4b, the respective domain size distributions do not significantly change. Therefore, the quantity ratios of the large, medium, and small PEDOT domains, listed in Table 7.2, remain unchanged under varying relative humidity conditions. Expressed more precisely, the size and the amount of the respective sized PEDOT domains (large, medium, and small) do not change with the humidity variation. This finding can be exhibited more clearly when comparing the evolution of the volume fraction distribution of all three EMIM DCA post-treated PEDOT:PSS thin film samples, plotted in Figure 7.4d-f and listed in Table 7.2.

A different behavior is observed for the inter-domain distances shown in Figure 7.4c. From the model fits it is possible to reveal domain center-to-center distances for the large D_l and medium D_m domains, being 125 nm and 90 nm for the 0 M reference sample, 145 nm and 70 nm for the 0.05 M sample, and 155 nm and 70 nm for the 0.35 M sample, respectively, at the starting state of 0 % RH. When the relative humidity is stepwise increased, to 20 % RH, 50 % RH and 80 % RH, it can be observed that all domain distances follow with a stepwise increase, with the reference sample reaching a maximum of 135 nm and 102 nm for the inter-domain distances between the large and medium domains, respectively. For the 0.05 M and 0.35 M EMIM DCA post-treated PEDOT:PSS films, it seems that the distances between the large domains increase stronger, reaching corresponding maxima of 185 nm and 198 nm, compared to the increase in medium domain distances with maxima of 73 nm and 75 nm, respectively.

This increase in the distances between the PEDOT domains can be led back to the fact that these domains are embedded in a matrix of PSS. As PSS is a hydrophilic polymer, it absorbs water when increasing the relative ambient humidity of the surrounding atmosphere, as it has been shown by Bießmann et al.[179] This water-uptake then leads to a swelling of the PSS matrix and results in the observed increase of the distances between the embedded hydrophobic PEDOT domains. As in the PEDOT:PSS polymer blend, only the PEDOT is the actual conductive polymer, it means that the free charge carriers, in this case holes, need to travel within and from one PEDOT chain to another. Since the PEDOT:PSS thin film structure consists of PEDOT enriched domains embedded in the PSS matrix, this means that the holes also need to travel between these conductive domains to yield conductivity throughout the film; working best the closer together these domains are. Consequently, the determined expansion in the PEDOT domain distances, caused by a swelling of the electrical insulating PSS matrix, means a reduction in the hole mobility. By this resulting in an increase of the electrical resistance,[58, 258, 259] as observed for the 0 M reference sample, shown in Figure 7.1a. This explanation matches well with the reversible behavior of the domain-domain distances, plotted in Figure 7.4c, when drying the thin films at 0 % RH and removing the water molecules again at the end of the experiment.

However, if an increasingly hindered inter-domain hole transport would be the only consequence of elevated humidity, it cannot explain why the film resistances of the 0.05 M and 0.35 M EMIM DCA post-treated samples show a completely reversed behavior. In fact, it suggests that additional effects are coming from the EMIM DCA post-treatment, which need to be considered.

7.4 Investigation of different conductivity contributions

During a post-treatment of PEDOT:PSS films with ILs, not only the domain morphology will be tailored by removal of the excessive PSS, but also the IL ions, in this case $EMIM^+$ and DCA^- will partially diffuse and stay inside the PEDOT:PSS structure.[100, 163] Subsequently, the thin PEDOT:PSS films now also comprise ionic species, which could contribute to the electrochemical behavior and, by this contribution, provide a reason why the resistance evolution under varying humidity is reversed.[119, 122, 124] To further investigate this effect, EIS measurements are performed with the IL post-treated and untreated PEDOT:PSS films. All specifics for the EIS sample geometry, measurement parameters, and equivalent circuit fitting are provided in Section 3.2.4. Furthermore, the applied humidity protocol and the actual R recorded within the measurement chamber are plotted in Figure 7.5. Unfortunately, for the 0.35 M EMIM DCA post-treated PEDOT:PSS sample it was not possible to measure EIS, because of difficulties with evaporation of the gold contacts as the gold did not stick on the thin film in the defined geometry and blurred out completely. Therefore, Figure 7.6 shows the Nyquist plots and equivalent circuit fitting results only for the 0 M and 0.05 M samples, for each sample examined at the relative humidity steps of 0 %, 20 %, 50 %, 80 %, and again 0 %.

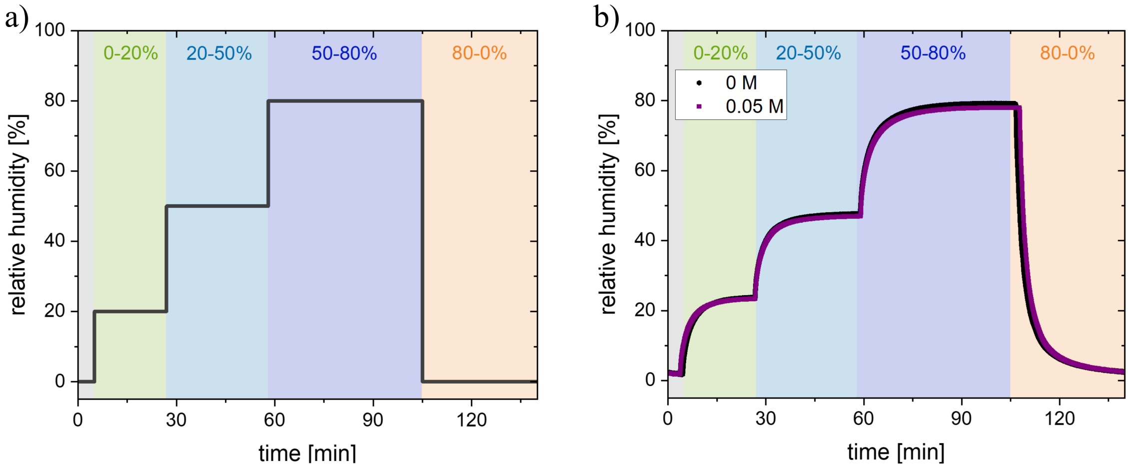

Figure 7.5 Humidity evolution during EIS examination of EMIM DCA treated PEDOT:PSS films. a) Relative humidity protocol applied during the EIS measurements. b) Relative humidity recorded simultaneously within the measurement chamber. Data shown for PEDOT:PSS thin films post-treated with pure THF 0 M (black hexagons) or with 0.05 M EMIM DCA (purple squares), respectively. Adapted with permission from Oechsle et al.[51] Copyright 2023 American Chemical Society.

In Figure 7.6a the Nyquist EIS data of the 0 M reference sample at different humidity steps are plotted, which all show one semicircle. This single semicircle implies that there is only one measurable contribution to the observed resistance behavior, namely an electronic one. By equivalent circuit modeling of these Nyquist data, using the model described in Figure 3.9d, the electronic resistance values displayed in Figure 7.6c are determined.[260]

The EIS resistance values for the 0 M reference sample are in the range of $10^5\ \Omega$, thus matching with the results of Figure 7.1a; although the exact values differ which is explainable by the use of completely different measurement techniques and geometries. Additionally, the resistance values obtained from EIS also show an increase/decrease of the electronic resistance upon increasing/decreasing the humidity similar to the results in Figure 7.1a. This can be also observed in the Nyquist plots in Figure 7.6a by the shift of the interception point with the Z' axis towards higher and then again lower Z' values. Overall, this behavior matches very well with the trend provided by the *in situ* resistance measurements in Section 7.2. Furthermore, it fits well with the assumption of increasing PEDOT domain distances, caused by reversible swelling of the PSS matrix at elevated humidities, and hence an increased hindrance of the hole transport; explaining the observed increase in the electronic resistance.[58, 258, 259]

In contrast to the reference sample, the Nyquist EIS data plots for the 0.05 M EMIM DCA post-treated PEDOT:PSS films in Figure 7.6b, show two semicircles instead of one; one depressed semicircle at the low frequency range and a segmented circle at the MHz frequency region.

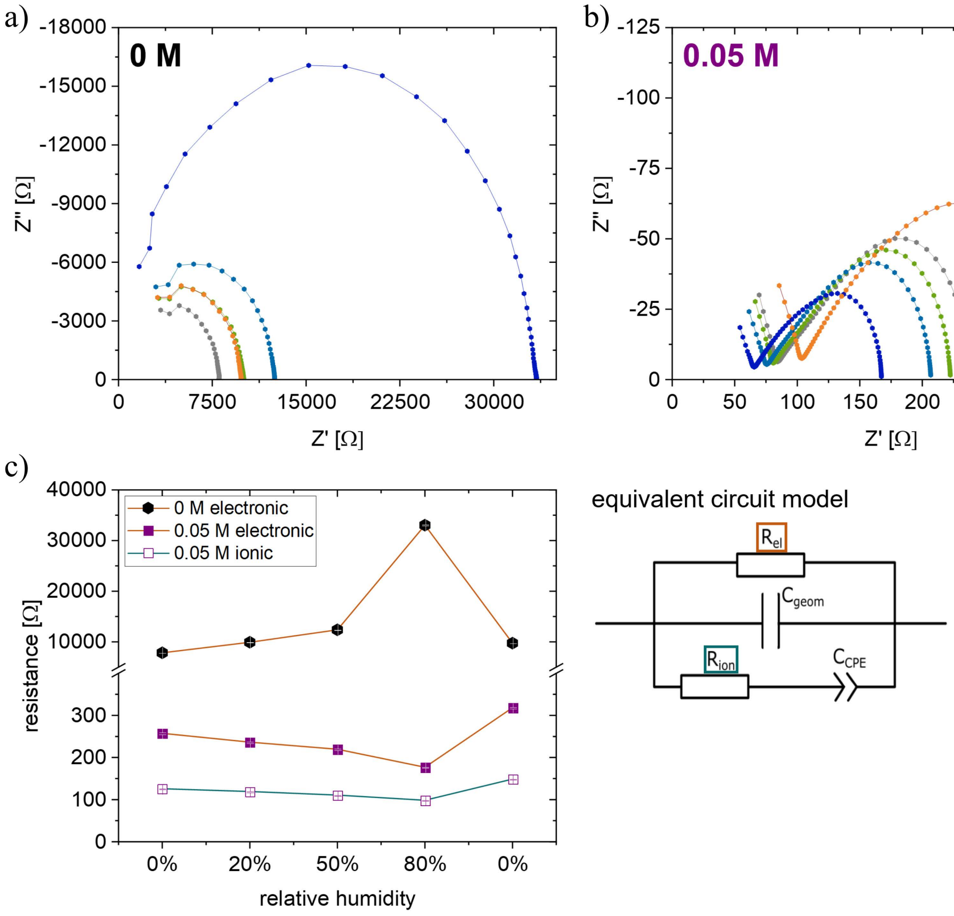

Figure 7.6 Humidity-dependent EIS results of EMIM DCA treated PEDOT:PSS films. Nyquist plots of the PEDOT:PSS films post-treated with a) 0 M and b) 0.05 M EMIM DCA, respectively measured at 0 % (gray), 20 % (green), 50 % (light blue), 80 % (blue), and 0 % (red) relative humidity values. c) Electronic (orange lines) and ionic resistance (cyan lines) values obtained from equivalent circuit fitting of the respective Nyquist plots at different relative humidities, for 0 M (black hexagons) and 0.05 M (purple squares) EMIM DCA post-treated PEDOT:PSS films. Adapted with permission from Oechsle et al.[51] Copyright 2023 American Chemical Society.

This finding indicates that there are two conduction contributions, namely an electronic and an ionic one.[119, 124, 260] Also for these Nyquist plots, equivalent circuit modeling according Section 3.2.4 is preformed and the results for the electronic and ionic resistances are shown in Figure 7.6c. Again, the exact resistance values differ, but the much lower order of 10^3 Ω for the resistance of the 0.05 M compared to the 0 M sample, matches well with the results of Figure 7.1a. The for this sample detected ionic resistance is assumed to arise from cationic charge transport, enabled due to the insertion of the ILs into the thin PEDOT:PSS film. For this, the cationic species, EMIM$^+$ and protons, are estimated to move within the PSS$^-$ matrix through a, in Section 2.2.4 detailed, continuous detachment and attachment along the polymer chains, which is facilitated by cation solvation and PSS chain movement.[21, 122, 261] When the ambient humidity increases, the ionic resistance decreases; and increases again, when the ambient atmosphere drops back to 0 % RH. This behavior can be explained, as the higher amount of water molecules leads to a better screening of the electrostatic attractions between the immobile sulfonate groups in the PSS chain and the cations, which enables a higher mobility of the cations.[124] Interestingly and at first counterintuitive, the electronic resistance also appears to decrease with increasing humidity for the 0.05 M EMIM DCA sample. One likely explanation could be that, due to the higher humidity, the water molecules solvate the PSS^- counter ion, which reduces the electrostatic traps for the holes. As a result, this increases the hole mobility and thus reduces the electronic resistance.[119] Upon removal of the water molecules by drying the films at the end of the experiment, the electronic resistance increases back, as consequently the electrostatic traps are exempt again. This effect on the electronic resistance possibly does not show for the 0 M reference sample, as here the conductive PEDOT domain distances and the amount of insulating PSS in between are so large that the hindrance of the inter-domain hole transport is the limiting factor.[163] Nevertheless, as the ionic resistance is the lowest, the ionic conduction appears to be the main contributor to the overall charge transport and by this explains why the combined resistance evolution, observed in Figure 7.1a, shows a reversed behavior for the films, which are post-treated with the IL.

7.5 Model description of the PEDOT:PSS charge transport behavior

Combining the information gained from the previously discussed *in situ* investigations, in this section a model is proposed, which describes the principles of the different behaviors of the with or without EMIM DCA post-treated PEDOT:PSS films. For a better perception this model is schematically depicted in Figure 7.7.

Figure 7.7a schematically illustrates the inner film morphology of PEDOT:PSS thin films. Within the PEDOT:PSS polymer blend films, PEDOT polymer enriched domains with enhanced crystallinity are present and are embedded within a matrix that mainly consists of the polymer PSS. As depicted, these PEDOT-rich domains are not clearly delineated from each other, but free ends, entanglements, and tie chains of the PEDOT polymer reaching inside the PSS matrix are present. From literature it is known that tie chains are relevant for the electrical conductivity in conjugated polymers because they bridge crystallites or local aggregates.[262, 263] In the case of PEDOT:PSS these tie chains can form connections between the PEDOT-rich domains and thus overcome the insulating PSS barrier, which enhances the charge carrier transport by the formation of a percolative network.[264, 265] In the graphical representation of this model the PEDOT-rich domains are presented as fringed blue dots, which are embedded inside the grey colored hole insulating PSS matrix.

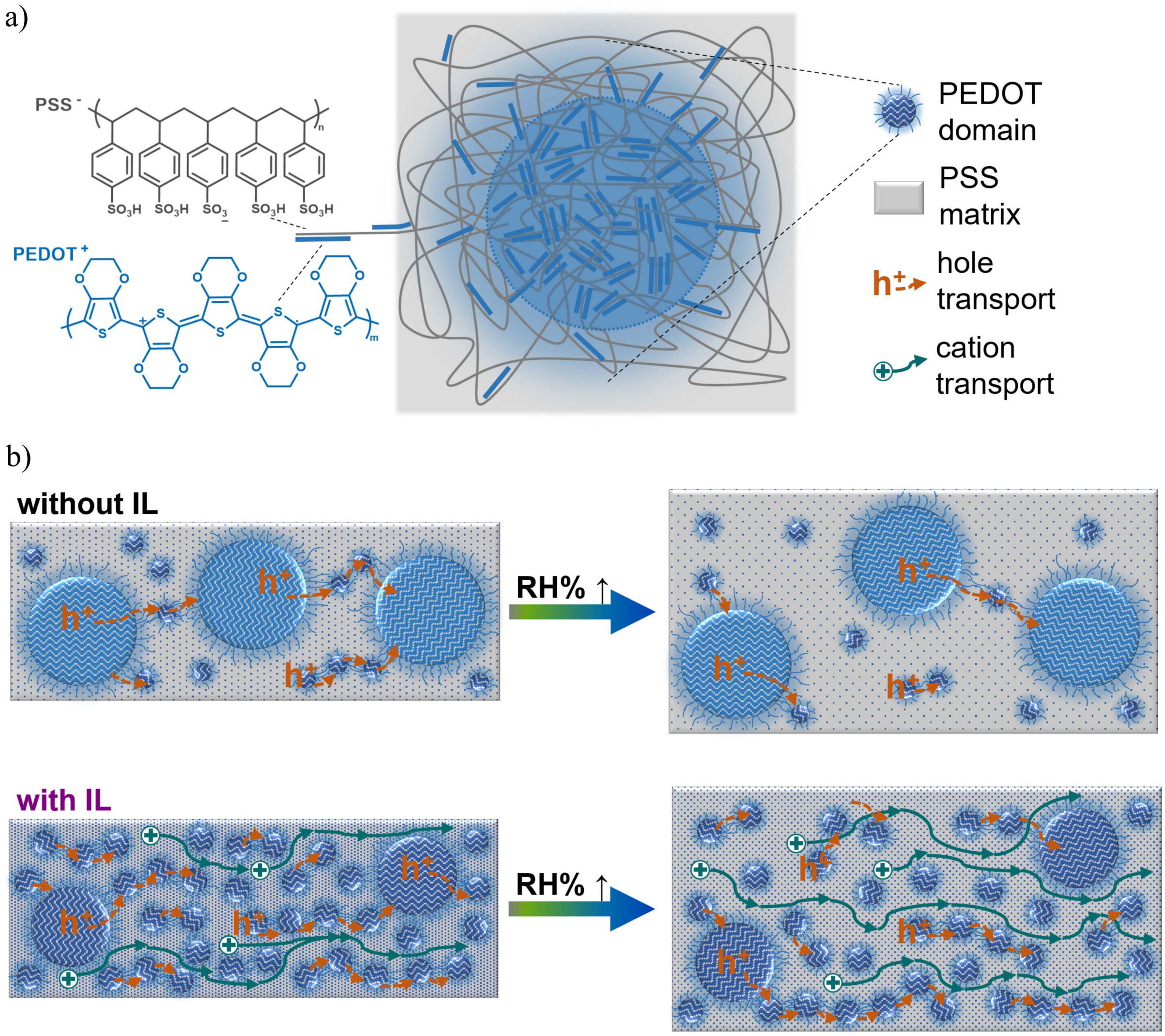

Figure 7.7 Model description of EMIM DCA post-treated PEDOT:PSS films at different humidities. a) Chemical structure of PEDOT and PSS, with a schematic illustration of the polymer blend inner film morphology, namely the PEDOT-rich domains embedded in a matrix of mainly PSS. b) Schematic representation of the morphology changes happening within the 0 M (top) and 0.05 M (bottom) EMIM DCA post-treated PEDOT:PSS films, upon the increase of the relative humidity (from left to right). Dashed orange arrows depict the electronic contribution, meaning the hole transport mainly via the PEDOT domains; and cyan arrows depict the ionic contribution, namely the cation transport predominantly happening through the PSS matrix. Adapted with permission from Oechsle et al.[51] Copyright 2023 American Chemical Society.

Figure 7.7b schematically shows the changes in the PEDOT:PSS thin film morphology upon humidity elevation, for the differently treated samples; reference sample without EMIM DCA treatment, upper row, and samples post-treated with EMIM DCA, bottom row. If first comparing the top left with the bottom left image, it can be seen that upon treatment with an IL, in this case EMIM DCA, the thereby induced removal of excess PSS leads to a change of the PEDOT:PSS morphology; from fewer and rather large PEDOT domains, towards smaller and more finely distributed PEDOT domains. In total shorter distances are achieved between the hole conductive domains, as seen from *in situ* GISAXS, resulting in an increased interconnection and coupling of the domains via tie chains, which enables the inter-domain hole transport.[264] This manifests in an increased electronic conductivity, depicted in Figure 7.7 by an increasing amount of dashed orange arrows in the bottom image. Furthermore, as observed by the EIS measurements, for the IL post-treated sample an additional transport of ionic charge carriers, in this case mainly cations, is detected, which is presented here by the cyan colored arrows. This additional transport is presumed to arise from the input of EMIM cations, which on the one hand can travel through the partially negatively charged PSS polymer matrix themselves, as detailed in Section 2.2.4. Or on the other hand, they can interact with the sulfonate groups in the PSS chain and thereby enable an easier dissociation of protons, which are smaller and thereby allow a higher transport mobility through the PSS matrix.[119] Overall, with this proposed model the considerably smaller resistances for the EMIM DCA post-treated samples compared to the 0 M reference sample in the dry state can be explained in a straightforward manner.

Furthermore, the model shown in Figure 7.7b, also schematically describes what happens upon exposure of the differently treated samples to an elevated humidity; respectively shown from left (low humidity) to right (high humidity). For the reference sample the, with *in situ* GISAXS measurements observed, increase in the domain-domain distances upon humidity elevation are illustrated, which lead to an increase in the hole transport barrier and by this explains the, in Figure 7.1 monitored raise of the film resistance.[35, 58, 179, 258, 259] Also for the EMIM DCA post-treated PEDOT:PSS films, Figure 7.7b bottom row, the domain-domain distances increase upon the increase of the humidity, which would in principle lead to an increase in the electronic resistance. However, for this sample, especially the small and medium domains are the significant contributions to the hole conductivity, because of their way higher count apparent in the associated domain size distributions in Figure 7.4b. As these small and medium domains are even in the swollen state still not as far away from each other, as compared to the domains in the reference sample, quite some PEDOT domain-domain interconnections are remaining, which facilitate the hole transport. As a result, the electronic resistance of the EMIM DCA post-treated samples is not as high.[163] More importantly, the EMIM DCA ions bring another resistance decreasing contribution into account, namely the screening of the PSS^- attraction towards the holes in the $PEDOT^+$, by increasing contributions from both water molecule solvation and $EMIM^+$ cations. This screening effect reduces the electrostatic traps for the hole transport and can account as explanation for the observed humidity-dependent reduction in the electronic resistance.[119] Within this model, the hole transport (electronic resistance) enhancing effect upon elevated humidity is represented in Figure 7.7b bottom right by a high amount of dashed orange arrows. As evidenced by EIS measurements, especially at elevated humidities the additional ionic contribution, here transport of cations, comes into play. The observed decrease in the ionic resistance can be explained, on the one hand, by the water molecules, which solvate the sulfonate groups in the immobile PSS chain. With this, they cause the screening of the electrostatic attractions towards the cations, which themselves are also surrounded by a mobile hydration shell, and thus, an easier cation transport through the PSS matrix is achieved.[122, 124, 261] On the other hand, upon hydration the polymer gets plasticized by water molecules, which enables a better chain motion and consequently a better cation transport.[122] This high contribution of the ionic transport leads to the, in Figure 7.1 observed, strong decrease of the film resistance upon humidity increase, and is depicted in our model by an increased number of cyan colored arrows through the PSS matrix. As all the above-described effects upon elevated humidity are caused by the increased presence of water molecules within the PEDOT:PSS films, they consequently exhibit a reversible behavior as observed when the films are dried and the water molecules are extracted again.

Summarizing, from the combination of knowledge gained from the in this chapter discussed *in situ* investigation methods, the schematic model is presented in Figure 7.7, which clarifies why the humidity induced resistance evolution of thin PEDOT:PSS films post-treated with 0.05 M or 0.35 M EMIM DCA is completely reversed compared to that of a 0 M pure PEDOT:PSS reference sample.

7.6 Summary

In this chapter, the contribution of electronic and ionic charge carrier transport to the resistance of thin PEDOT:PSS films post-treated with different concentrations of EMIM DCA (0 M, 0.05 M, 0.35 M), is examined dependent on the ambient humidity. *In situ* resistance measurements performed while exposing the samples to a defined protocol of stepwise increase and decrease of the humidity, reveal a difference in the conductance behavior of 0.05 M and 0.35 M EMIM DCA post-treated samples compared to the 0 M reference sample. For the reference sample the resistance increases with increasing humidity, which can be explained by a swelling of the PSS matrix, resulting in an increase of the overall domain-domain distances; as evidenced by *in situ* GISAXS measurements. This increase in the distances causes a higher hindrance of the inter-domain hole transport, proven by the increased electronic resistance observed in the EIS measurements. For the EMIM DCA post-treated samples on the one hand a morphological rearrangement towards smaller, more finely distributed, and thereby more densely packed PEDOT enriched domains is found, which boosts the hole transport and strongly decreasing the electronic resistance compared to the reference sample. On the other hand, by means of the EIS technique the emergence of an additional ionic charge transport contribution is shown, caused by the introduction of the IL ions. This ionic resistance decreases upon elevated humidity, due to the improved cation transport through water solvation and electrostatic screening of the PSS^- charge; and explains the reversed film resistance evolution in comparison to a 0 M reference sample. Supported by these *in situ* morphology and impedance measurements a model is introduced, which describes the charge transport behavior under elevated humidity. This model provides a contribution to a better understanding of the possible influences of the ambient environment on the variety of PEDOT:PSS based devices.

8 Humidity influence on electric and ionic charge transport in PEDOT:PSS films

This chapter is based on the publication "*Unraveling the Humidity Influence on the Electrical Properties of Ionic Liquid Posttreated Poly(3,4-ethylene dioxythiophene): Poly(styrenesulfonate) Films*" (A. L. Oechsle, T. Schöner, C. Geiger, S. Tu, P. Wang, R. Cubitt, P. Müller-Buschbaum, Macromolecules 2023, 56, 22, 9117-9126; DOI: 10.1021/acs.macromol.3c01842). Reprinted with permission from Oechsle et al.[52] Copyright 2023 American Chemical Society. Experiments were performed in collaboration with master student Tobias Schöner.

In this chapter, the conductive polymer blend PEDOT:PSS, popular for numerous organic applications, is investigated in terms of the influences that ionic liquid treatment and ambient humidity have on its conductivity properties. PEDOT:PSS thin films post-treated with different concentrations of the IL EMIM DCA are exposed to different relative humidity steps from 0 % RH up to 90 % RH. Simultaneously, the film swelling and increase in the scattering length density (SLD), indicating a water uptake of the films, are monitored $in\ situ$ with spectral reflectance (SR) and time-of-flight neutron reflectometry (ToF-NR). Additional $in\ situ$ electrochemical impedance spectroscopy (EIS) shows that the pristine PEDOT:PSS only has an electronic conductivity, while for the IL treated samples an additional ionic conductivity contribution is observed. Upon humidity increase, the electronic conductivity of all PEDOT:PSS thin films decreases, while the ionic conductivity for IL post-treated thin films is enhanced by the intake of water molecules.

8.1 In situ humidity investigation of IL post-treated PEDOT:PSS

Organic electronics are becoming of increasing importance in our everyday lives. Whether as organic light-emitting diodes[226, 248], bioelectronics[245, 266], displays[251, 267], transistors[232, 247, 268], solar cells[33, 225], or sensors[58, 217], organic electronics will be indispensable in the future, as they have huge advantages compared to their inorganic counterparts. Besides being typically low or non-toxic, lightweight, transparent, and mechanically flexible, organic electronics usually can be processed in a wet chemical route from solution, which allows for a fast and cost-efficient large-scale device fabrication process by making use of spraying, printing, or dip coating.[6, 7] In general, these devices are likely exposed to various environmental influences, during synthesis but also during their use in diverse applications, which can sometimes strongly condition the performance of the materials. Therefore, during the development of materials for future devices, it is essential to consider and investigate possible effects of different environmental influences like temperature or atmospheric composition, e.g. the presence of water and oxygen, on the performance and stability. Numerous organic materials, with a variety of characteristics, are presently under extensive investigation or already in use. Either based on organic small molecules, for example, anthracene derivatives, oligothiophenes and fullerenes,[269] or based on polymers, such as polythiophenes, polyacetylenes, and polypyrroles.[190] One particular organic polymer semiconductor is especially popular and is regularly used for multiple purposes in organic electronics, namely the polymer blend PEDOT:PSS.[17, 21, 244] On the one hand it consists of PEDOT with an oxidized polythiophene backbone, thus making it an excellent positive charge carrier conductor. On the other hand, it consists of PSS, which is a polyanion that stabilizes the positive charge carriers and additionally renders the entire polymer blend water-soluble.[16] Previous research with a view on the improvement of PEDOT:PSS properties for specific applications, for instance the electrical conductivity (σ) for organic photovoltaics,[24, 30] the Seebeck coefficient (S) for thermoelectrics,[38, 53] or the flexibility for transparent electrodes,[34, 35] mostly utilize the high and easy tunability of PEDOT:PSS, which is facilitated by its special nanoscale domain structure. As introduced in Section 2.1.2, if prepared as thin films, PEDOT:PSS forms pancake-shaped PEDOT enriched domains embedded within a PSS matrix. This structure results from the typical fabrication out of aqueous solution, where the non-soluble PEDOT shapes into spherical cores that are surrounded by shells of water-soluble PSS.[19, 84] As PEDOT is the actual p-conductor and PSS is an insulator, the free charge carriers need to travel from one PEDOT domain to another to enable the electrical conductivity of PEDOT:PSS thin films. With different treatment approaches, like inorganic salts[27, 29], acids or bases[33, 192], solvents[34, 93], surfactants[36, 37], or ionic liquids[46, 100], this special domain structure can be tuned and the properties of PEDOT:PSS are desirably altered. As presented in Chapter 5, for the PEDOT:PSS application as a thermoelectric material, an IL treatment procedure where thin PEDOT:PSS films are post-treated with EMIM DCA turned out to be especially promising. With this treatment, a simultaneous strong increase of the electrical conductivity (1126 S cm^{-1}) and the Seebeck coefficient (46 μV K^{-1}) was achieved, thus facilitating a thermoelectric power factor of 236 μW m^{-1}K^{-2}.[163] Here, two main underlying effects caused this property improvement.[44, 48, 100] On the one hand, the IL anions interact with the PEDOT, leading to a dedoping of the conductive polymer by reducing the positive charge carriers, i. e. polarons and bipolarons within the PEDOT chain. Such a reduction of the positive charge carriers is beneficial for the Seebeck coefficient in TE materials and results in an increased S. On the other hand, the IL cations simultaneously interact with the polyanion PSS, weakening the electrostatic attraction between the PEDOT and PSS chains, and thus enable a removal of some PSS from the films. This removal of excessive PSS, which was evidenced via XPS measurements by Saxena et al.[100] or Yemata et al.[48], induces a reorientation of the PEDOT:PSS domain morphology towards small and finely distributed PEDOT enriched conductive domains with less electronically insulating PSS matrix in between.[50, 163] The thus resulting network of overall closer-packed conductive domains and hence a reduced energy barrier for the positive charge carrier-transport can explain the observed increase in electrical conductivity σ.[24, 163] However, as mentioned before, it is not enough to only tune the properties of a material to a desired extent, it is also necessary to consider and investigate possible effects of different environmental influences,[50, 51, 179] like the temperature influence discussed in Chapter 6, or the ambient humidity, which was already presented in Chapter 7, but will be more focused in the study presented in this chapter. The investigations discussed in the previous Chapter 7, have shown that the properties of PEDOT:PSS change strongly upon experiencing different humidity values, and even more interestingly that the trends of the humidity influence completely reverse dependent on if the films have been post-treated with the IL EMIM DCA or not.[51]

To further determine the different underlying effects of the humidity influence, in this study PEDOT:PSS thin films post-treated with different concentrations of the IL EMIM DCA are exposed to a defined humidity protocol while simultaneously investigate the occurring property changes. With systematic *in situ* SR measurements the swelling behavior of the films is followed and with *in situ* ToF-NR changes in the film SLD profiles are determined. Both techniques give information about the film thickness, while ToF-NR further provides information about the amount of water incorporated into the film at different ambient humidity values. As the conductivity is the most important material parameter for the usage in various organic electronic applications, additionally *in situ* EIS is performed, to monitor the charge carrier conductance of the EMIM DCA post-treated PEDOT:PSS films. By combining all results from these *in situ* experiments, the influence of humidity on IL treated PEDOT:PSS thin films can be explained in more detail, and thus contribute crucial knowledge for the application of this popular material in numerous organic electronic devices.

Based on the results in the Chapter 5, the two most promising EMIM DCA post-treatment concentrations of 0.05 M and 0.35 M are selected and an additionally 0 M reference sample is investigated. For this study, it was necessary to prepare two sets of samples, in order to meet the respective requirements of the utilized measurement techniques. For the ToF-NR & SR silicon wafers were used as substrates because they own a very smooth, well reflecting surface and are mechanically stable. Therefore, they facilitate a large sample size of 70 x 70 mm^2 with low substrate bending, which is especially important for the large footprint of the ToF-NR measurements. The samples for the EIS can be smaller, 25 x 25 mm^2, but need a defined geometry of conductive and non-conductive areas on the surface, which is possible to obtain by etching of ITO substrates. However, even though different geometries and sample substrates have to be used, the thin film fabrication is kept as similar as possible to sustain a comparability of the data. The precise descriptions of the respective sample preparation procedures are provided in Chapter 4. Furthermore, the pre-characterization and *in situ* measurement methods are detailed in Chapter 3.

8.2 Humidity-dependent film swelling and water uptake

For a closer investigation of the humidity influence on EMIM DCA post-treated PEDOT:PSS thin films SR and ToF-NR, respectively detailed in Section 3.1.3 and Section 3.4.3, were chosen as measurement techniques. Unfortunately, for the 0.35 M concentration the film surface is too rough to be measurable with ToF-NR & SR and therefore an additional sample with 0.01 M concentration is investigated. All measurements are performed *in situ* during exposure of the respective films with a defined humidity protocol shown for the 0 M and 0.05 M samples in Figure 8.1a, and for the 0.01 M sample in Figure 8.1b.

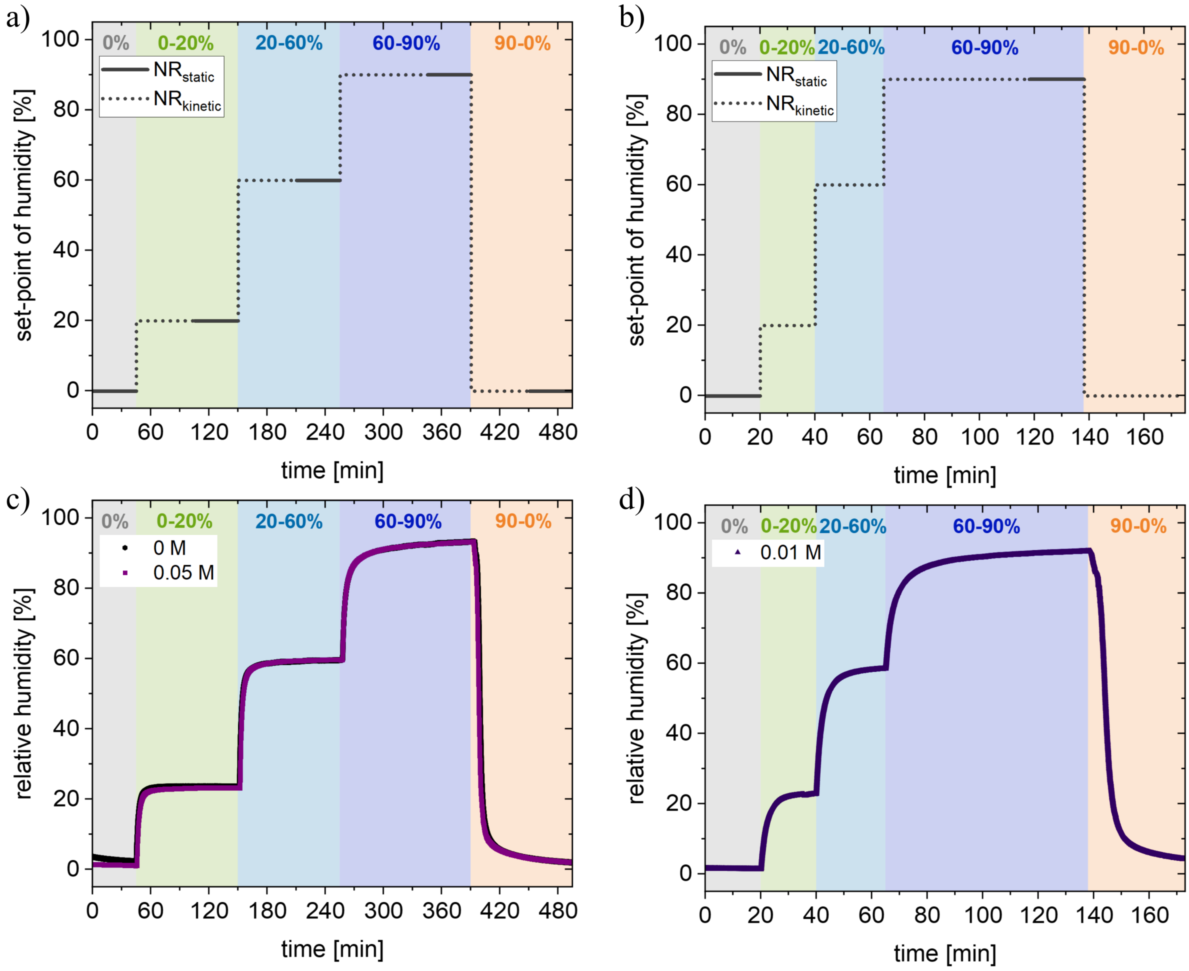

Figure 8.1 Humidity evolution during the SR & ToF-NR examination of EMIM DCA treated PEDOT:PSS films. a) & b) Applied humidity protocol, and c) & d) actual relative humidity recorded during *in situ* ToF-NR and SR measurements for the thin PEDOT:PSS films post-treated with 0 M (black hexagon) and 0.05 M (purple squares), and 0.01 M (dark purple triangle) EMIM DCA concentration. Solid lines in a) & b) show the measurement period when static ToF-NR and dashed lines when kinetic ToF-NR measurements were performed. The respective humidity stages are marked with different background colors; 0 % RH (gray), 0 – 20 % RH (green), 20 – 60 % RH (light blue), 60 – 90 % RH (blue), and re-drying 90-0 % RH (orange). Adapted with permission from Oechsle et al.[52] Copyright 2023 American Chemical Society.

Due to time-limited usage of the neutron facility, the protocol of the 0.01 M sample is shortened. However, this means that a complete achievement of the equilibrium state, especially at high RH, is not always guaranteed. Therefore, the results of this sample should be carefully regarded as merely additional input. The 0 M and 0.05 M samples (and 0.01 M in brackets) are exposed to the following set-point of the humidity: a first N_2 drying stage at 0 % RH for 45 min (20 min), then an increase of the humidity to 20 % RH for 105 min (20 min), then to 60 % RH for 105 min (25 min), followed by a 90 % RH step for 135 min (73 min) and finally a further drying at 0 % RH for 105 min (35 min). During the experiments the actual humidity inside the chamber was always recorded and is plotted in Figure 8.1c and d for the respective samples. Facilitated by a window in the chamber lid, SR measurements are conducted simultaneously, which allow to *in situ* observe the evolution of the film thickness following the defined humidity protocol. The results for the 0 M and 0.05 M samples, and the 0.01 M sample are plotted in Figure 8.2.

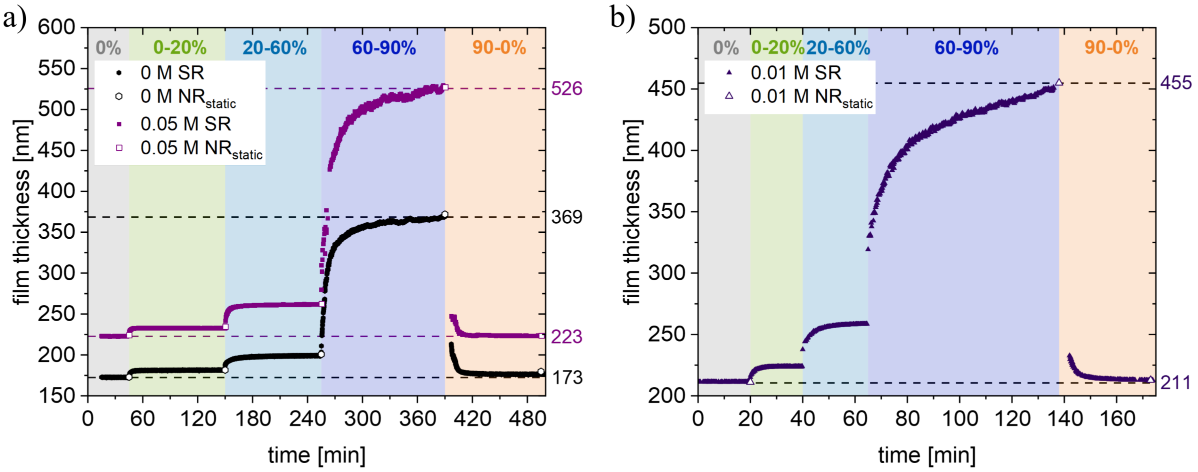

Figure 8.2 Film thickness evolution of EMIM DCA post-treated PEDOT:PSS films at different humidities Humidity-dependent film thickness evolution obtained from *in situ* SR (full symbols) and static ToF-NR (hollow symbols) measurements of a) 0 M (black hexagon) and 0.05 M (purple squares), and b) 0.01 M (dark purple triangle) EMIM DCA post-treated PEDOT:PSS films. The respective humidity stages are marked with different background colors; 0 % RH (gray), 0 – 20 % RH (green), 20 – 60 % RH (light blue), 60 – 90 % RH (blue), and re-drying 90-0 % RH (orange). Dashed lines mark the respective thicknesses for the dried and fully swollen state. Adapted with permission from Oechsle et al.[52] Copyright 2023 American Chemical Society.

From Figure 8.2, the initial thickness values t_{SR} for the 0 M, 0.01 M, and 0.05 M samples determined with SR are 173 nm, 211 nm, and 223 nm, respectively. A comparison of these values with the thickness values obtained from the pre-characterization with surface profilometer t_{profil} and X-ray reflectometry t_{XRR}, listed in the table in Figure 8.3a, shows that the values match well and thus confirms reliable SR results. The corresponding XRR curves are plotted in Figure 8.3b, and the surface profilometry and XRR measurement details are provided in Section 3.3.1 and Section 3.4.1, respectively.

Furthermore, it can be seen in Figure 8.2 that upon a stepwise increase of the chamber humidity, all samples follow with a stepwise increase of the film thickness, whereby the most substantial swelling happens during the 90 % RH step. The maximum film thicknesses, and the corresponding relative thickness, calculated by dividing the actual bulk layer thickness by the respective initial value ($rel. t_{SR} = t_{SR}/t_{SR,0}$), are: 369 nm and 2.13 for the 0 M sample, 451 nm and 2.14 for the 0.01 M sample, and 526 nm and 2.36 for the 0.05 M sample. Therefore, indicating that the relative film swelling is more significant for a higher EMIM DCA post-treatment concentration. All film thickness values of the different post-treated PEDOT:PSS samples, obtained with SR at the equilibrium of every humidity step, are listed in Table 8.1.

	NR & SR samples		
	0 M	0.01 M	0.05 M
t_{profil} [Å]	1783 ± 209	2059 ± 322	2143 ± 321
t_{XRR} [Å]	1811 ± 2	2245 ± 2	2344 ± 2
SLD_{XRR} [10^{-6} Å^{-2}]	13.34 ± 0.01	12.55 ± 0.01	12.56 ± 0.01
$rough_{XRR}$ [Å]	23 ± 2	38 ± 4	20 ± 2

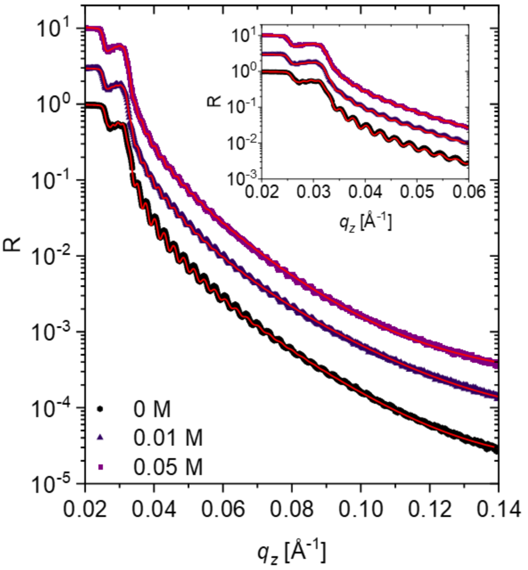

Figure 8.3 Pre-characterization results of EMIM DCA post-treated PEDOT:PSS films for ToF-NR & SR. Table listing the from surface profilometry obtained thin film thickness values (t_{profil}), and XRR fitting results for the thicknesses (t_{XRR}), scattering length densities (SLD_{XRR}) and roughnesses ($rough_{XRR}$) of the 0 M, 0.01 M, and 0.05 M EMIM DCA post-treated PEDOT:PSS films on silicon for the ToF-NR & SR measurements. XRR pre-characterization curves. X-ray reflectivity curves of the ToF-NR and SR samples, 0 M (black hexagon), 0.01 M (dark purple triangle) and 0.05 M (purple squares) EMIM DCA post-treated PEDOT:PSS films together with their corresponding fit results (red lines).

Table 8.1 Film thicknesses of EMIM DCA post-treated PEDOT:PSS films at different humidities obtained with SR. From SR data obtained sample thickness (t_{SR}) and the corresponding relative thickness ($rel. t_{SR}$), calculated by dividing the actual bulk layer thickness by the respective initial value ($t_{SR}/t_{SR,0}$), of 0 M, 0.01 M, and 0.05 M EMIM DCA post-treated PEDOT:PSS films, in equilibrium at different humidity stages.

SR results		0 % RH	20 % RH	60 % RH	90 % RH	re-dried
0 M	t_{SR} [Å]	1728	1816	1993	3688	1763
	$rel. t_{SR}$	1.00	1.05	1.15	2.13	1.02
0.01 M	t_{SR} [Å]	2114	2241	2586	4508	2127
	$rel. t_{SR}$	1.00	1.06	1.22	2.14	1.00
0.05 M	t_{SR} [Å]	2229	2326	2618	5262	2232
	$rel. t_{SR}$	1.00	1.04	1.17	2.36	1.00

Additionally, the custom-made sample environment, described in Section 3.5.3, allows to simultaneously perform *in situ* ToF-NR measurements, from which information about changes in the SLD profiles along the direction perpendicular to the substrate surface can be obtained. From these SLD profiles the water uptake as well as information about the polymer layer thickness evolution is independently extracted as described in Section 2.3.4. In general, displayed in Figure 8.1, static ToF-NR measurements are conducted at times when the films are in equilibrium or approaching equilibrium, and kinetic ToF-NR measurements with high time resolution are performed during the swelling of the post-treated PEDOT:PSS thin films. The static ToF-NR reflectivity (R) curves of the three tested samples conducted at the different equilibrated humidity stages are presented in Figure 8.4a-c, together with their corresponding fit curves obtained by using the two-layered model described in Section 2.3.4.

From these model fits, information about the equilibrated polymer film thicknesses t_{NR} at the end of each respective humidity step can be obtained, and the results are listed in Table 8.2 and marked in Figure 8.2 as hollow symbols. Overall, it shows that the thickness evolution obtained from modeling the static ToF-NR data matches with the results from the SR measurements.

Table 8.2 Static ToF-NR fitting results for EMIM DCA post-treated PEDOT:PSS films at different humidities. From static ToF-NR data fits obtained polymer bulk layer thickness ($\boldsymbol{t_{NR}}$) and corresponding relative thickness ($\boldsymbol{rel. t_{NR}}$), calculated by dividing the actual bulk layer thickness by the respective initial value ($\boldsymbol{t_{NR}/t_{NR,0}}$), scattering length density ($\boldsymbol{SLD_{NR}}$), and roughness ($\boldsymbol{rough_{NR}}$) of 0 M, 0.01 M, and 0.05 M EMIM DCA post-treated PEDOT:PSS films, in equilibrium at different humidity stages.

ToF-NR results		0 % RH	20 % RH	60 % RH	90 % RH	re-dried
0 M	t_{NR} [Å]	1730 ± 2	1816 ± 2	2008 ± 2	3719 ± 4	1798 ± 2
	$rel. t_{NR}$	1.00	1.05	1.16	2.15	1.04
	SLD_{NR} [10^{-6} Å^{-2}]	2.26 ± 0.01	2.84 ± 0.01	3.32 ± 0.01	4.83 ± 0.01	2.42 ± 0.01
	$rough_{NR}$ [Å]	14 ± 1	15 ± 2	18 ± 2	23 ± 2	14 ± 1
0.01 M	t_{NR} [Å]	2111 ± 2	-	-	4549 ± 5	2128 ± 2
	$rel. t_{NR}$	1.00	-	-	2.16	1.01
	SLD_{NR} [10^{-6} Å^{-2}]	2.01 ± 0.01	-	-	4.30 ± 0.01	2.13 ± 0.01
	$rough_{NR}$ [Å]	18 ± 2	-	-	24 ± 2	16 ± 1
0.05 M	t_{NR} [Å]	2246 ± 2	2348 ± 2	2626 ± 3	5271 ± 5	2239 ± 2
	$rel. t_{NR}$	1.00	1.05	1.17	2.35	1.00
	SLD_{NR} [10^{-6} Å^{-2}]	2.03 ± 0.01	2.30 ± 0.01	2.82 ± 0.01	4.48 ± 0.01	2.09 ± 0.01
	$rough_{NR}$ [Å]	18 ± 2	19 ± 2	20 ± 2	24 ± 2	14 ± 1

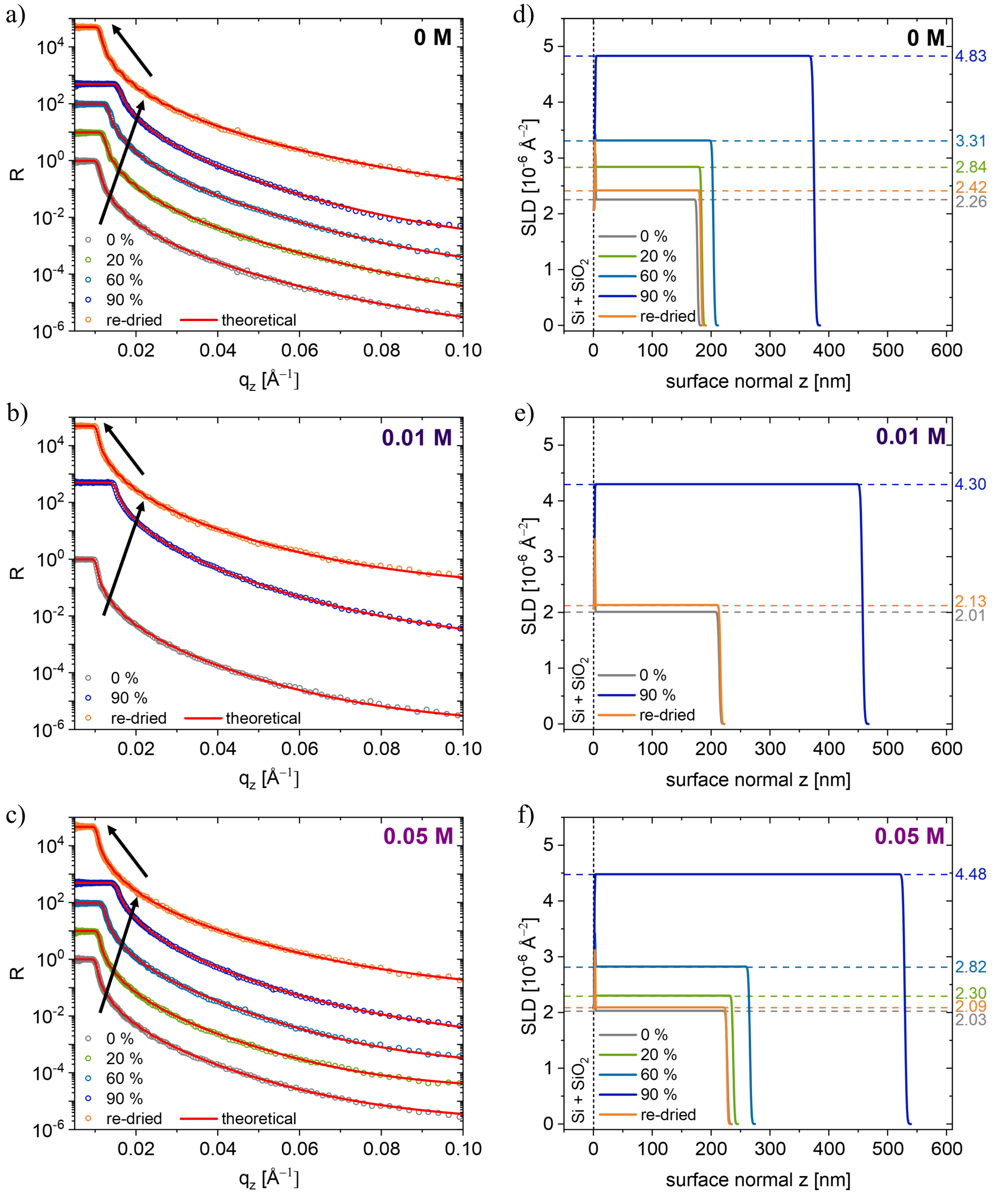

Figure 8.4 *In situ* static ToF-NR data of EMIM DCA post-treated PEDOT:PSS films at different humidities. Static reflectivity R curves for a) the 0 M reference, b) 0.01 M and c) 0.05 M EMIM DCA post-treated PEDOT:PSS films, collected in equilibrium at the end of each humidity stage, namely 0 % RH (gray), 20 % RH (green), 60 % RH (light blue), 90 % RH (blue), and re-drying 0 % RH (orange). The reflectivity data are shifted along the y-axis for sake of clarity and the black arrows emphasize the shifts of the critical edge. The red solid lines present the fits to the data using a two-layer model. d), e) and f) Corresponding ***SLD*** profiles obtained from fits of the static ToF-NR data, with dashed lines marking the ***SLD*** values for the respective humidity step. Adapted with permission from Oechsle et al.[52] Copyright 2023 American Chemical Society.

As marked by black arrows in Figure 8.4a-c, the static ToF-NR data show a clear shift of the critical edge towards higher q_z-values with increasing humidity and back to lower q_z-values when redrying the thin film samples. As explained in Section 2.3, this shift means a change in the SLD of the post-treated PEDOT:PSS films following the humidity increase and indicates the uptake of D_2O into the thin films. From the results of the fits (red lines) of the static ToF-NR data, listed in Table 8.2, the respective SLD profiles along the surface normal of the different samples can be obtained, shown in Figure 8.4d-f. This representation gives a clear view of what is happening with the film thickness and SLD of the EMIM DCA post-treated PEDOT:PSS films while experiencing the applied humidity protocol. After the initial N_2 drying, the SLD value ($SLD_{0\%}$ = 2.26×10^{-6} Å^{-2}) of the 0 M reference sample, is higher compared to the 0.01 M and 0.05 M post-treated films, with 2.01×10^{-6} Å^{-2} and 2.03×10^{-6} Å^{-2}, which is ascribed to the intake of the IL molecules into the PEDOT:PSS polymer. If now stepwise increasing the chamber humidity, for all three studied films a stepwise swelling of the film thickness and an additional rise in the SLD can be observed; achieving maxima for both values once the equilibrium is reached at 90 % RH. The 0 M reference sample hereby shows a strong increase of the SLD, to an overall maximum of 4.83×10^{-6} Å^{-2}, while compared to this, the 0.05 M sample only reaches a maximum SLD of 4.48×10^{-6} Å^{-2}. Interestingly the PEDOT:PSS thin film post-treated with 0.01 M EMIM DCA reaches an even lower SLD maximum of 4.30×10^{-6} Å^{-2} at 90 % RH, which is strongly believed to be due to the shortened humidity protocol and thus caused insufficient time for the film to fully reach the swollen state equilibrium. In general, it can be concluded that the post-treatment with EMIM DCA shows an influence on the SLD evolution and therefore on the uptake of D_2O into the PEDOT:PSS films. Additionally, it can be noted that the formation of a D_2O enrichment layer on top or below the polymer bulk layer could not be detected. This finding indicates that the D_2O molecules easily diffuse and evenly integrate into the polymer bulk layer, possibly favored due to the hygroscopic PSS matrix and the additional intake of the IL ions. As can also be seen clearly from Figure 8.4d-f, for all three samples the increase in the SLD and the film thickness is nearly completely reversible upon redrying the samples at the very end of the humidity protocol.

For a further investigation of the uptake of the D_2O not only during the equilibrium stage, but also dynamically during the film swelling, kinetic ToF-NR measurements are also performed, as marked in Figure 8.1. Exemplary ToF-NR data of these kinetic experiments are shown in Figure 8.5 together with their fits as solid red lines. The increase in the film roughness (Table

8.2) upon higher relative humidities causes a smearing of the Kiessig fringes. Therefore, in the following only the shift of the critical edge and the kinetic evolution of the samples SLDs are discussed, with the results being presented in Figure 8.6a and b.

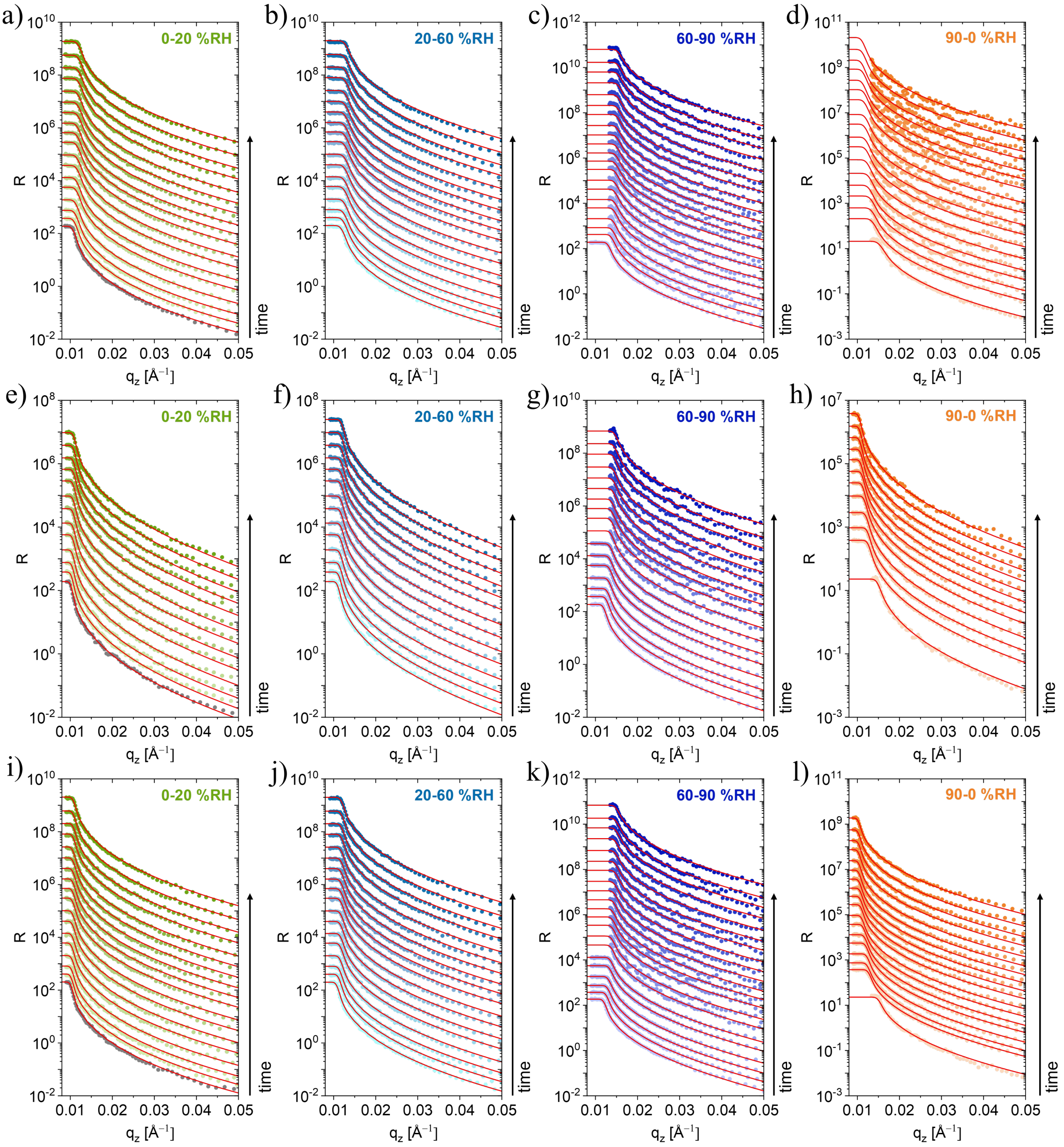

Figure 8.5 Kinetic ToF-NR curves of EMIM DCA post-treated PEDOT:PSS films at different humidities. Kinetic ToF-NR curves for a)-d) 0 M, e)-h) 0.01 M, and i)-l) 0.05 M EMIM DCA post-treated PEDOT:PSS films, respectively shown from left to right during the different humidity steps. The reflectivity data are shifted along the y-axis for sake of clarity, from bottom to top with proceeding experiment time, and the red solid lines present the fits of the data. Adapted with permission from Oechsle et al.[52] Copyright 2023 American Chemical Society.

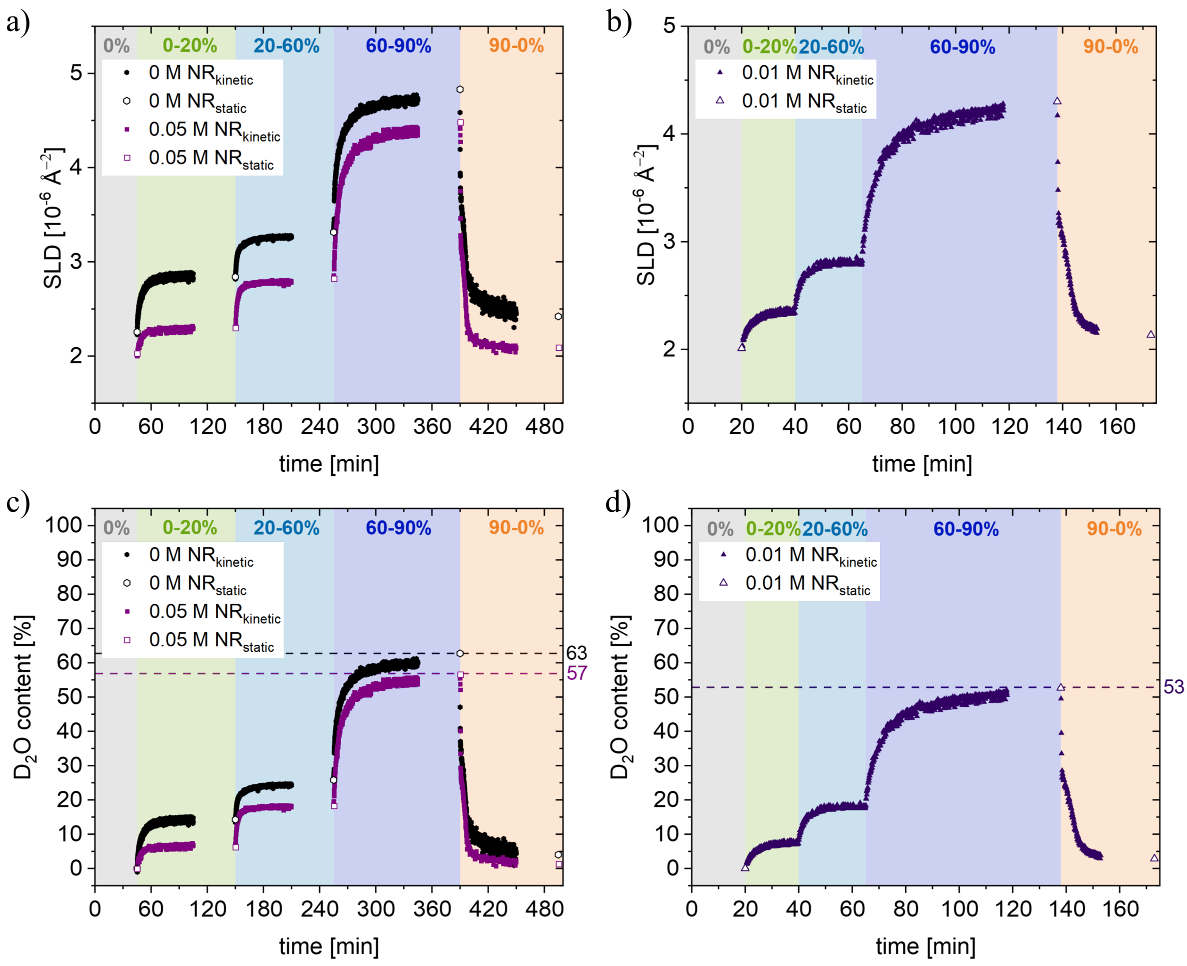

Figure 8.6 *SLD* and D_2O content evolution of EMIM DCA post-treated PEDOT:PSS films at different humidities. a), b) ***SLD*** evolution during the *in situ* ToF-NR experiment of the 0 M (black hexagon), 0.01 M (dark purple triangle), and 0.05 M (purple squares) EMIM DCA post-treated PEDOT:PSS sample, obtained from fits of the kinetic (full symbols) and static (hollow symbols) ToF-NR data. c), d) Corresponding incorporated D_2O content, with dashed lines marking the maximum D_2O content for each sample in the equilibrium state of the 90 % RH humidity stage. Adapted with permission from Oechsle et al.[52] Copyright 2023 American Chemical Society.

As introduced in Section 3.4.3, following Equation (3.39), the D_2O volume fraction ($\phi(t)$) inside the thin films can be calculated using the obtain SLD evolution plotted in Figure 8.6:

$$\phi(t) = \frac{SLD_{exp}(t) - SLD_{dry}}{SLD_{D_2O} - SLD_{dry}} \tag{3.39}$$

containing the experimentally measured polymer bulk SLD at the time t ($SLD_{exp}(t)$), the SLD of the dry film in equilibrium at the end of the first 0 % RH humidity stage (SLD_{dry}), and the SLD of D_2O obtained from the literature (SLD_{D_2O}= 6.36 × 10^{-6} Å^{-2}).[177] From the plotted D2O volume fraction in Figure 8.6c and d, it is clearly visible that with the stepwise raise in the chamber environment humidity, all three thin films increasingly incorporate D_2O. In doing so they follow a similar kinetic trend for each humidity step, namely a strong initial incline and then a slow leveling and reaching of the respective equilibrium, with the strongest D_2O uptake happening during the 60 - 90 % RH stage. Maximum D_2O contents of 63 %, 53 % and 57 % are obtained for the 0 M, 0.01 M, and 0.05 M EMIM DCA post-treated samples, respectively.

Furthermore, it can be noted that the D_2O uptake kinetics of the post-treated sample compared to the untreated samples do not strongly distinguish from each other. Meaning that both incorporate D_2O nearly equally fast. This trend can be observed in Figure 8.7, where the relative D_2O uptake is fitted to obtain the corresponding water uptake time constants τ_{humid}, as detailed in the Section 3.4.3. Hereby, only the time constants for the 0 M and 0.05 M EMIM DCA post-treated films are compared, as they were applied to the same humidity protocol. It shows that even though the values for the 0.05 M sample are a bit smaller, implying a bit faster water uptake, overall, the values differ only minimally, so that no significant conclusion about differences in the water uptake kinetics can be ascertained.

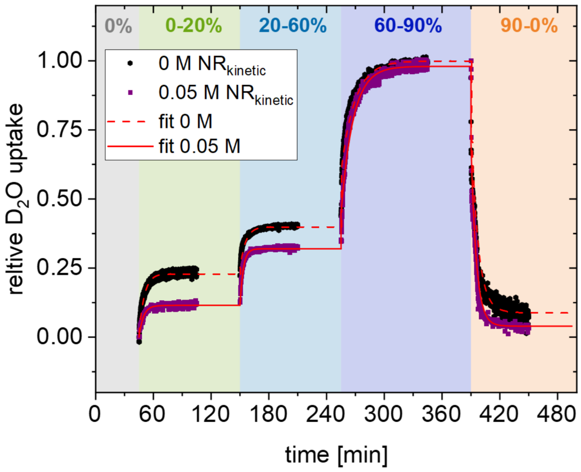

	D_2O uptake time constant τ_{humid}[min]	
	0M	0.05 M
0 - 20 % RH	5.55	4.55
20 - 60 % RH	5.88	3.33
60 - 90 % RH	14.29	12.5
90 - 0 % RH	7.14	5.55

Figure 8.7 D_2O uptake kinetics of EMIM DCA post-treated PEDOT:PSS films at different humidities. Relative D_2O uptake of the 0 M and 0.05 M EMIM DCA post-treated PEDOT:PSS samples, calculated from the respective D_2O contents obtained from kinetic ToF-NR measurements. Corresponding fits are shown with red solid and dashed lines. Table listing the resulting D_2O uptake time constants τ_{humid}. Adapted with permission from Oechsle et al.[52] Copyright 2023 American Chemical Society.

From *in situ* ToF-NR and SR experiment it can be concluded that the differently post-treated films all incorporate D_2O when the humidity is increased inside the measurement chamber. However, the PEDOT:PSS films post-treated with EMIM DCA show a more significant swelling compared to the 0 M reference sample. While in contrast, the EMIM DCA post-treatment seems to reduce the overall D_2O uptake, which might be caused by the treatment accompanying effect of hygroscopic PSS removal and reorientation of the PEDOT:PSS domain structure.[100, 163]

8.3 Electrochemical investigation of conductivity contributions

One outstanding property of PEDOT:PSS, which makes it so popular for a wide range of organic electronic applications, is its conductivity. Therefore, in this thesis the humidity-dependent conductivity behavior of PEDOT:PSS films post-treated with the different concentrations, 0 M, 0.05 M, and 0.35 M of EMIM DCA, is investigated. For this, *in situ* EIS measurements, detailed in Section 3.2.4, are performed on the differently prepared samples inside the custom-built measurement chamber, described in Section 3.5.1. Combining this chamber with the gas flow system introduced in Section 3.5.2, it allows to adjust the sample environment according to a defined humidity protocol plotted in Figure 8.8a Since the EIS measurement chamber is, in contrast to the ToF-NR & SR chamber, not optimized for high humidity experiments, the humidity is limited to a maximum of 80 % RH. The actual chamber humidity recorded during the respective EIS experiments is plotted in Figure 8.8b.

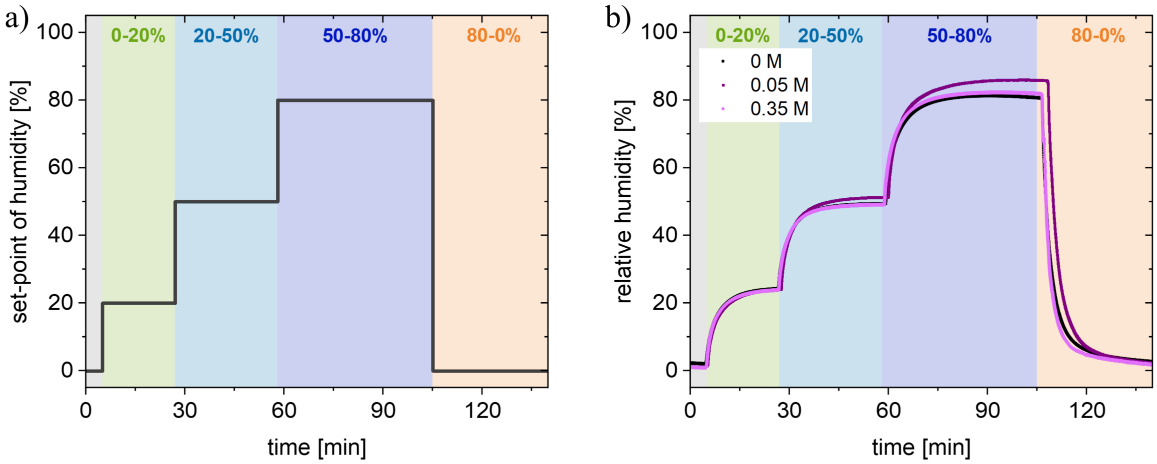

Figure 8.8 Humidity evolution during the EIS examination of EMIM DCA treated PEDOT:PSS films. a) Applied humidity protocol and b) actual recorded relative humidity inside the measurement chamber, during the EIS measurements. The respective humidity stages are marked with different background colors; 0 % RH (gray), 0 – 20 % RH (green), 20 – 50 % RH (light blue), 50 – 80 % RH (blue), and re-drying 90-0 % RH (orange). Adapted with permission from Oechsle et al.[52] Copyright 2023 American Chemical Society.

From the EIS measurements acquired Nyquist plots of representative samples of each concentration, 0 M, 0.05 M and 0.35 M, are shown in Figure 8.9a-c, and the used EIS parameters are listed provided in Section 3.2.4. For all three samples the *in situ* EIS measurements were conducted during the kinetic humidity incline (bright lines), and in the equilibrium state (dark lines with dots) of the respective humidity stages.

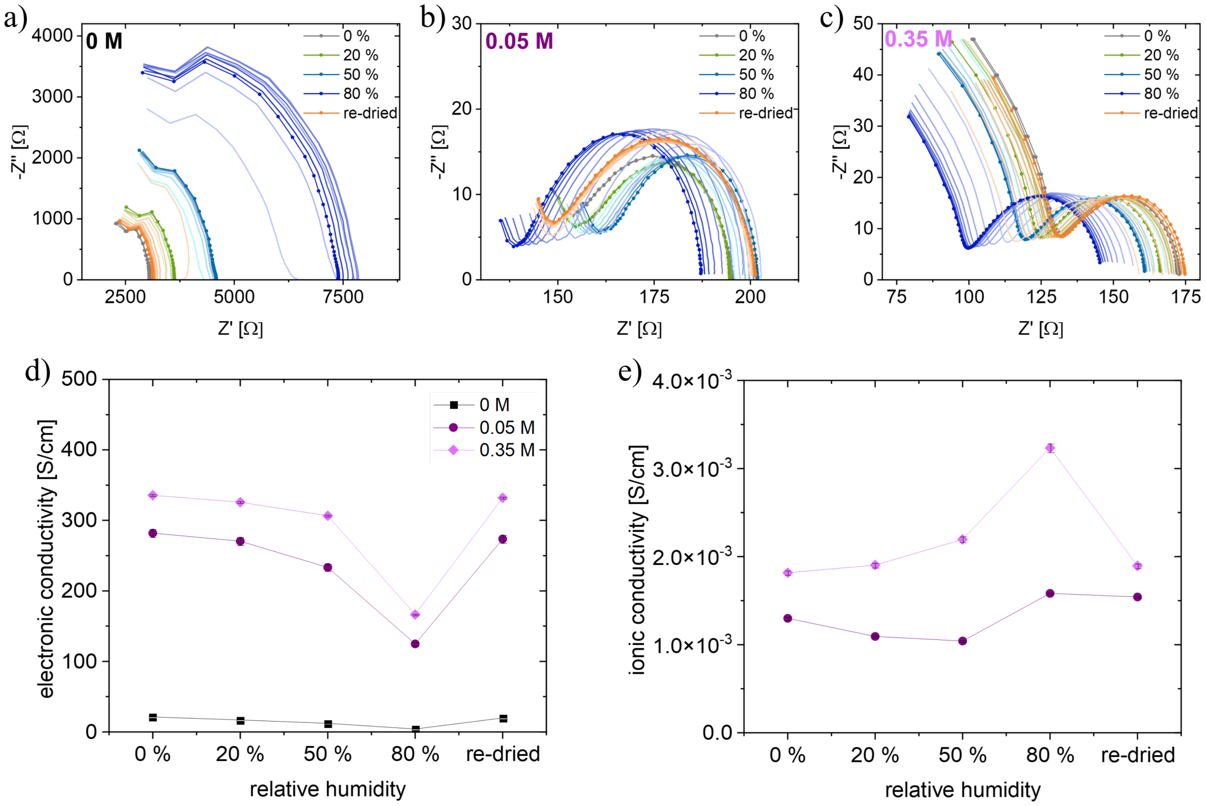

Figure 8.9 EIS results of EMIM DCA post-treated PEDOT:PSS films at different humidities. Nyquist plots of the PEDOT:PSS films post-treated with a) 0 M, b) 0.05 M, and c) 0.35 M EMIM DCA measured during (bright line) and at the end (dark line with dots) of the different humidity stages; 0 % RH (gray), 0 – 20 % RH (green), 20 – 50 % RH (light blue), 50 – 80 % RH (blue), and re-drying 80-0 % RH (orange). d) Electronic and e) ionic conductivities of 0 M (black hexagons), 0.05 M (purple squares), and 0.35 M (light purple diamonds), obtained from equivalent circuit fits of the respective Nyquist plots. Adapted with permission from Oechsle et al.[52] Copyright 2023 American Chemical Society.

The Nyquist plots of the 0 M reference sample show one segmented semicircle for all humidity steps, which implies the presence of just one, in fact, an electronic resistance contribution. The humidity-induced shift of the plots intersection with the x-axis towards higher Z’ values indicates an increase in the electronic resistance upon water uptake, which matches previous reports in the literature.[257–260] For the 0.05 M EMIM DCA concentration, the Nyquist plots consist of a depressed semicircle at low frequencies and the indication of a segmented semicircle at the high frequency range, the latter becoming more pronounced for the 0.35 M sample. This evolution means that both EMIM DCA post-treated samples hold two resistance contributions, an electronic and ionic one.[119, 124, 260] As explained in Section 3.2.4 and depicted in Figure 3.9d, from the shifts of the right Z’-plot-intersection and of the semicircle crossings, the electronic and the ionic resistances of the thin films seem to be both influenced by the applied humidity. However, to get more precise details about the resistance behavior of the post-treated PEDOT:PSS thin films, equivalent circuit model (ECM) fits as detailed in Section 3.2.4 are performed on the Nyquist plots of the one semicircle of the 0 M reference sample and the two semicircles of the 0.05 M and 0.35 M samples.[119, 260] With the thickness values from pre-characterization with surface profilometry (t_{profil}) and the relative thickness evolution from the *in situ* static ToF-NR, the thickness changes of the EIS samples are approximated as listen in Table 8.3. With these thickness values and the resistance values obtained from the ECM fits, the electronic and ionic conductivity of the different post-treated samples can be calculated. The results are plotted in Figure 8.9d and e for the different humidity steps.

Table 8.3 Thicknesses evolution of EMIM DCA post-treated PEDOT:PSS films for EIS. From surface profilometry obtained initial thin film thickness values ($\boldsymbol{t_{profil}}$), and the, with the relative thicknesses of static ToF-NR ($\boldsymbol{rel.t_{NR}}$), approximated thickness evolution ($\boldsymbol{t_{cal}}$) of the 0 M, 0.05 M, and 0.35 M EMIM DCA post-treated PEDOT:PSS films on etched ITO during the EIS measurements.

		0 % RH	20 % RH	50 % RH	80 % RH	re-dried
0 M	t_{profil} [Å]	1303 ± 14	-	-	-	-
	$rel.t_{NR}$	1.00	1.05	1.16	2.15	1.04
	t_{cal} [Å]	1303 ± 14	1368 ± 14	1513 ± 16	2803 ± 30	1355 ± 14
0.05 M	t_{profil} [Å]	1515 ± 29	-	-	-	-
	$rel.t_{NR}$	1.00	1.05	1.17	2.35	1.00
	t_{cal} [Å]	1515 ± 29	1584 ± 30	1772 ± 34	3556 ± 68	1511 ± 29
0.35 M	t_{profil} [Å]	1425 ± 2	-	-	-	-
	$rel.t_{NR}$	1.00	1.05	1.17	2.35	1.00
	t_{cal} [Å]	1425 ± 2	1490 ± 2	1666 ± 2	3344 ± 4	1421 ± 2

Since for the 0 M reference sample only an electronic resistance is observed, also only an electronic conductivity is obtained, which is furthermore far lower than the electronic conductivities achieved for the 0.05 M and 0.35 M EMIM DCA post-treated PEDOT:PSS films. The electronic conductivity reaches maxima values of 21 S cm^{-1}, 282 S cm^{-1}, and 336 S cm^{-1}, respectively for the 0 M, 0.05 M, and 0.35 M samples, during the first 0 % RH drying step. The higher conductivity values for the samples post-treated with EMIM DCA, very well demonstrate the already in the literature and previous chapters discussed effect of PSS removal and rearrangement of the conductive PEDOT-rich domains upon IL treatment, resulting in a better positive charge carrier mobility.[46, 163] For all three samples the electronic conductivity decreases upon the increase of the RH inside the measurement chamber, and increases when the thin films are re-dried, almost reaching the respective initial electronic conductivities. In doing so, the values still follow the trend of higher electronic conductivities for higher EMIM DCA concentrations, reaching values of 4 S cm^{-1} (0 M), 125 S cm^{-1} (0.05 M), and 166 S cm^{-1} (0.35 M) at the highest humidity stage of 80 % RH. In contrast to the electronic conductivity evolution, the ionic conductivity of the 0.35 M sample shows an opposite behavior, namely an increase upon increase of the relative humidity, from 1.8×10^{-3} S cm^{-1} at 0 % RH, to 3.2×10^{-3} S cm^{-1} at 80 % RH, and back to 1.9×10^{-3} S cm^{-1} at 0 % RH. The ionic conductivity of the 0.05 M EMIM DCA post-treated PEDOT:PSS film starts at 1.3×10^{-3} S cm^{-1}, then first decreases during the 20 % RH and 50 % RH humidity stages to 1.1×10^{-3} S cm^{-1} and 1.0×10^{-3} S cm^{-1} respectively, but then raises to 1.6×10^{-3} S cm^{-1} for the highest humidity stage of 80 % RH. Interestingly, for this sample, the ionic conductivity, even though decreasing again upon re-drying the film, stays quite high compared to the initial value.

Nevertheless, from the EIS measurements it can be overall summarized that, on the one hand, only the EMIM DCA post-treated PEDOT:PSS films show an ionic conductivity contribution in addition to the electronic conductivity. On the other hand, while the electronic conductivity for all samples reciprocally decreases or increases with a raise or reduction of the RH, the ionic conductivity seems to be boosted by a higher RH and achieves maxima at the 80 % RH stage for both, the 0.05 M and 0.35 M, samples.

8.4 Model description of the humidity influence on PEDOT:PSS

The results from the *in situ* experiments conducted during this study can be combined in a model description, which is graphically illustrated in Figure 8.10, to make them easier comprehensible.

As introduced in in Section 2.1.2, the polymer blend composition of PEDOT:PSS and its particular morphology formed in thin films, enables the broad property tunability of this popular material and affects its behavior under different ambient influences. When in aqueous solution, PEDOT:PSS forms a core shell-like structure where the hydrophobic PEDOT is accumulated in the core, surrounded, and stabilized by a shell of hydrophilic PSS. Spin-casting this solution to thin films and evaporating the water, causes the core-shell structures to form pancake-shaped PEDOT-rich domains, which are embedded in a matrix of PSS.

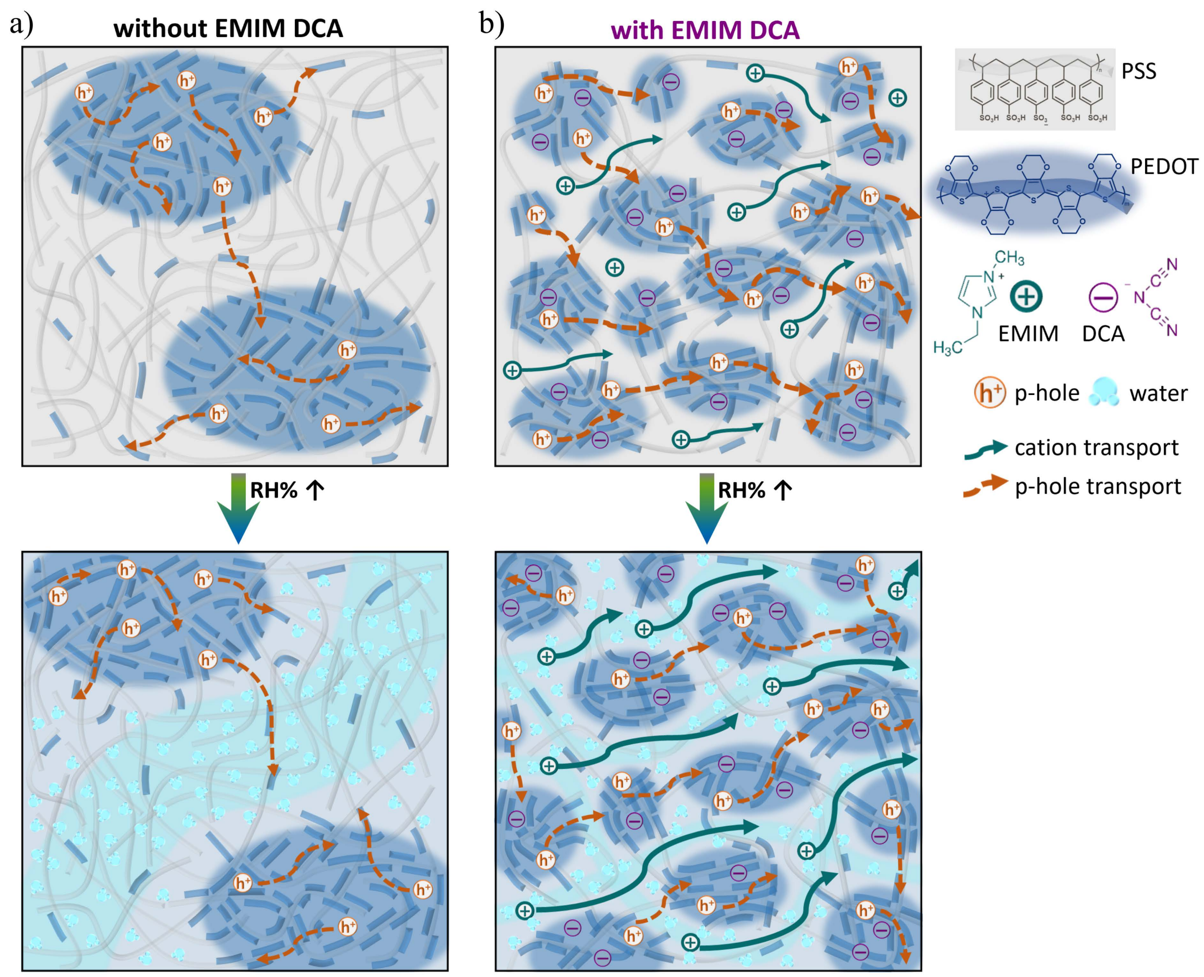

Figure 8.10 Model description of the humidity influence on the charge transport in EMIM DCA post-treated PEDOT:PSS films. Graphical illustration of the differences in morphology and charge carrier transport in PEDOT:PSS thin films a) without and b) with EMIM DCA post-treatment, from top to bottom upon increase of the relative humidity. Adapted with permission from Oechsle et al.[52] Copyright 2023 American Chemical Society.

In Figure 8.10a this dried pristine PEDOT:PSS thin film is schematically pictured in the top image, with blue rods and areas representing PEDOT, and the grey lines and background representing PSS. In these initial films, free positive charge carriers (orange), namely polarons and bipolarons, are present in the PEDOT polymer chain, which will be denoted as polymeric-holes in the following. These holes can travel within and from one PEDOT chain to another, depicted by the dashed orange arrows, thus leading to a high conductivity within the PEDOT-rich domains. However, for electronic conductivity throughout the film the holes are required to overcome the electronically insulating PSS matrix to travel from one PEDOT-rich domain to another. In the pristine, untreated PEDOT:PSS thin films a fair amount of PSS is present and the distances between the PEDOT-rich domains are rather large, thus this explains why the electronic conductivity is locally hindered and the overall electronic film conductivity is quite low, with 21 S cm^{-1}, obtained from EIS. If now exposing this untreated PEDOT:PSS film to increasing humidity, an uptake of water into the thin film and a swelling of the entire film thickness is observed with *in situ* SR and *in situ* ToF-NR. Reaching 63 % water content and 2.15 times swelling of the film thickness at the highest humidity stage of 90 % RH. Depicted in Figure 8.10a bottom image, the incorporated water accumulates inside the hygroscopic PSS matrix (light blue color), swelling it up, and causing the PEDOT-rich domains to further move away from each other. This results in an increase of the domain-domain distances, which was directly evidenced with *in situ* GISAXS as presented in the previous work in Chapter 7.[51] Because of that, the barrier, which the positive charge carriers need to overcome to travel from one conductive domain to another is heightened. Therefore, it can directly explain why the electronic conductivity of this film measured with EIS decreases to 4 S cm^{-1} at the equilibrium of the highest humidity stage. Overall, this model concludes and well explains why the electronic conductivity decreases for the 0 M sample upon increased RH.

However, the previous investigations of Chapter 7,[51] and the present study show that PEDOT:PSS thin films, which have been post-treated with ILs appear to demonstrate a different conductivity behavior. Differences in the film structure become already visible when comparing the top images of Figure 8.10a and b. First of all, as previously discussed evidenced with performed GIWAXS and GISAXS studies,[100, 163] upon post-treatment with EMIM DCA, the PEDOT:PSS domain morphology changes, towards smaller and finer distributed PEDOT-rich domains, with less electronically insulating PSS matrix in between. This change is caused by an interaction of the EMIM DCA ions with the polymer chains, which weakens the PEDOT to PSS attraction and thus allows a removal of excessive PSS during the post-treatment procedure. As thereby the PEDOT-rich domains move closer together, the holes can now easily travel from one to another (dashed orange arrows in Figure 8.10b top image), endowing these dry EMIM DCA post-treated thin films with high electronic film conductivities; of 282 S cm^{-1} (0.05 M) and 336 S cm^{-1} (0.35 M). Another difference is the within the PEDOT:PSS polymers incorporated IL ions. While the DCA anions (purple) interact with the positively charged PEDOT chain and therefore are mainly present inside the PEDOT-rich domains, the EMIM cations (turquoise) interact and accumulate inside the negatively charged PSS matrix. These EMIM cations are able to travel within the PSS matrix by intra-chain, interchain, or anionic site-to-site hopping mechanisms, already known from polymer electrolytes and facilitated by PSS chain movement, as detailed in Section 2.2.4.[270] This cation movement, depicted with turquoise arrows in Figure 8.10b, is giving rise to the with EIS measured additional ionic conductivity contribution of 1.3×10^{-3} S cm^{-1} and 1.8×10^{-3} S cm^{-1} at 0 % RH for the 0.05 M and 0.35 M post-treated samples, respectively. Upon increase of the relative humidity inside the measurement chamber, similar to the pristine PEDOT:PSS thin film, a thickness swelling and water uptake for the EMIM DCA post-treated thin films is observed with *in situ* SR and *in situ* ToF-NR measurements. As mentioned before, the water incorporation is mainly happening within the hygroscopic PSS matrix, which is reduced due to the EMIM DCA post-treatment, and therefore explains why the 0.05 M sample only reaches a water content of 57 % at the maximum humidity of 90 % RH. The enlarged distances between the conductive PEDOT domains, caused by the swelling of the PSS matrix, lead also for these samples to an impaired hole mobility and decreased electronic conductivity. This decrease in the electronic conductivity is evidenced with *in situ* EIS and is depicted in Figure 8.10b bottom image by a lower amount of orange arrows traveling between the blue PEDOT-rich domains. However, with *in situ* EIS it can be detected that in contrast to the electronic conductivity, the ionic conductivity increases upon higher humidity, illustrated by turquoise arrows, reaching maximum values of up to 1.6×10^{-3} S cm^{-1} (0.05 M) and 3.2×10^{-3} S cm^{-1} (0.35 M). This rise in the ionic conductivity is enabled by an eased movement of cationic species inside the swollen PSS matrix due to the water uptake.[271] More precisely, the water molecules (light blue) solvate the negatively charged sulfonate groups in the PSS chain and by this screen the electrostatic attraction towards the cations. Furthermore, also the cations themselves are enclosed in a hydration shell, facilitating an easier cation transport through the PEDOT:PSS thin film.[122, 124, 261] In addition, the water molecules have a plasticizing effect on the polymer chains and can assist the motion of the PSS for a better cation mobility.[122, 271]

Overall, with this explicit and plain schematic sketch in Figure 8.10 combining the results from in this chapter presented *in situ* studies, the differences in the conductivity behavior between PEDOT:PSS thin films with or without IL post-treatment can be easily comprehended. The knowledge gained from this research, is crucial for the planning of future PEDOT:PSS applications in diverse organic electronic devices.

8.5 Summary

To conclude, the humidity-dependent conductivity behavior of PEDOT:PSS thin films can be strongly influenced by a post-treatment with ILs. With *in situ* EIS at different relative humidity stages, it is shown that untreated PEDOT:PSS only possesses a low electronic conductivity of around 21 S cm^{-1}, while thin films post-treated with EMIM DCA have a higher electronic conductivity of up to 336 S cm^{-1}. This higher conductivity is caused by a removal of the positive charge carrier-transport impeding PSS between conducting PEDOT-rich domains. As evidenced by *in situ* SR and *in situ* ToF-NR, with higher RH the PSS matrix incorporates water molecules and swells up. This leads to an increased distance between the conductive domains and thus impairs the positive charge carrier mobility, which can be detected with EIS in the reduction of the electronic conductivity for all PEDOT:PSS samples. However, for the EMIM DCA post-treated samples, an additional ionic conductivity is observed, which comes from the intake of IL ions inside the polymer. This ionic conductivity is assumed to arise from mobile cations traveling inside the PSS polymer and it is found with *in situ* EIS to be enhanced by a rise in the RH up to 3.2×10^{-3} S cm^{-1}. These findings contribute to a better understanding of the influences that an IL post-treatment of PEDOT:PSS thin films can have on the materials humidity-dependent conductivity behavior. Therefore, it is suggested, to take them into account when considering the usage of PEDOT:PSS for organic device applications exposed to various environmental conditions.

9 Conclusion

Thermoelectric materials are in the spotlight of research, as they can be applied in solar thermal energy harvesting or waste heat recovery and thus have the potential to greatly contribute to global sustainable energy solutions. Organic semiconducting polymers offer the potential for non-toxic, cheap, lightweight, and flexible thin-film devices, and thus prove to be useful for a variety of organic electronic and thermoelectric applications. The organic polymer blend PEDOT:PSS is especially promising as it provides the possibility to easily tune and improve its properties by modifying its particular domain morphology. So far, the precise underlying effects of these different improvement approaches, like ionic liquid (IL) post-treatment, are poorly understood, and the effects of environmental influences on, and the stability of these post-treated PEDOT:PSS based materials are not yet adequately known. These are crucial topics that need to be addressed to achieve a strategic improvement and successful usability of PEDOT:PSS in respective future applications. Therefore, in this thesis the following scientific topics were discussed by investigation of the PEDOT:PSS morphology, oxidation level, and property relations: 1) The unraveling of the underlying effects on PEDOT:PSS upon IL post-treatment. 2) The investigation of the influence of elevated temperature on the properties and stability of these IL post-treated PEDOT:PSS thin films. 3) The impact of relative humidity with a focus on the function-morphology correlation and the charge carrier transport specifics of PEDOT:PSS thin films either with or without IL post-treatment.

First, it is demonstrated that with a post-treatment approach using various concentrations of the different ILs (AMIM DCA, EMIM DCA, and EMIM TCB) a strong improvement of the thermoelectric properties of PEDOT:PSS thin films can be successfully achieved. More precisely, the Seebeck coefficient and the electrical conductivity of these thermoelectric films are simultaneously increased by this IL post-treatment. Stronger effects are seen for higher IL concentrations and most significantly when applying EMIM DCA. The underlying effect for the occurring Seebeck coefficient improvement upon IL post-treatment is shown to be caused by a decrease of the charge carrier concentration due to a reduction in the PEDOT oxidation level. This oxidation level reduction, evidenced by UV-Vis spectroscopy, is attributed to the anions of the respective ILs, which migrate into the polymer blend and interact with the positively charged PEDOT chains. Furthermore, an additional IL post-treatment-caused effect on the PEDOT:PSS domain morphology, responsible for the simultaneously occurring electrical conductivity enhancement, is unraveled. Demonstrated using GISAXS and conductive AFM, the particular PEDOT:PSS thin film morphology, consisting of electrically conductive PEDOT-rich domains embedded in a non-conductive PSS matrix, undergoes a rearrangement upon the post-treatment with ILs. For this rearrangement, mainly the respective IL cations are responsible, as they diffuse into the PEDOT:PSS thin film and interact with the negatively charged PSS chains, thereby they weaken the PEDOT-to-PSS interactions and thus induce a partially removal of PSS during the post-treatment procedure. Consequently, the PEDOT-rich domains become smaller, more evenly distributed, and overall more densely packed upon IL post-treatment. Due to the reduced amount of non-conductive PSS matrix in between these domains, the inter-domain charge carrier mobility is facilitated, thus enhancing the electrical conductivity. A fundamental understanding is developed combining the respective underlying effects of IL anions and cations on the oxidation level and domain morphology of PEDOT:PSS thin films, promoting the comprehension of the IL post-treatment influences on the thermoelectric film properties. Furthermore, it shows the importance of IL selection for the strategic improvement towards desired PEDOT:PSS applications, and reveals that especially ILs that contain small, sterically unhindered ions with a strong localized charge, like EMIM DCA, are favorable for the thermoelectric property enhancement.

The properties of these PEDOT:PSS thin films successfully improved with EMIM DCA post-treatment are promising for a potential future thermoelectric application. However, for an accurate assessment of their applicability as a thermoelectric material, an examination of their thermal stability over time is crucial. Time-resolved investigations are achieved by performing *in situ* conductivity, *in situ* GISAXS, and *in situ* UV-Vis measurements of PEDOT:PSS thin films post-treated with various concentrations of EMIM DCA at elevated temperatures for 4.5 h. Heating of EMIM DCA post-treated films at 100 °C results in a continuous and irreversible decrease in their electrical conductivity, which is proven to be mainly caused by coarsening of the inner PEDOT:PSS domain morphology. Hereby the large PEDOT domains embedded in the non-conductive PSS matrix undergo a growth in size to the detriment of coalescing and disappearing small domains, which results in increased distances between the conductive PEDOT domains and thus an impeded inter-domain hole transport. Furthermore, the oxidation level, and consequently the charge carrier concentration of PEDOT decreases during the heat treatment at 100°C, which also contributes to the decrease in the electrical conductivity. These temperature-dependent conductivity degradation processes are shown to be more pronounced for PEDOT:PSS thin films treated with high EMIM DCA concentrations, which is dedicated to the plasticizing effect of ILs and the thereby facilitated domain rearrangement. Consequently, an untreated PEDOT:PSS reference sample demonstrates no significant conductivity change upon being heated at 100 °C. Furthermore, heating of EMIM DCA post-treated PEDOT:PSS thin films at 50 °C does not lead to a decrease in their conductivity, nor does it result in a coarsening of the domain morphology or a reduction of the PEDOT oxidation level. The hereby gained understanding of the temperature driven irreversible degradation effects underlines the significance of a careful IL concentration-dependent selection of moderate operation temperatures for the long-term thermoelectric applications of EMIM DCA post-treated PEDOT:PSS thin films.

For commercialization purposes, the operational capability of these EMIM DCA post-treatment improved PEDOT:PSS thin films in terms of the impact of the environmental factor, relative humidity, on the material's properties is of great interest and is evaluated in the next step. Untreated PEDOT:PSS thin films demonstrate a stepwise increase in their electrical resistance directly following a stepwise increase of the relative humidity. This effect is shown to be caused by the incorporation of water molecules into the PEDOT:PSS thin film, which is driven by the hygroscopic PSS matrix and directly verifiable with *in situ* ToF-NR and *in situ* SR measurements. The water uptake leads to a swelling of the PSS matrix and results in continuously increasing distances between the PEDOT-rich domains, demonstrated by *in situ* GISAXS, which consequently impedes the inter-domain hole conductivity and causes the electrical resistance to increase. However, especially notable is the finding that with an EMIM DCA post-treatment, this disadvantageous humidity-dependent resistance evolution can be completely reversed. Thus, for PEDOT:PSS thin films post-treated with different concentrations of EMIM DCA, the electrical resistance is shown to decrease with increasing relative humidity. Hereby, the water uptake and morphology investigations with *in situ* ToF-NR, *in situ* SR, and *in situ* GISAXS, evidence a similar behavior as the untreated PEDOT:PSS thin films, namely an incorporation of water and swelling of the PSS matrix, which results in a distance increase between the PEDOT domains. However, compared to the untreated films the water uptake is lower, as the EMIM DCA post-treatment procedure results in a partial removal of the hygroscopic PSS matrix. Eventually, it is demonstrated that the observed reversed humidity-dependent behavior stems from an additional ionic charge carrier transport contribution, attributed to the intake of EMIM DCA ions into the PEDOT:PSS thin film. Proven by *in situ* EIS experiments, this ionic conductivity contribution arises in the PEDOT:PSS thin film upon EMIM DCA post-treatment and increases with increasing relative humidity. Hereby the EMIM cations are the cause as they are predominantly located and can freely move within the PSS matrix. Upon increasing relative humidity and water uptake into the PSS matrix, these cations become more mobile through water solvation and electrostatic screening, consequently increasing the ionic conductivity and with this determining the reversed behavior for the EMIM DCA post-treated PEDOT:PSS films. Finally, the discovered and investigated reversible conductivity enhancement of PEDOT:PSS thin films upon increasing relative humidity, which is induced by the IL post-treatment, is visually described in an explanation model combining the morphology correlations and charge carrier transport specifics. From this model, it becomes clear how the humidity-dependent property behavior can be favorably tuned with a selected EMIM DCA post-treatment approach, and this provides a promising new aspect for respective potential applications of PEDOT:PSS thin films.

In summary, the underlying effects of IL post-treatment on PEDOT:PSS thin films are unraveled, which enables a more efficient and application-focused selection of the utilized IL ions. A deeper understanding of the temperature influence on the properties and stability of these EMIM DCA post-treated PEDOT:PSS thin films is provided, suggesting a limitation to moderate operation temperatures. Furthermore, the humidity-dependent function-morphology correlations and charge carrier transport specifics of PEDOT:PSS thin films are demonstrated to present a way for a favorable reversible conductivity enhancement upon increasing relative humidity, induced by the EMIM DCA post-treatment. The combined findings of this thesis provide a better understanding of the basic underlying effects and impact of different influences on PEDOT:PSS, significantly contributing to its usability in organic electronics and thermoelectric applications.

An interesting aspect for the future research is the investigation of additional ionic contributions from IL post-treatment to the Seebeck coefficient of PEDOT:PSS thin films at increasing relative humidity. Thermal conductivity measurements of these promising EMIM DCA post-treated PEDOT:PSS thin films are beneficial to determine the capability of these materials for thermoelectric applications more precisely. Additionally, the steps for future implementation of these thermoelectric thin films into application are worth considering, in terms of realization of large-scale film deposition and post-treatment experiments, and regarding the development of a suitable device design. For this, it is also necessary to select and further develop a matching n-type thermoelectric material, for example, one candidate could be poly[3-(potassium-6-hexanoate)thiophene-2,5-diyl], which is a water-soluble organic polymer that demonstrates promising Seebeck coefficients when doped with chloroauric acid.

Bibliography

[1] M. Hamid Elsheikh, D. A. Shnawah, M. F. M. Sabri, S. B. M. Said, M. Haji Hassan, M. B. Ali Bashir, and M. Mohamad, "A review on thermoelectric renewable energy: Principle parameters that affect their performance", *Renewable and Sustainable Energy Reviews*, vol. 30, pp. 337–355, **2014**, DOI: 10.1016/j.rser.2013.10.027.

[2] B. Informationsdienst, "Thermoelektrik: Strom aus Abwärme: Thermoelektrische Generatoren machen Systeme energieautark und sparen Energie", *BINE-Themeninfo*, vol. 1, pp. 1–24, **2016**.

[3] P. Sundarraj, D. Maity, S. S. Roy, and R. A. Taylor, "Recent advances in thermoelectric materials and solar thermoelectric generators – a critical review", *RSC Advances*, vol. 4, no. 87, pp. 46860–46874, **2014**, DOI: 10.1039/C4RA05322B.

[4] Fitriani, R. Ovik, B. D. Long, M. C. Barma, M. Riaz, M. Sabri, S. M. Said, and R. Saidur, "A review on nanostructures of high-temperature thermoelectric materials for waste heat recovery", *Renewable and Sustainable Energy Reviews*, vol. 64, pp. 635–659, **2016**, DOI: 10.1016/j.rser.2016.06.035.

[5] M. F. Sanad, A. E. Shalan, S. O. Abdellatif, E. S. A. Serea, M. S. Adly, and M. A. Ahsan, "Thermoelectric Energy Harvesters: A Review of Recent Developments in Materials and Devices for Different Potential Applications", *Topics in Current Chemistry*, vol. 378, 48, **2020**, DOI: 10.1007/s41061-020-00310-w.

[6] C. S. Buga and J. C. Viana, "A Review on Materials and Technologies for Organic Large-Area Electronics", *Advanced Materials Technologies*, vol. 6, no. 6, 2001016, **2021**, DOI: 10.1002/admt.202001016.

[7] Z. Lan, M.-H. Lee, and F. Zhu, "Recent Advances in Solution-Processable Organic Photodetectors and Applications in Flexible Electronics", *Advanced Intelligent Systems*, vol. 4, no. 3, 2100167, **2022**, DOI: 10.1002/aisy.202100167.

[8] S. Masoumi, S. O'Shaughnessy, and A. Pakdel, "Organic-based flexible thermoelectric generators: From materials to devices", *Nano Energy*, vol. 92, 106774, **2022**, DOI: 10.1016/j.nanoen.2021.106774.

[9] M. Culebras, C. M. Gómez, and A. Cantarero, "Review on Polymers for Thermoelectric Applications", *Materials*, vol. 7, no. 9, pp. 6701–6732, **2014**, DOI: 10.3390/ma7096701.

[10] H. Yao, Z. Fan, H. Cheng, X. Guan, C. Wang, K. Sun, and J. Ouyang, "Recent Development of Thermoelectric Polymers and Composites", *Macromolecular Rapid Communications*, vol. 39, no. 6, 1700727, **2018**, DOI: 10.1002/marc.201700727.

[11] O. Bubnova and X. Crispin, "Towards polymer-based organic thermoelectric generators", *Energy & Environmental Science*, vol. 5, no. 11, pp. 9345–9362, **2012**, DOI: 10.1039/c2ee22777k.

[12] G. J. Snyder and E. S. Toberer, "Complex thermoelectric materials", *Nature Materials*, vol. 7, no. 2, pp. 105–114, **2008**, DOI: 10.1038/nmat2090.

[13] K. Fehse, K. Walzer, K. Leo, W. Lövenich, and A. Elschner, "Highly Conductive Polymer Anodes as Replacements for Inorganic Materials in High-Efficiency Organic Light-Emitting Diodes", *Advanced Materials*, vol. 19, no. 3, pp. 441–444, **2007**, DOI: 10.1002/adma.200602156.

[14] J. Ouyang, "Solution-processed PEDOT:PSS films with conductivities as indium tin oxide through a treatment with mild and weak organic acids", *ACS Applied Materials & Interfaces*, vol. 5, no. 24, pp. 13082–13088, **2013**, DOI: 10.1021/am404113n.

[15] N. Kim, S. Kee, S. H. Lee, B. H. Lee, Y. H. Kahng, Y.-R. Jo, B.-J. Kim, and K. Lee, "Highly conductive PEDOT:PSS nanofibrils induced by solution-processed crystallization", *Advanced Materials*, vol. 26, no. 14, pp. 2268-2272, **2014**, DOI: 10.1002/adma.201304611.

[16] R. Kroon, D. A. Mengistie, D. Kiefer, J. Hynynen, J. D. Ryan, L. Yu, and C. Müller, "Thermoelectric Plastics: from Design to Synthesis, Processing and Structure-Property Relationships", *Chemical Society Reviews*, vol. 45, no. 22, pp. 6147–6164, **2016**, DOI: 10.1039/c6cs00149a.

[17] K. Sun, S. Zhang, P. Li, Y. Xia, X. Zhang, D. Du, F. H. Isikgor, and J. Ouyang, "Review on Application of PEDOTs and PEDOT:PSS in Energy Conversion and Storage Devices", *Journal of Materials Science: Materials in Electronics*, vol. 26, no. 7, pp. 4438–4462, **2015**, DOI: 10.1007/s10854-015-2895-5.

[18] K. Jain, A. Y. Mehandzhiyski, I. Zozoulenko, and L. Wågberg, "PEDOT:PSS nano-particles in aqueous media: A comparative experimental and molecular dynamics study of particle size, morphology and z-potential", *Journal of Colloid and Interface Science*, vol. 584, pp. 57–66, **2021**, DOI: 10.1016/j.jcis.2020.09.070.

[19] A. M. Nardes, M. Kemerink, R. A. J. Janssen, J. A. M. Bastiaansen, N. M. M. Kiggen, B. M. W. Langeveld, A. J. J. M. van Breemen, and M. M. de Kok, "Microscopic Understanding of the Anisotropic Conductivity of PEDOT:PSS Thin Films", *Advanced Materials*, vol. 19, no. 9, pp. 1196–1200, **2007**, DOI: 10.1002/adma.200602575.

[20] A. M. Nardes, R. A. J. Janssen, and M. Kemerink, "A Morphological Model for the Solvent-Enhanced Conductivity of PEDOT:PSS Thin Films", *Advanced Functional Materials*, vol. 18, no. 6, pp. 865–871, **2008**, DOI: 10.1002/adfm.200700796.

[21] M. N. Gueye, A. Carella, J. Faure-Vincent, R. Demadrille, and J.-P. Simonato, "Progress in Understanding Structure and Transport Properties of PEDOT-based Materials: A Critical Review", *Progress in Materials Science*, vol. 108, 100616, **2020**, DOI: 10.1016/j.pmatsci.2019.100616.

[22] T. Unuma, M. Yoshikawa, A. Nakamura, and H. Kishida, "Segmentation of conducting domains in PEDOT:PSS films induced by an additive for conductivity enhancement", *Applied Physics Express*, vol. 9, no. 5, 051601, **2016**, DOI: 10.7567/APEX.9.051601.

[23] C. M. Palumbiny, F. Liu, T. P. Russell, A. Hexemer, C. Wang, and P. Müller-Buschbaum, "The Crystallization of PEDOT:PSS Polymeric Electrodes Probed In Situ during Printing", *Advanced Materials*, vol. 27, no. 22, pp. 3391–3397, **2015**, DOI: 10.1002/adma.201500315.

[24] C. M. Palumbiny, C. Heller, C. J. Schaffer, V. Körstgens, G. Santoro, S. V. Roth, and P. Müller-Buschbaum, "Molecular Reorientation and Structural Changes in Cosolvent-Treated Highly Conductive PEDOT:PSS Electrodes for Flexible Indium Tin Oxide-Free Organic Electronics", *The Journal of Physical Chemistry C*, vol. 118, no. 25, pp. 13598–13606, **2014**, DOI: 10.1021/jp501540y.

[25] S. Lee, "Conductivity Enhancement of PEDOT:PSS Films Through the Surface Treatment with Organic Solvent", *Journal of Nanoscience and Nanotechnology*, vol. 16, no. 3, pp. 2880–2882, **2016**, DOI: 10.1166/jnn.2016.11051.

[26] J. Dong and G. Portale, "Role of the Processing Solvent on the Electrical Conductivity of PEDOT:PSS", *Advanced Materials Interfaces*, vol. 7, no. 18, 2000641, **2020**, DOI: 10.1002/admi.202000641.

[27] N. Saxena, J. Keilhofer, A. K. Maurya, G. Fortunato, J. Overbeck, and P. Müller-Buschbaum, "Facile Optimization of Thermoelectric Properties in PEDOT:PSS Thin Films through Acido-Base and Redox Dedoping Using Readily Available Salts", *ACS Applied Energy Materials*, vol. 1, no. 2, pp. 336–342, **2018**, DOI: 10.1021/acsaem.7b00334.

[28] Z. Fan, D. Du, Z. Yu, P. Li, Y. Xia, and J. Ouyang, "Significant Enhancement in the Thermoelectric Properties of PEDOT:PSS Films through a Treatment with Organic Solutions of Inorganic Salts", *ACS Applied Materials & Interfaces*, vol. 8, no. 35, pp. 23204–23211, **2016**, DOI: 10.1021/acsami.6b07234.

[29] Y. Xia and J. Ouyang, "Salt-Induced Charge Screening and Significant Conductivity Enhancement of Conducting Poly(3,4-ethylenedioxythiophene):Poly(styrenesulfonate)", *Macromolecules*, vol. 42, no. 12, pp. 4141–4147, **2009**, DOI: 10.1021/ma900327d.

[30] L. Bießmann, N. Saxena, N. Hohn, M. A. Hossain, J. G. C. Veinot, and P. Müller-Buschbaum, "Highly Conducting, Transparent PEDOT:PSS Polymer Electrodes from Post-Treatment with Weak and Strong Acids", *Advanced Electronic Materials*, vol. 5, no. 2, 1800654, **2019**, DOI: 10.1002/aelm.201800654.

[31] Y. Xia and J. Ouyang, "Significant conductivity enhancement of conductive poly(3,4-ethylenedioxythiophene): poly(styrenesulfonate) films through a treatment with organic carboxylic acids and inorganic acids", *ACS Applied Materials & Interfaces*, vol. 2, no. 2, pp. 474–483, **2010**, DOI: 10.1021/am900708x.

[32] Z. Fan, P. Li, D. Du, and J. Ouyang, "Significantly Enhanced Thermoelectric Properties of PEDOT:PSS Films through Sequential Post-Treatments with Common Acids and Bases", *Advanced Energy Materials*, vol. 7, no. 8, 1602116, **2017**, DOI: 10.1002/aenm.201602116.

[33] W. Meng, R. Ge, Z. Li, J. Tong, T. Liu, Q. Zhao, S. Xiong, F. Jiang, L. Mao, and Y. Zhou, "Conductivity Enhancement of PEDOT:PSS Films via Phosphoric Acid Treatment for Flexible All-Plastic Solar Cells", *ACS Applied Materials & Interfaces*, vol. 7, no. 25, pp. 14089–14094, **2015**, DOI: 10.1021/acsami.5b03309.

[34] E. Dauzon, A. E. Mansour, M. R. Niazi, R. Munir, D.-M. Smilgies, X. Sallenave, C. Plesse, F. Goubard, and A. Amassian, "Conducting and Stretchable PEDOT:PSS Electrodes: Role of Additives on Self-Assembly, Morphology, and Transport", *ACS Applied Materials & Interfaces*, vol. 11, no. 19, pp. 17570–17582, **2019**, DOI: 10.1021/acsami.9b00934.

[35] R. Chen, H. He, X. Z. Hong, Q. Le, K. Sun, and J. Ouyang, "PEDOT:PSS as Stretchable Conductors with Good Wettability on the Substrate through the Simultaneous Plasticization and Secondary Doping with a Cationic or Anionic Surfactant", *Macromolecules*, vol. 55, no. 12, pp. 4967–4978, **2022**, DOI: 10.1021/acs.macromol.2c00592.

[36] C. M. Palumbiny, J. Schlipf, A. Hexemer, C. Wang, and P. Müller-Buschbaum, "The Morphological Power of Soap: How Surfactants Lower the Sheet Resistance of

PEDOT:PSS by Strong Impact on Inner Film Structure and Molecular Interface Orientation", *Advanced Electronic Materials*, vol. 2, no. 4, 1500377, **2016**, DOI: 10.1002/aelm.201500377.

[37] S. Savagatrup, E. Chan, S. M. Renteria-Garcia, A. D. Printz, A. V. Zaretski, T. F. O'Connor, D. Rodriquez, E. Valle, and D. J. Lipomi, "Plasticization of PEDOT:PSS by Common Additives for Mechanically Robust Organic Solar Cells and Wearable Sensors", *Advanced Functional Materials*, vol. 25, no. 3, pp. 427–436, **2015**, DOI: 10.1002/adfm.201401758.

[38] S. Tu, T. Tian, A. L. Oechsle, S. Yin, X. Jiang, W. Cao, N. Li, M. A. Scheel, L. K. Reb, S. Hou, A. S. Bandarenka, M. Schwartzkopf, S. V. Roth, and P. Müller-Buschbaum, "Improvement of the Thermoelectric Properties of PEDOT:PSS Films via DMSO Addition and DMSO/Salt Post-Treatment Resolved from a Fundamental View", *Chemical Engineering Journal*, vol. 429, 132295, **2022**, DOI: 10.1016/j.cej.2021.132295.

[39] S. H. Lee, H. Park, S. Kim, W. Son, I. W. Cheong, and J. H. Kim, "Transparent and flexible organic semiconductor nanofilms with enhanced thermoelectric efficiency", *Journal of Materials Chemistry A*, vol. 2, no. 20, pp. 7288–7294, **2014**, DOI: 10.1039/C4TA00700J.

[40] H. Park, S. H. Lee, F. S. Kim, H. H. Choi, I. W. Cheong, and J. H. Kim, "Enhanced thermoelectric properties of PEDOT:PSS nanofilms by a chemical dedoping process", *Journal of Materials Chemistry A*, vol. 2, no. 18, pp. 6532–6539, **2014**, DOI: 10.1039/C3TA14960A.

[41] N. Massonnet, A. Carella, O. Jaudouin, P. Rannou, G. Laval, C. Celle, and J.-P. Simonato, "Improvement of the Seebeck coefficient of PEDOT:PSS by chemical reduction combined with a novel method for its transfer using free-standing thin films", *Journal of Materials Chemistry C*, vol. 2, no. 7, pp. 1278–1283, **2014**, DOI: 10.1039/C3TC31674B.

[42] E. Yang, J. Kim, B. J. Jung, and J. Kwak, "Enhanced thermoelectric properties of sorbitol-mixed PEDOT:PSS thin films by chemical reduction", *Journal of Materials Science: Materials in Electronics*, vol. 26, no. 5, pp. 2838–2843, **2015**, DOI: 10.1007/s10854-015-2766-0.

[43] J. Luo, D. Billep, T. Blaudeck, E. Sheremet, R. D. Rodriguez, D. R. T. Zahn, M. Toader, M. Hietschold, T. Otto, and T. Gessner, "Chemical post-treatment and thermoelectric properties of poly(3,4-ethylenedioxylthiophene):poly(styrenesulfonate) thin films", *Journal of Applied Physics*, vol. 115, no. 5, 054908, **2014**, DOI: 10.1063/1.4864749.

[44] J. Luo, D. Billep, T. Waechtler, T. Otto, M. Toader, O. Gordan, E. Sheremet, J. Martin, M. Hietschold, D. R. T. Zahn, and T. Gessner, "Enhancement of the Thermoelectric Properties of PEDOT:PSS Thin Films by Post-Treatment", *Journal of Materials Chemistry A*, vol. 1, no. 26, pp. 7576–7583, **2013**, DOI: 10.1039/c3ta11209h.

[45] C. Liu, J. Xu, B. Lu, R. Yue, and F. Kong, "Simultaneous Increases in Electrical Conductivity and Seebeck Coefficient of PEDOT:PSS Films by Adding Ionic Liquids into a Polymer Solution", *Journal of Electronic Materials*, vol. 41, no. 4, pp. 639–645, **2012**, DOI: 10.1007/s11664-012-1942-8.

[46] M. Döbbelin, R. Marcilla, M. Salsamendi, C. Pozo-Gonzalo, P. M. Carrasco, J. A. Pomposo, and D. Mecerreyes, "Influence of Ionic Liquids on the Electrical Conductivity and Morphology of PEDOT:PSS Films", *Chemistry of Materials*, vol. 19, no. 9, pp. 2147–2149, **2007**, DOI: 10.1021/cm070398z.

[47] Y. Wang, C. Zhu, R. Pfattner, H. Yan, L. Jin, S. Chen, F. Molina-Lopez, F. Lissel, J. Liu, N. I. Rabiah, Z. Chen, J. W. Chung, C. Linder, M. F. Toney, B. Murmann, and Z. Bao, "A highly stretchable, transparent, and conductive polymer", *Science Advances*, vol. 3, no. 3, e1602076, **2017**, DOI: 10.1126/sciadv.1602076.

[48] T. A. Yemata, Y. Zheng, A. K. K. Kyaw, X. Wang, J. Song, W. S. Chin, and J. Xu, "Improved Thermoelectric Properties and Environmental Stability of Conducting PEDOT:PSS Films Post-treated With Imidazolium Ionic Liquids", *Frontiers in Chemistry*, vol. 7, 870, **2019**, DOI: 10.3389/fchem.2019.00870.

[49] A. de Izarra, C. Choi, Y. H. Jang, and Y. Lansac, "Ionic Liquid for PEDOT:PSS Treatment. Ion Binding Free Energy in Water Revealing the Importance of Anion Hydrophobicity", *The Journal of Physical Chemistry B*, vol. 125, no. 7, pp. 1916–1923, **2021**, DOI: 10.1021/acs.jpcb.0c10068.

[50] A. L. Oechsle, J. E. Heger, N. Li, S. Yin, S. Bernstorff, and P. Müller-Buschbaum, "In Situ Observation of Morphological and Oxidation Level Degradation Processes within Ionic Liquid Post-treated PEDOT:PSS Thin Films upon Operation at High Temperatures", *ACS Applied Materials & Interfaces*, vol. 14, no. 27, pp. 30802–30811, **2022**, DOI: 10.1021/acsami.2c05745.

[51] A. L. Oechsle, T. Schöner, L. Deville, T. Xiao, T. Tian, A. Vagias, S. Bernstorff, and P. Müller-Buschbaum, "Ionic Liquid-Induced Inversion of the Humidity-Dependent Conductivity of Thin PEDOT:PSS Films", *ACS Applied Materials & Interfaces*, vol. 15, no. 40, pp. 47682–47691, **2023**, DOI: 10.1021/acsami.3c08208.

[52] A. L. Oechsle, T. Schöner, C. Geiger, S. Tu, P. Wang, R. Cubitt, and P. Müller-Buschbaum, "Unraveling the Humidity Influence on the Electrical Properties of Ionic Liquid Posttreated Poly(3,4-ethylene dioxythiophene):Poly(styrenesulfonate) Films", *Macromolecules*, vol. 56, no. 22, pp. 9117–9126, **2023**, DOI: 10.1021/acs.macromol.3c01842.

[53] Y. Xu, Z. Liu, X. Wei, J. Wu, J. Guo, B. Zhao, H. Wang, S. Chen, and Y. Dou, "Morphological Modulation to Improve Thermoelectric Performances of PEDOT:PSS Films by DMSO Vapor Post-Treatment", *Synthetic Metals*, vol. 271, 116628, **2021**, DOI: 10.1016/j.synthmet.2020.116628.

[54] L. Zhang, K. Yang, R. Chen, Y. Zhou, S. Chen, Y. Zheng, M. Li, C. Xu, X. Tang, Z. Zang, and K. Sun, "The Role of Mineral Acid Doping of PEDOT:PSS and Its Application in Organic Photovoltaics", *Advanced Electronic Materials*, vol. 6, no. 1, 1900648, **2020**, DOI: 10.1002/aelm.201900648.

[55] S.-M. Kim, C.-H. Kim, Y. Kim, N. Kim, W.-J. Lee, E.-H. Lee, D. Kim, S. Park, K. Lee, J. Rivnay, and M.-H. Yoon, "Influence of PEDOT:PSS crystallinity and composition on electrochemical transistor performance and long-term stability", *Nature Communications*, vol. 9, 3858, **2018**, DOI: 10.1038/s41467-018-06084-6.

[56] S. Panigrahy and B. Kandasubramanian, "Polymeric thermoelectric PEDOT: PSS & composites: Synthesis, progress, and applications", *European Polymer Journal*, vol. 132, 109726, **2020**, DOI: 10.1016/j.eurpolymj.2020.109726.

[57] H. Xu, X. Zhao, G. Yang, X. Ji, X. Zhang, L. Li, B. Wu, X. Ouyang, Y. Ni, L. Chen, and H.-C. Hu, "Modification of PEDOT:PSS towards high-efficiency OLED electrode via synergistic effect of carboxy and phenol groups from biomass derivatives", *Chemical Engineering Journal*, vol. 430, 133014, **2022**, DOI: 10.1016/j.cej.2021.133014.

[58] X. Zhang, W. Yang, H. Zhang, M. Xie, and X. Duan, "PEDOT:PSS: From Conductive Polymers to Sensors", *Nanotechnology and Precision Engineering*, vol. 4, no. 4, 045004, **2021**, DOI: 10.1063/10.0006866.

[59] Y. Liang, A. Offenhäusser, S. Ingebrandt, and D. Mayer, "PEDOT:PSS-Based Bioelectronic Devices for Recording and Modulation of Electrophysiological and Biochemical Cell Signals", *Advanced Healthcare Materials*, vol. 10, no. 11, 2100061, **2021**, DOI: 10.1002/adhm.202100061.

[60] M. D. Lechner, K. Gehrke, and E. H. Nordmeier. *Makromolekulare Chemie: Ein Lehrbuch für Chemiker, Physiker, Materialwissenschaftler und Verfahrenstechniker,* 4th ed. Basel, Boston, Berlin: Birkhäuser, **2010**.

[61] C. K. Chiang, C. R. Fincher, Jr., Y. W. Park, A. J. Heeger, H. Shirakawa, E. J. Louis, S. C. Gau, and and Alan G. MacDiarmid, "Electrical Conductivity in Doped Polyacetylene", *Physical Review Letters*, vol. 39, no. 17, pp. 1098–1101, **1977**.

[62] N. Kim, I. Petsagkourakis, S. Chen, M. Berggren, X. Crispin, M. P. Jonsson, and I. Zozoulenko, "Electric Transport Properties in PEDOT Thin Films", in: *Conjugated Polymers,* 4th ed. Boca Raton: CRC Press, **2019**, pp. 45–128.

[63] W. Demtröder. *Experimentalphysik 3,* Berlin, Heidelberg: Springer Berlin Heidelberg, **2010**.

[64] M. Heydari Gharahcheshmeh and K. K. Gleason, "Texture and nanostructural engineering of conjugated conducting and semiconducting polymers", *Materials Today Advances*, vol. 8, 100086, **2020**, DOI: 10.1016/j.mtadv.2020.100086.

[65] H. J. Keller, Ed. *Low-Dimensional Cooperative Phenomena: The Possibility of High-Temperature Superconductivity* Nato Advanced Study Institutes Series, Series B vol. 7 Boston, MA: Springer US, **1975**.

[66] M. Cardona, P. Fulde, K. von Klitzing, H.-J. Queisser, H. K. V. Lotsch, H. K. V. Lotsch, and H. G. Kiess, Eds. *Conjugated Conducting Polymers* Springer series in solid-state sciences vol. 102 Berlin, Heidelberg: Springer Berlin Heidelberg, **1992**.

[67] J.-P. Gaspard, "Structure of covalently bonded materials: From the Peierls distortion to Phase-Change Materials", *Comptes Rendus Physique*, vol. 17, no. 3-4, pp. 389–405, **2016**, DOI: 10.1016/j.crhy.2015.12.009.

[68] Franziska Carina Löhrer. *Relating Morphology and Function in Low-Bandgap Polymer-Based Solar Cells,* PhD dissertation, Physik-Department, Technische Universität München, München, **2021**.

[69] W. P. Su, J. R. Schrieffer, and A. J. Heeger, "Solitons in Polyacetylene", *Physical Review Letters*, vol. 42, no. 25, pp. 1698–1701, **1979**, DOI: 10.1103/PhysRevLett.42.1698.

[70] C. Liu, K. Huang, W.-T. Park, M. Li, T. Yang, X. Liu, L. Liang, T. Minari, and Y.-Y. Noh, "A unified understanding of charge transport in organic semiconductors: the importance of attenuated delocalization for the carriers", *Materials Horizons*, vol. 4, no. 4, pp. 608–618, **2017**, DOI: 10.1039/C7MH00091J.

[71] H. Bässler, "Localized states and electronic transport in single component organic solids with diagonal disorder", *Physica Status Solidi B*, vol. 107, no. 1, pp. 9–54, **1981**, DOI: 10.1002/pssb.2221070102.

[72] H. Bässler and A. Köhler, "Charge transport in organic semiconductors", *Topics in Current Chemistry*, vol. 312, pp. 1–65, **2012**, DOI: 10.1007/128_2011_218.

[73] R. Schmechel, "Gaussian disorder model for high carrier densities: Theoretical aspects and application to experiments", *Physical Review B*, vol. 66, no. 23, 235206, **2002**, DOI: 10.1103/PhysRevB.66.235206.

[74] R. A. Marcus, "On the Theory of Oxidation-Reduction Reactions Involving Electron Transfer. I", *The Journal of Chemical Physics*, vol. 24, no. 5, pp. 966–978, **1956**, DOI: 10.1063/1.1742723.

[75] R. A. Marcus, "Electron transfer at electrodes and in solution: Comparison of theory and experiment", *Electrochimica Acta*, vol. 13, no. 5, pp. 995–1004, **1968**, DOI: 10.1016/0013-4686(68)80031-3.

[76] A. Miller and E. Abrahams, "Impurity Conduction at Low Concentrations", *Physical Review*, vol. 120, no. 3, pp. 745–755, **1960**, DOI: 10.1103/PhysRev.120.745.

[77] C. Deibel and V. Dyakonov, "Polymer–fullerene bulk heterojunction solar cells", *Reports on Progress in Physics*, vol. 73, no. 9, 096401, **2010**, DOI: 10.1088/0034-4885/73/9/096401.

[78] S. D. Baranovskii, "Theoretical description of charge transport in disordered organic semiconductors", *Physica Status Solidi B*, vol. 251, no. 3, pp. 487–525, **2014**, DOI: 10.1002/pssb.201350339.

[79] J. Lee, "Physical modeling of charge transport in conjugated polymer field-effect transistors", *Journal of Physics D: Applied Physics*, vol. 54, no. 14, 143002, **2021**, DOI: 10.1088/1361-6463/abd271.

[80] A. V. Nenashev, J. O. Oelerich, and S. D. Baranovskii, "Theoretical tools for the description of charge transport in disordered organic semiconductors", *Journal of Physics: Condensed Matter*, vol. 27, no. 9, 093201, **2015**, DOI: 10.1088/0953-8984/27/9/093201.

[81] L. Bießmann. *Functional Layers for Enhanced Photon Extraction in ITO-free OLEDs,* PhD dissertation, Physik-Department, Technische Universität München, München, **2019**.

[82] P. Kar. *Doping in conjugated polymers,* Salem, Massachusetts.: Scrivener Publishing LLC, **2013**.

[83] T. Stöcker, A. Köhler, and R. Moos, "Why Does the Electrical Conductivity in PEDOT:PSS Decrease with PSS Content? A Study CombiningThermoelectric Measurements with Impedance Spectroscopy", *Journal of Polymer Science Part B: Polymer Physics*, vol. 50, no. 14, pp. 976–983, **2012**, DOI: 10.1002/polb.23089.

[84] J. Rivnay, S. Inal, B. A. Collins, M. Sessolo, E. Stavrinidou, X. Strakosas, C. Tassone, D. M. Delongchamp, and G. G. Malliaras, "Structural Control of Mixed Ionic and Electronic Transport in Conducting Polymers", *Nature Communications*, vol. 7, 11287, **2016**, DOI: 10.1038/ncomms11287.

[85] S. Nie, Z. Li, Y. Yao, and Y. Jin, "Progress in Synthesis of Conductive Polymer Poly(3,4-Ethylenedioxythiophene)", *Frontiers in Chemistry*, vol. 9, 803509, **2021**, DOI: 10.3389/fchem.2021.803509.

[86] S. N. Karri and P. Srinivasan, "Synthesis of PEDOT:PSS using benzoyl peroxide as an alternative oxidizing agent for ESD coating and electro-active material in supercapacitor", *Materials Science for Energy Technologies*, vol. 2, no. 2, pp. 208–215, **2019**, DOI: 10.1016/j.mset.2019.01.008.

[87] Y. Jiang, T. Liu, and Y. Zhou, "Recent Advances of Synthesis, Properties, Film Fabrication Methods, Modifications of Poly(3,4-ethylenedioxythiophene), and Applications in Solution-Processed Photovoltaics", *Advanced Functional Materials*, vol. 30, no. 51, 2006213, **2020**, DOI: 10.1002/adfm.202006213.

[88] J. Wang, K. Cai, and S. Shen, "Enhanced thermoelectric properties of poly(3,4-ethylenedioxythiophene) thin films treated with H 2 SO 4", *Organic Electronics*, vol. 15, no. 11, pp. 3087–3095, **2014**, DOI: 10.1016/j.orgel.2014.09.012.

[89] C. Yeon, S. J. Yun, J. Kim, and J. W. Lim, "PEDOT:PSS Films with Greatly Enhanced Conductivity via Nitric Acid Treatment at Room Temperature and Their Application as Pt/TCO-Free Counter Electrodes in Dye-Sensitized Solar Cells", *Advanced Electronic Materials*, vol. 1, no. 10, 1500121, **2015**, DOI: 10.1002/aelm.201500121.

[90] J. R. Reynolds, B. C. Thompson, and T. A. Skotheim, Eds. *Conjugated Polymers* 4th ed. Boca Raton: CRC Press, **2019**.

[91] H. Shi, C. Liu, Q. Jiang, and J. Xu, "Effective Approaches to Improve the Electrical Conductivity of PEDOT:PSS: A Review", *Advanced Electronic Materials*, vol. 1, no. 4, 1500017, **2015**, DOI: 10.1002/aelm.201500017.

[92] N. A. Shahrim, Z. Ahmad, A. Wong Azman, Y. Fachmi Buys, and N. Sarifuddin, "Mechanisms for doped PEDOT:PSS electrical conductivity improvement", *Materials Advances*, vol. 2, no. 22, pp. 7118–7138, **2021**, DOI: 10.1039/D1MA00290B.

[93] J. Y. Kim, J. H. Jung, D. E. Lee, and J. Joo, "Enhancement of Electrical Conductivity of Poly(3,4-ethylenedioxythiophene)/Poly(4-styrenesulfonate) by a Change of Solvents", *Synthetic Metals*, vol. 126, 2-3, pp. 311–316, **2002**, DOI: 10.1016/S0379-6779(01)00576-8.

[94] G.-H. Kim, L. Shao, K. Zhang, and K. P. Pipe, "Engineered doping of organic semiconductors for enhanced thermoelectric efficiency", *Nature Materials*, vol. 12, no. 8, pp. 719–723, **2013**, DOI: 10.1038/nmat3635.

[95] S. Liu, H. Deng, Y. Zhao, S. Ren, and Q. Fu, "The optimization of thermoelectric properties in a PEDOT:PSS thin film through post-treatment", *RSC Advances*, vol. 5, no. 3, pp. 1910–1917, **2015**, DOI: 10.1039/C4RA09147G.

[96] D. Bagchi and R. Menon, "Conformational modification of conducting polymer chains by solvents: Small-angle X-ray scattering study", *Chemical Physics Letters*, vol. 425, 1-3, pp. 114–117, **2006**, DOI: 10.1016/j.cplett.2006.05.014.

[97] L. A. Pettersson, S. Ghosh, and O. Inganäs, "Optical anisotropy in thin films of poly(3,4-ethylenedioxythiophene)–poly(4-styrenesulfonate)", *Organic Electronics*, vol. 3, 3-4, pp. 143–148, **2002**, DOI: 10.1016/S1566-1199(02)00051-4.

[98] H. J. Snaith, H. Kenrick, M. Chiesa, and R. H. Friend, "Morphological and electronic consequences of modifications to the polymer anode ‘PEDOT:PSS’", *Polymer*, vol. 46, no. 8, pp. 2573–2578, **2005**, DOI: 10.1016/j.polymer.2005.01.077.

[99] D. A. Mengistie, P.-C. Wang, and C.-W. Chu, "Effect of molecular weight of additives on the conductivity of PEDOT:PSS and efficiency for ITO-free organic solar cells", *Journal of Materials Chemistry A*, vol. 1, no. 34, pp. 9907–9915, **2013**, DOI: 10.1039/c3ta11726j.

[100] N. Saxena, B. Pretzl, X. Lamprecht, L. Bießmann, D. Yang, N. Li, C. Bilko, S. Bernstorff, and P. Müller-Buschbaum, "Ionic Liquids as Post-Treatment Agents for Simultaneous Improvement of Seebeck Coefficient and Electrical Conductivity in PEDOT:PSS Films", *ACS Applied Materials & Interfaces*, vol. 11, no. 8, pp. 8060–8071, **2019**, DOI: 10.1021/acsami.8b21709.

[101] A. de Izarra, S. Park, J. Lee, Y. Lansac, and Y. H. Jang, "Ionic Liquid Designed for PEDOT:PSS Conductivity Enhancement", *Journal of the American Chemical Society*, vol. 140, no. 16, pp. 5375–5384, **2018**, DOI: 10.1021/jacs.7b10306.

[102] N. Kim, S. Lienemann, I. Petsagkourakis, D. Alemu Mengistie, S. Kee, T. Ederth, V. Gueskine, P. Leclère, R. Lazzaroni, X. Crispin, and K. Tybrandt, "Elastic conducting polymer composites in thermoelectric modules", *Nature Communications*, vol. 11, no. 1, 1424, **2020**, DOI: 10.1038/s41467-020-15135-w.

[103] J. Atoyo, M. R. Burton, J. McGettrick, and M. J. Carnie, "Enhanced Electrical Conductivity and Seebeck Coefficient in PEDOT:PSS via a Two-Step Ionic liquid and NaBH4 Treatment for Organic Thermoelectrics", *Polymers*, vol. 12, no. 3, 559, **2020**, DOI: 10.3390/polym12030559.

[104] W. A. Muñoz, X. Crispin, M. Fahlman, and I. V. Zozoulenko, "Understanding the Impact of Film Disorder and Local Surface Potential in Ultraviolet Photoelectron Spectroscopy of PEDOT", *Macromolecular Rapid Communications*, vol. 39, no. 4, 1700533, **2018**, DOI: 10.1002/marc.201700533.

[105] J. T. Seebeck, "Magnetische Polarisation der Metalle und Erze durch Temperatur-Differenz", in: *Ostwald's Klassiker der Exakten Wissenschaften,* 70th ed. Leipzig: Verlag von Wilhelm Engelmann, **1822-1823**.

[106] J. C. A. Peltier, "Nouvelle Expériences sur la Caloricité des courans électriques.", *Annales de Chimie et de Physique*, vol. 56, no. 4, pp. 371–386, **1834**.

[107] Thomson, William (Baron Kelvin), "On the dynamical theory of heat; with numerical results deduced from Mr. Joule's equivalent of a thermal unit and M. Regnault's observations on steam", *Mathematical and Physical Papers*, no. 1, pp. 175–183, **1851**.

[108] L. Onsager, "Reciprocal Relations in Irreversible Processes. I", *Physical Review*, vol. 37, no. 4, pp. 405–426, **1931**, DOI: 10.1103/PhysRev.37.405.

[109] H. B. Callen, "The Application of Onsager's Reciprocal Relations to Thermoelectric, Thermomagnetic, and Galvanomagnetic Effects", *Physical Review*, vol. 73, no. 11, pp. 1349–1358, **1948**, DOI: 10.1103/PhysRev.73.1349.

[110] A. Feldhoff, "Thermoelectric Material Tensor Derived from the Onsager–de Groot–Callen Model", *Energy Harvesting and Systems*, vol. 2, no. 1, pp. 5–13, **2015**, DOI: 10.1515/ehs-2014-0040.

[111] W. Demtröder. *Experimentalphysik 2,* Berlin, Heidelberg: Springer Berlin Heidelberg, **2013**.

[112] H. E. Katz and T. O. Poehler, Eds. *Innovative thermoelectric materials: Polymer, nanostructure and composite thermoelectrics* London, Hackensack NJ: Imperial College Press; Distributed by World Scientific Publishing Co. Pte Ltd, **2016**.

[113] P. Wellmann. *Materialien der Elektronik und Energietechnik,* Wiesbaden: Springer Fachmedien Wiesbaden, **2017**.

[114] O. Bubnova. *Thermoelectric properties of conducting polymers,* PhD dissertation, Department of science and technology, Linköping University, Norrköping, **2013**.

[115] R. Franz and G. Wiedemann, "Ueber die Wärme-Leitungsfähigkeit der Metalle", *Annalen der Physik*, vol. 165, no. 8, pp. 497–531, **1853**, DOI: 10.1002/andp.18531650802.

[116] L. Lorenz, "Bestimmung der Wärmegrade in absolutem Maasse", *Annalen der Physik*, vol. 223, no. 11, pp. 429–452, **1872**, DOI: 10.1002/andp.18722231107.

[117] Q. Zhang, Y. Sun, W. Xu, and D. Zhu, "Organic thermoelectric materials: emerging green energy materials converting heat to electricity directly and efficiently", *Advanced Materials*, vol. 26, no. 40, pp. 6829–6851, **2014**, DOI: 10.1002/adma.201305371.

[118] Y. Zhang, W. Wang, F. Zhang, K. Dai, C. Li, Y. Fan, G. Chen, and Q. Zheng, "Soft Organic Thermoelectric Materials: Principles, Current State of the Art and Applications", *Small*, vol. 18, no. 12, 2104922, **2022**, DOI: 10.1002/smll.202104922.

[119] H. Wang, U. Ail, R. Gabrielsson, M. Berggren, and X. Crispin, "Ionic Seebeck Effect in Conducting Polymers", *Advanced Energy Materials*, vol. 5, no. 11, 1500044, **2015**, DOI: 10.1002/aenm.201500044.

[120] B. Yang and G. Portale, "Ionic thermoelectric materials for waste heat harvesting", *Colloid and Polymer Science*, vol. 299, no. 3, pp. 465–479, **2021**, DOI: 10.1007/s00396-020-04792-4.

[121] Z. Li, J. Fu, X. Zhou, S. Gui, L. Wei, H. Yang, H. Li, and X. Guo, "Ionic Conduction in Polymer-Based Solid Electrolytes", *Advanced Science*, vol. 10, no. 10, 2201718, **2023**, DOI: 10.1002/advs.202201718.

[122] B. D. Paulsen, S. Fabiano, and J. Rivnay, "Mixed Ionic-Electronic Transport in Polymers", *Annual Review of Materials Research*, vol. 51, no. 1, pp. 73–99, **2021**, DOI: 10.1146/annurev-matsci-080619-101319.

[123] Z. Xue, D. He, and X. Xie, "Poly(ethylene oxide)-based electrolytes for lithium-ion batteries", *Journal of Materials Chemistry A*, vol. 3, no. 38, pp. 19218–19253, **2015**, DOI: 10.1039/C5TA03471J.

[124] U. Ail, M. J. Jafari, H. Wang, T. Ederth, M. Berggren, and X. Crispin, "Thermoelectric Properties of Polymeric Mixed Conductors", *Advanced Functional Materials*, vol. 26, no. 34, pp. 6288–6296, **2016**, DOI: 10.1002/adfm.201601106.

[125] M. Tolan. *X-ray scattering from soft-matter thin films: Materials science and basic research,* Springer tracts in modern physics vol. 148, Berlin, Heidelberg: Springer, **1999**.

[126] M. Schmidbauer, Ed. *X-Ray Diffuse Scattering from Self-Organized Mesoscopic Semiconductor Structures* Springer tracts in modern physics vol. 199, Berlin, Heidelberg: Springer, **2004**.

[127] D. S. Sivia. *Elementary scattering theory: For X-ray and neutron users,* Oxford, New York: Oxford University Press, **2011**.

[128] J. Als-Nielsen and Des McMorrow. *Elements of modern X-ray physics,* Chichester: Wiley, **2017**.

[129] B. L. Henke, E. M. Gullikson, and J. C. Davis, "X-Ray Interactions: Photoabsorption, Scattering, Transmission, and Reflection at E = 50-30,000 eV, Z = 1-92", *Atomic Data and Nuclear Data Tables*, vol. 54, no. 2, pp. 181–342, **1993**, DOI: 10.1006/adnd.1993.1013.

[130] P. Müller-Buschbaum, "GISAXS and GISANS as metrology technique for understanding the 3D morphology of block copolymer thin films", *European Polymer Journal*, vol. 81, pp. 470–493, **2016**, DOI: 10.1016/j.eurpolymj.2016.04.007.

[131] J. Daillant and A. Gibaud, Eds. *X-ray and Neutron Reflectivity: Principles and Applications* Lecture Notes in Physics vol. 770, Berlin, Heidelberg: Springer Berlin Heidelberg, **2008**.

[132] C. M. Palumbiny. *Polymeric PEDOTPSS electrodes for organic electronics Understanding the conductivity-structure relation,* PhD dissertation, Physik-Department, Technische Universität München, München, **2015**.

[133] Y. Yoneda, "Anomalous Surface Reflection of X Rays", *Physical Review*, vol. 131, no. 5, pp. 2010–2013, **1963**, DOI: 10.1103/PhysRev.131.2010.

[134] R. Cubitt and G. Fragneto, "Neutron Reflection: Principles and Examples of Applications", in: *Scattering: Scattering and inverse scattering in pure and applied science*, E. R. Pike and P. C. Sabatier, Eds., San Diego: Academic Press, **2002**.

[135] D. Grigoriev, M. Hanke, M. Schmidbauer, P. Schäfer, O. Konovalov, and R. Köhler, "Grazing incidence x-ray diffraction at free-standing nanoscale islands: fine structure of diffuse scattering", *Journal of Physics D: Applied Physics*, vol. 36, no. 10A, pp. A225-A230, **2003**, DOI: 10.1088/0022-3727/36/10A/347.

[136] S. K. Sinha, E. B. Sirota, S. Garoff, and H. B. Stanley, "X-ray and neutron scattering from rough surfaces", *Physical review. B, Condensed matter*, vol. 38, no. 4, pp. 2297–2311, **1988**, DOI: 10.1103/PhysRevB.38.2297.

[137] L. G. Parratt, "Surface Studies of Solids by Total Reflection of X-Rays", *Physical Review*, vol. 95, no. 2, pp. 359–369, **1954**, DOI: 10.1103/PhysRev.95.359.

[138] O. Filies, O. Böling, K. Grewer, J. Lekki, M. Lekka, Z. Stachura, and B. Cleff, "Surface roughness of thin layers—a comparison of XRR and SFM measurements", *Applied Surface Science*, vol. 141, 3-4, pp. 357–365, **1999**, DOI: 10.1016/S0169-4332(98)00524-8.

[139] L. Névot and P. Croce, "Caractérisation des surfaces par réflexion rasante de rayons X. Application à l'étude du polissage de quelques verres silicates", *Revue de Physique Appliquée*, vol. 15, no. 3, pp. 761–779, **1980**, DOI: 10.1051/rphysap:01980001503076100.

[140] P. Müller-Buschbaum, "Structure Determination in Thin Film Geometry Using Grazing Incidence Small-Angle Scattering", in: *Polymer Surfaces and Interfaces*, M. Stamm, Ed., Berlin, Heidelberg: Springer Berlin Heidelberg, **2008**, pp. 17–46.

[141] A. Hexemer and P. Müller-Buschbaum, "Advanced grazing-incidence techniques for modern soft-matter materials analysis", *IUCrJ*, vol. 2, Pt 1, pp. 106–125, **2015**, DOI: 10.1107/S2052252514024178.

[142] R. Lazzari, "IsGISAXS : a program for grazing-incidence small-angle X-ray scattering analysis of supported islands", *Journal of Applied Crystallography*, vol. 35, no. 4, pp. 406–421, **2002**, DOI: 10.1107/S0021889802006088.

[143] G. H. Vineyard, "Grazing-incidence diffraction and the distorted-wave approximation for the study of surfaces", *Physical review. B, Condensed matter*, vol. 26, no. 8, pp. 4146–4159, **1982**, DOI: 10.1103/PhysRevB.26.4146.

[144] P. Müller-Buschbaum, "A Basic Introduction to Grazing Incidence Small-Angle X-Ray Scattering", in: *Applications of Synchrotron Light to Scattering and Diffraction in Materials and Life Sciences*, vol. 776, M. Gomez, A. Nogales, M. C. Garcia-Gutierrez, and T. A. Ezquerra, Eds., Berlin, Heidelberg: Springer Berlin Heidelberg, **2009**, pp. 61–89.

[145] J. Burle, C. Durniak, J. M. Fisher, M. Ganeva, G. Pospelov, and W. v. Herck, "BornAgain: *Software for Simulating and Fitting X-Ray and Neutron Small-Angle Scattering at Grazing Incidence.*", **2018**, http://www.bornagainproject.org/ (accessed Nov. 14, 2023).

[146] D. Babonneau, "FitGISAXS : software package for modelling and analysis of GISAXS data using IGOR Pro", *Journal of Applied Crystallography*, vol. 43, no. 4, pp. 929–936, **2010**, DOI: 10.1107/S0021889810020352.

[147] S. T. Chourou, A. Sarje, X. S. Li, E. R. Chan, and A. Hexemer, "HipGISAXS : a high-performance computing code for simulating grazing-incidence X-ray scattering data",

Journal of Applied Crystallography, vol. 46, no. 6, pp. 1781–1795, **2013**, DOI: 10.1107/S0021889813025843.

[148] P. Müller-Buschbaum, "Grazing incidence small-angle X-ray scattering: an advanced scattering technique for the investigation of nanostructured polymer films", *Analytical and Bioanalytical Chemistry*, vol. 376, no. 1, pp. 3–10, **2003**, DOI: 10.1007/s00216-003-1869-2.

[149] T. Salditt, T. H. Metzger, J. Peisl, B. Reinker, M. Moske, and K. Samwer, "Determination of the Height-Height Correlation Function of Rough Surfaces from Diffuse X-Ray Scattering", *Europhysics Letters*, vol. 32, no. 4, pp. 331–336, **1995**, DOI: 10.1209/0295-5075/32/4/008.

[150] T. Salditt, T. H. Metzger, J. Peisl, and G. Goerigk, "Non-specular X-ray scattering from thin films and multilayers with small-angle scattering equipment", *Journal of Physics D: Applied Physics*, vol. 28, no. 4A, pp. A236-A240, **1995**, DOI: 10.1088/0022-3727/28/4A/046.

[151] A. Naudon, D. Babonneau, D. Thiaudière, and S. Lequien, "Grazing-incidence small-angle X-ray scattering applied to the characterization of aggregates in surface regions", *Physica B: Condensed Matter*, vol. 283, 1-3, pp. 69–74, **2000**, DOI: 10.1016/S0921-4526(99)01894-3.

[152] G. Renaud, R. Lazzari, and F. Leroy, "Probing surface and interface morphology with Grazing Incidence Small Angle X-Ray Scattering", *Surface Science Reports*, vol. 64, no. 8, pp. 255–380, **2009**, DOI: 10.1016/j.surfrep.2009.07.002.

[153] C. J. Schaffer. *Morphological Degradation in Polymer-Fullerene Solar Cells,* PhD dissertation, Physik-Department, Technische Universität München, München, **2016**.

[154] J. Schlipf. *The Morphology of Hybrid Perovskite ThinFilms for Photovoltaic Application: ~ Formation & Disintegration ~,* PhD dissertation, Physik-Department, Technische Universität München, München, **2018**.

[155] R. Hosemann, W. Vogel, D. Weick, and F. J. Baltá-Calleja, "Novel aspects of the real paracrystal", *Acta Crystallographica Section A*, vol. 37, no. 1, pp. 85–91, **1981**, DOI: 10.1107/S0567739481000156.

[156] P. Müller-Buschbaum, E. Bauer, E. Maurer, A. Nelson, and R. Cubitt, "In-situ neutron reflectometry probing competitive swelling and de-swelling of thin polystyrene films", *Physica Status Solidi (RRL) – Rapid Research Letters*, vol. 1, no. 2, pp. R68-R70, **2007**, DOI: 10.1002/pssr.200600066.

[157] T. Gutberlet, R. Steitz, G. Fragneto, and B. Klösgen, "Phospholipid bilayer formation at a bare Si surface: a time-resolved neutron reflectivity study", *Journal of Physics: Condensed Matter*, vol. 16, no. 26, pp. S2469-S2476, **2004**, DOI: 10.1088/0953-8984/16/26/020.

[158] D. G. Bucknall, S. A. Butler, and J. S. Higgins, "Neutron reflectivity of polymer interfaces", *Journal of Physics and Chemistry of Solids*, vol. 60, no. 8-9, pp. 1273–1277, **1999**, DOI: 10.1016/S0022-3697(99)00101-8.

[159] R. Cubitt and G. Fragneto, "D17: the New Reflectometer at the ILL", *Applied Physics A: Materials Science & Processing*, vol. 74, pp. s329-s331, **2002**, DOI: 10.1007/s003390201611.

[160] M. Rawolle. *Structuring and Filling of Titania Films for Applications in Photovoltaics,* PhD dissertation, Physik-Department, Technische Universität München, München, **2013**.

[161] L. P. Kreuzer. *Dual Thermo-Responsive DiblockCopolymer Thin Films,* PhD dissertation, Physik-Department, Technische Universität München, München, **2021**.

[162] R. Cubitt, T. Saerbeck, R. A. Campbell, R. Barker, and P. Gutfreund, "An Improved Algorithm for Reducing Reflectometry Data Involving Divergent Beams or Non-Flat Samples", *Journal of Applied Crystallography*, vol. 48, no. 6, pp. 2006–2011, **2015**, DOI: 10.1107/S1600576715019500.

[163] A. L. Oechsle, J. E. Heger, N. Li, S. Yin, S. Bernstorff, and P. Müller-Buschbaum, "Correlation of Thermoelectric Performance, Domain Morphology and Doping Level in PEDOT:PSS Thin Films Post-Treated with Ionic Liquids", *Macromolecular Rapid Communications*, vol. 42, no. 20, 2100397, **2021**, DOI: 10.1002/marc.202100397.

[164] F. S. Rocha, A. J. Gomes, C. N. Lunardi, S. Kaliaguine, and G. S. Patience, "Experimental methods in chemical engineering: Ultraviolet visible spectroscopy—UV-Vis", *The Canadian Journal of Chemical Engineering*, vol. 96, no. 12, pp. 2512–2517, **2018**, DOI: 10.1002/cjce.23344.

[165] Dr. Gerhard Zwick, presentation-"FTIR Gasanalysatoren Möglichkeiten und Grenzen.", Ansyco GmbH, Karlsruhe.

[166] Filmetrics Inc., handbook-"Thin-Film Measurement", **2012**.

[167] X. Lamprecht. *Influence of ionic liquids on thermoelectric properties of polymer thin films and design of a new Seebeck coefficient measurement setup,* Bachelor thesis, Physik-Department, Technische Universität München, München, **2016**.

[168] N. Saxena. *Thermoelectric thin films based on conducting polymers - Saxena,* PhD dissertation, Physik-Department, Technische Universität München, München, **2019**.

[169] T. Schöner. *Investigation of the Charge Transport in Ionic Liquid Post-treated Poly(3,4-ethylene dioxythiophene):poly(styrene sulfonate) Thin Films with Electrochemical Impedance Spectroscopy,* Master thesis, Physik-Department, Technische Universität München, München, **2022**.

[170] Park Systems, handbook-"Conductive AFM: *Mode Notes*", **2021**.

[171] R. Asmatulu and W. S. Khan, Eds. *Synthesis and applications of electrospun nanofibers* Micro & nano technologies series Oxford, United Kingdom: Elsevier, **2019**.

[172] A. Nelson, "Co-Refinement of Multiple-Contrast Neutron/X-Ray Reflectivity Data Using MOTOFIT", *Journal of Applied Crystallography*, vol. 39, no. 2, pp. 273–276, **2006**, DOI: 10.1107/S0021889806005073.

[173] H. Kiessig, "Interferenz von Röntgenstrahlen an dünnen Schichten", *Annalen der Physik*, vol. 402, no. 7, pp. 769–788, **1931**, DOI: 10.1002/andp.19314020702.

[174] G. Benecke, W. Wagermaier, C. Li, M. Schwartzkopf, G. Flucke, R. Hoerth, I. Zizak, M. Burghammer, E. Metwalli, P. Müller-Buschbaum, M. Trebbin, S. Förster, O. Paris, S. V. Roth, and P. Fratzl, "A customizable software for fast reduction and analysis of large X-ray scattering data sets: applications of the new DPDAK package to small-angle X-ray scattering and grazing-incidence small-angle X-ray scattering", *Journal of Applied Crystallography*, vol. 47, no. 5, pp. 1797–1803, **2014**, DOI: 10.1107/S1600576714019773.

[175] T. Saerbeck, R. Cubitt, A. Wildes, G. Manzin, K. H. Andersen, and P. Gutfreund, "Recent upgrades of the neutron reflectometer D17 at ILL", *Journal of Applied Crystallography*, vol. 51, no. 2, pp. 249–256, **2018**, DOI: 10.1107/S160057671800239X.

[176] P. Gutfreund, T. Saerbeck, M. A. Gonzalez, E. Pellegrini, M. Laver, C. Dewhurst, and R. Cubitt, "Towards Generalized Data Reduction on a Chopper-Based Time-of-Flight Neutron Reflectometer", *Journal of Applied Crystallography*, vol. 51, no. 3, pp. 606–615, **2018**, DOI: 10.1107/S160057671800448X.

[177] V. F. Sears, "Neutron Scattering Lengths and Cross Sections", *Neutron News*, vol. 3, no. 3, pp. 26–37, **1992**, DOI: 10.1080/10448639208218770.

[178] D. Magerl, M. Philipp, X.-P. Qiu, F. M. Winnik, and P. Müller-Buschbaum, "Swelling and Thermoresponsive Behavior of Linear versus Cyclic Poly(N -isopropylacrylamide)

Thin Films", *Macromolecules*, vol. 48, no. 9, pp. 3104–3111, **2015**, DOI: 10.1021/acs.macromol.5b00436.

[179] L. Bießmann, L. P. Kreuzer, T. Widmann, N. Hohn, J.-F. Moulin, and P. Müller-Buschbaum, "Monitoring the Swelling Behavior of PEDOT:PSS Electrodes under High Humidity Conditions", *ACS Applied Materials & Interfaces*, vol. 10, no. 11, pp. 9865–9872, **2018**, DOI: 10.1021/acsami.8b00446.

[180] T. Widmann, L. P. Kreuzer, G. Mangiapia, M. Haese, H. Frielinghaus, and P. Müller-Buschbaum, "3D Printed Spherical Environmental Chamber for Neutron Reflectometry and Grazing-Incidence Small-Angle Neutron Scattering Experiments", *The Review of Scientific Instruments*, vol. 91, no. 11, 113903, **2020**, DOI: 10.1063/5.0012652.

[181] R. L. Vekariya, "A review of ionic liquids: Applications towards catalytic organic transformations", *Journal of Molecular Liquids*, vol. 227, pp. 44–60, **2017**, DOI: 10.1016/j.molliq.2016.11.123.

[182] D. M. Correia, L. C. Fernandes, P. M. Martins, C. García-Astrain, C. M. Costa, J. Reguera, and S. Lanceros-Méndez, "Ionic Liquid–Polymer Composites: A New Platform for Multifunctional Applications", *Advanced Functional Materials*, vol. 30, no. 24, 1909736, **2020**, DOI: 10.1002/adfm.201909736.

[183] P. Müller-Buschbaum, "Influence of Surface Cleaning on Dewetting of Thin Polystyrene Films", *The European Physical Journal. E, Soft matter*, vol. 12, no. 3, 443-448, **2003**, DOI: 10.1140/epje/e2004-00014-7.

[184] S. Riffat and X. Ma, "Thermoelectrics: a review of present and potential applications", *Applied Thermal Engineering*, vol. 23, no. 8, pp. 913–935, **2003**, DOI: 10.1016/S1359-4311(03)00012-7.

[185] I. Petsagkourakis, K. Tybrandt, X. Crispin, I. Ohkubo, N. Satoh, and T. Mori, "Thermoelectric materials and applications for energy harvesting power generation", *Science and Technology of Advanced Materials*, vol. 19, no. 1, pp. 836–862, **2018**, DOI: 10.1080/14686996.2018.1530938.

[186] J. Liu, M. P. Garman, J. Dong, B. van der Zee, L. Qiu, G. Portale, J. C. Hummelen, and L. J. A. Koster, "Doping Engineering Enables Highly Conductive and Thermally Stable n-Type Organic Thermoelectrics with High Power Factor", *ACS Applied Energy Materials*, vol. 2, no. 9, pp. 6664–6671, **2019**, DOI: 10.1021/acsaem.9b01179.

[187] D. Zhao and G. Tan, "A review of thermoelectric cooling: Materials, modeling and applications", *Applied Thermal Engineering*, vol. 66, no. 1-2, pp. 15–24, **2014**, DOI: 10.1016/j.applthermaleng.2014.01.074.

[188] J. Liu, G. Ye, H. G. O. Potgieser, M. Koopmans, S. Sami, M. I. Nugraha, D. R. Villalva, H. Sun, J. Dong, X. Yang, X. Qiu, C. Yao, G. Portale, S. Fabiano, T. D. Anthopoulos, D. Baran, R. W. A. Havenith, R. C. Chiechi, and L. J. A. Koster, "Amphipathic Side Chain of a Conjugated Polymer Optimizes Dopant Location toward Efficient N-Type Organic Thermoelectrics", *Advanced Materials*, vol. 33, no. 4, 2006694, **2021**, DOI: 10.1002/adma.202006694.

[189] J. Liu, B. van der Zee, R. Alessandri, S. Sami, J. Dong, M. I. Nugraha, A. J. Barker, S. Rousseva, L. Qiu, X. Qiu, N. Klasen, R. C. Chiechi, D. Baran, M. Caironi, T. D. Anthopoulos, G. Portale, R. W. A. Havenith, S. J. Marrink, J. C. Hummelen, and L. J. A. Koster, "N-type organic thermoelectrics: demonstration of ZT 0.3", *Nature Communications*, vol. 11, 5694, **2020**, DOI: 10.1038/s41467-020-19537-8.

[190] M. Goel, C. D. Heinrich, G. Krauss, and M. Thelakkat, "Principles of Structural Design of Conjugated Polymers Showing Excellent Charge Transport toward Thermoelectrics and Bioelectronics Applications", *Macromolecular Rapid Communications*, vol. 40, no. 10, 1800915, **2019**, DOI: 10.1002/marc.201800915.

[191] K.-H. Yim, G. L. Whiting, C. E. Murphy, J. J. M. Halls, J. H. Burroughes, R. H. Friend, and J.-S. Kim, "Controlling Electrical Properties of Conjugated Polymers via a Solution-Based p-Type Doping", *Advanced Materials*, vol. 20, no. 17, pp. 3319–3324, **2008**, DOI: 10.1002/adma.200800735.

[192] E. H. Suh, J. G. Oh, J. Jung, S. H. Noh, T. S. Lee, and J. Jang, "Brønsted Acid Doping of P3HT with Largely Soluble Tris(pentafluorophenyl)borane for Highly Conductive and Stable Organic Thermoelectrics Via One-Step Solution Mixing", *Advanced Energy Materials*, vol. 10, no. 47, 2002521, **2020**, DOI: 10.1002/aenm.202002521.

[193] C. Pan, L. Wang, T. Liu, X. Zhou, T. Wan, S. Wang, Z. Chen, C. Gao, and L. Wang, "Polar Side Chain Effects on the Thermoelectric Properties of Benzo1,2-b:4,5-b'Dithiophene-Based Conjugated Polymers", *Macromolecular Rapid Communications*, vol. 40, no. 12, 1900082, **2019**, DOI: 10.1002/marc.201900082.

[194] S. Wu, X. Wu, W. Xing, Y. Sun, Y. Zou, W. Xu, and D. Zhu, "Backbone Structure Effect on the Thermoelectric Properties of IDT-Based p-Type Conjugated Polymers",

Macromolecular Rapid Communications, vol. 41, no. 1, 1900322, **2020**, DOI: 10.1002/marc.201900322.

[195] Y. Zhang and S.-J. Park, "Flexible Organic Thermoelectric Materials and Devices for Wearable Green Energy Harvesting", *Polymers*, vol. 11, no. 5, 909, **2019**, DOI: 10.3390/polym11050909.

[196] L. Hu, J. Song, X. Yin, Z. Su, and Z. Li, "Research Progress on Polymer Solar Cells Based on PEDOT:PSS Electrodes", *Polymers*, vol. 12, no. 1, 145, **2020**, DOI: 10.3390/polym12010145.

[197] R. J. Murphy, K. M. Weigandt, D. Uhrig, A. Alsayed, C. Badre, L. Hough, and M. Muthukumar, "Scattering Studies on Poly(3,4-ethylenedioxythiophene)–Polystyrenesulfonate in the Presence of Ionic Liquids", *Macromolecules*, vol. 48, no. 24, pp. 8989–8997, **2015**, DOI: 10.1021/acs.macromol.5b02320.

[198] X. Wu, A. Surendran, J. Ko, O. Filonik, E. M. Herzig, P. Müller-Buschbaum, and W. L. Leong, "Ionic-Liquid Doping Enables High Transconductance, Fast Response Time, and High Ion Sensitivity in Organic Electrochemical Transistors", *Advanced Materials*, vol. 31, no. 2, 1805544, **2019**, DOI: 10.1002/adma.201805544.

[199] Q. Li, Q. Zhou, L. Wen, and W. Liu, "Enhanced thermoelectric performances of flexible PEDOT:PSS film by synergistically tuning the ordering structure and oxidation state", *Journal of Materiomics*, vol. 6, no. 1, pp. 119–127, **2020**, DOI: 10.1016/j.jmat.2020.01.001.

[200] S. Kee, N. Kim, B. S. Kim, S. Park, Y. H. Jang, S. H. Lee, J. Kim, J. Kim, S. Kwon, and K. Lee, "Controlling Molecular Ordering in Aqueous Conducting Polymers Using Ionic Liquids", *Advanced Materials*, vol. 28, no. 39, pp. 8625–8631, **2016**, DOI: 10.1002/adma.201505473.

[201] S. Kee, H. Kim, S. H. K. Paleti, A. El Labban, M. Neophytou, A.-H. Emwas, H. N. Alshareef, and D. Baran, "Highly Stretchable and Air-Stable PEDOT:PSS/Ionic Liquid Composites for Efficient Organic Thermoelectrics", *Chemistry of Materials*, vol. 31, no. 9, pp. 3519–3526, **2019**, DOI: 10.1021/acs.chemmater.9b00819.

[202] C. Badre, L. Marquant, A. M. Alsayed, and L. A. Hough, "Highly Conductive Poly(3,4-ethylenedioxythiophene):Poly (styrenesulfonate) Films Using 1-Ethyl-3-methylimidazolium Tetracyanoborate Ionic Liquid", *Advanced Functional Materials*, vol. 22, no. 13, pp. 2723–2727, **2012**, DOI: 10.1002/adfm.201200225.

[203] S. D. Kang and G. J. Snyder, "Charge-transport model for conducting polymers", *Nature Materials*, vol. 16, no. 2, pp. 252–257, **2017**, DOI: 10.1038/nmat4784.

[204] J. Han, C. Ganley, Q. Hu, X. Zhao, P. Clancy, T. P. Russell, and H. E. Katz, "Using Preformed Meisenheimer Complexes as Dopants for n-Type Organic Thermoelectrics with High Seebeck Coefficients and Power Factors", *Advanced Functional Materials*, vol. 31, no. 18, 2010567, **2021**, DOI: 10.1002/adfm.202010567.

[205] A. F. M. Cláudio, L. Swift, J. P. Hallett, T. Welton, J. A. P. Coutinho, and M. G. Freire, "Extended scale for the hydrogen-bond basicity of ionic liquids", *Physical Chemistry Chemical Physics*, vol. 16, no. 14, pp. 6593–6601, **2014**, DOI: 10.1039/c3cp55285c.

[206] W. B. Chang, H. Fang, J. Liu, C. M. Evans, B. Russ, B. C. Popere, S. N. Patel, M. L. Chabinyc, and R. A. Segalman, "Electrochemical Effects in Thermoelectric Polymers", *ACS Macro Letters*, vol. 5, no. 4, pp. 455–459, **2016**, DOI: 10.1021/acsmacrolett.6b00054.

[207] H. He and J. Ouyang, "Enhancements in the Mechanical Stretchability and Thermoelectric Properties of PEDOT:PSS for Flexible Electronics Applications", *Accounts of Materials Research*, vol. 1, no. 2, pp. 146–157, **2020**, DOI: 10.1021/accountsmr.0c00021.

[208] X. Guan, H. Cheng, and J. Ouyang, "Significant enhancement in the Seebeck coefficient and power factor of thermoelectric polymers by the Soret effect of polyelectrolytes", *Journal of Materials Chemistry A*, vol. 6, no. 40, pp. 19347–19352, **2018**, DOI: 10.1039/C8TA08387H.

[209] Z. Fan, D. Du, X. Guan, and J. Ouyang, "Polymer films with ultrahigh thermoelectric properties arising from significant seebeck coefficient enhancement by ion accumulation on surface", *Nano Energy*, vol. 51, pp. 481–488, **2018**, DOI: 10.1016/j.nanoen.2018.07.002.

[210] D.-J. Yun, J. Jung, K.-H. Kim, H. Ra, J.-M. Kim, B. S. Choi, J. Jang, M. Seol, and Y. J. Jeong, "Simultaneous increases in electrical conductivity and work function of ionic liquid treated PEDOT:PSS: In-depth investigation and thermoelectric application", *Applied Surface Science*, vol. 553, 149584, **2021**, DOI: 10.1016/j.apsusc.2021.149584.

[211] B. Huang, X. Luo, Q. Zou, S. Wang, and J. Zhang, "Highly elastic and flexible transparent conductive films derived from latex copolymerization: P(SSNa-BA-St)/PEDOT/graphene", *RSC Advances*, vol. 9, no. 72, pp. 42335–42342, **2019**, DOI: 10.1039/c9ra09099a.

[212] Y. Xie, S.-H. Zhang, H.-Y. Jiang, H. Zeng, R.-M. Wu, H. Chen, Y.-F. Gao, Y.-Y. Huang, and H.-L. Bai, "Properties of carbon black-PEDOT composite prepared via in-situ chemical oxidative polymerization", *e-Polymers*, vol. 19, no. 1, pp. 61–69, **2019**, DOI: 10.1515/epoly-2019-0008.

[213] S. Xiong, L. Zhang, and X. Lu, "Conductivities enhancement of poly(3,4-ethylenedioxythiophene)/poly(styrene sulfonate) transparent electrodes with diol additives", *Polymer Bulletin*, vol. 70, no. 1, pp. 237–247, **2013**, DOI: 10.1007/s00289-012-0833-8.

[214] P. Li, D. R. Paul, and T.-S. Chung, "High performance membranes based on ionic liquid polymers for CO2 separation from the flue gas", *Green Chemistry*, vol. 14, no. 4, pp. 1052–1063, **2012**, DOI: 10.1039/c2gc16354c.

[215] S. Kee, N. Kim, H. Park, B. S. Kim, M. Y. Teo, S. Lee, J. Kim, and K. Lee, "Tuning the Mechanical and Electrical Properties of Stretchable PEDOT:PSS/Ionic Liquid Conductors", *Macromolecular Chemistry and Physics*, vol. 221, no. 23, 2000291, **2020**, DOI: 10.1002/macp.202000291.

[216] N. Kim, B. H. Lee, D. Choi, G. Kim, H. Kim, J.-R. Kim, J. Lee, Y. H. Kahng, and K. Lee, "Role of interchain coupling in the metallic state of conducting polymers", *Physical Review Letters*, vol. 109, no. 10, 106405, **2012**, DOI: 10.1103/PhysRevLett.109.106405.

[217] Q. Jiang, C. Liu, H. Song, H. Shi, Y. Yao, J. Xu, G. Zhang, and B. Lu, "Improved Thermoelectric Performance of PEDOT:PSS Films prepared by Polar-Solvent vapor annealing method", *Journal of Materials Science: Materials in Electronics*, vol. 24, no. 11, pp. 4240–4246, **2013**, DOI: 10.1007/s10854-013-1391-z.

[218] Y.-J. Lin, J.-Y. Lee, and S.-M. Chen, "Changing electrical properties of PEDOT:PSS by incorporating with dimethyl sulfoxide", *Chemical Physics Letters*, vol. 664, pp. 213–218, **2016**, DOI: 10.1016/j.cplett.2016.10.038.

[219] Q. Wei, M. Mukaida, Y. Naitoh, and T. Ishida, "Morphological change and mobility enhancement in PEDOT:PSS by adding co-solvents", *Advanced Materials*, vol. 25, no. 20, pp. 2831–2836, **2013**, DOI: 10.1002/adma.201205158.

[220] S. Fabiano, S. Braun, X. Liu, E. Weverberghs, P. Gerbaux, M. Fahlman, M. Berggren, and X. Crispin, "Poly(ethylene imine) impurities induce n-doping reaction in organic (semi)conductors", *Advanced Materials*, vol. 26, no. 34, pp. 6000–6006, **2014**, DOI: 10.1002/adma.201401986.

[221] C. Duc, G. G. Malliaras, V. Senez, and A. Vlandas, "Long-term ageing of PEDOT:PSS: wettability Study", *Synthetic Metals*, vol. 238, pp. 14–21, **2018**, DOI: 10.1016/j.synthmet.2018.02.003.

[222] A. M. Nardes, M. Kemerink, M. M. de Kok, E. Vinken, K. Maturova, and R. Janssen, "Conductivity, work function, and environmental stability of PEDOT:PSS thin films treated with sorbitol", *Organic Electronics*, vol. 9, no. 5, pp. 727–734, **2008**, DOI: 10.1016/j.orgel.2008.05.006.

[223] J. Yu, Y. Zheng, and J. Huang, "Towards High Performance Organic Photovoltaic Cells: A Review of Recent Development in Organic Photovoltaics", *Polymers*, vol. 6, no. 9, pp. 2473–2509, **2014**, DOI: 10.3390/polym6092473.

[224] D. Yang, S. Grott, X. Jiang, K. S. Wienhold, M. Schwartzkopf, S. V. Roth, and P. Müller-Buschbaum, "In Situ Studies of Solvent Additive Effects on the Morphology Development during Printing of Bulk Heterojunction Films for Organic Solar Cells", *Small Methods*, vol. 4, no. 9, 2000418, **2020**, DOI: 10.1002/smtd.202000418.

[225] K. S. Wienhold, V. Körstgens, S. Grott, X. Jiang, M. Schwartzkopf, S. V. Roth, and P. Müller-Buschbaum, "Effect of Solvent Additives on the Morphology and Device Performance of Printed Nonfullerene Acceptor Based Organic Solar Cells", *ACS Applied Materials & Interfaces*, vol. 11, no. 45, pp. 42313–42321, **2019**, DOI: 10.1021/acsami.9b16784.

[226] B. Geffroy, P. Le Roy, and C. Prat, "Organic Light-Emitting Diode (OLED) Technology: Materials, Devices and Display Technologies", *Polymer International*, vol. 55, no. 6, pp. 572–582, **2006**, DOI: 10.1002/pi.1974.

[227] G. Hong, X. Gan, C. Leonhardt, Z. Zhang, J. Seibert, J. M. Busch, and S. Bräse, "A Brief History of OLEDs-Emitter Development and Industry Milestones", *Advanced Materials*, vol. 33, no. 9, 2005630, **2021**, DOI: 10.1002/adma.202005630.

[228] I. Verboven and W. Deferme, "Printing of flexible light emitting devices: A review on different technologies and devices, printing technologies and state-of-the-art applications and future prospects", *Progress in Materials Science*, vol. 118, 100760, **2021**, DOI: 10.1016/j.pmatsci.2020.100760.

[229] M. A. Rahman, P. Kumar, D.-S. Park, and Y.-B. Shim, "Electrochemical Sensors Based on Organic Conjugated Polymers", *Sensors*, vol. 8, no. 1, pp. 118–141, **2008**, DOI: 10.3390/s8010118.

[230] J. T. Mabeck and G. G. Malliaras, "Chemical and biological sensors based on organic thin-film transistors", *Analytical and Bioanalytical Chemistry*, vol. 384, no. 2, pp. 343–353, **2006**, DOI: 10.1007/s00216-005-3390-2.

[231] S. Wang, Y. Kang, L. Wang, H. Zhang, Y. Wang, and Y. Wang, "Organic/inorganic hybrid sensors: A review", *Sensors and Actuators B: Chemical*, vol. 182, pp. 467–481, **2013**, DOI: 10.1016/j.snb.2013.03.042.

[232] B. Lüssem, C.-M. Keum, D. Kasemann, B. Naab, Z. Bao, and K. Leo, "Doped Organic Transistors", *Chemical Reviews*, vol. 116, no. 22, pp. 13714–13751, **2016**, DOI: 10.1021/acs.chemrev.6b00329.

[233] K. Liu, B. Ouyang, X. Guo, Y. Guo, and Y. Liu, "Advances in flexible organic field-effect transistors and their applications for flexible electronics", *npj Flexible Electronics*, vol. 6, no. 1, **2022**, DOI: 10.1038/s41528-022-00133-3.

[234] Y. Yamashita, "Organic semiconductors for organic field-effect transistors", *Science and Technology of Advanced Materials*, vol. 10, no. 2, 024313, **2009**, DOI: 10.1088/1468-6996/10/2/024313.

[235] W. Cao, J. Li, H. Chen, and J. Xue, "Transparent electrodes for organic optoelectronic devices: a review", *Journal of Photonics for Energy*, vol. 4, no. 1, 040990, **2014**, DOI: 10.1117/1.JPE.4.040990.

[236] L. Wang and X. Hu, "Transparent Electrodes for Energy Storage Devices", *Batteries & Supercaps*, vol. 3, no. 12, pp. 1275–1286, **2020**, DOI: 10.1002/batt.202000187.

[237] M. Wang, P. Baek, A. Akbarinejad, D. Barker, and J. Travas-Sejdic, "Conjugated polymers and composites for stretchable organic electronics", *Journal of Materials Chemistry C*, vol. 7, no. 19, pp. 5534–5552, **2019**, DOI: 10.1039/C9TC00709A.

[238] M. G. Sumdani, M. R. Islam, A. N. A. Yahaya, and S. I. Safie, "Recent advancements in synthesis, properties, and applications of conductive polymers for electrochemical energy storage devices: A review", *Polymer Engineering & Science*, vol. 62, no. 2, pp. 269–303, **2022**, DOI: 10.1002/pen.25859.

[239] S. Tajik, H. Beitollahi, F. G. Nejad, I. S. Shoaie, M. A. Khalilzadeh, M. S. Asl, Q. van Le, K. Zhang, H. W. Jang, and M. Shokouhimehr, "Recent developments in conducting polymers: applications for electrochemistry", *RSC Advances*, vol. 10, no. 62, pp. 37834–37856, **2020**, DOI: 10.1039/d0ra06160c.

[240] J. Gasiorowski, R. Menon, K. Hingerl, M. Dachev, and N. S. Sariciftci, "Surface morphology, optical properties and conductivity changes of poly(3,4-

ethylenedioxythiophene):poly(styrenesulfonate) by using additives", *Thin Solid Films*, vol. 536, no. 100, pp. 211–215, **2013**, DOI: 10.1016/j.tsf.2013.03.124.

[241] E. Vitoratos, S. Sakkopoulos, E. Dalas, N. Paliatsas, D. Karageorgopoulos, F. Petraki, S. Kennou, and S. Choulis, "Thermal degradation mechanisms of PEDOT:PSS", *Organic Electronics*, vol. 10, no. 1, pp. 61–66, **2009**, DOI: 10.1016/j.orgel.2008.10.008.

[242] L. Stepien, A. Roch, R. Tkachov, B. Leupolt, L. Han, N. van Ngo, and C. Leyens, "Thermal operating window for PEDOT:PSS films and its related thermoelectric properties", *Synthetic Metals*, vol. 225, pp. 49–54, **2017**, DOI: 10.1016/j.synthmet.2016.11.017.

[243] M. Y. Teo, N. Kim, S. Kee, B. S. Kim, G. Kim, S. Hong, S. Jung, and K. Lee, "Highly Stretchable and Highly Conductive PEDOT:PSS/Ionic Liquid Composite Transparent Electrodes for Solution-Processed Stretchable Electronics", *ACS Applied Materials & Interfaces*, vol. 9, no. 1, pp. 819–826, **2017**, DOI: 10.1021/acsami.6b11988.

[244] X. Fan, W. Nie, H. Tsai, N. Wang, H. Huang, Y. Cheng, R. Wen, L. Ma, F. Yan, and Y. Xia, "PEDOT:PSS for Flexible and Stretchable Electronics: Modifications, Strategies, and Applications", *Advanced Science*, vol. 6, no. 19, 1900813, **2019**, DOI: 10.1002/advs.201900813.

[245] L.-W. Lo, J. Zhao, H. Wan, Y. Wang, S. Chakrabartty, and C. Wang, "An Inkjet-Printed PEDOT:PSS-Based Stretchable Conductor for Wearable Health Monitoring Device Applications", *ACS Applied Materials & Interfaces*, vol. 13, no. 18, pp. 21693–21702, **2021**, DOI: 10.1021/acsami.1c00537.

[246] Y. Jiang, X. Dong, L. Sun, T. Liu, F. Qin, C. Xie, P. Jiang, L. Hu, X. Lu, X. Zhou, W. Meng, N. Li, C. J. Brabec, and Y. Zhou, "An alcohol-dispersed conducting polymer complex for fully printable organic solar cells with improved stability", *Nature Energy*, vol. 7, no. 4, pp. 352–359, **2022**, DOI: 10.1038/s41560-022-00997-9.

[247] F. Hempel, J. K. Y. Law, T. C. Nguyen, R. Lanche, A. Susloparova, X. T. Vu, and S. Ingebrandt, "PEDOT:PSS Organic Electrochemical Transistors for Electrical Cell-Substrate Impedance Sensing Down to Single Cells", *Biosensors & Bioelectronics*, vol. 180, 113101, **2021**, DOI: 10.1016/j.bios.2021.113101.

[248] G. Wang, X. Tao, and R. Wang, "Fabrication and Characterization of OLEDs using PEDOT:PSS and MWCNT Nanocomposites", *Composites Science and Technology*, vol. 68, no. 14, pp. 2837–2841, **2008**, DOI: 10.1016/j.compscitech.2007.11.004.

[249] H. S. Kang, D. H. Kim, and T. W. Kim, "Organic light-emitting devices based on conducting polymer treated with benzoic acid", *Scientific Reports*, vol. 11, no. 1, 3885, **2021**, DOI: 10.1038/s41598-021-82980-0.

[250] M. Beccatelli, M. Villani, F. Gentile, L. Bruno, D. Seletti, D. M. Nikolaidou, M. Culiolo, A. Zappettini, and N. Coppedè, "All-Polymeric Pressure Sensors Based on PEDOT:PSS-Modified Polyurethane Foam", *ACS Applied Polymer Materials*, vol. 3, no. 3, pp. 1563–1572, **2021**, DOI: 10.1021/acsapm.0c01389.

[251] J. Kawahara, P. A. Ersman, I. Engquist, and M. Berggren, "Improving the Color Switch Contrast in PEDOT:PSS-based Electrochromic Displays", *Organic Electronics*, vol. 13, no. 3, pp. 469–474, **2012**, DOI: 10.1016/j.orgel.2011.12.007.

[252] D. Levasseur, I. Mjejri, T. Rolland, and A. Rougier, "Color Tuning by Oxide Addition in PEDOT:PSS-Based Electrochromic Devices", *Polymers*, vol. 11, no. 1, 179, **2019**, DOI: 10.3390/polym11010179.

[253] J. N. Arthur, S. Burns, C. M. Cole, Q. T. Barthelme, and S. D. Yambem, "PEDOT:PSS hydrogel gate electrodes for OTFT sensors", *Journal of Materials Chemistry C*, vol. 10, no. 37, pp. 13964–13973, **2022**, DOI: 10.1039/D2TC01096H.

[254] J. Huang, P. F. Miller, J. S. Wilson, A. J. de Mello, J. C. de Mello, and D. D. C. Bradley, "Investigation of the Effects of Doping and Post-Deposition Treatments on the Conductivity, Morphology, and Work Function of Poly(3,4-ethylenedioxythiophene)/Poly(styrene sulfonate) Films", *Advanced Functional Materials*, vol. 15, no. 2, pp. 290–296, **2005**, DOI: 10.1002/adfm.200400073.

[255] Y.-F. Wang, T. Sekine, Y. Takeda, K. Yokosawa, H. Matsui, D. Kumaki, T. Shiba, T. Nishikawa, and S. Tokito, "Fully Printed PEDOT:PSS-based Temperature Sensor with High Humidity Stability for Wireless Healthcare Monitoring", *Scientific Reports*, vol. 10, no. 1, 2467, **2020**, DOI: 10.1038/s41598-020-59432-2.

[256] F. Hossein-Babaei, T. Akbari, and B. Harkinezhad, "Dopant passivation by adsorbed water monomers causes high humidity sensitivity in PEDOT: PSS thin films at ppm-level humidity", *Sensors and Actuators B: Chemical*, vol. 293, pp. 329–335, **2019**, DOI: 10.1016/j.snb.2019.05.018.

[257] S. Taccola, F. Greco, A. Zucca, C. Innocenti, C. d. J. Fernández, G. Campo, C. Sangregorio, B. Mazzolai, and V. Mattoli, "Characterization of Free-Standing PEDOT:PSS/Iron Oxide Nanoparticle Composite Thin Films and Application as

Conformable Humidity Sensors", *ACS Applied Materials & Interfaces*, vol. 5, no. 13, pp. 6324–6332, **2013**, DOI: 10.1021/am4013775.

[258] C. Zhou, X. Zhang, N. Tang, Y. Fang, H. Zhang, and X. Duan, "Rapid Response Flexible Humidity Sensor for Respiration Monitoring Using Nano-Confined Strategy", *Nanotechnology*, vol. 31, no. 12, 125302, **2020**, DOI: 10.1088/1361-6528/ab5cda.

[259] M. Kuş and S. Okur, "Electrical Characterization of PEDOT:PSS Beyond Humidity Saturation", *Sensors and Actuators B: Chemical*, vol. 143, no. 1, pp. 177–181, **2009**, DOI: 10.1016/j.snb.2009.08.055.

[260] R. A. Huggins, "Simple Method to Determine Electronic and Ionic Components of the Conductivity in Mixed Conductors a Review", *Ionics*, vol. 8, no. 3-4, pp. 300–313, **2002**, DOI: 10.1007/BF02376083.

[261] C.-Y. Lo, Y. Wu, E. Awuyah, D. Meli, D. M. Nguyen, R. Wu, B. Xu, J. Strzalka, J. Rivnay, D. C. Martin, and L. V. Kayser, "Influence of the Molecular Weight and Size Distribution of PSS on Mixed Ionic-Electronic Transport in PEDOT:PSS", *Polymer Chemistry*, vol. 13, no. 19, pp. 2764–2775, **2022**, DOI: 10.1039/d2py00271j.

[262] K. Gu, C. R. Snyder, J. Onorato, C. K. Luscombe, A. W. Bosse, and Y.-L. Loo, "Assessing the Huang-Brown Description of Tie Chains for Charge Transport in Conjugated Polymers", *ACS Macro Letters*, vol. 7, no. 11, pp. 1333–1338, **2018**, DOI: 10.1021/acsmacrolett.8b00626.

[263] R. Noriega, J. Rivnay, K. Vandewal, F. P. V. Koch, N. Stingelin, P. Smith, M. F. Toney, and A. Salleo, "A general relationship between disorder, aggregation and charge transport in conjugated polymers", *Nature Materials*, vol. 12, no. 11, pp. 1038–1044, **2013**, DOI: 10.1038/nmat3722.

[264] M. Modarresi and I. Zozoulenko, "Why does solvent treatment increase the conductivity of PEDOT : PSS? Insight from molecular dynamics simulations", *Physical Chemistry Chemical Physics*, vol. 24, no. 36, pp. 22073–22082, **2022**, DOI: 10.1039/d2cp02655d.

[265] N. Rolland, J. F. Franco-Gonzalez, R. Volpi, M. Linares, and I. V. Zozoulenko, "Understanding morphology-mobility dependence in PEDOT:Tos", *Physical Review Materials*, vol. 2, no. 4, 045605, **2018**, DOI: 10.1103/PhysRevMaterials.2.045605.

[266] D. T. Simon, E. O. Gabrielsson, K. Tybrandt, and M. Berggren, "Organic Bioelectronics: Bridging the Signaling Gap between Biology and Technology", *Chemical Reviews*, vol. 116, no. 21, pp. 13009–13041, **2016**, DOI: 10.1021/acs.chemrev.6b00146.

[267] T. A. Welsh and E. R. Draper, "Water Soluble Organic Electrochromic Materials", *RSC Advances*, vol. 11, no. 9, pp. 5245–5264, **2021**, DOI: 10.1039/d0ra10346b.

[268] S. Nam, J. Kim, H. Lee, H. Kim, C.-S. Ha, and Y. Kim, "Doping Effect of Organosulfonic Acid in Poly(3-hexylthiophene) Films for Organic Field-Effect Transistors", *ACS Applied Materials & Interfaces*, vol. 4, no. 3, pp. 1281–1288, **2012**, DOI: 10.1021/am300141m.

[269] J. Chen, W. Zhang, L. Wang, and G. Yu, "Recent Research Progress of Organic Small-Molecule Semiconductors with High Electron Mobilities", *Advanced Materials*, vol. 35, no. 11, 2210772, **2023**, DOI: 10.1002/adma.202210772.

[270] J. Gao, C. Wang, D.-W. Han, and D.-M. Shin, "Single-Ion Conducting Polymer Electrolytes as a Key Jigsaw Piece for Next-Generation Battery Applications", *Chemical Science*, vol. 12, no. 40, pp. 13248–13272, **2021**, DOI: 10.1039/d1sc04023e.

[271] G. Foran, D. Mankovsky, N. Verdier, D. Lepage, A. Prébé, D. Aymé-Perrot, and M. Dollé, "The Impact of Absorbed Solvent on the Performance of Solid Polymer Electrolytes for Use in Solid-State Lithium Batteries", *iScience*, vol. 23, no. 10, 101597, **2020**, DOI: 10.1016/j.isci.2020.101597.

List of figures

Figure 1.1 Schematic overview of the research topics covered in this thesis. 3
Figure 2.1 Molecular orbital structure in polyacetylene. 9
Figure 2.2 Schematic representation of the Peierl’s instability theorem................................. 10
Figure 2.3 Quasi particles in polyacetylene. 11
Figure 2.4 Charge transport mechanism in conductive polymers.. 13
Figure 2.5 Structure of PEDOT:PSS.. 15
Figure 2.6 Primary doping of PEDOT:PSS.. 17
Figure 2.7 Secondary doping of PEDOT:PSS. 18
Figure 2.8 Thermoelectric effects. 22
Figure 2.9 Seebeck effect and thermoelectric generators.. 24
Figure 2.10 Thermoelectric efficiency and parameters.. 26
Figure 2.11 Ionic influence on the thermoelectric behavior of PEDOT PSS.......................... 29
Figure 2.12 Scattering geometry for specular and diffuse scattering..................................... 34
Figure 2.13 Functions of the Fresnel reflection and Fresnel transmission............................. 36
Figure 2.14 X-ray reflectometry investigation method.. 38
Figure 2.15 Scattering and reflection events in the frame of the DWBA. 41
Figure 2.16 Gravitational effect in neutron scattering methods... 43
Figure 3.1 Working principle of UV-Vis spectroscopy. 46
Figure 3.2 Working principle of ATR-FTIR spectroscopy.. 49
Figure 3.3 Exemplary FTIR spectra and their processing into an absorption spectrum. 50
Figure 3.4 Working principle of the SR method.. 52
Figure 3.5 Seebeck coefficient measurement setup. 54
Figure 3.6 2-point probe resistance measurement setup. 56
Figure 3.7 4-point probe resistance measurement setup. 57
Figure 3.8 EIS sample geometry and measurement setup. 59
Figure 3.9 Operating principle of EIS.. 61
Figure 3.10 Validation factors for EIS. 62

Figure 3.11 Working principle of surface profilometry. 64
Figure 3.12 Working principle of conductive AFM. 65
Figure 3.13 XRR setup and working principle.. 68
Figure 3.14 GISAXS measurement geometry and evaluation. 70
Figure 3.15 GISAXS data modeling. 72
Figure 3.16 ToF-NR setup of the D17 beamline at ILL. 74
Figure 3.17 XAVER measurement chamber. 76
Figure 3.18 Gas flow setup. 78
Figure 3.19 UNICORN measurement chamber. 79
Figure 4.1 Ionic liquids. 83
Figure 4.2 Additive, solvents, and cleaning agents. 84
Figure 4.3 Chemical etching of ITO substrates. 89
Figure 4.4 Sample preparation procedure. 91
Figure 4.5 Sample contacting. 94
Figure 5.1 ILs post-treatment effect on the oxidation level of PEDOT:PSS. 101
Figure 5.2 Exemplary Seebeck coefficient measurement procedure. 104
Figure 5.3 ILs post-treatment effect on PEDOT:PSS thin film properties. 105
Figure 5.4 ATR-FTIR spectra of IL post-treated PEDOT:PSS films. 107
Figure 5.5 Exemplary 2D GISAXS data of IL post-treated PEDOT:PSS films. 108
Figure 5.6 Horizontal line cuts of IL post-treated PEDOT:PSS films. 109
Figure 5.7 ILs post-treatment effect on the inner morphology of PEDOT:PSS films. 110
Figure 5.8 Model description of the IL doping effect on PEDOT:PSS films. 114
Figure 5.9 Aging investigation of IL post-treated PEDOT:PSS films. 116
Figure 6.1 Heat treatment dependent electrical conductivity of EMIM DCA treated PEDOT:PSS films. 124
Figure 6.2 Reversibility test of the heat treatment dependent conductivity. 125
Figure 6.3 2D GISAXS data of EMIM DCA post-treated PEDOT:PSS films upon heating. 127
Figure 6.4 Horizontal line cuts of EMIM DCA post-treated PEDOT:PSS films upon heating. 128
Figure 6.5 Morphological evolution of EMIM DCA post-treated PEDOT:PSS films upon heating. 129
Figure 6.6 Domain volume fraction evolution in EMIM DCA post-treated PEDOT:PSS films upon heating. 132

Figure 6.7 Oxidation level evolution of EMIM DCA post-treated PEDOT:PSS films upon heating. 134
Figure 6.8 Model description of EMIM DCA post-treated PEDOT:PSS films upon heat treatment. 135
Figure 7.1 Humidity dependent electrical resistance of EMIM DCA treated PEDOT:PSS films. 143
Figure 7.2 2D GISAXS data of EMIM DCA post-treated PEDOT:PSS films at different humidities. 145
Figure 7.3 Horizontal line cuts of EMIM DCA post-treated PEDOT:PSS films at different humidities. 146
Figure 7.4 Morphological features of EMIM DCA post-treated PEDOT:PSS films at different humidities. 147
Figure 7.5 Humidity evolution during EIS examination of EMIM DCA treated PEDOT:PSS films. 151
Figure 7.6 Humidity dependent EIS results of EMIM DCA treated PEDOT:PSS films. 152
Figure 7.7 Model description of EMIM DCA post-treated PEDOT:PSS films at different humidities. 154
Figure 8.1 Humidity evolution during the SR & ToF-NR examination of EMIM DCA treated PEDOT:PSS films. 163
Figure 8.2 Film thickness evolution of EMIM DCA post-treated PEDOT:PSS films at different humidities. 164
Figure 8.3 Pre-characterization results of EMIM DCA post-treated PEDOT:PSS films for ToF-NR & SR. 165
Figure 8.4 *In situ* static ToF-NR data of EMIM DCA post-treated PEDOT:PSS films at different humidities. 167
Figure 8.5 Kinetic ToF-NR curves of EMIM DCA post-treated PEDOT:PSS films at different humidities. 169
Figure 8.6 SLD and D_2O content evolution of EMIM DCA post-treated PEDOT:PSS films at different humidities. 170
Figure 8.7 D2O uptake kinetics of EMIM DCA post-treated PEDOT:PSS films at different humidities. 171
Figure 8.8 Humidity evolution during the EIS examination of EMIM DCA treated PEDOT:PSS films. 172

Figure 8.9 EIS results of EMIM DCA post-treated PEDOT:PSS films at different humidities. 173

Figure 8.10 Model description of the humidity influence on the charge transport in EMIM DCA post-treated PEDOT:PSS films. 176

List of publications

Publications related to this dissertation

- **A. L. Oechsle**, T. Schöner, C. Geiger, S. Tu, P. Wang, R. Cubitt, P. Müller-Buschbaum: „Unraveling the Humidity Influence on the Electrical Properties of Ionic Liquid Posttreated Poly(3,4-ethylene dioxythiophene):Poly(styrenesulfonate) Films"; *Macromolecules* 2023, 56, 22, 9117-9126 (DOI: 10.1021/acs.macromol.3c01842)
- **A. L. Oechsle**, T. Schöner, L. Deville, T. Xiao, T. Tian, A. Vagias, S. Bernstorff, P. Müller-Buschbaum: „Ionic Liquid-Induced Inversion of the Humidity-Dependent Conductivity of Thin PEDOT:PSS Films"; *ACS Applied Materials and Interfaces* 2023, 15, 40, 47682-47691 (DOI: 10.1021/acsami.3c08208)
- **A. L. Oechsle**, J. E. Heger, N. Li, S. Yin, S. Bernstorff, P. Müller-Buschbaum: „In Situ Observation of Morphological and Oxidation Level Degradation Processes within Ionic Liquid Post-treated PEDOT:PSS Thin Films upon Operation at High Temperatures"; *ACS Applied Materials and Interfaces* 2022, 14, 27, 30802-30811 (DOI: 10.1021/acsami.2c05745)
- **A. L. Oechsle**, J. E. Heger, N. Li, S. Yin, S. Bernstorff, P. Müller-Buschbaum: „Correlation of Thermoelectric Performance, Domain Morphology and Doping Level in PEDOT:PSS Thin Films Post-Treated with Ionic Liquids"; *Macromolecular Rapid Communication* 2021, 42, 20, 2100397 (DOI: 10.1002/marc.202100397)

Further publications

- T. Tian, S. Tu, A. Xu, S. Yin, **A. L. Oechsle**, T. Xiao, A. Vagias, J. Eichhorn, J. Suo, Z. Yang, S. Bernstorff, P. Müller-Buschbaum: „Unraveling the Morphology-Function Correlation of Mesoporous ZnO Films upon Water Exposure"; *Advanced Functional Materials* 2023, 2311793 (DOI: 10.1002/adfm.202311793)

- N. Li, R. Guo, **A. L. Oechsle**, M. A. Reus, S. Liang, L. Song, K. Wang, D. Yang, F. Allegretti, A. Kumar, M. Number, J. Berger, S. Bernstorff, H. Iglev, J. Hauer, R. A. Fischer, J. V. Barth, P. Müller-Buschbaum: „Operando Study of Structure Degradation in Solid-State Dye-Sensitized Solar Cells with a TiO_2 Photoanode Having Ordered Mesopore Arrays"; *Solar RRL* 2022, 6, 2200373 (DOI: 10.1002/solr.202200373)
- S. Tu, T. Tian, **A. L. Oechsle**, S. Yin, X. Jiang, W. Cao, N. Li, M. A. Scheel, L. K. Reb, S. Hou, A. S. Bandarenka, M. Schwartzkopf, S. V. Roth, P. Müller-Buschbaum: „Improvement of the thermoelectric properties of PEDOT:PSS films via DMSO addition and DMSO/salt post-treatment resolved from a fundamental view"; *Chemical Engineering Journal* 2022, 429, 10, 132295 (DOI: 10.1016/j.cej.2021.132295)
- R. Guo, D. Han, W. Chen, L. Dai, K. Ji, Q. Xiong, S. Li, L. K. Reb, M. A. Scheel, S. Pratap, N. Li, S. Yin, T. Xiao, S. Liang, **A. L. Oechsle**, C. L. Weindl, M. Schwartzkopf, H. Ebert, P. Gao, K. Wang, M. Yuan, N. C. Greenham, S. D. Stranks, S. V. Roth, R. H. Friend, P. Müller-Buschbaum: „Degradation mechanisms of perovskite solar cells under vacuum and one atmosphere of nitrogen"; *Nature Energy* 2021, 6, 10, 977-986 (DOI: 10.1038/s41560-021-00912-8)
- M. Günther, D. Blätte, **A. L. Oechsle**, S. S. Rivas, A. A. Y. Amin, P. Müller-Buschbaum, T. Bein, T. Ameri: „Increasing Photostability of Inverted Nonfullerene Organic Solar Cells by Using Fullerene Derivative Additives"; *ACS Applied Materials and Interfaces* 2021, 13, 16, 19072-19084 (DOI: 10.1021/acsami.1c00700)
- **A. L. Oechsle**, L. Lewis, W. Y. Hamad, S. G. Hatzikiriakos, M. J. MacLachlan: „CO_2 -Switchable Cellulose Nanocrystal Hydrogels"; *Chemistry of Materials* 2018, 30, 2, 376-385 (DOI: 10.1021/acs.chemmater.7b03939)
- F. Stempfle, B. Schemmer, **A. L. Oechsle**, S. Mecking: „Thermoplastic polyester elastomers based on long-chain crystallizable aliphatic hard segments"; *Polymer Chemistry* 2015, 6, 40, 7133-7137 (DOI: 10.1039/C5PY01209K)

Scientific reports

- **A. L. Oechsle**, R. Cubitt, P. Müller-Buschbaum: „Humidity influence on ionic liquid post-treated PEDOT:PSS films"; *Lehrstuhl für Funktionelle Materialien*, *Annual Report* 2023, to be published

- **A. L. Oechsle**, S. Bernstorff, P. Müller-Buschbaum: „In situ investigation of the electrical conductivity degradation in EMIM DCA post-treated PEDOT:PSS thin films upon heat treatment"; *Lehrstuhl für Funktionelle Materialien*, *Annual Report* 2022, pp. 40-41
- **A. L. Oechsle**, S. Bernstorff, P. Müller-Buschbaum: „Revealing the positive influence on thermoelectric properties of ionic liquid post-treatment of PEDOT:PSS thin films on the domain morphology and doping level"; *Lehrstuhl für Funktionelle Materialien*, *Annual Report* 2021, pp. 40-41
- **A. L. Oechsle**, S. Bernstorff, P. Müller-Buschbaum: „In-situ investigation of the thermal stability of thermoelectric thin films based on EMIM DCA post-treated PEDOT:PSS"; *Lehrstuhl für Funktionelle Materialien*, *Annual Report* 2020, pp. 42-43
- **A. L. Oechsle**, P. Müller-Buschbaum: „Improvement of the thermoelectric properties of PEDOT:PSS thin films by posttreatment with ionic liquids"; *Lehrstuhl für Funktionelle Materialien*, *Annual Report* 2019, pp. 42-43
- **A. L. Oechsle**, N. Saxena, P. Müller-Buschbaum: „Post-treatment of thermoelectric polymer thin films with ionic liquids"; *Lehrstuhl für Funktionelle Materialien*, *Annual Report* 2018, pp. 32-33

Conference talks

- **A. L. Oechsle**, J. E. Heger, N. Li, S. Yin, S. Bernstorff, P. Müller-Buschbaum: „In situ investigation of the domain morphology and doping level of thermoelectric PEDOT:PSS thin films under different ambient conditions"; *ACS Spring Meeting, Indianapolis (USA)*, 26 – 30 March 2023
- **A. L. Oechsle**, J. E. Heger, N. Li, S. Yin, S. Bernstorff, P. Müller-Buschbaum: „In situ investigation of thermoelectric thin films based on ionic liquid post-treated PEDOT:PSS"; *DPG-Herbsttagung, Regensburg (Germany)*, 04 – 09 September 2022
- **A. L. Oechsle**, J. E. Heger, N. Li, S. Yin, S. Bernstorff, P. Müller-Buschbaum: „In situ investigations of morphology degradation and oxidation level changes in EMIM DCA post-treated PEDOT:PSS thin films upon external influence"; *12th Energy Colloquium of the MEP, Garching (Germany)*, 28 July 2022
- **A. L. Oechsle**, J. E. Heger, N. Li, S. Yin, S. Bernstorff, P. Müller-Buschbaum: „In-situ investigation of thermoelectric thin films based on ionic liquid post-treated PEDOT:PSS"; *E-MRS Spring Meeting, (virtual)*, 30 Mai – 03 June 2022

Conference poster presentations

- **A. L. Oechsle**, J. E. Heger, N. Li, S. Yin, S. Bernstorff, P. Müller-Buschbaum: „In Situ Investigation of the Domain Morphology and Doping Level of Thermoelectric PEDOT:PSS Thin Films under Different Ambient Conditions"; *MLZ User Meeting, München (Germany)*, 08 – 09 December 2022
- **A. L. Oechsle**, J. E. Heger, N. Li, S. Yin, S. Bernstorff, P. Müller-Buschbaum: „In Situ Investigation of the Domain Morphology and Doping Level of Thermoelectric PEDOT:PSS Thin Films under Different Ambient Conditions"; *e-conversion Conference, Venice (Italy)*, 04 – 07 October 2022
- **A. L. Oechsle**, J. E. Heger, N. Li, S. Yin, S. Bernstorff, P. Müller-Buschbaum: „Thermal degradation of EMIM DCA post-treated PEDOT:PSS thermoelectric thin films, investigated via in-situ GISAXS"; *DPG-Herbsttagung, (virtual)*, 21 September – 01 October 2021
- **A. L. Oechsle**, J. E. Heger, N. Li, S. Yin, S. Bernstorff, P. Müller-Buschbaum: „Conductivity stability of EMIM DCA post-treated semi-conducting PEDOT:PSS polymer thin films under elevated temperatures"; *11th Energy Colloquium of the Munich School of Engineering, (virtual)*, 28 – 29 July 2021
- **A. L. Oechsle**, J. E. Heger, N. Li, S. Yin, S. Bernstorff, P. Müller-Buschbaum: „Conductivity stability of EMIM-DCA post-treated semi-conducting PEDOT:PSS polymer thin films under elevated temperatures"; *DPG-Frühjahrstagung, (virtual)*, 22 – 24 March 2021
- **A. L. Oechsle**, J. E. Heger, N. Li, S. Yin, S. Bernstorff, P. Müller-Buschbaum: „Conductivity stability of EMIM-DCA post-treated semi-conducting PEDOT:PSS polymer thin films under elevated temperatures"; *MLZ User Meeting, (virtual)*, 08 – 09 December 2020
- **A. L. Oechsle**, J. E. Heger, N. Li, S. Yin, H. Stadler, S. Bernstorff, P. Müller-Buschbaum: „EMIM-DCA post-treatment of semi-conducting PEDOT:PSS polymer thin films to improve their thermoelectric properties"; *MLZ User Meeting, Munich (Germany)*, 10 – 11 December 2019
- **A. L. Oechsle**, J. E. Heger, N. Li, S. Yin, H. Stadler, S. Bernstorff, P. Müller-Buschbaum: „Investigation of different treatment methods on semi-conducting polymer thin films to improve their thermoelectric properties"; *9th Energy Colloquium of the Munich School of Engineering, Garching (Germany)*, 1 August 2019

- **A. L. Oechsle**, N. Saxena, P. Müller-Buschbaum: „Preparation of semiconducting polymer thin films and methods of post-treatment to influence their thermoelectric properties"; *3rd Winter School "Food and Energy" of the Graduate Center MSE, Raitenhaslach (Germany)*, 18 – 21 February 2019

Acknowledgments

As I write these last lines of my dissertation and look back on my time as a PhD student, I am overwhelmed with deep gratitude to all the countless people who have made these years so exciting, beautiful, and memorable.

First of all, I would like to thank Peter Müller-Buschbaum, who gave me the opportunity to join the Chair for Functional Materials and introduced me to the topic of organic thermoelectric materials. I am grateful for his trust in my abilities and for providing me with resources, time, and space to work on my research projects. Furthermore, I would like to thank him for his guidance within the academic research environment, the several opportunities to participate in international conferences, and the possibilities to go on numerous beamtimes at synchrotron facilities like ELETTRA and DESY, or neutron sources like the MLZ and ILL; something I would not have imagined experiencing before starting at E13.

In this context, I would also like to thank all the beamline scientists and collaborators for not getting tired of answering countless questions and helping us beamline users with problems even during the night shift. I want to thank Sigrid Bernstorff for her awesome support and patience, but also for her excellent qualities as a tourist guide during some after-work trips to Trieste. Furthermore, I want to name Christian Morello from ELETTRA, Stephan Roth, Matthias Schwartzkopf, Mark Gensch, Jan Rubeck from DESY, Robert Cubitt, and Thomas Saerbeck from ILL. Also, a big thanks to all my beamtime team members who contributed so immensely to make these beamtimes not just successful but also always so fun, even through times of severe sleep deprivation, failing experiments, and hours of beam dump.

I would also like to thank Christine Papadakis for always having an open door and for her support in several matters of my journey as a PhD. Furthermore, a warm thank you to our always friendly secretaries, Carola Kappauf and Marion Waletzki, for their substantial help with mastering the bureaucratic jungle. A big thanks to Reinhold Funer in our E13 workshop for his patience with the not-always-accurate technical drawings and his dedication to realizing all the crazy setup ideas we come up with nearly every day, many of which made my experiments possible in the first place.

During my time as a PhD student, I had the chance to supervise some bachelor's and master's students on their way into research. I am grateful for this experience, as they did not just contribute to some of my research work but, more importantly, brought new perspectives, ideas, and always interesting discussions. Therefore, thank you to Christian Schott, Hagen Übele, Lewin Deville, Andreas Steinhart, and Florian Maly, and especially thank you to Tobias Schöner and Simon Wegener for your dedication and interest in my research topic.

When I moved to Munich five years ago to start my PhD I hardly knew anyone here, but that did not matter because the warm welcome I received in this group was simply incredible. Soon, this chair was not just the place where I worked, but it quickly became a place filled with friendship and happiness. For this, I am more grateful than I can ever express with words. Shout out to all the members of E13 and E59, who I cannot possibly name all but who made these past years and the PhD experience so unforgettable.

Thank you to the previous PhD generations, especially Franziska Löhrer, Nitin Saxena, Lucas Kreuzer, Shambhavi Pratap, Lorenz Bießmann, Nian Li, Sebastian Grott, Simon Schaper, Tobias Widmann, Wei Chen, Johannes Schlipf, Xinyu Jiang, Nuri Hohn, and many more, for showing me the labs and devices, and teaching me how everything works at the chair. However, more importantly, thank you for immediately including me in the group and introducing me to Schwasi escalations, the best Mexicaner at Rennbahn, Hopfendolde, and thank you for sharing your knowledge on how to survive DPG meetings and beamtimes.

The PhD journey, but also life itself, can be pretty tough sometimes, but there were people who, even in the hardest moments, made everything seem easier and are the reason why I stuck to it and kept smiling. For you guys, I am so deeply thankful. Julian Heger, I will never forget my very first beamtime with you in Bella Italia. Manuel Reus, thank you for so many conversations and always having an open ear. Lennart Reb, all those happy moments during late-night shifts and flunky ball in the corridor will be fondly remembered. Christina Geiger, thanks for being my office buddy almost the whole time. Christian Weindl, I am waiting for the opening of your pizza restaurant. Julija Reitenbach, thank you for being this always supportive and incredibly funny person. Simon Wegener, thanks for spending time with me, even though I knit and do puzzles. Lukas Spanier, I hope the meme supply will never end. Big thanks also to, Dominik Schwaiger, Morgan Le Dü, Christopher Everett, Fabian Apfelbeck, Linus Huber, Yanan Li, Huaying Zhong, Ivana Pivarnikova, Thien An Pham, Benjamin Predeschly, Kaltrina Shehu, Renjun Guo, Kerstin Wienhold, Altantulga Buyan-Arivjikh, Thomas Baier, Christoph Lindenmeir, Suo Tu, Ting Tian, Volker Körstgens, Yuxin Liang, Kun Sun, Lea Westphal,

David Kosbahn, Peixi Wang, Apostolos Vagias, Wenqi Xu, Tobias Hölderle, and Constantin Harder. Last but not least, thanks the several bachelor and master students joining and leaving E13 on a regular basis. I will keep all of you in loving memory, be it our shared conference experiences, our summer school hikes, our countless fruitful discussions, our karaoke evenings, Käsespätzle cooking evenings, lab cleans, numerous dinners and celebrations, our boulder meetings, chilled evenings on the balcony in summer (sometimes with hat and scarf), beer garden events and so many more. Some of you are not just colleagues anymore; I am lucky to call some of you my friends now, and you cannot imagine how grateful I am for having met you.

Even though the dissertation takes up a significant amount of time, there is also a life beyond the university. I am talking about all the people who helped me keep the balance alongside work; thanks to my beach volleyball people, my climbing and boulder buddies, my painting and crafting people, my Canada boys, and my party, cocktail, or coffee chat people.

One particular person in my life besides (well, at least partly beside) from university is Marci. You are this incredible friend I know will be in my life no matter what. Thank you for all the knitting evenings, the countless phone calls, the 90ies parties, the anti-stress Aperol, for sometimes being my rational voice, and thank you for making even throwing away spoiled onions or washing dishes back in our flat in Würzburg to such happy memories. In this context, I also want to mention two more of my most precious achievements from my chemistry studies, Steffi and Maike. Thank you for your indescribable friendship, for always having open ears, for the craziness and fun you brought into my life, for being by my side whatever the film director of my life will think of next, and especially for making the sound effects.

A special thanks goes to Sebastian. Thanks for patiently listening to me whenever I excitedly talked about PEDOT:PSS domains or, in the next minute, complained about everything. I do not love the word ‘unravel’ more than I love you ;) Thank you for constantly reminding and convincing me to take breaks, reassuring me, and putting everything into perspective again. But mainly, thank you for being there for me during one of the hardest times in my life.

Mein aller größter Dank gilt meiner Familie, meiner Schwester Lisa aber ganz besonders meinen Eltern Ilse und Thomas. Danke, dass ihr wirklich immer hinter mir steht, nie auch nur eine Sekunde an mir und meinen Entscheidungen zweifelt. Ihr habt mir all das überhaupt erst ermöglicht und dafür bin ich so sehr dankbar. Ich kann mich so unheimlich glücklich schätzen euch zu haben.